Robust and Durable Liquid-Repellent Surfaces

Faze Chen,[1, 2] Yaquan Wang,[3] Yanling Tian,[4]* Dawei Zhang,[1, 2] Jinlong Song,[5]* Colin R. Crick,[6] Claire J. Carmalt,[7] Ivan P. Parkin[7] and Yao Lu[3]*

[1] School of Mechanical Engineering, Tianjin University, Tianjin 300350, China
[2] Key Laboratory of Mechanism Theory and Equipment Design of Ministry of Education, Tianjin University, Tianjin 300350, China
[3] Department of Chemistry, Queen Mary University of London, London E1 4NS, UK
[4] School of Engineering, University of Warwick, Coventry CV4 7AL, UK
[5] School of Mechanical Engineering, Dalian University of Technology, Dalian 116024, China
[6] School of Engineering and Materials Science, Queen Mary University of London, London E1 4NS, UK
[7] Department of Chemistry, University College London, 20 Gordon Street, London WC1H 0AJ, UK

*Corresponding author.

E-mail addresses: yao.lu@qmul.ac.uk (Y. Lu); y.tian.1@warwick.ac.uk (Y. Tian); songjinlong@dlut.edu.cn (J. Song).

Content

Abstract

Liquid-repellent surfaces, such as superhydrophobic surfaces, superoleophobic surfaces, and slippery liquid-infused surfaces, have drawn keen research interest from the communities engaged in chemical synthesis, interfacial chemistry, surface engineering, bionic manufacturing and micro-nano machining. This is due to their great potential applications in liquid-proofing, self-cleaning, chemical resistance, anti-icing, water/oil remediation, biomedicine, *etc*. However, poor robustness and durability that notably hinders the real-world applications of such surfaces remains their Achilles heel. The past few years have witnessed rapidly increasing publications that address the robustness and durability of liquid-repellent surfaces, and many breakthroughs have been achieved. This review provides an overview of the recent progress made towards robust and durable liquid-repellent surfaces. First, we discuss the wetting of solid surface and its generally-adopted characterisation methods, and introduce typical liquid-repellent surfaces. Second, we focus on various evaluation methods of the robustness and durability of liquid-repellent surfaces. Third, the recent advances in design and fabrication of robust and durable liquid-repellent surfaces are reviewed in detail. Fourth, we present the applications where these surfaces have been employed in fields like chemistry, engineering, biology and in daily life. Finally, we discuss the possible research perspectives in robust and durable liquid-repellent surfaces. By presenting such state-of-the-art of this significant and fast-developing area, we believe that this review will inspire multidisciplinary scientific communities and industrial circles to develop novel liquid-repellent surfaces that can meet the requirements of various real-world applications.

1 Introduction

Wetting, referring to the process of making contact between a liquid and a solid (or liquid) surface, is a ubiquitous phenomenon that exists in our daily life, industry, agriculture, biology, *etc*., from raindrops on a car windshield to drastic shape transition of living tissues.[1-8] Wetting shows a range of curious, yet useful behaviors which make the fields concerned with their study intrinsically multidisciplinary, spanning across several areas of chemistry, biology, physics, engineering, *etc*. Since the introduction of Young's equation in 1805,[9] research on wetting and wettability has continued for over two hundred years. As an important and fascinating subfield of wetting, non-wettable surfaces, which are also termed as liquid-repellent surfaces, have drawn keen yet continuously increasing interests from both academic and industrial communities.[10-14] Upon the discovery of the underlying mechanism (*i.e.*, rough structures and low surface energy) of the self-cleaning and super water repellence of Lotus leaf,[15,16] superhydrophobic surfaces became the earliest research focus for the topic of liquid repellence. Subsequently, the key structural feature (*i.e.*, re-entrant microstructures) of super oil-repellent surfaces was revealed,[17] and the natural oil-repellence of the cuticle of springtail was also discovered,[18] both of which boosted the development of superoleophobic surfaces in air. Later, the fish scale was demonstrated to be super oil-repellent underwater due to its superhydrophilicity in air,[19] which introduced underwater superoleophobicity to the family of super liquid-repellent surface. Moreover, a novel *Nepenthes* pitcher plant-inspired slippery liquid-/lubricant-infused surface (SLIS) with excellent non-wettable performance (*e.g.*, negligible contact angle hysteresis and low sliding angles) was reported in 2011,[20] which further broadened the research scope of liquid-repellent surfaces. During the last 20 years, much attention has been paid on superhydrophobic surfaces, superoleophobic surfaces (both in air and underwater), and SLISs, and plentiful and significant achievements on these liquid-repellent surfaces have been obtained. As depicted in Fig. 1, when searching the topic of "superhydrophobi*, superoleophobi* or slippery l*-infused surface" in the *Web of Science*, significant numbers of research articles and reviews could be indexed, which showed a rapid increase most years. Recently, the topic of "superwettability" was selected as one of the 2021 Top Ten Emerging Technologies in Chemistry released by the International Union of Pure and Applied Chemistry (IUPAC).[21] Based on the comprehensive and in-depth study of the anti-wetting property of liquid-repellent surfaces, diverse potential applications have been explored and verified especially at a lab-scale, such as self-cleaning,[22] drag reduction,[23] oily wastewater remediation,[24,25] liquid/gas manipulation,[26-28] anti-icing,[29,30] anti-fouling/-corrosion,[31,32] enhanced heat transfer,[33-35] energy harvesting/conversion,[36,37] and biomedical engineering,[38-41] just to name a few.

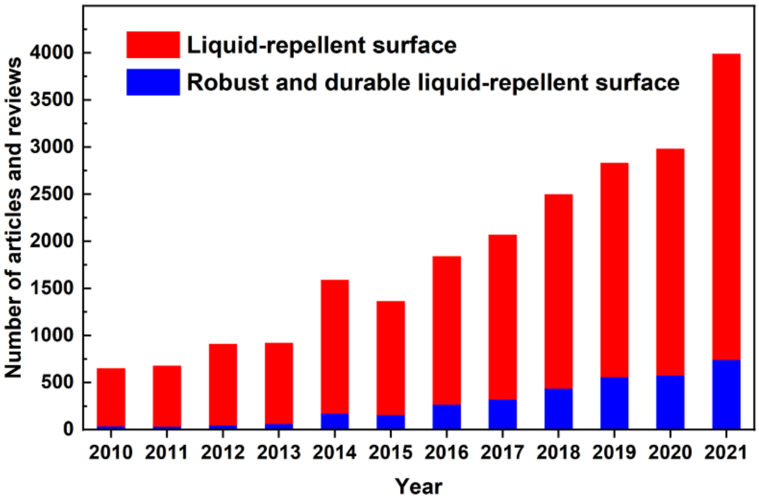

Fig. 1 Number of published articles and reviews per year indexed in the *Web of Science*. Topic of "superhydrophobi*, superoleophobi* or slippery l*-infused surface" was used to search the publications on "liquid-repellent surfaces", and topic of "robust or durable" was combined to refine the papers on "robust and durable liquid-repellent surfaces".

Although tremendous progress has been made on the research of these liquid-repellent surfaces, the realization of their real-world applications and industrializations remains challenging. This mainly originates from the poor robustness and durability of the liquid-repellent surfaces.[14,42-45] Firstly, it is well known that the liquid repellence of superhydrophobic and superoleophobic surfaces is attributed to the locked air cushion within the rough structures, and that of SLIS originates from the infused lubricant layer, both of which are thermodynamically unstable under some conditions, such as long-term immersion in the repelling liquid, vapor condensation, increased hydraulic pressure, *etc*. As a result, the super-liquid-repellent surfaces change their wetting from the Cassie-Baxter to the Wenzel state due to the lost air cushion, while the SLIS suffers from the depletion of infused lubricant, thus rendering the loss of liquid repellence. Secondly, micro/nanoscale rough structures and special surface chemistry are generally two essential factors of liquid-repellent surfaces, but these features (especially the rough surface textures) are intrinsically fragile and thereby are highly susceptible to mechanical abrasion, dynamic impacting, peeling, *etc*., since the local pressure applied on the surface textures is high even when the corresponding mechanical loading is small. Mechanical damage of surface architectures and/or surface chemistry always results in the deterioration of the liquid repellence. Lastly, when liquid-repellent surfaces are exposed to chemically active conditions, such as being immersed in corrosive aqueous solutions, exposed to UV, or treated by plasma, *etc*., chemical processes often occur on the surfaces either slowly or rapidly, which may change their surface textures and/or surface chemistry, leading to the loss of their liquid repellence. Therefore, extensive efforts have been made to address the robustness and durability of liquid-repellent surfaces in recent years. As shown in Fig. 1, when the topics of "robust or durable" and "superhydrophobi*, superoleophobi* or slippery l*-infused surface" were used to search the publications in the *Web of Science*, a large number of research articles and reviews could also be found, and the number of these papers increased annually, but its relative proportion was less than a quarter of the publications of liquid-repellent surfaces, indicating that plenty of room exists for the study of robust and durable liquid-repellent surfaces.

To improve the robustness and durability of artificial liquid-repellent surfaces, various strategies have been proposed to address the thermodynamic durability, mechanical durability, chemical durability, or several aspects of them. First of all, the matrix and surface chemistry should be considered, for example, abrasion-tolerant substrates could partially improve the mechanical durability of liquid-repellent surfaces,[46,47] while carbon-fluorine-based surface agents usually generate better chemical durability than carbon-hydrogen-based groups.[48] Next, various special surface textures, such as re-entrant microstructures,[49,50] densely and closely packed nanostructures,[51] self-similar rough structures,[52] hierarchical micro/nano structures,[53] *etc*., have been designed to enhance the robustness and durability of liquid-repellent surfaces from different aspects. For those substrates covered with liquid-repellent coatings, increasing the bonding strength among them is a universal and effective strategy.[54] In addition, imparting liquid-repellent surfaces with self-healing property, such as restorable microstructure, self-healable surface chemistry, or both, is another alternative method to improve their durability.[55,56] Moreover, selective combination of the proposed strategies have been recently demonstrated to be more effective in further improving the robustness and durability of liquid-repellent surfaces,[47,57-59] which should be a promising solution for moving liquid-repellent surfaces towards real-world applications.

This review provides an overview of recent progress towards robust and durable liquid-repellent surfaces and lays foundation for further in-depth research of this topic. Fig. 2 schematically illustrates the main context of this review, including the robustness and durability of liquid-repellent surfaces, the recently proposed design and fabrication strategies for robust and durable liquid-repellent surfaces, as well as their emerging applications. Specifically, the wetting of solid surface in both air and liquid and the common wettability characterisation methods will be discussed, followed by a brief summary of typical liquid-repellent surfaces, including superhydrophobic, superoleophobic and SLISs (Section 2). After introducing the thermodynamic, mechanical and chemical durability of liquid-repellent surfaces, as well as their general evaluation methods (Section 3), we will present a detailed discussion of recent progress on the design and fabrication of robust and durable liquid-repellent surfaces (Section 4). Then we briefly discuss several applications of robust and durable liquid-repellent surfaces, such as protection of solid substrate, liquid/gas harvesting/transport/manipulation, immiscible liquids separation, electricity generation, and enhanced heat transfer (Section 5). Finally, we draw conclusions and propose possible research perspectives in robust and durable liquid-repellent surfaces (Section 6). This review will draw great attention from researchers engaged in functional surfaces fabrication, especially those in chemical synthesis, interfacial chemistry, surface engineering, bionic manufacturing, micro-nano machining, *etc*. Moreover, this review may appeal to those communities that are devoted to promoting commercial applications of liquid-repellent surfaces towards our daily lives.

2 Liquid-Repellent Surfaces

Liquid repellence is a fundamental phenomenon of wetting, and liquid-repellent surfaces are generally characterised by extremely anti-wetting property and high liquid droplet mobility. Firstly, a brief introduction of the basic theories of the wetting of solid surface (both in air and liquid) is provided followed by a summary of the commonly used wettability characterisation methods, and finally three typical liquid-repellent surfaces: superhydrophobic surfaces, superoleophobic surfaces, and slippery liquid-infused surfaces (SLISs) are introduced.

2.1 Wetting of Solid Surface

Wetting generally involves the spreading of a liquid on a solid/liquid surface and the formation of contact line and contact angle (CA) at the triple-phase interface. The solid surface may be exposed to either a gas (usually air, or any other gaseous environment that is chemically inert to the solid and liquid) or another immiscible liquid.

2.1.1 Solid surface in air

When the wetting of a solid surface occurs in air, a triple-phase interface consisting of solid, gas (*i.e.*, air) and liquid is built, and a CA, θ, which is defined as the angle between the tangent to the liquid-gas interface and the solid surface at the three-phase contact line can be observed, as shown in Fig. 3a. The CA is an indication of how likely the surface is to be wetted by the liquid: low CA means a tendency of the liquid to spread and adhere to the surface, whereas high CA suggests the liquid-repellent tendency of the surface. In 1805, Young first described the CA of an ideal solid surface (*i.e.*, one that is atomically smooth, chemically homogeneous, nonreactive and nondeformable by the liquid or gas) by proposing the Young's model, as depicted in Fig. 3a.[9] For an ideal solid surface wetted by a liquid droplet, the formed CA depends only on the physico-chemical nature (*i.e.*, the surface tension) of the three phases and is independent of both the system geometry and gravity, which is expressed by the Young's equation:

$$\gamma_{SV}=\gamma_{SL}+\gamma_{LV}\cos\theta_Y \tag{1}$$

where γ is the surface tension (or surface free energy) and the subscripts SV, SL and LV respectively refer to the solid-vapor, solid-liquid and liquid-vapor interfaces; θ_Y is the intrinsic CA, or Young CA, of the liquid droplet on the solid surface. This equation was justified as the result of an equilibrium of forces at that time, and the "up" component, $\gamma_{LV}\sin\theta_Y$, was balanced by the strain field existing near the three-phase contact line in the solid.[60,61]

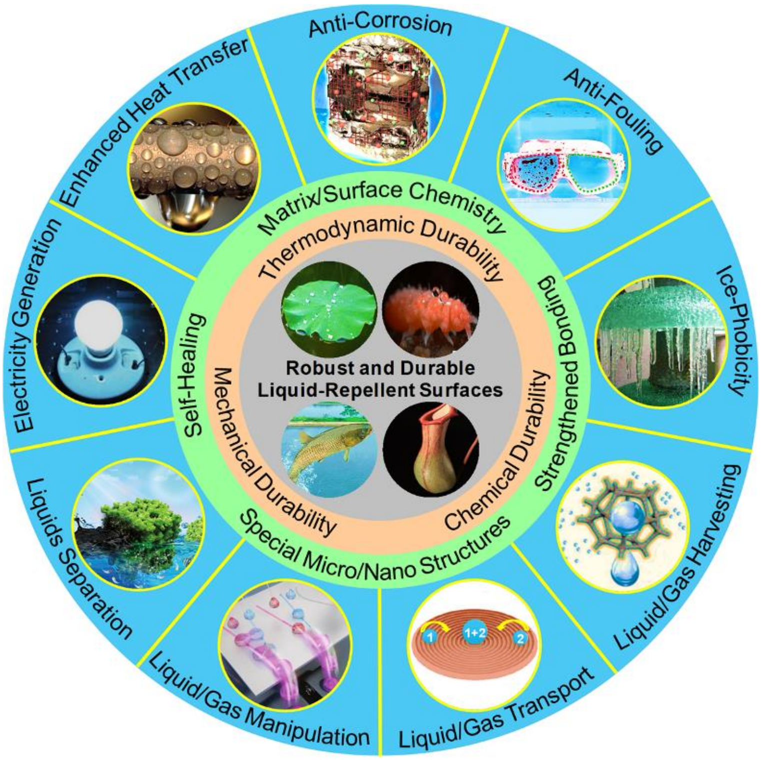

Fig. 2 A schematic summary of the robustness and durability of liquid-repellent surfaces, as well as the fabrication strategies and emerging applications of robust and durable liquid-repellent surfaces. Lotus leaf: Reproduced with permission from ref. 62. Copyright (2020) Elsevier B.V. Springtail: Reproduced with permission from ref. 63. Copyright (2019) Li *et al*. Fish scale: Reproduced with permission from ref. 64. Copyright (2017) The Royal Society of Chemistry. *Nepenthes* pitcher plant: Reproduced with permission from ref. 65. Copyright (2016) Nature Publishing Group. Anti-corrosion: Reproduced with permission from ref. 66. Copyright (2017) The Royal Society of Chemistry. Anti-fouling: Reproduced with permission from ref. 67. Copyright (2020) WILEY-VCH GmbH. Ice-phobicity: Reproduced with permission from ref. 68. Copyright (2013) American Chemical Society. Liquid/gas harvesting: Reproduced with permission from ref. 69. Copyright (2021) Elsevier B.V. Liquid/gas transport: Reproduced with permission from ref. 70. Copyright (2020) WILEY-VCH Verlag GmbH & Co. KGaA, Weinheim. Liquid/gas manipulation: Reproduced with permission from ref. 71. Copyright (2017) The Royal Society of Chemistry. Liquids separation: Reproduced with permission from ref. 72. Copyright (2017) Chen *et al*. Electricity generation: Reproduced with permission from ref. 73. Copyright (2014) Nature Publishing Group. Enhanced heat transfer: Reproduced with permission from ref. 74. Copyright (2013) Materials Research Society.

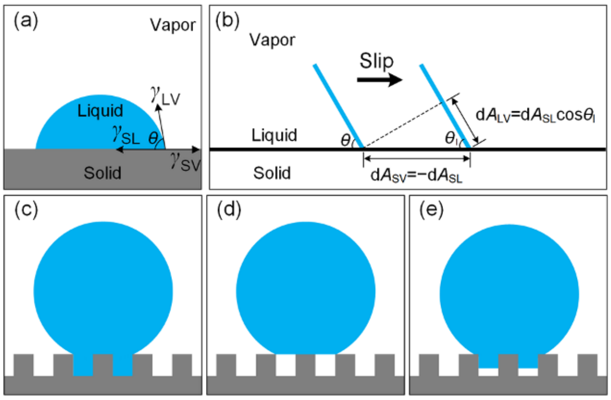

Fig. 3 (a) Illustration of Young's model. (b) Thermodynamic derivation of Young's equation. Reproduced with permission from ref. 75. Copyright (2011) IOP Publishing. (c–e) Schematic of Wenzel's model, Cassie-Baxter's model, and mixed model, respectively.

From the point of thermodynamics, the Gibbs free energy, G, of the solid-liquid-gas system can be written as[76]:

$$G=\gamma_{SL}A_{SL}+\gamma_{SV}A_{SV}+\gamma_{LV}A_{LV} \tag{2}$$

where A is the contact interface area. When the three-phase system achieved equilibrium state, G must be a minimum, that is, the thermodynamic derivation $dG = 0$. As shown in Fig. 3b, when the liquid-vapor interface slips freely at a certain inclination θ_I along the solid surface, the variation of the contact areas must meet the geometrical conditions of $dA_{SV} = -dA_{SL}$ and $dA_{LV} = dA_{SL}\cos\theta_I$. Then eqn (1) could be deduced thermodynamically, and the inclination θ_I is equal to θ_Y.

However, ideal solid surfaces rarely exist, and real surfaces are usually topographically rough and chemically heterogeneous. For a topographically rough but chemically homogeneous solid surface, its actual (*i.e.*, microscopic) surface is greater than its geometrical (*i.e.*, apparent or macroscopic) surface by a coefficient r, the roughness factor introduced by Wenzel in 1936.[77] In addition, the rough structures at solid-liquid contact area are supposed to be completely filled with the liquid (Fig. 3c). Therefore, the solid-liquid and solid-vapor contact interfacial area (*i.e.*, A_{SL} and A_{SV}, respectively) should be mathematically multiplied by the factor r, and the Gibbs free energy of the wetting system on such a rough solid surface, G_r, can be written as:

$$G_r=r\gamma_{SL}A_{SL}+r\gamma_{SV}A_{SV}+\gamma_{LV}A_{LV} \tag{3}$$

The minimum of G_r ($dG_r = 0$) yields the well-known Wenzel equation:[77]

$$r\gamma_{SV}=r\gamma_{SL}+\gamma_{LV}\cos\theta_W \tag{4}$$

where θ_W is the apparent CA in Wenzel model. Eqns (1) and (4) provide the relationship between θ_W and θ_Y:

$$\cos\theta_W=r\cos\theta_Y \tag{5}$$

Since $r > 1$ for a rough surface, eqns (4) and (5) clearly show that the surface roughness amplifies both wetting and non-wetting properties of a solid surface, depending on the intrinsic wettability (*i.e.*, θ_Y) of the corresponding smooth surface. For a smooth surface with intrinsic CA < 90°, roughening enables it to become more wettable, while a surface with intrinsic CA > 90° becomes more non-wettable when roughness is present. These tendencies are generally valid for a rough solid surface, but when r is made arbitrarily large ($r >> 1$), complete wetting ($\cos\theta_W > 1$) or complete drying ($\cos\theta_W < -1$) seems to be implied. However, such features could not be obtained because Wenzel's assumptions, such as the liquid completely wets the rough structures at the solid-liquid contact area and there is a single Gibbs free energy minimum, *etc*. are not satisfied.[78,79] Additionally, one essential condition to approximate the stable CA by eqn (5) is employing sufficiently large droplet volume, which is supposed to be 10^2–10^3 orders of magnitude compared to the roughness scale.[78,80] The typical scale of a real solid surface roughness is in the range of nanometers to micrometers, so a liquid droplet with a volume of a few microliters (*i.e.*, diameter in millimeter scale) may be sufficiently large for the estimation of θ_W.

In 1944, Cassie and Baxter investigated the wettability of rough porous surfaces by considering the trapped air in the microporous structures.[81] When liquid wets a rough porous surface, the apparent solid-liquid contact interface is actually composed of microscopic solid-liquid interface and vapor-liquid interface (Fig. 3d), so it can be regarded as the wetting on a chemically heterogeneous surface. By taking surface chemical heterogeneities into consideration, the water CA of a rough solid surface could be described as:[81]

$$\cos\theta_{\text{C-B}} = f_1 \cos\theta_Y - f_2 \tag{6}$$

where $\theta_{\text{C-B}}$ is the apparent CA in the Cassie-Baxter model, f_1 and f_2 are respectively the fractional area of the solid-liquid interface and the liquid-vapor interface ($f_1 + f_2 = 1$) in the composite contact interface. When the rough surface is completely wetted by water (*i.e.*, no air is trapped and $f_2 = 0$), eqn (6) reduces to Wenzel's equation (eqn (5)) for the apparent CA of a rough solid surface with the roughness factor of f_1. The Cassie-Baxter model can be easily generalised to more complex solid-vapor-liquid wetting systems in which the rough solid surfaces show different surface chemistries. For a surface with n kinds of chemistries, the surface free energy of the solid-vapor and solid-liquid interfaces are:

$$\gamma_{\text{SV}} = \sum_i^n f_i\,\gamma_{i,\,\text{SV}}, \quad \gamma_{\text{SL}} = \sum_i^n f_i\,\gamma_{i,\,\text{SL}} \tag{7}$$

where f_i is the area fraction characterised by a given chemistry at domain i ($\sum_i^n f_i = 1$), $\gamma_{i,\,\text{SV}}$ and $\gamma_{i,\,\text{SL}}$ are the surface free energy at domain i. Then the universal equation can be expressed as:

$$\cos\theta_{\text{C-B}} = \sum_i^n f_i \cos\theta_i \tag{8}$$

where θ_i is the CA on the flat domain i with homogeneous chemistry. For liquid wetted rough surfaces with two different surface chemistries (*i.e.*, $n = 2$), eqn (8) becomes:

$$\cos\theta_{\text{C-B}} = f_1\cos\theta_1 + f_2\cos\theta_2 \tag{9}$$

For example, when a rough and chemically-homogeneous surface with trapped air is wetted by liquid, the actual surface chemistries for the liquid could be regarded as a composite chemistry of solid and air, and θ_1 and θ_2 respectively refers to the CAs on flat solid surface (*i.e.*, $\theta_1 = \theta_Y$) and air. Considering that the liquid CA on air is always equal to 180° (*i.e.*, $\cos\theta_2 = -1$), eqn (9) could be rewritten as eqns (6) and (10):

$$\cos\theta_{\text{C-B}} = f_1(\cos\theta_1 + 1) - 1 \tag{10}$$

Milne *et al*. reported that for a wetting system with a composite interface, eqn (6) could be used generally, whereas eqn (10) was only valid for the case of flat topped pillar structures without any liquid penetration, and its incorrect use in CA estimation would result in errors from ~ 3° to 13° for superhydrophobic surfaces.[82]

In a mixed wetting state, as described in Fig. 3e, a liquid droplet partially wets the side walls of asperities and partially sits on the trapped air pockets, it is also referred as the transition state from the Wenzel to the Cassie-Baxter state. The apparent CA (θ_{mix}) in such a mixed wetting state is described as:[83,84]

$$\cos\theta_{\text{mix}} = rf_1\cos\theta_Y + f_1 - 1 \tag{11}$$

2.1.2 Solid surface in liquid

When a solid surface is covered with a layer of liquid or directly immersed in liquid, its wetting by another immiscible liquid will be different from that directly exposed to air, and the difference mainly focuses on the three phases and thus the contact interfaces in the wetting system. Notably, the interfacial tension between the two liquids should be positive, otherwise they will fully mix with each other.

2.1.2.1 Solid surface covered with a layer of liquid. When a solid surface is covered with a thin layer of Liquid A, its wetting by another immiscible Liquid B in air is governed by the interfacial interactions between the four phases (solid, Liquid A, Liquid B, and the surrounding air) and by the geometry of the solid surface.[85] Referring to the interfacial tensions of solid-Liquid A, Liquid A-vapor, Liquid A-Liquid B and Liquid B-vapor interfaces as $\gamma_{\text{SL}_\text{A}}$, $\gamma_{\text{L}_\text{A}\text{V}}$, $\gamma_{\text{L}_\text{A}\text{L}_\text{B}}$ and $\gamma_{\text{L}_\text{B}\text{V}}$, respectively, when eqn (12):

$$\gamma_{\text{SV}} - (\gamma_{\text{SL}_\text{A}} + \gamma_{\text{L}_\text{A}\text{V}}) > 0 \tag{12}$$

is satisfied, Liquid A will keep infusing the solid surface despite the presence of Liquid B, and Liquid B will form a discrete droplet anchoring on the layer of Liquid A (Fig. 4a, left part).[85] This condition refers to a stable liquid-liquid contact interface, and is known as slippery liquid-infused surface (SLIS),[20,85-87] in which liquids A and B are respectively termed as infused lubricant and repelling liquid. Wong *et al*. proposed two criteria that describe such a stable wetting state of liquid layer infused solid surface:[20]

$$\begin{aligned} &r(\gamma_{\mathrm{L_AV}}\cos\theta_{\mathrm{L_A}} - \gamma_{\mathrm{L_BV}}\cos\theta_{\mathrm{L_B}}) - \gamma_{\mathrm{L_AL_B}} > 0 \\ &r(\gamma_{\mathrm{L_AV}}\cos\theta_{\mathrm{L_A}} - \gamma_{\mathrm{L_BV}}\cos\theta_{\mathrm{L_B}}) + \gamma_{\mathrm{L_BV}} - \gamma_{\mathrm{L_AV}} > 0 \end{aligned} \tag{13}$$

where $\theta_{\mathrm{L_A}}$ and $\theta_{\mathrm{L_B}}$ are the CAs of Liquid A and Liquid B on the flat solid surface. Notably, when

$$\gamma_{\mathrm{L_BV}} - (\gamma_{\mathrm{L_AL_B}} + \gamma_{\mathrm{L_AV}}) > 0 \tag{14}$$

Liquid A spontaneously spreads over and encapsulates the droplet of Liquid B, resulting in coating of the droplet with a thin layer of Liquid A, termed as cloaking (Fig. 4a. right part).[85-87] The formed droplets (both uncloaked and cloaked ones) are usually surrounded by a annular wetting ridge (Fig. 4a, b), at which four CAs, the apparent CA of the droplet (θ_{app}), and CAs between the three phases of Liquid A, Liquid B and vapor (*i.e.*, $\theta_{\mathrm{L_AV}}$, $\theta_{\mathrm{L_BV}}$, and $\theta_{\mathrm{L_AL_B}}$), can be found (Fig. 4b). θ_{app} can be described *via* the modified Young' equation (eqn (15)):

$$\gamma_{\mathrm{eff}}\theta_{\mathrm{app}} = \gamma_{\mathrm{L_AV}} - \gamma_{\mathrm{L_AL_B}} \tag{15}$$

where $\gamma_{\mathrm{eff}} = \gamma_{\mathrm{L_AV}} + \gamma_{\mathrm{L_AL_B}}$ or $\gamma_{\mathrm{L_BV}}$ for Liquid B with or without a cloaking layer, respectively.[88] Similarly, CAs between the three phases can be expressed as eqn (16):

$$\gamma_{\alpha\beta}\cos\theta_{\alpha\beta,\,\mathrm{Y}} = \gamma_{\beta\mathrm{S}} - \gamma_{\alpha\mathrm{S}} \tag{16}$$

where the subscripts α and β correspond to Liquid B, Liquid A and vapor phases, and S represents solid phase. If pinning effects and the related energy barriers are negligible, they can be further given by the modified Cassie-Baxter equation (eqn (17)):[88]

$$\cos\theta_{\alpha\beta,\mathrm{C\text{-}B}} = f\cos\theta_{\alpha\beta,\mathrm{Y}} + (1-f) \tag{17}$$

where α represents the Liquid A phase, β is either the Liquid B or vapor phase, and *f* is the fraction of the projected solid area exposed to the β phase.

In comparison, when eqn (18):

$$\gamma_{\mathrm{L_AV}} - (\gamma_{\mathrm{L_AL_B}} + \gamma_{\mathrm{L_BV}}) \geq 0 \tag{18}$$

is satisfied, Liquid B spreads indefinitely over the covered layer of Liquid A, leading to the formation of a Liquid B film instead of discrete droplets (Fig. 4c).[85] If eqn (19):

$$\gamma_{\mathrm{SV}} - (\gamma_{\mathrm{SL_A}} + \gamma_{\mathrm{L_AV}}) \leq -\frac{r-1}{r-f_1}\gamma_{\mathrm{L_AL_B}} \tag{19}$$

is met, Liquid B impales the Liquid A layer and constructs a new solid-Liquid B interface (Fig. 4d).

2.1.2.2 Solid surface immersed in liquid. When a solid surface is totally immersed in Liquid A, and the wetting by another immiscible Liquid B occurs under Liquid A, its wetting behavior becomes similar to that in air, except that the vapor phase is replaced by the Liquid A phase. Therefore, Young's equation could be expressed as:[19,89]

$$\gamma_{L_AL_B}\cos\theta_{BA,\,Y}=\gamma_{L_BV}\cos\theta_{B,\,Y}-\gamma_{L_AV}\cos\theta_{A,\,Y} \tag{20}$$

where $\theta_{A,\,Y}$, $\theta_{B,\,Y}$ and $\theta_{BA,\,Y}$ are the CAs of Liquid A on flat solid surface in vapor, Liquid B on flat solid surface in vapor, and Liquid B on flat solid surface in Liquid A, respectively. Similarly, the Cassie-Baxter equation could be expressed as:[19]

$$\cos\theta_{BA,\,C\text{-}B}=f_{SL_B}(\cos\theta_{BA,\,Y}+1)-1 \tag{21}$$

where f_{SL_B} is the area fraction of solid-Liquid B interface in the composite contact interface, and $\theta_{BA,\,C\text{-}B}$ is the CA of Liquid B droplet on a rough solid surface in Liquid A.

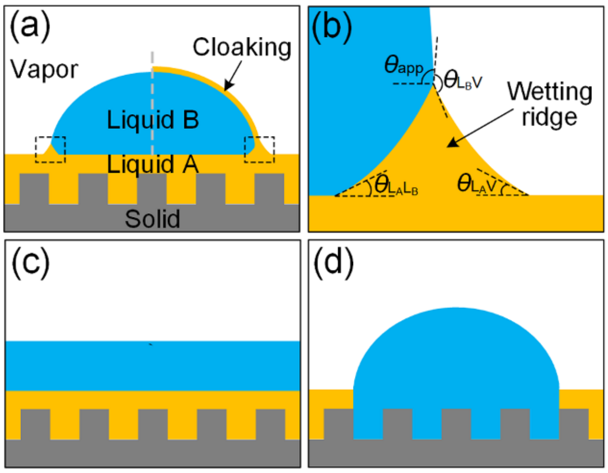

Fig. 4 Wetting modes of a solid surface covered by a layer of Liquid A. (a) Liquid B forms a stable droplet anchoring on the layer of Liquid A. The left part shows the droplet without being cloaked, while the right part shows the droplet with a cloaking layer. The dashed boxes indicate the wetting ridges. (b) The enlarged view of the wetting ridge, and the related CAs. (c) Liquid B spreads indefinitely over the layer of Liquid A. (d) Liquid B impales Liquid A and forms a new solid-Liquid B interface.

2.1.3 Contact angle hysteresis

Classical wetting models proposed by Young,[9] Wenzel[77] and Cassie-Baxter[81] are all based on rigorous thermodynamics, and are thus established on the assumption that Gibbs free energy versus apparent CA of an ideal wetting system has only a single free energy minimum, indicating that a given solid surface has a unique CA value (Fig. 5a).[90,91] However, even mirror-like, nearly atomically smooth and chemically controlled silicon wafer surface has a range of measurable CAs.[92] Fig. 5b shows the Gibbs free energy of a real wetting system as a function of apparent CA, in which multiple free energy minima (*i.e.*, thermodynamic equilibrium states) can be observed, corresponding to the most stable CA at the global minimum and some metastable CAs at the local minima of a real solid surface. Taking 2D droplet wetting on smooth but chemically heterogeneous solid surface with 2D periodic chemical patterns (Fig. 5c) as an example, the relationship between the ideal/apparent CAs and the position of the contact line for a given volume is shown in Fig. 5d. Practical thermodynamic equilibrium can only be achieved when the ideal

CA curve intersects with the apparent CA curve (namely, the local ideal CA equal the apparent CA).[93] Therefore, multiple equilibrium positions could be obtained, which correspond to the extremum points in the Gibbs free energy curve (Fig. 5b). Meanwhile, as a finite energy barrier separating every two adjacent equilibrium states exists (Fig. 5b), these CAs can be reached and measured depending on the balance between the energy barrier and the available drop energy. For example, mechanical vibration was suggested to overcome the energy barriers so as to evaluate the most-stable CA.[94] The maximum and minimum apparent CA values in this range are termed as advancing and receding CAs (ACA and RCA, or, θ_{adv} and θ_{rec}), respectively, and their difference, $\Delta\theta = \theta_{\mathrm{adv}} - \theta_{\mathrm{rec}}$, is defined as contact angle hysteresis (CAH). A measurable static CA could thereby be any value between ACA and RCA, which makes CA to be less meaningful while ACA and RCA to be more important in characterising surface wettability.[95-97] CAH is one of the most effective parameters to evaluate the mobility of a liquid droplet on a solid surface, and smaller CAH usually represent better liquid mobility and liquid repellence.

CAH is related to the pinning of the three-phase line. For Young wetting state on an ideal solid surface, the $\theta_{\mathrm{adv}} = \theta_{\mathrm{rec}} = \theta_{\mathrm{Y}}$ and there is no CAH, while Wenzel wetting state generally shows low θ_{rec} and high $\Delta\theta$ due to particularly strong contact line pinning in this state, and Cassie-Baxter state is always characterised by low $\Delta\theta$. CAH has been extensively studied both from theoretical and experimental viewpoints, and some causes, such as surface heterogeneity, roughness, reorientation of molecules in the solid surface, transport of molecules from the liquid, interactions between molecules of solid and liquid at the three-phase line region, motion rate of the three-phase line on the solid surface, liquid sorption/retention on the surface, surface deformation, *etc.* were proposed early on to understand the fundamental underlying mechanism.[60,92,98] Additionally, Lam *et al.* found that the CAH decreased with the chain length of the liquid, and when the alkane molecules were infinitely large θ_{rec} equals θ_{adv}, therefore the chain length and size of the liquid molecule could contribute to the CAH.[99] Brandon *et al.* computationally investigated the partial wetting of 3D droplets, and showed that the CAH was droplet volume dependent.[100] For a surface with very low CAH, the relation among θ_{Y}, θ_{adv} and θ_{rec} can be roughly written as:

$$\theta_{\mathrm{Y}} = \frac{\theta_{\mathrm{adv}} + \theta_{\mathrm{rec}}}{2} \tag{22}$$

Adam *et al.* claimed that a “frictional force” accounted for the CAH and it disappeared when the wetting system reached its equilibrium CA.[101] They also proposed the following cosine relation of θ_{Y}, θ_{adv} and θ_{rec}:

$$\theta_{\mathrm{Y}} = \arccos\left(\frac{\cos\theta_{\mathrm{adv}} + \cos\theta_{\mathrm{rec}}}{2}\right) \tag{23}$$

2.2 Characterisation of Wettability

Wettability refers to the ability or tendency of a liquid to wet a solid (or liquid) surface, and it can be regarded as the degree of wetting. Therefore, characterisation of wettability is a basic yet important branch in the wetting research. General wettability characterisations include CA and CAH, sliding-/rolling-off angle, measurement of the adhesive forces between solid and liquid, and solid-liquid interface imaging, *etc*.[102,103]

2.2.1 Contact angle and contact angle hysteresis

CA is one of the most important values measured experimentally during characterisation of solid properties, and is regarded as the gold standard to characterise the wettability of a solid surface.[97,104] Although static CA is always reported in the literature, it is highly recommended to measure the ACA and RCA (*i.e.*, the CAH), which can indicate the wettability of the surface more comprehensively.[95-97] Most techniques for CA and CAH measurement can be classified into two groups: direct methods mainly including sessile-drop goniometry and captive bubble method, and indirect methods such as the Wilhelmy balance method.

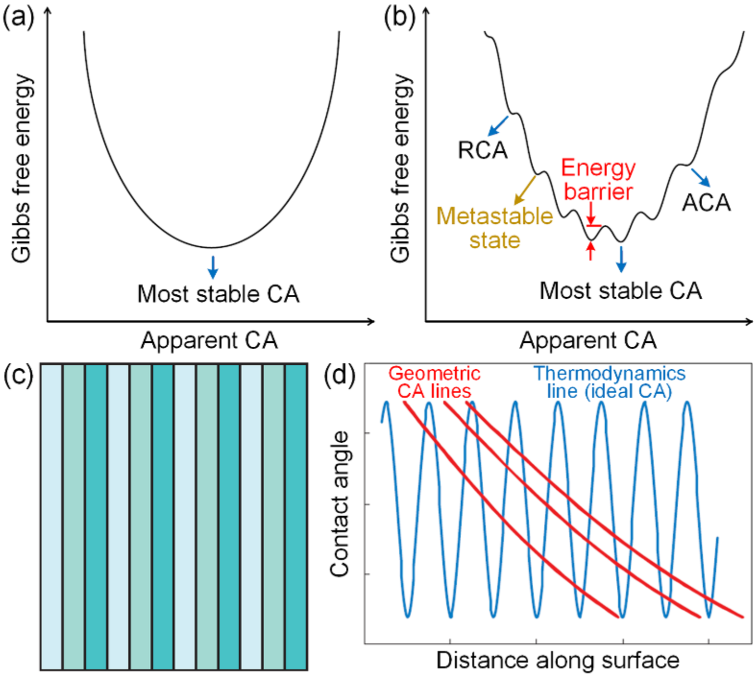

Fig. 5 Illustration of the Gibbs free energies of ideal (a) and real (b) wetting systems as a function of the apparent CA. (c) Sketch of a smooth but chemically heterogeneous solid surface with 2D periodic chemical patterns. (d) Relationship between CA and location of a 2D droplet on the surface shown in (c), and each intersection of the thermodynamics line with a geometric CA line indicates an extremum point in the Gibbs energy curve. (a, b) reproduced with permission from ref. 90. Copyright (2018) Nature Publishing Group. (c, d) reproduced with permission from ref. 91. Copyright (2009) Annual Reviews.

2.2.1.1 Sessile-drop goniometry. Due to its simplicity and versatility, sessile-drop goniometry is probably the most widely used method to measure the static CA and CAH. Typically, in terms of static CA measurement, a liquid droplet with given volume is gently deposited on the solid surface by a dispensing system and a 2D profile of the droplet is then captured by a software-operated high-resolution camera under the assistance of a light source from behind (Fig. 6a). Software-based fitting *via* image analysis algorithms is then performed to estimate the CA value from the fitted drop shape, baseline and tangent line (Fig. 6b). With regard to CAH (*i.e.*, ACA and RCA) measurement by sessile-drop goniometry, digital images are captured during increasing or decreasing the droplet volume with the needle until the contact line starts to advance or recede on the surface, and the CA values obtained by the software-based fitting are ACA and RCA, respectively (Fig. 6c). More details about the guidelines of sessile-drop goniometry can be found in refs. [105] and [90]. The sessile-drop method requires small amount of testing liquids, and can measure both plane and non-planar surfaces with small areas so as to provide their 2D wettability distribution though an amount of time is required.[106,107] However, this method is susceptible to measurement details, such as image analysis, droplet volume, *etc*.

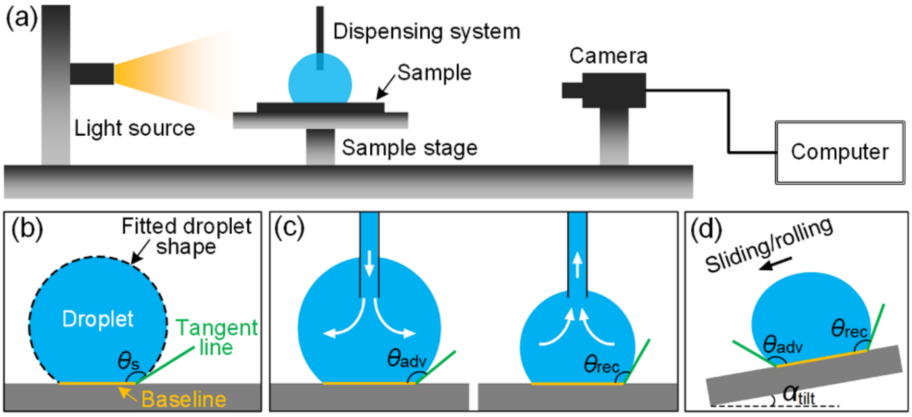

Fig. 6 CA and CAH measurement by sessile-drop goniometry method. (a) Sketch of a goniometer setup consisting of light source, sample stage, dispensing system, camera, and computer. Reproduced with permission from ref. 90. Copyright (2018) Nature Publishing Group. (b) Static CA by software-operated fitting procedure. (c) ACA and RCA measurement by increasing or decreasing the volume of the droplet. (d) ACA and RCA measurement *via* tilting-plate method.

Software-based image analysis of sessile-drop method causes inaccuracies due to optical distortions or blurs originating from experimental details such as magnification, lighting, contrast and camera resolution.[97,108] The optical distortions are obvious at the area close to the three-phase contact line, and become conspicuous for surfaces with large CAs, especially for super liquid-repellent surfaces. Diffuse droplet edge and pixelation make it difficult to precisely determine the droplet shape and baseline even when a high-resolution digital image is taken, leading to systematic errors in CA measurement. For example, as illustrated in Fig. 7a, though a digital image with resolution of 1984 × 1264 pixels is used, error in CA measurement appears due to the baseline displacement providing that the droplet shape is fitted: setting baseline too high decreases CA, while setting it too low increases CA, which is a subjective process. Both simulated and experimental data showed that one-pixel displacement of the baseline would result in errors in CA value from ~ 1° to > 10°, and the error dramatically increased for a super liquid-repellent surface with CA > 150° (Fig. 7b).[97,108] The systematic errors in CA measurement will inevitably be propagated to CAH, and even make the uncertainty of CAH worse. The error can be slightly reduced by improving measurement details, such as using high resolution cameras and enhancing droplet reflection, but cannot be eliminated entirely.

Droplet volume (*i.e.*, size) is another key yet under-debated factor that needs to be considered in the sessile-drop method. Shahraz *et al*. reported that water CA measured on a periodically grooved hydrophobic surface increased when the droplet volume increased from 0.4 nL to 4.5 μL.[109] By contrast, Cansoy studied the effect of water droplet size on CA measurement of superhydrophobic surfaces with varying square pillar sizes and solid area fraction.[110] The results demonstrated that the variation in droplet volume (0.5 μL to 19 μL) had no significant influence on the experimentally measured CA and the deviations between the predicted CAs by the Cassie-Baxter equation and the experimental values. Bell *et al*. showed that gravity enabled the droplet with small size to flatten and spread across the surface, and even to penetrate surface asperities more favorably, which would tend to lower the measured CA value, while CA became independent of gravity when the size of the droplet was much larger than that of the surface features.[111] A recent work by Ren *et al*. showed that the volume (5.0 μL to 20 μL) of four resting liquids (water, glycerol, ethylene glycol and hexadecane) had no significant effect on the measured CA values of both natural Lotus leaf and artificial superhydrophobic coating. It was also demonstrated theoretically that only a small change in the three-phase line length was needed to re-balance the forces exerted to the droplet when its volume changed, so the contact ratio of solid-liquid and gas-liquid changed insignificantly, resulting in negligible change in CA.[112] Therefore, to reliably characterise surface wettability *via* CA and CAH measurements by sessile-drop goniometry, larger droplet should be preferably employed, and the volume of a few microliters is generally recommended.

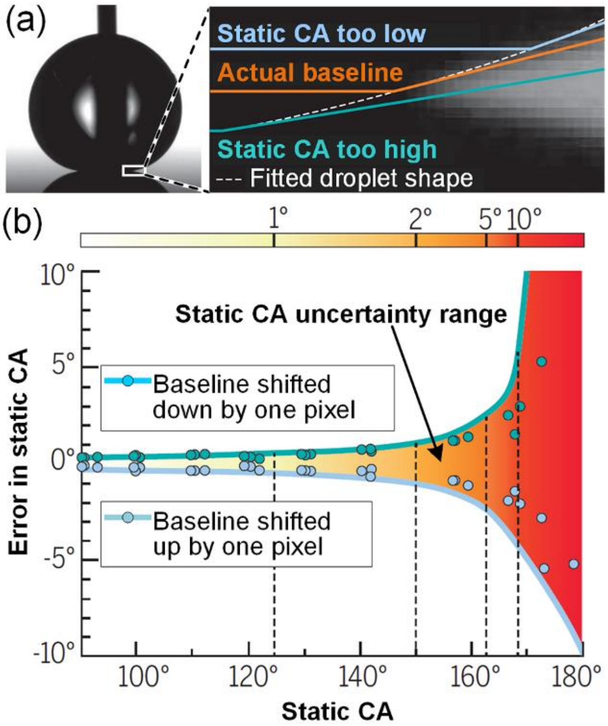

Fig. 7 Systematic errors in static CA measurement on a superhydrophobic surface *via* sessile-drop goniometry method. (a) Inaccurate baseline position causes errors in static CA measurement. (b) Simulated and experimental error in static CA caused by one-pixel displacement of the baseline. Reproduced with permission from ref. 97. Copyright (2019) American Association for the Advancement of Science.

Most work conventionally considered the effect of gravity on CA measurement by the sessile drop technique to be negligible because the radius of the adopted droplets was generally smaller than the capillary length.[90] However, Extrand *et al*. clarified that gravity-induced sagging or distortion of sessile droplet always led to the underprediction of the CA *via* conventional circular-segment approximation method, especially for those droplets with lower surface tension or larger density depositing on super-liquid-repellent surfaces, the underestimation could reach up to tens of degrees.[113] To address this concern, strategies like employing small sessile droplets (on the order of hundreds of picolitres),[113] estimating CA by using the maximum droplet width and height,[114] and Cassie-levitating droplet model[115] have been proposed to improve the accuracy of CA measurement. Moreover, Kim *et al*. demonstrated that the ACA and RCA were not affected by gravity, while the overall shape of the droplet and the position of the pinning point were affected by gravity, and that the gravitational effect played a key role in the movement of the droplet tip during continuously increasing or decreasing the volume of the droplet.[116]

Additionally, other measurement details such as the resting time of deposited droplet on surface,[117,118] temperature,[119] and dispense rate as well as the distance between the dispense needle and the surface should also be considered in CA and CAH measurement by the sessile-drop goniometry.[120]

Another commonly-used yet under-debated optical method to measure CAH is tilting-plate method, in which the tilting angle of the surface with a droplet is gradually increased until the droplet starts moving, and after fitting the corresponding digital image, the CAs measured from the leading and trailing edges of the distorted droplet are regarded as ACA and RCA, respectively (Fig. 6d). However, the CAs on two edges of a droplet on a tilted plate are not independent of each other. Krasovitski *et al.* found that the CAs at the leading and trailing edges did not always simultaneously equal the ACA and RCA, respectively.[121] They clarified that on a hydrophobic surface, the CA at the trailing edge tended to be approximately equal to the RCA, while the CA at the leading edge might be much lower than the ACA; but for a hydrophilic surface, the CA at the trailing edge was lower than the RCA, whereas the CA at the leading edge was roughly equal to the ACA. Pierce *et al.* demonstrated that CAH measured by tilting-plate method was liquid volume-dependent, which is contrary to the fact that the CAH is a surface property that does not depend on droplet size.[122] Therefore, the obtained results from the tilting-plate method are not necessarily representing reliable CAH, and this method is sometimes not recommended.

2.2.1.2 Captive bubble method. Captive bubble method is another optical technique widely used for CA and CAH measurements. As shown in Fig. 8a, the solid sample is pre-immersed horizontally in the liquid with the surface to be measured downward, and a bubble with a certain volume is gently released by a needle, which is subsequently captured by the lower surface. Then the 2D profile of the bubble is recorded and analyzed *via* software-based fitting of the bubble shape, baseline, and tangent line to the liquid-gas interface. The fitting procedure is similar to the procedure of sessile-drop method described in 2.2.1.1, while the difference is that the CA, θ, of the testing liquid on the surface is complementary to the angle between the baseline and tangent line (θ_b), that is:[93]

$$\theta = 180° - \theta_b \tag{24}$$

Similarly, the ACA and RCA of the bubble on the surface ($\theta_{b,adv}$ and $\theta_{b,rec}$) can be obtained by increasing or decreasing the volume of the bubble (Fig. 8b), thereby achieving the θ_{adv} and θ_{rec} of the testing liquid on the surface as follows:

$$\begin{aligned} \theta_{adv} &= \theta_{s,adv} = 180° - \theta_{b,rec} \\ \theta_{rec} &= \theta_{s,rec} = 180° - \theta_{b,adv} \end{aligned} \tag{25}$$

where $\theta_{s,adv}$ and $\theta_{s,rec}$ respectively represent the ACA and RCA from sessile-drop goniometry. Eqn (25) describes the complementary relationship of ACA and RCA measured by sessile-drop and captive-bubble methods, which indicates that captive bubble method can be readily used for the ACA and RCA calculations,[93,123] especially for cases where the sessile-drop method cannot be adopted. However, the recent works demonstrated that for a rough hydrophilic surface, the $\theta_{s,adv}$ and $\theta_{b,rec}$ tended to deviate from the complementary rule, which could be attributed to the contrasting wetting states: the liquid droplet totally wets the rough surface in sessile-drop method (*i.e.*, Wenzel state), while the bubble cannot totally dry the surface in captive bubble method since the trapped liquid in rough structures cannot be completely replaced by the captive bubble (termed as "inverted Cassie-Baxter state").[124,125]

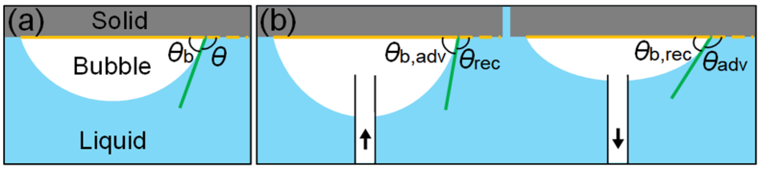

Fig. 8 (a) CA and (b) CAH measurement by captive bubble method.

Practical use of the captive bubble method is severely limited by its complex operation, however, this method is suitable for the wettability characterisation of solid surfaces that are always applied in liquid environments, such as biomaterials that are used in human body or other living bodies.[126-128] Biomaterials are generally hydrophilic and are immersed in tissue fluids during long-time utilization so as to form long-lasting hydrated surfaces. When the captive bubble method is used to measure the CA and CAH of the biomaterials, pre-immersion in liquids that are similar to the tissue fluids simulates a real service condition and imparts the surface with hydratability, thereby enabling accurate *in vivo* wettability evaluation *via in vitro* CA and CAH measurements.

Xue *et al*. proposed a modified captive bubble method, in which the bubble volume was adjusted by the pressure of the testing chamber instead of using a needle.[129] This modification eliminated the distortion of the bubble induced by needle, and thus provided more accurate and repeatable ACA and RCA values. They also confirmed that the captive bubble method was only available for surfaces with ACA and RCA values below 130°.

2.2.1.3 Wilhelmy balance method. The Wilhelmy balance method[130] proposed in 1863 is another ancient technique used for measuring CA and CAH of a solid surface.[131] Generally, as shown in Fig. 9a, a thin plate sample is dipped vertically into the testing liquid, the total forces acting on the plate include the gravity (G_p), the capillary force due to surface tension of the liquid (F_c), the buoyancy force (F_b), and the plate holding force measured by the microbalance force sensor (F_m). Since the thickness of the plate is much smaller than the other two dimensions, the form drag (*i.e.*, pressure drag) is negligible. The CA of the plate surface cannot be directedly measured but can be determined based on the following force balance equation:

$$F_{\mathrm{m}} + F_{\mathrm{b}} = G_{\mathrm{p}} + F_{\mathrm{c}} \cos\theta \tag{26}$$

G_p, F_c and F_b can be described as:

$$\begin{aligned} G_{\mathrm{p}} &= mg \\ F_{\mathrm{c}} &= P_{\mathrm{cl}}\gamma \\ F_{\mathrm{b}} &= \rho g V_{\mathrm{h}} \end{aligned} \tag{27}$$

where m is the mass of the plate, P_{cl} is the length of contact line between the plate and liquid, which is roughly equal to the perimeter of the plate, γ and ρ are respectively the surface tension and density of the testing liquid, V_h denotes the volume of the plate immersed in the liquid with immersion depth of h, g is the gravitational acceleration. Notably, the direction of F_c depends on the wettability of the plate's surfaces. For example, as depicted in Fig. 9a, when the surface is hydrophobic, the cosine component of F_c is upward (*i.e.*, opposite to G_p). Combination of eqns (26) and (27) yields the CA value measured by the Wilhelmy balance method as:

$$\theta = \arccos\frac{F_{\mathrm{m}} + \rho g V_{\mathrm{h}} - mg}{P_{\mathrm{cl}}\gamma} \tag{28}$$

Similarly, the ACA and the RCA can be respectively obtained *via* F_m measurements during the advancing and receding of the plate (Fig. 9b), which is also termed as the dynamic Wilhelmy balance method. Fig. 9c illustrates a typical curve of F_m *vs* immersion depth h for the dynamic Wilhelmy balance method.

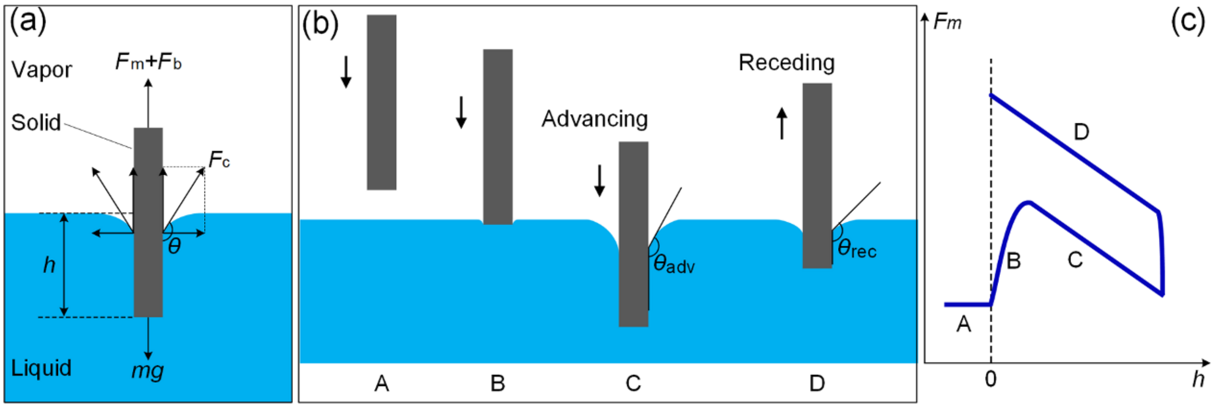

Fig. 9 CA and CAH measurement by Wilhelmy balance method. (a) Schematic diagram of the forces acting on the solid sample in a typical Wilhelmy balance method, and the CA can be calculated *via* forces balance equations. (b) Illustration of CAH measurement *via* advancing and receding of the plate. (c) A typical relationship between the plate holding force (F_m) and immersion depth (h) corresponding to the four stages (*i.e.*, A, B, C, and D) in (b).

The Wilhelmy plate method is regarded as a fully automatic and thus “operator-error-free” technique for CA characterisation, and had been expected to obtain more accurate and highly reproducible CA values than other experimental methods, but this advantage is gradually diminishing due to rapid development of sessile-drop goniometry. A large surface area is analyzed in the Wilhelmy balance method, thereby making the influence of small surface imperfections/contaminations on the measured CA to be negligible. Additionally, 1D resolution of surface wettability along the advancing/receding direction can be achieved by the Wilhelmy technique. This method is much preferred for CA measurement of plain plate,[132,133] fabric[134] and fiber[135] with rectangular or cylindrical shapes (*i.e.*, a constant perimeter) and same chemistries in both sides. For samples with different wettability on the two sides, back-to-back bonding is suggested to expose two same surfaces for measurement. Recently, it was shown that the Wilhelmy balance technique could also be used for the CA measurement of irregular shaped samples with a variable perimeter.[136,137] For example, Park *et al*. proposed to determine the perimeter of the sample as a function of the immersion depth by profile plot obtained from the optical image, and then measured the ACA and RCA *via* the Wilhelmy balance method, which was verified with triangular and irregular PTFE sheets in water.[136] However, the precise estimation of P_{cl} in eqns (27) and (28) is always difficult, especially for those porous or textured surfaces, the contact line is significantly different from the geometric perimeter, which can be a large source of error.

Sample thickness is traditionally negligible in this method, and the viscous frictions acting on the bottom and sides due to sample movement are ignored in eqn (26). However, recent researches showed that taking viscous frictions into consideration could well guarantee the measurement accuracy of CAH *via* the Wilhelmy balance method, especially when thick sample, highly viscous liquid and high moving speed of the sample were used.[138,139] Furthermore, Zhang *et al*. found that the viscous drag forces acting on the submerged plate surface during a dynamic Wilhelmy plate experiment could be of the same order of magnitude as surface tension forces, which were always highly underestimated due to the ignorance of the interface curvature, the tip of the plate, or the flow formed between the plate and liquid container.[140] They further proposed a new viscous drag force model that incorporated the effects of the moving contact line, the leading edge of a flat plate and a Couette-Poiseuille flow to measure CA by the Wilhelmy plate method, and the results of their demonstrative example showed that CA values of glycerin advancing on glass plate increased by 20° while the capillary number varied from 10^{-3} to 10^{-1}.

Table 1 summarizes the advantages and disadvantages of the above-discussed CA and CAH measurement methods. It has to be noted that each measurement method has its own strengths and shortcomings, and the most suitable method should be selected based on the specific features of the substrate (*e.g.*, size, shape, composition, and estimated CA range), the application condition, as well as the measurement purposes.

2.2.2 Sliding/rolling-off angle

Sliding/rolling-off angle (SA/RA) is another common characteristic for the wettability of solid surfaces, especially for liquid-repellent surfaces, since it can easily reflect the mobility of the liquid droplets deposited on the surfaces. Generally, the SA/RA can be measured by the same instruments used in CA measurement *via* sessile-drop goniometry method with the assistance of a tilting plate. During the measurement process, the solid sample is firstly fixed on the plate horizontally, and then the plate is tilted slowly until the droplet starts to slide or roll, by which time the tilt angle of the plate can be regarded as the SA/RA (*i.e.*, the α_{tilt} shown in Fig. 6d). Thus, the SA/RA denotes the tilting angle at which the gravitational force component of the droplet along the inclined surface (*i.e.*, $mg\sin\alpha_{\mathrm{tilt}}$, where m is the mass of the droplet, g is the acceleration of gravity) overcomes the lateral moving resistance that mainly originates from the adhesion force between the solid and liquid, as well as rough structures induced obstruction. Therefore, small SA/RA always indicates weak solid-liquid adhesion and high liquid droplet mobility on the surface, making SA/RA indispensable in evaluating the liquid repellence of a solid surface.

Table 1 Comparison between different CA and CAH measurement methods.

Method	Advantages	Disadvantages
Sessile-drop goniometry	Simple. Testing liquids saving. Only small surface areas are required. Provide 2D wettability uniformity. Wide measuring range of CA and CAH.	Susceptible to measurement details. Difficult to measure the CA and CAH of non-planar surfaces. CAH measured *via* tilting plate is unreliable.
Captive bubble	Only small surface areas are required. Provide 2D wettability uniformity. More accurate measurement of CA and CAH for surfaces that are always applied in liquid conditions.	Relatively complicated operation. Limited measuring range of CA and CAH.
Wilhelmy balance	Available for the measurement of CA and CAH of non-planar surfaces. Free of operator error. Ease of automation.	Shape and surface composition of the sample are severely restricted. Actual contact line may be difficult to determine. Unable to characterise wettability uniformity.

Although the measurement of SA/RA is easy to be realized, it’s sensitive to operational details, such as droplet volume, dropping speed of the droplet, resting time of the droplet on the surface, tilting speed of the plate, *etc*. Droplet volume is widely considered in literatures, and it was demonstrated that increasing the droplet volume could generally lower the SA/RA.[141] However, other measurement details are always reported intangibly, and the specific influence have been rarely focused on, making it difficult and even unreliable for the quantitative comparison among different reports.

2.2.3 Adhesive force measurement

A liquid droplet is usually in molecular contact with the underneath solid surface, the intermolecular forces, commonly referred as adhesive forces, will inevitably impede the motion of the droplet. The adhesive forces are closely related to the wettability of the surface, so their measurement can also be used to characterise the wettability of solid surfaces, especially those with liquid repellence.[102]

2.2.3.1 Lateral adhesive force. When a liquid droplet is moved along a solid surface, the lateral adhesive force (F_{lat}) acts as the friction force. Conventionally, the tilting method is used to measure the ACA and RCA of the moving droplet, and then F_{lat} can be roughly calculated by eqn (29):[142]

$$F_{\text{lat}} = \pi \gamma_{\text{LV}} R(\cos\theta_{\text{rec}} - \cos\theta_{\text{adv}}) \tag{29}$$

where R is the base radius of the droplet. Thus, the tilting method is actually dependent on the accurate measurement of CAH and determination of the baseline. Therefore, when the ACA and RCA of the surface approach each other, for example, an ultra-slippery PDMS-chains grafted surface with CAH lower than 2°,[143] this method becomes unapplicable owing to the limited accuracy of CAH measurement and baseline determination (see Section 2.1.1).[144] Additionally, it is difficult to study the time-dependence and velocity-dependence of F_{lat} by the traditional tilting method.

Recently, force measurement by elastic cantilevers have been employed to measure F_{lat} as an important emerging technique.[102,145,146] Generally, a liquid droplet deposited on the surface is attached through capillary force to a force-calibrated elastic cantilever (effective spring constant k). When the substrate is moved and relative motion between the droplet and the surface appears, F_{lat} works and results in a deflection of the cantilever (Δx). Then F_{lat} can be directly calculated by eqn (30):

$$F_{\text{lat}} = k\Delta x \tag{30}$$

The deflection can be easily detected by a high-resolution camera from the side. For example, Backholm *et al*. designed a micropipette cantilever-based setup to measure the lateral friction of water droplet moving on a superhydrophobic surface (Fig. 10a).[144] During the measurement, as shown in Fig. 10b, the pre-deposited water droplet with radius of ~ 620 μm was firstly attached to the micropipette cantilever, and was then pulled along the substrate with a constant speed of v ~ 0.1 mm s^{-1} until the elastic force from the deflected micropipette matched the lateral friction force of the substrate. At this moment, the deflection (Δx) remained nearly constant while the droplet started to slide along the surface. In the recorded force-time curve (Fig. 10c), the average equilibrium position of the micropipette was first recorded for ~ 5 s after which the surface started moving, and the difference between the average zero and kinetic plateau force represented the kinetic friction (F_{lat} ~ 10 ± 4 nN). It was also demonstrated that this method achieved a force resolution of as low as ~ 4 nN, which was up to three orders of magnitude more precise than using eqn (29). The same group further used this method to study the pinning behavior of water droplets on various superhydrophobic surfaces with high spatial resolution.[147] Similarly, the lateral adhesive force measurement of an oil droplet on underwater superoleophobic surface,[148] and that of droplets on SLISs,[149] have also been reported.

Gao *et al.* employed a position-sensitive detector (PSD) to record the laser beam incident on the capillary (Fig. 10d), which could be then used to calculate Δx with high resolution and accuracy.[150] The authors thereby measured the friction that impeded the lateral motion of liquid droplets on various solid surfaces. As a representative example, Fig. 10e shows the F_{lat} (measured and calculated by both eqns (30) and (29)) during the motion of an ionic liquid (1-butyl-2,3-dimethylimidazolium bis(trifluoromethanesulfonyl)imide) on fluorinated silicon wafer. Moving the wafer laterally increased the force until a threshold force of ~ 50 μN was reached (the static regime), upon which the droplet started to slide. Then the force gradually decreased and stabilized at ~ 33 μN (the kinetic regime). It could be seen that the threshold static force was higher than the force required for continuous motion of the droplet, which is analogous to well-known solid-solid friction. Once the threshold adhesion force was overcome, the liquid-solid interaction changed from a static regime to a steady kinetic regime, and the F_{lat} in the two regimes were substantially different due to their dissimilar CAs and contact widths. Their results also showed that F_{lat} depended on the interplay between surface tension and CAH, and for a specific liquid droplet, lower F_{lat} could sometimes indicate better liquid repellence for the solid surface. Moreover, it was demonstrated that F_{lat} could be used to characterise the time-resolved pinning-depinning dynamics of the droplet by moving it across the surface.[151]

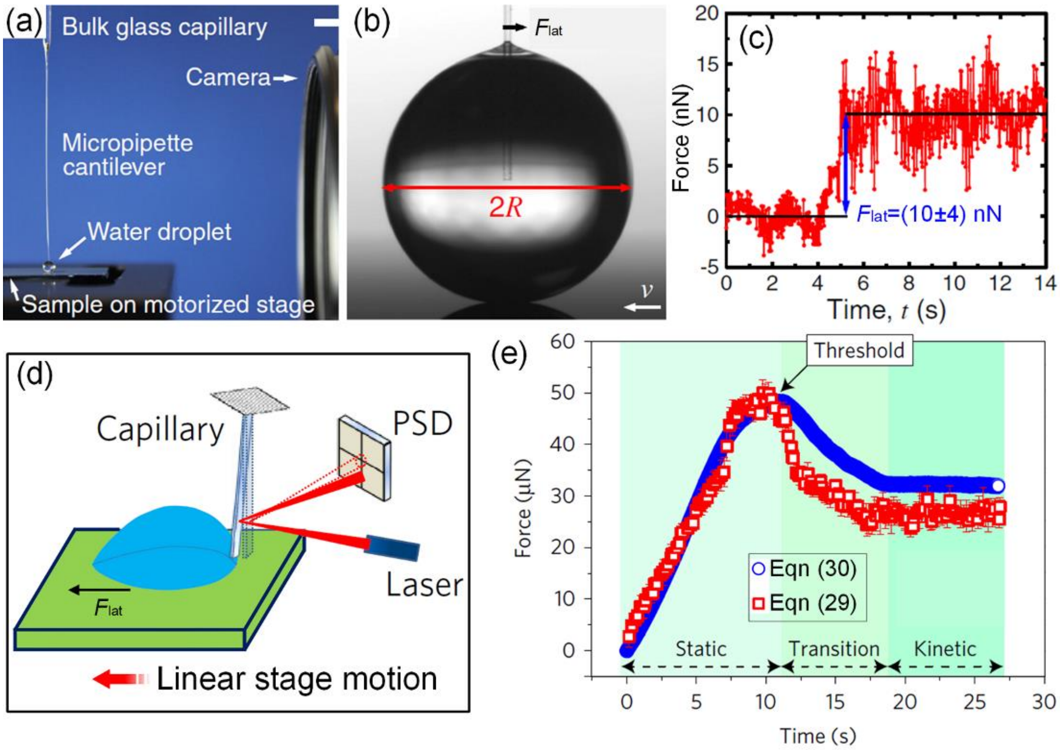

Fig. 10 Lateral adhesive force measurement of a liquid droplet on solid surface based on capillary deflection. (a–c) *F*lat measurement of a water droplet moving on a superhydrophobic surface. (d, e) *F*lat measurement of liquid droplet on solid surface by recording Δ*x* *via* a laser beam. (a–c) Reproduced with permission from ref. 144. Copyright (2020) Backholm *et al*. (d, e) Reproduced with permission from ref. 150. Copyright (2018) Macmillan Publishers Limited, part of Springer Nature.

2.2.3.2 Normal adhesive force. Compared to lateral adhesive force (friction force, to be more precise) which is surface structures-dependent due to the liquid meniscus trapped within the rough structures, normal adhesive force (F_{nor}) reflects the liquid-solid adhesion more directly. Therefore, F_{nor} has been widely employed to characterise the wettability of liquid-repellent surfaces.[152-154] Daniel *et al.* measured the F_{nor} between liquid and superhydrophobic surfaces by attaching a micrometric-sized 40-wt% glycerin-water droplet to an atomic force microscope (AFM) cantilever (Fig. 11a).[151] The vertical force acting on the droplet was linearly proportional to the flexular deflection (Δz) of the AFM cantilever (*i.e.*, be similar to eqn (30)), and Δz was detected by focusing a laser beam onto the cantilever and reflected into a 4-quadrant sensor. Fig. 11b is the measured force spectroscopy for a 30-µm-diameter droplet with volume of 20 ± 2 pL approaching and retracting from one of the superhydrophobic scales of a butterfly wing at $v = 10$ µm s^{-1}. It could be seen that when the droplet was approaching towards the solid surface, there was a sudden attractive snap-in force (132 nN) upon contact ($z = 0$ µm); after slight continuous pressing and then retracting, a maximum adhesion force, $F_{\mathrm{nor}} = 720$ nN, was obtained when the droplet was completely detached from the surface. Liimatainen *et al*. measured the F_{nor} of single hydrophobic micro pillar by a vertically mounted force sensor with a water droplet probe (Fig. 11c), and found that the $F_{\mathrm{nor}} < 4500$ nN for a 5 µm radius pillar (Fig. 11d), and the force increased with the droplet radius.[155] They also measured the F_{nor} for various (super)hydrophobic surfaces, and showed that the force was related to both CA and CAH of the surface.

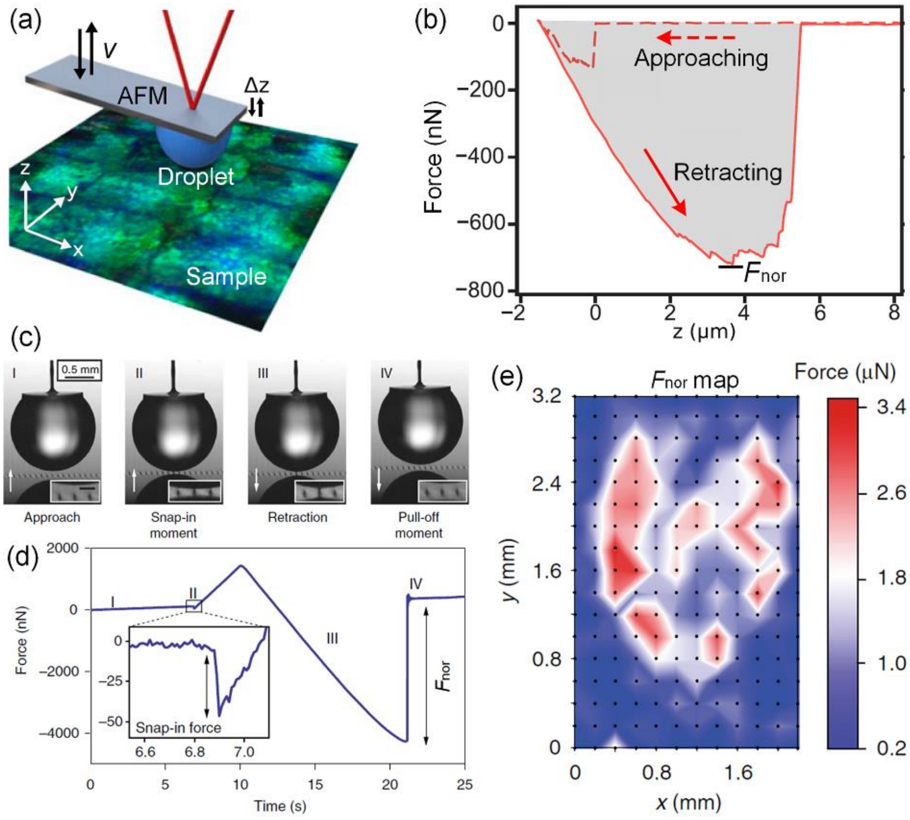

Fig. 11 Normal adhesive force measurement of a liquid droplet on solid surface. (a) Schematic of measurement of the *F*nor between water droplet and butterfly wing by droplet probe AFM, and (b) the corresponding force-z curve. (c) Images of individual force measurement on a single hydrophobic micro pillar by a vertically mounted force sensor with a water droplet probe, and (d) the corresponding force-time curve. (e) The *F*nor map of the eyespot area on a wing of blue crow butterfly. (a, b) Reproduced with permission from ref. 151. Copyright (2019) PNAS. (c–e) Reproduced with permission from ref. 155. Copyright (2017) Liimatainen *et al*.

More importantly, F_{nor} measurement can be a desired technique to map the wetting properties of solid surfaces with high spatial and force resolution, even for those non-flat surfaces, which is almost impossible by traditional CA method.[147,151,155] For example, Fig. 11e illustrates the F_{nor} map of a eyespot area on a butterfly wing, clearly showing low adhesive force (< 3.4 μN) and microscale wettability inhomogeneity of the surface.[155] Recently, Hokkanen *et al.* used the same technique to map the F_{nor} of various commercial superhydrophobic coatings, and found that even the best coatings showed regional wettability heterogeneity in sub-mm scale.[147]

2.2.4 Others

According to the above discussion, the wettability of macroscopically flat surface with clearly visible contact line between testing liquid and substrate can be well characterised by CA and SA/RA measurements. However, these techniques are sometimes not applicable to soft porous materials (*e.g.*, textile and cotton wool) since their contact lines cannot be defined and the macroscopically rough structures make SA/RA measurements unreliable.[156,157] Aiming at this problem, Zimmermann *et al.* proposed to evaluate the water repellence of superhydrophobic textiles qualitatively by water shedding angle (WSA).[156] Briefly, a water droplet was released onto the inclined superhydrophobic surface from a defined height, and the minimum tilting angle at which the droplet completely rolled off from the surface was defined as the WSA. The authors compared the qualitative differences in water repellence of superhydrophobic silicone nanofilament coated textiles, and found that the textile parameters such as fiber dimension, yarn, and weave influenced the WSA. It is obvious that the WSA can only reflect the short-term wetting resistance of a liquid-repellent surface. If a water droplet deposited on a soft porous material maintained a high CA for a while before being completely wicked into the substrate, the WSA was inadequate to judge the overall wetting behavior of the substrate, and additional wettability characterisation methods would be required.

Bouncing is a common dynamic behavior when liquid droplet impinges liquid-repellent surfaces, it indicates a redefined air gap between the liquid droplet and the solid surface after impacting. Crick *et al.* proposed to evaluate the hydrophobicity based on the ability of water to bounce on a solid surface.[158] They tested a wide range of surfaces with static water CAs between 0–175°, and found that the surfaces with rounded microstructure showed water bouncing when the CAs were larger than 151°, while surfaces promoting water pinning disabled water to bounce unless the CAs exceed 156°. Moreover, the number of water bouncing increased linearly with the water CA of superhydrophobic surfaces with similar microstructures. This characterisation method for liquid repellence ruled out personal errors in classic CA measurement, enabling it to be a more accessible technique providing results that could be directly compared among different works. Lu *et al.* further demonstrated that liquid droplet bouncing occurred on soft porous materials, and thereby liquid bouncing could be used to define a soft surface as being super liquid-repellent.[157]

In addition, solid-liquid/liquid-liquid interface imaging by environmental scanning electron microscope (ESEM),[159,160] AFM,[161] confocal microscopy,[47,162,163] *etc.* has also been widely used to characterise the wettability of solid surfaces. Taking confocal microscopy as an example, liquids (and solids) are generally fluorescently dyed, which enabled fluorescence emission under photoexcitation. Then the emission signals from different dyes and the reflected light from the interfaces are recorded, for example, by laser scanning confocal microscopy. As shown in Fig. 12a, when a water droplet was deposited on a superhydrophobic surface, a visible air layer (*i.e.*, Cassie-Baxter wetting state) could be seen with the assistance of solid-liquid interface imaging.[47] The confocal microscopy image of SLIS could visualize the lubricant layer underneath the droplet and the wetting ridge (Fig. 12b), as well as the cloaking (wrapping) layer,[162] which favors the understanding of the special wetting properties of SLIS. Li *et al*. used confocal fluorescence and reflection interference contrast microscopy to demonstrate the role of hierarchical micro- and nano- structures on underwater superoleophobicity (Fig. 12c).[163] Imaging of the solid-liquid interfaces can be an alternative technique to study the dynamic behaviors of the moving droplet (*e.g.*, measurement of ACA and RCA, pinning and depinning, Fig. 12d),[164] and wetting state transition (Fig. 12e).[165] Moreover, these confocal microscopy images could be used to determine the droplet shape and baseline more accurately, thus facilitating the static CA measurement, as shown in Fig. 12b and c.

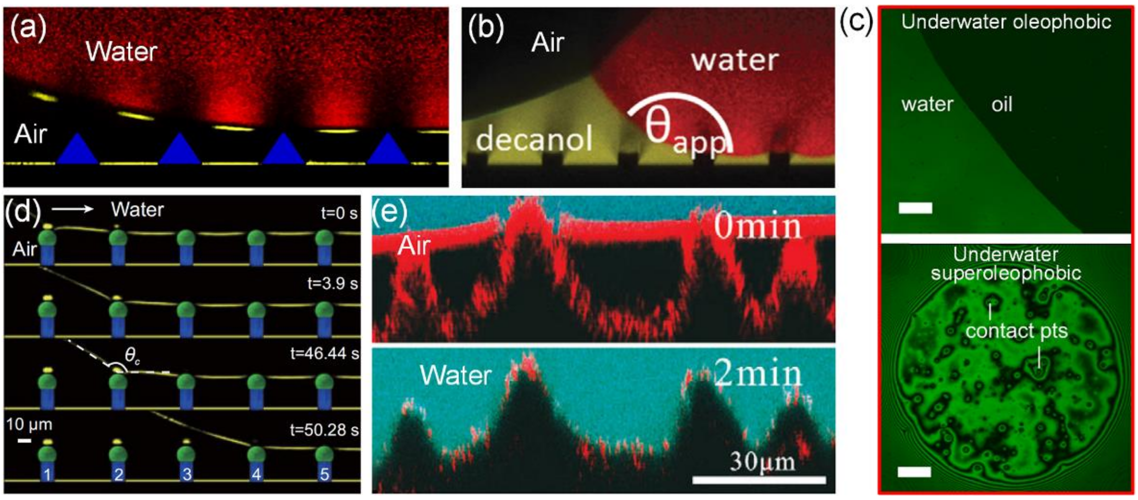

Fig. 12 Surface wettability characterisation by solid-liquid interface imaging. (a) Water droplet on superhydrophobic surface. (b) Water droplet on slippery decanol-infused surface. (c) Oil droplet on underwater oleophobic/superoleophobic surfaces. (d) Receding side of a water droplet moving on a *Salvinia*-like slippery surface. (e) Imaging of an unstable underwater superhydrophobic state. (a) Reproduced with permission from ref. 47. Copyright (2020) Nature Publishing Group. (b) Reproduced with permission from ref. 162. Copyright (2015) The Royal Society of Chemistry. (c) Reproduced with permission from ref. 163. Copyright (2021) American Chemical Society. (d) Reproduced with permission from ref. 164. Copyright (2020) Li *et al*. (e) Reproduced with permission from ref. 165. Copyright (2017) American Physical Society.

2.3 Typical Liquid-Repellent Surfaces

Liquid-repellent surfaces are characterised by non-wetting property and high mobility of liquid droplets deposited on them, that is, the droplets can easily roll- or slide-off from the surfaces without liquid residue. Usually, the CAHs of liquid-repellent surfaces are small, and thereby the maximum lateral force F_{lat} of a distorted droplet build up, which depends on θ_{adv} and θ_{rec}, should be small. Typical and most widely studied liquid-repellent surfaces can be roughly classified into three main categories: superhydrophobic surface, superoleophobic surface, and SLIS.

2.3.1 Superhydrophobic surface

Due to their extremely low CAH, low adhesion, and high mobility towards water droplets (*i.e.*, the Cassie-Baxter wetting state), superhydrophobic surfaces with water CAs larger than 150° and RAs smaller than 10° are the most fascinating water-repellent surfaces. The research of superhydrophobic surfaces can be dated back to 1944 when duck feather was reported to be water-repellent, and the importance of rough structure for water repellence was first emphasized.[81] Barthlott *et al*. studied the self-cleaning property of the Lotus leaf (Fig. 13a), and found that the epidermal microscale papillae (Fig. 13b) and epicuticular wax crystalloids were the key to its water repellence.[15] Jiang's group further reported that the micro- and nano-scale two-tier structures (*i.e.*, microscale papillae covered with branch-like nanostructures, Fig. 13c) enabled the upper surface of a Lotus leaf to possess high CA (~ 161.0 ± 2.7°) and low SA (~ 2°).[16] Since then, various superhydrophobic surfaces in nature, such as rice leaf,[16] legs of water strider,[166] butterfly wings,[167] mosquito compound eyes,[168] taro leaf,[169] *etc*. have been discovered, and shown that the air cushion underneath the water droplet and the low solid-liquid fractional area (*i.e.*, the Cassie-Baxter wetting state) are critical for superhydrophobic surfaces with large CA and small CAH, which further boost the modern development of artificial super water-repellent surfaces.[170-172] Comparatively, nature also provides some superhydrophobic but not super water-repellent surfaces, referred to as high-adhesive superhydrophobic surfaces, such as rose petal,[173] Salvinia leaf,[174] gecko feet,[175] peanut leaf,[176] *etc*. The water CAs of rose petal and peanut leaf are indeed larger than 150°, but water droplets adhere to the surfaces and cannot roll off even when the petal or leaf are turned upside down due to the formed Cassie impregnating wetting state on the petal surface[173] and quasi-continuous three-phase contact line at the microscale on the peanut leaf surface.[176] The high water adhesive forces of Salvinia leaf and gecko feet, respectively, originate from the hydrophilic patches distributed on superhydrophobic surfaces[174] and the contact between water and high-density nanopillars.[175] Therefore, these high-adhesive superhydrophobic surfaces are not discussed in this review.

The past twenty years have witnessed an all-round development of superhydrophobic surfaces. Based on the strategy of "micro- and/or nanoscale rough structures + low surface energy chemistry", various elegant methods and their combinations have been proposed to prepare superhydrophobic surfaces, such as chemical etching/deposition,[177-179] self-assembly,[180,181] electrochemical methods,[182,183] electrospinning,[184,185] hydrothermal method,[186,187] plasma exposure,[188,189] laser based ablation and 3D printing,[190-193] templating,[72,194,195] spraying,[196-198] and so on.[171,172]

2.3.2 Superoleophobic surface

Organic liquids such as oils are ubiquitous and are widely-used in our daily life and industries. Imparting solid surfaces with oil-repellence is therefore significant sometimes in order to prevent them from being wetted or contaminated by oils. Superoleophobic surfaces with oil CAs > 150° and SAs < 10° in air or underwater have drawn keen research interests recently due to their remarkable repellence towards oily liquids.

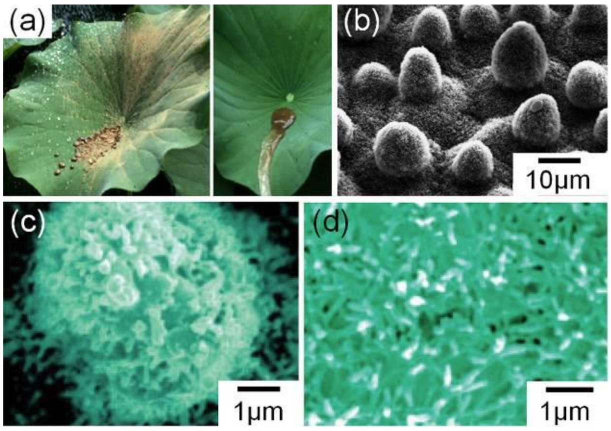

Fig. 13 (a) Self-cleaning of Lotus leaf. (b) Epidermal microscale papillae of Lotus leaf. (c, d) Two-tier micro/nano structures of the surface of Lotus leaf. (a) Reproduced with permission from ref. 199. Copyright (2015) Elsevier B.V. (b) Reproduced with permission from ref. 15. Copyright (1997) Springer-Verlag. (c, d) Reproduced with permission from ref. 16. Copyright (2002) WILEY-VCH Verlag GmbH & Co. KGaA, Weinheim.

2.3.2.1 Superoleophobic surface in air. Oily liquids generally have much lower surface tensions than that of water,[200,201] making it energetically favorable for oils to wet most of the super water-repellent surfaces. Therefore, surfaces with superoleophobicity could be more desired in terms of liquid repellence in oily environments. To the best of our knowledge, the first superoleophobic surface in air was reported in 1997 by Tsujii *et al*. who modified an anodically oxidized aluminum surface with fluorinated monoalkylphosphates.[202] They showed that a rapeseed oil droplet on the prepared surface remained spherical shape with a CA of 150°, and could roll around without attaching when the surface was slightly tilted. However, insufficient understanding of the critical factors for superoleophobicity limited the continuous development of super oil-repellent surfaces in the following 10 years. In 2007, Tuteja *et al*. demonstrated that re-entrant surface curvature, in conjunction with low surface energy and roughened texture, allows for the construction of surfaces that show non-wetting ability towards a number of oily liquids with low surface tension.[17] They further clarified that when an oil droplet is deposited on a surface with re-entrant texture, the net force acting on the liquid-gas interface is directed upward, so the oil cannot penetrate the rough structures, thereby stabilizing the air pockets beneath the oil droplets and forming a solid-liquid-gas composite interface in the Cassie-Baxter state.[203] These works shed light on the key to designing superoleophobic surfaces and thus initiated the rapid development of super oil-repellent surfaces.[12,64,204] Subsequently, the skin of springtails was demonstrated to be super oil-repellent due to its overhanging microstructures (Fig. 14a), which benefit their living in habitats with surface-active substances contaminated water and potentially harmful microorganisms.[18]

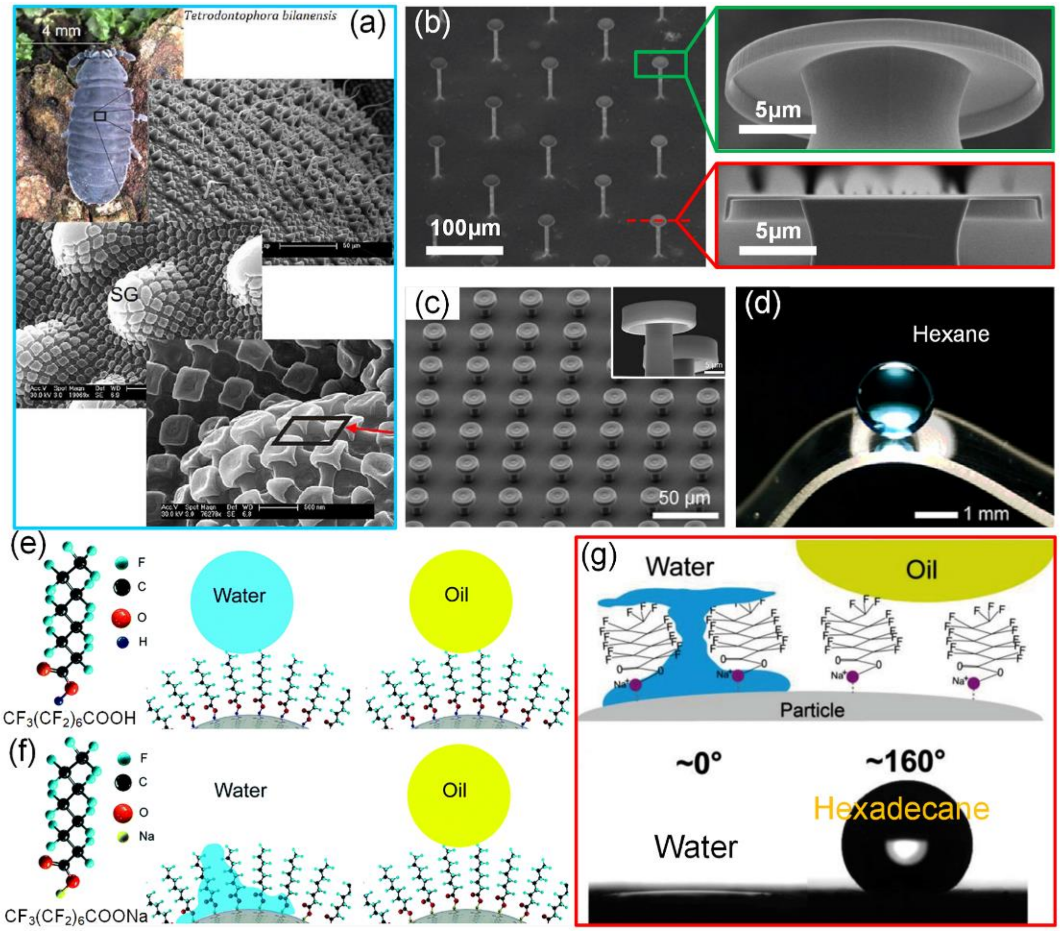

Fig. 14 (a) Digital image of springtail and surface microstructures of its skin. (b) Doubly re-entrant microstructures render any solid surface super repellent towards all available liquids. (c) Doubly re-entrant microstructures fabricated by harnessing the configurable elastic crack engineering, and (d) the resultant superoleophobic surface could repel hexane. (e) PFOA modified nanoparticles showed both superhydrophobicity and superoleopobicity in air, while (f) sodium perfluorooctanoate treated nanoparticles showed superoleophobicity but superhydrophilicity in air. (g) The fluorocarbon chain induces a low dispersive component of surface energy and repels the nonpolar oil (the CA of hexadecane was ~ 160°), whereas the hydrophilic units (sodium ions) enhance the polar component of surface energy and attract the polar water (the water CA was ~ 0°). (a) Reproduced with permission from ref. 18. Copyright (2011) Helbig *et al*. (b) Reproduced with permission from ref. 188. Copyright (2014) American Association for the Advancement of Science. (c, d) Reproduced with permission from ref. 63. Copyright (2019) PNAS. (e, f) Reproduced with permission from ref. 205. Copyright (2018) The Royal Society of Chemistry. (g) Reproduced with permission from ref. 206. Copyright (2018) WILEY-VCH Verlag GmbH & Co. KGaA, Weinheim.

Re-entrant structure for superoleophobic surfaces can be realized with well-defined overhang geometries, like micro inverted trapezoid,[207,208] micro/nano hoodoo,[17,209,210] and mushroom-like micropillars,[211-216] or with randomly aggregated micro-/nanostructures with inward curvature.[217-222] Li *et al*. designed surface textures with re-entrant curvature on both micro- and nanoscales, and found that compared with the single micro and single nano re-entrant superoleophobic surfaces, the micro/nano re-entrant-coordinated superoleophobic surface showed higher CA, lower CAH and smaller adhesion towards various liquids with surface tensions ranging from 26.5–72 mN m^{-1}.[223] Therefore, micro re-entrant structures can enhance the oil-repellence of superoleophobic surfaces. Liu *et al.* reported that a doubly re-entrant microstructure (Fig. 14b) can render any solid surfaces super repellent towards all available liquids (including perfluorohexane) even without low surface energy chemistry.[188] These specific doubly and even triply re-entrant structures show incomparable advantages in creating the structural basis for superoleophobicity, and have been widely employed in the design of excellent super oil-repellent surfaces.[191,192,224-227] However, these well-defined re-entrant microstructures are usually fabricated by reactive ion etching,[188] photopolymerization based 3D printing,[191,192,224-229] or recently-reported laser-induced localised heating and ablation of a bilayer matrix,[216] which suffer from limited substrate selection and difficulty for scale-up production. Recently, by harnessing the configurable elastic crack engineering, Li *et al*. proposed a facile and high-efficient method to construct arbitrary hierarchical structures (including well-defined, regular array structures) with broad material compatibility by harnessing the configurable elastic crack engineering, and as an example, they fabricated a superoleophobic polypropylene surface with an array of doubly re-entrant structures (Fig. 14c), which exhibited excellent repellence to various liquids including hexane with surface tension of ~ 18.6 mN m^{-1} (Fig. 14d).[63] Yet despite this, randomly structured super oil-repellent surfaces by spraying,[220] templating,[217] *etc.* could possess higher potential for scale-up production.

Due to the higher surface tension of water, most surfaces that are superoleophobic in air are also superhydrophobic, which has led them to be termed as superamphiphobic,[17,204,217] omniphobic[49,188,209] or superomniphobic[188,230,231] surfaces. However, some studies show that special design of the surface chemistry (*e.g.*, using fluorosurfactant that contains a low surface tension fluorinated tail and a high surface tension head group) enables the as-prepared surfaces to be both superoleophobic and superhydrophilic in air.[205,206,232-234] Water molecules induced surface reconfiguration is widely adopted to explain this counterintuitive phenomenon since complete water spreading (*i.e.*, water CA decreased to ~ 0°) always takes some time (typically tens of seconds to several minutes or even longer).[232,233] Brown *et al*. fabricated a superoleophobic-superhydrophilic surface by a layer-by-layer technique and deposition of fluorosurfactant (Capstone FS-50, DuPont), which showed super oil-repellence and rapid water wetting (within 2 s).[234] They attributed this to the molecule size difference between oil and water: larger oil molecules are blocked by the top fluorinated layer while smaller water molecules can penetrate through the top layer and contacting with the underlying hydrophilic region.[234,235] Recently, Pan's group fabricated various superoleophobic-superhydrophilic surfaces with rapid response for both oil repellence and water spreading, and proposed a theory based on the dispersive and non-dispersive component of surface free energy.[205,206] For example, the sprayed coating from the mixture of TiO_2 nanoparticles and perfluorooctanoic acid (PFOA, $CF_3(CF_2)_6COOH$) showed superamphobicity (Fig. 14e) because the non-dispersive and dispersive components of its surface free energy are both low. However, after replacing the hydrogen atom of PFOA with sodium (Na) atom, the non-dispersive component became higher while the dispersive component remained low since the fluorocarbon chains were unchanged. Therefore, the sprayed coating consisting of TiO_2 nanoparticles and sodium perfluorooctanoate ($CF_3(CF_2)_6COONa$) showed superoleophobicity and superhydrophilicity (Fig. 14f and g) as the fluorocarbon chains repels the nonpolar oil, whereas the hydrophilic Na^+ attracts the polar water. Similarly, Sun *et al*. fabricated superoleophobic-superhydrophilic surfaces by using Capstone FS-50 modified SiO_2 nanoparticles, which could be rapidly wetted by highly polar liquids (*e.g.*, water) while completely repel nonpolar oily liquids (*e.g.*, *n*-hexadecane).[236]

2.3.2.2 Superoleophobic surface underwater. In 2009, Liu *et al*. reported that fish scales (Fig. 15a) with superhydrophilicity in air shows superoleophobicity underwater.[19] Fish scales are composed of calcium phosphate, protein, and a thin layer of mucus; the surface morphology is characterised by oriented rough micropapillae with length of 100–300 μm and width of 30–40 μm (Fig. 15b), enabling the scales to be superhydrophilic and superoleophilic in air (Fig. 15c). When an oil droplet comes into contact with the fish scales that were immersed in water, the trapped water in the micro/nano structures assists the formation of an oil-water-solid composite interface that coincides with the Cassie-Baxter wetting model, thereby showing underwater superoleophobicity with CA of 156.4 ± 3.0° for 1,2-dichloroethane droplet (Fig. 15d). In the following years, some other natural creatures with underwater superoleophobic surfaces have also been discovered, such as the lower side of Lotus leaf,[237] clam's shell,[238] filefish skin,[239] seaweed,[240] aloe vera mucilage,[241] pomfret skin,[242] *etc*.

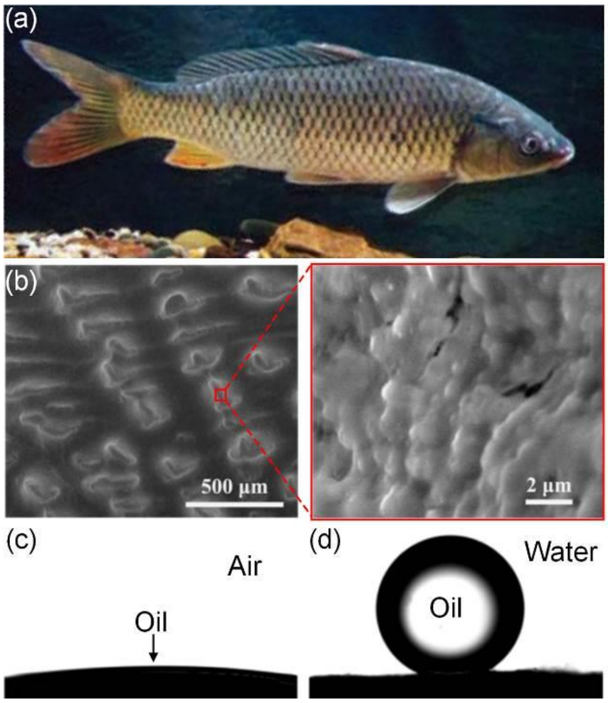

Fig. 15 Underwater superoleophobicity of fish scales. (a) Photo of a fish under water. (b) Surface morphology of fish scales. (c) Superoleophilicity in air and (d) superoleophobicity under water. (a) Reproduced with permission from ref. 10. Copyright (2019) Zhang *et al*. (b–d) Reproduced with permission from ref. 19. Copyright (2009) WILEY-VCH Verlag GmbH & Co. KGaA, Weinheim.

The construction of underwater superoleophobic surface is based on introducing the repulsive water phase into the roughly structured hydrophilic surface, which opens up a new research area for super oil-repellent surfaces.[19] It has been proven that the combination of hydrophilicity in air and roughness generally endows surfaces with superoleophobicity underwater.[19,64,237-240] Therefore, the strategy to fabricate underwater superoleophobic surface focuses on creating superhydrophilic surface in air, and many methods have been employed to construct such underwater super oil-repellent surfaces, such as dip-/spray-coating,[243,244] chemical treatment,[245,246] electrochemical method,[247,248] plasma exposure,[249-251] electrospinning,[184,252] thermal treatment,[253,254] lithography,[255] laser texturing,[256] *etc*.

2.3.3 Slippery liquid-infused surface

Although superhydrophobic and superoleophobic surfaces always possess excellent liquid repellence, most of them suffer from poor mechanical durability, weak air cushion stability in terms of high pressure or liquid intrusion.[11] Inspired by carnivorous plants such as *Nepenthes* pitcher plant (Fig. 16a), which captures prey by a slippery, water-infused surface at the rim of the pitcher,[257] Wong *et al*. reported slippery liquid-infused surfaces (SLISs) by infiltrating epoxy-resin-based nanofabricated post array or Teflon-based porous nanofiber network with perfluorinated liquids (such as 3M Fluorinert FC-70, DuPont Krytox 100 and 103) (Fig. 16b).[20] The infused liquid (*i.e.*, lubricant) is locked in place by the micro/nano structures and forms a physically smooth and chemically homogeneous lubricating film on the solid surface. When a droplet of another immiscible liquid contacts the SLIS, a liquid-liquid interface between the infused liquid and droplet is created, and an infused liquid “cushion” retains beneath the testing liquid, preventing the solid surface from being wetted by the testing liquid (Fig. 16c). Depending on the surface tension of the infused liquid, SLIS is characterised by exceptional liquid repellence (negligible CAHs and low SAs for low surface tension liquids and their complex mixtures), instantaneous and repeatable self-healing after mechanical damage, and extreme pressure stability, all of which are advantages over traditional superhydrophobic and superoleophobic surfaces,[11] thereby making SLIS to become another fascinating candidate of liquid-repellent surfaces in the past decade. Besides SLIS, some other terms are also adopted to describe slippery liquid-repellent surface in the literature, such as slippery liquid-infused porous surface,[11,20] slippery pre-suffused surface,[258] liquid-infused surface,[14,259] lubricant-infused surface,[11,85,87] and lubricant-impregnated surface,[86,260] and we use the “SLIS” to represent this kind of slippery liquid-repellent surface throughout this review.

To prepare SLIS successfully, three main design criteria must be met:[20] (i) the infused liquid must wick into, wet and stably adhere within the substrate, (ii) the solid surface must be preferentially wetted by the infused liquid rather than by the testing liquid that is to be repelled, namely, the surface tensions of the infused liquid and testing liquid, and the interfacial tension at the liquid-liquid interface must satisfy eqns (12)–(14), and (iii) the infused liquid and the testing liquid must be immiscible. Hydrophobic and porous/textured substrates are generally combined to construct SLISs since micro/nano structures and low solid surface energy favor the immobilization and stabilization of the infused liquids *via* capillary forces and intermolecular forces.[20,261,262] However, recent works have demonstrated that hydrophilic smooth surfaces can also be imparted with slippery liquid repellence *via* some ingenious strategies, such as immobilizing infused liquid *via* π-OH or π-COOH interactions,[263,264] and covalent graft of liquid-like polydimethylsiloxane (PDMS)-based brushes.[143,265-273] For example, Wang *et al*. prepared slippery liquid-like omniphobic coatings on hydrophilic smooth glass slides by covalently grafting PDMS brushes through rapid acid-catalyzed polycondensation of dimethyldimethoxysilane monomers (Fig. 17a, b).[143] Fang *et al*. fabricated a highly smooth (roughness of < 1 nm), ultrathin (thickness of ~ 2 nm) and transparent slippery "liquid-like" coating on silicon wafer substrate through one-step condensation under heating (100 °C for 24 h).[274] The grafted PDMS chains possess high mobility through rotational and/or bending motions since only one end is covalently grafted to the surface,[275] and the mobile PDMS chains can facilitate the motion of triple-phase contact lines by minimizing the Gibbs free energy barriers between metastable states, which imparts the coated surfaces with excellent liquid repellence (Fig. 17c).[143] It is further demonstrated that the PDMS-grafted layer creates chemical affinity to nonpolar liquids, enabling the immobilization of silicone oil, which makes hydrophilic flat surfaces to be slippery and repellent towards various liquids and even soft viscoelastic solids.[276,277] Additionally, swelling flat polymer matrixes by suitable infusing liquids are also proved to be effective in preparing SLISs, and the most common combination is PDMS swelling in silicon oil.[278-281] Recently, Salbaum *et al*. proposed to confine ionic liquids to the underlying flat substrate by swelling of polymeric gels that were functionalized to match the chemical structure of the ionic liquids, their molecular interactions were maximized and thus yielded an enduring slippery ionic liquid-infused organogels.[282]

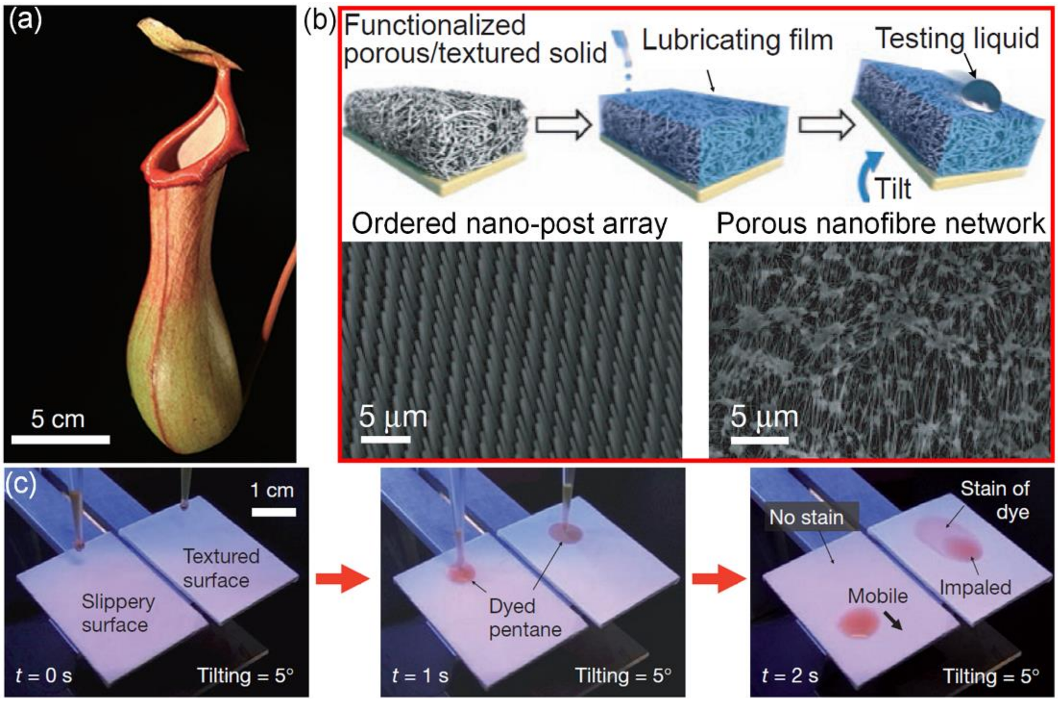

Fig. 16 *Nepenthes* pitcher plant inspired SLIS. (a) Photograph of *Nepenthes* pitcher plant. (b) Creating SLIS by infusing epoxy-resin-based nano-post array or Teflon-based porous nanofiber network with lubricants. (c) Anti-wetting property of the SLIS. (a) Reproduced with permission from ref. 65. Copyright (2016) Nature Publishing Group. (b, c) Reproduced with permission from ref. 20. Copyright (2011) Nature Publishing Group.

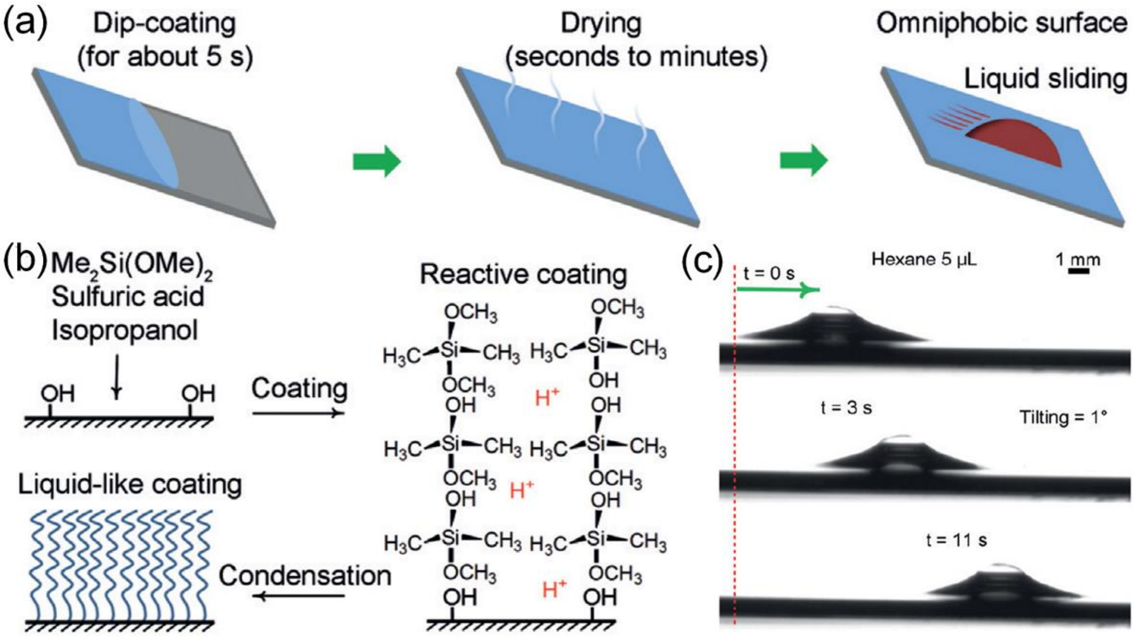

Fig. 17 (a) Preparation of slippery liquid-like surface with covalently grafted PDMS brushes. (b) Formation of the PDMS coating by rapid acid-catalyzed polycondensation of dimethyldimethoxysilane. (c) Time-sequence images of a hexane droplet sliding down the tilted slippery surface. Reproduced with permission from ref. 143. Copyright (2016) WILEY-VCH Verlag GmbH & Co. KGaA, Weinheim.

Immiscibility of the infused liquid and testing liquid is another major requirement for preparing SLIS.[20,85,87] Sett *et al*. investigated the miscibility of a range of testing liquids (surface tensions of 12−73 mN m^{-1}) with widely used lubricants (viscosities of 5−2700 cSt) in SLIS design.[87] The tested lubricants included fluorinated Krytox oils (Krytox 1506, 1525, and 16256), hydrocarbon silicone oils (with viscosities of 5, 100, 500, and 1000 cSt), carnation mineral oil, and ionic liquids (1-butyl-3-methylimidazolium bis(trifluoromethylsulfonyl)-imide, BMIm), while water, alcohols, alkanes, ethylene glycol, toluene, and perfluorohexane (Fluorinert FC-72) were used as testing liquids. Results indicated that no single lubricant was suitable for all of the testing liquids. As depicted in Fig. 18, Krytox oils should be the preferred lubricants for most of the studied testing liquids except perfluorohexane, carnation oil might be suitable for polar organic compounds (such as ethylene glycol, ethanol, and perfluorohexane), ionic liquid BMIm was the desired lubricant for repelling alkanes, and silicone oils should be infused to build SLIS that repelled perfluorohexane.

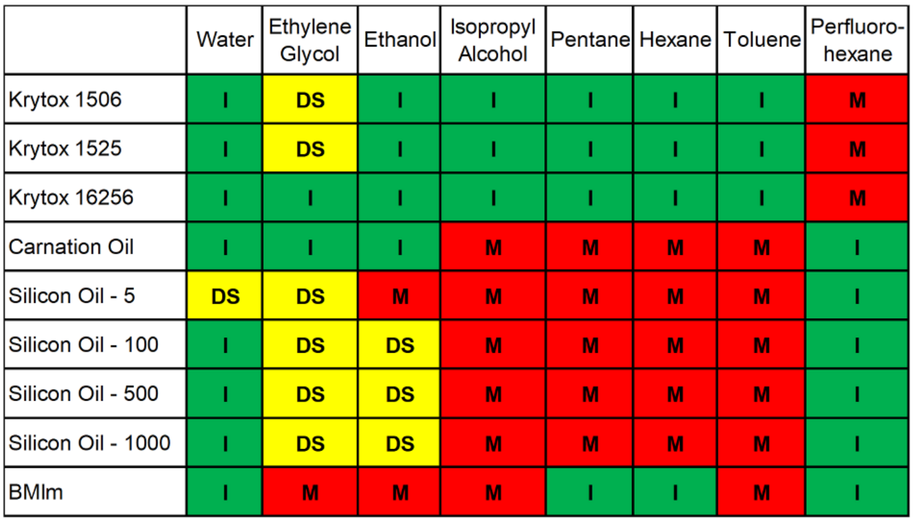

	Water	Ethylene Glycol	Ethanol	Isopropyl Alcohol	Pentane	Hexane	Toluene	Perfluorohexane
Krytox 1506	I	DS	I	I	I	I	I	M
Krytox 1525	I	DS	I	I	I	I	I	M
Krytox 16256	I	I	I	I	I	I	I	M
Carnation Oil	I	I	I	M	M	M	M	I
Silicon Oil - 5	DS	DS	M	M	M	M	M	I
Silicon Oil - 100	I	DS	DS	M	M	M	M	I
Silicon Oil - 500	I	DS	DS	M	M	M	M	I
Silicon Oil - 1000	I	DS	DS	M	M	M	M	I
BMIm	I	M	M	M	I	I	M	I

Fig. 18 Miscibility testing results of various lubricants and testing liquids. Green, yellow, and red correspond to immiscible (I), delayed separation (DS), and completely miscible (M) liquids. Reproduced with permission from ref. 87. Copyright (2017) American Chemical Society.

3 Robustness and Durability of Liquid-Repellent Surfaces

Despite over nearly two decades of intense research, liquid-repellent surfaces are, however, still plagued with problems that severely limit their real-world applications: thermodynamic instability, mechanical fragility, and poor chemical resistance.[14,43,44,283-285] In recent years, much attention has been paid to the development of liquid-repellent surfaces that can last their liquid repellence for a long time without obvious deterioration under various thermodynamic, mechanical, or chemical stimuli. Meanwhile, some related terminologies, such as thermodynamic/mechanical/chemical stability/robustness/durability,[43,44,286-291] wear/abrasion-resistance,[286,292-295] chemical/corrosion resistance,[72,291,296] *etc.*, have been employed to describe the ability of liquid-repellent surfaces to survive in various conditions. Among them, "stability" alone sometimes implies that the surfaces are not liable to undergo the damage of liquid repellence on short-term scale, and "wear-resistance" only covers the stability of liquid-repellent surfaces towards mechanical wear partially. "Robustness" is usually used to describe the stability of biological and control systems,[297,298] so it can be used to describe the liquid-repellent surfaces that are strong enough to be intensively used and thereby to ensure the system to run stably. "Durability" indicates that the liquid-repellent surfaces are able to withstand dynamic impacting, wear, or corrosion, *etc*., and the liquid repellence can last for a long time without obvious deterioration, indicating the long-lasting stability of liquid-repellent surfaces comprehensively. Accordingly, to unify the terminology, we use "thermodynamic durability", "mechanical durability" and "chemical durability" to describe the long-term stability of liquid-repellent surfaces under corresponding external conditions throughout this review. In this section, the thermodynamic, mechanical and chemical durability of liquid-repellent surfaces, as well as their corresponding typical testing methods, are summarized.

3.1 Thermodynamic Durability

The liquid repellence of superhydrophobic and superoleophobic (both in air and underwater) surfaces relies on the air or water cushion trapped/locked in the rough structures (*i.e.*, the Cassie-Baxter wetting state), and that of SLIS originates from the infused liquid layer. The cushion layer may be thermodynamically damaged under some conditions, such as diffusion, evaporation, drainage, *etc*. Therefore, the thermodynamic durability of these liquid-repellent surfaces refers to the persistence or recovery of the air or liquid cushions during contact with testing liquids or exposure to other medium.

It is well established that the air cushion beneath testing liquid is indispensable to build the Cassie-Baxter wetting state of superhydrophobic and superoleophobic (in air) surfaces with super liquid repellence. However, the trapped air cushion could be destroyed under some conditions that the surfaces typically undergo during use, which finally leads to a so-called Cassie-Baxter to Wenzel transition (also termed as impalement), and thereby resulting in the pinning of liquid droplet and loss of super liquid repellence.[13,283,285,299,300] The wetting transition occurs when the wetting pressure exceeds the capillary pressure of the meniscus,[300] and it has been observed in many scenarios. For example, pressing the water droplet placed on a superhydrophobic surface can trigger its wetting state transition from Cassie-Baxter to Wenzel, leaving the droplet to stick on the surface (Fig. 19a).[300,301] Liquid droplet/jet impacting on super liquid-repellent surface leads to either complete rebound of the droplet with the air cushion retained (*i.e.*, Cassie-Baxter state) or partial/total sticking with the cushion abated (*i.e.*, Wenzel state), as illustrated in Fig. 19b, which depends on the surface tension of the impacting liquid, impacting speed, surface structure and ambient conditions.[299,302-306] It has also been demonstrated that the impalement of liquid droplet happens when its volume decreased due to evaporation (Fig. 19c), which is attributed to the increased Laplace pressure of small droplet.[307-310] Vapor condensation on super liquid-repellent surfaces forms randomly distributed nanodroplets within rough textures, which gradually bridge together and grow to be droplets in the Wenzel wetting state (*i.e.*, flooding condensation), resulting in the loss of liquid repellence when vapor condensation occurred or hot water contacted the surface (Fig. 19d).[159,183,311,312] Meanwhile, condensation-induced blisters through nanoscale pinholes on the hydrophobic thin coatings will result in the delamination of the coatings if the condensed droplets cannot overcome the Laplace pressure barrier generated by the pinned three-phase contact line at the pinhole, which finally develop into the failure of liquid repellence.[313-315] Another frequently-meet and significant situation for the wetting model transition is immersing the surface in the repelled liquid (either static or flowing), where a gradual disappearance of the cushion is observed (Fig. 19e), and this generally results from liquid static pressure, air diffusion driven by chemical potential gradient, and/or shear stress induced deformation/detachment of the air bubbles.[283,316-319] Additionally, some other mechanisms, such as vibration,[320,321] water hammer pressure,[322-324] electrowetting,[325-327] electrostatic attraction[154] and electric field adaptive deformation,[153] have also been reported to induce the cushion instability and thus wetting transition.

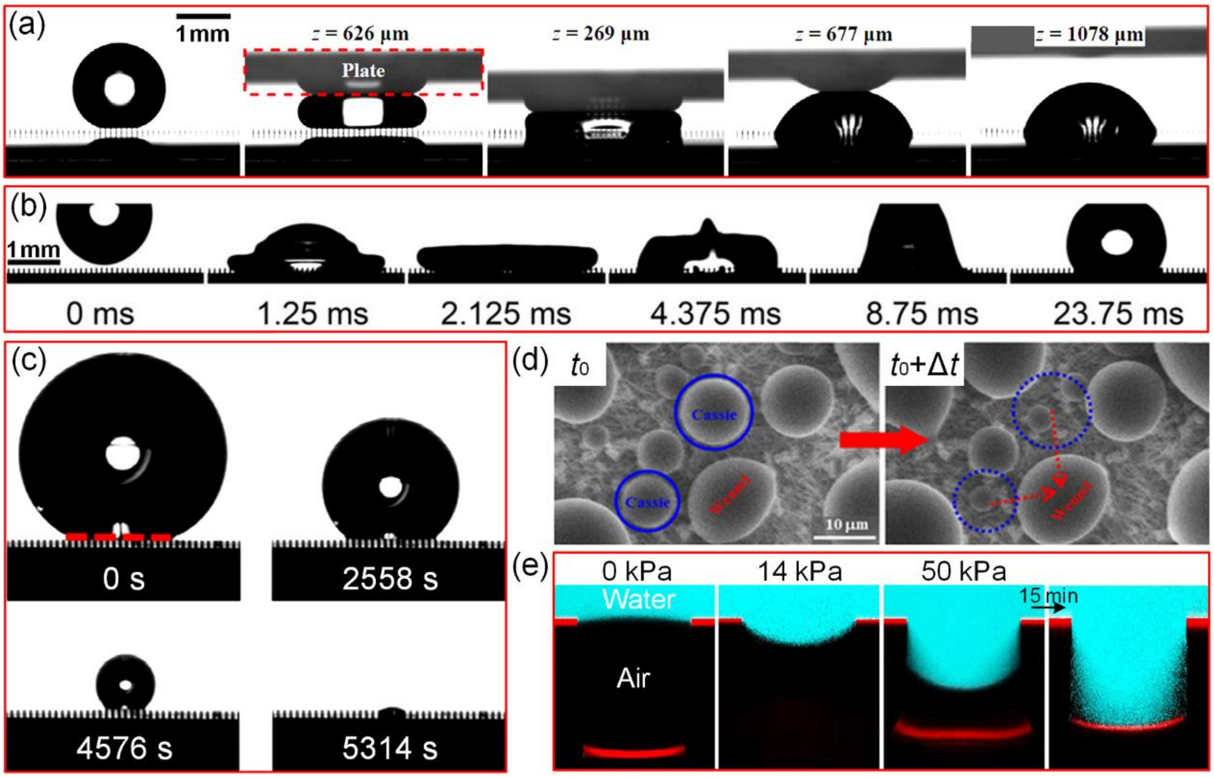

Fig. 19 Thermodynamic wetting transition from Cassie-Baxter state to Wenzel state. (a) Pressing the droplet. (b) Droplet impinging. (c) Droplet evaporation. (d) Vapor condensation. (e) Immersing in water and increasing the hydrostatic pressure. (a) Reproduced with permission from ref. 301. Copyright (2017) Li *et al*. (b) Reproduced with permission from ref. 302. Copyright (2019) American Chemical Society. (c) Reproduced with permission from ref. 308. Copyright (2012) American Physical Society. (d) Reproduced with permission from ref. 159. Copyright (2019) American Chemical Society. (e) Reproduced with permission from ref. 317. Copyright (2014) American Physical Society.

For the underwater superoleophobic surface, the locked water within the rough micro/nano structures serves as a repulsive cushion that prevents oil from contacting with the solid surface directly. The underwater Cassie-Baxter state for oil/water/solid wetting system is documented to be thermodynamically stable during long-term immersion in water,[242,245,249,328] and the destruction of the water cushion has been rarely observed hitherto even if the testing oil droplet is severely pressured by a preloading force.[247] However, as superoleophobicity underwater is closely connected with the superhydrophilicity in air (*i.e.*, water hydration ability),[19,64,237-240] it should be emphasized that superhydrophilic surfaces exposed to air often (not always) show thermodynamical instability,[329-331] although the quantitative/qualitative relationship between the instability of water wettability in air and resultant change of underwater oil wettability has not been well-addressed yet. Superhydrophilic surface exposed to air tends to reorganize in order to minimize its interfacial energy to maintain equilibrium, this thermodynamically driven instability is extensively observed in plasma induced (super)hydrophilic modification, which is also termed as aging behavior, and some possible mechanisms for the instability are proposed, such as reorientation of polar groups, diffusion of low molecular weight species and adsorption of organic contaminants from air.[332-334] Chen *et al.* elucidated that the instability of superhydrophilic surfaces in air is closely related to the surface micro/nano structure, surface chemistry, ambient temperature and relative humidity, *etc*.[330,331,335] It was also showed that storing in water favors the long-term stability of superhydrophilic surface (Fig. 20a),[330] which is consistent with the ever-lasting underwater superoleophobicity (Fig. 20b).[242,245,249,328]

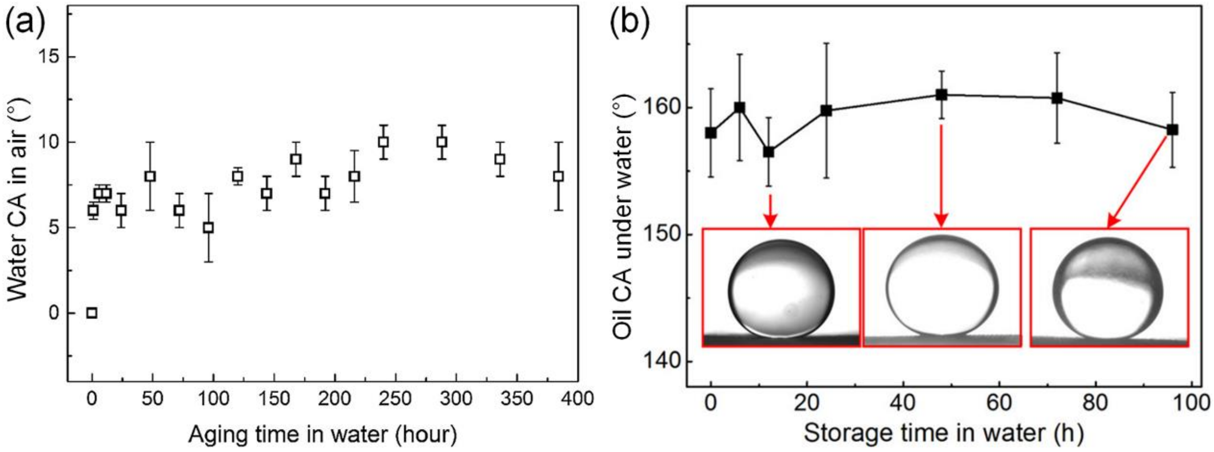

Fig. 20 Stability of (a) superhydrophilic surface and (b) underwater superoleophobic surface that are stored in water. (a) Reproduced with permission from ref. 330. Copyright (2016) Elsevier Inc. (b) Reproduced with permission from ref. 249. Copyright (2016) American Chemical Society.

The infused liquid layer is critical for the liquid repellence of SLIS due to its defect-free and smooth features, and intrinsically immiscibility towards testing liquid, which nearly eliminates the pinning of liquid contact line.[20] SLIS is reported to be surprisingly stable towards pressure up to ~ 680 atm, which is equivalent to the hydrostatic pressure at a depth of ~ 7 km.[20] However, thermodynamic instability of the lubricant always leads to its depletion, which inevitably results in the failure of SLISs. Gravimetric drainage,[279] evaporation,[336,337] immersing in other liquids,[338-340] and liquid droplets/jet impinging or sliding[337,341,342] are mostly considered incentives for the lubricant loss. When a testing droplet is deposited on SLIS, the redistribution of the lubricant layer on the surfaces occurs, and the interconnected lubricant dynamics subsequently results in the formation of wetting ridge around the droplet. Then the movement of the droplet generates shear force and drags the lubricant meniscus downhill, which dominates the depletion of the lubricant.[341] Tress *et al.* demonstrated that decreasing the lubricant thickness would increase the extra height of the wetting ridge, leading to the acceleration of lubricant depletion *via* droplet sliding.[337] Kreder *et al.* found that the lubricant depletion rate was related to the capillary number of the two liquid-phases system ($Ca = \eta v/\gamma_{\mathrm{LV}}$, where η, v, and γ_{LV} is the viscosity, velocity and surface tension of the droplet, respectively).[341] Their findings showed that droplets with higher Ca deplete much less lubricant than slower-moving droplets on less viscous lubricants (Fig. 21a), indicating counterintuitively that those faster moving droplets created higher shearing force but less lubricant depletion. It was also demonstrated that the volume of the wetting ridge nearly equaled that of the lost lubricant (Fig. 21b), confirming that wetting ridge was the main source of lubricant depletion during a moving droplet swept across a SLIS.

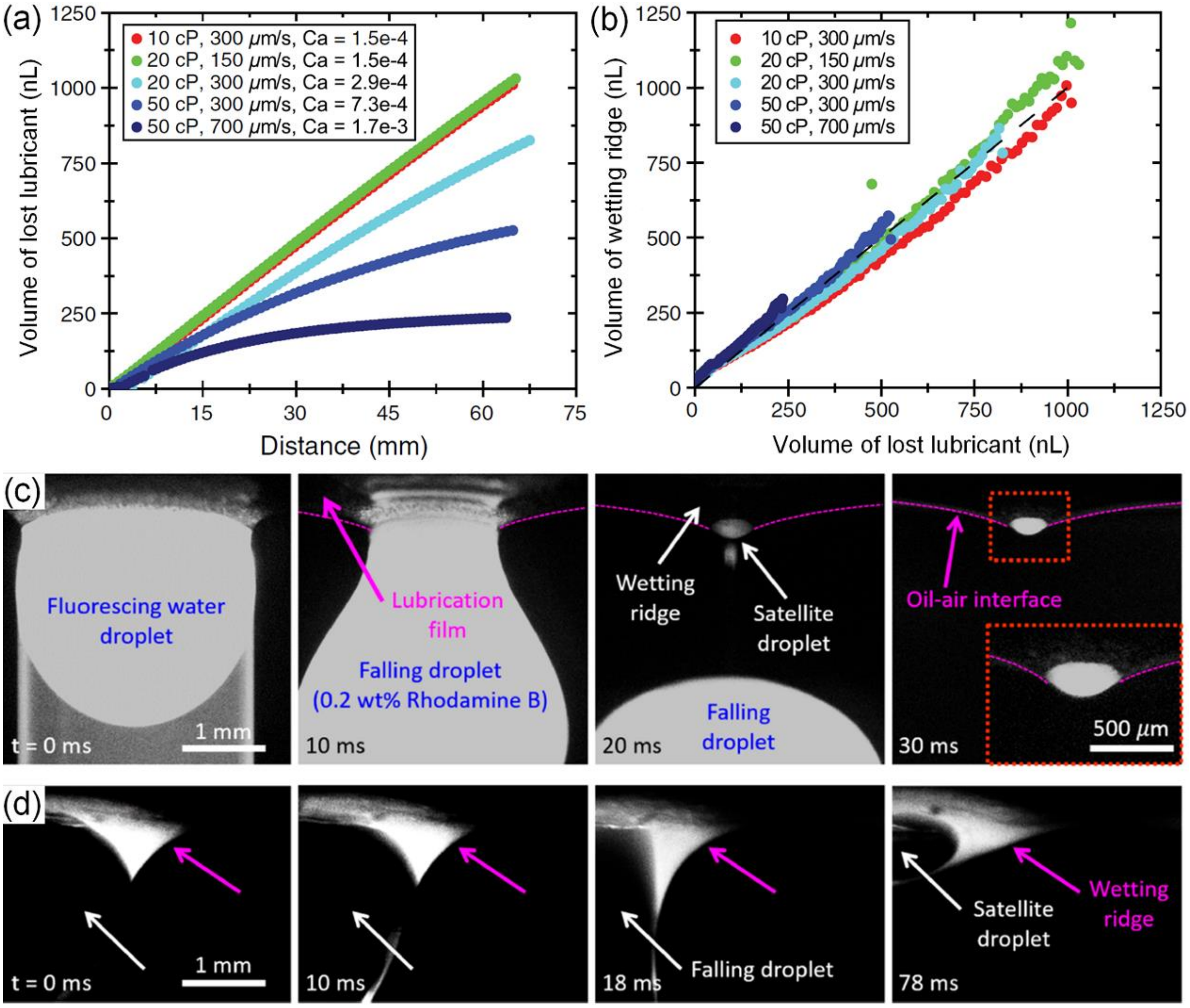

Fig. 21 (a) Relationship between the volume of lost lubricant and capillary number (*Ca*). (b) Relationship between the volume of lost lubricant and that of wetting ridge. Time-lapse images of (c) fluorescently labeled water droplet falling in a gravitational field, and (d) the corresponding fluorescently dyed lubricant layer. (a, b) Reproduced with permission from ref. 341. Copyright (2018) Kreder *et al*. (c, d) Reproduced with permission from ref. 342. Copyright (2020) American Chemical Society.

Adera *et al*. studied the lubricant depletion caused by pendant water droplets on horizontal copper tube with nanostructured outside SLIS during condensation.[342] They revealed that droplets falling from tube surface broke unequally and left behind small satellite droplets that retained the bulk of the lubricant in the wetting ridge (Fig. 21c and d), which was totally different from the droplets sliding off from tilted flat SLISs where the entire wetting ridge left the surface upon droplet departure. In addition, when eqn (14) was met, a highly non-uniform both spatially and temporally layer of lubricant wrapped on the droplet (*i.e.*, cloaking). Although the lubricant depletion by cloaking layer was demonstrated to be much less than that by wetting ridge,[341,342] it still needs to be well considered in terms of the thermodynamic durability of SLIS.

3.2 Mechanical Durability

Liquid-repellent surfaces are generally characterised by micro/nano structures and specific surface chemistry, and will be always exposed to direct action of various external forces in real environments. For example, superhydrophobic clothes will inevitably be rubbed by hands, stretched and bended; superhydrophobic windshield of a car will suffer from the impacting of raindrops and sands blown by the wind; medical implants with SLISs often serve under severe abrasion with tissues, to name a few. However, if the surface textures are highly susceptible to external forces caused by rubbing, impacting, stretching, peeling, *etc*., different morphological changes like abrasion, rupture, flattening and exfoliation will be generated, leading to increased sticking or even spreading of the testing liquid and thus the loss of liquid repellence. Consequently, the mechanical robustness and durability, which imply the ability of liquid-repellent surfaces to withstand the destructions of surface textures and/or chemistries under continuous external force action, are practically important for these surfaces. Usually, according to the direct results of the force action, mechanical durability testing methods can be classified as tangential abrasion, dynamic impacting, tape peeling, substrate deformation, *etc*., which are depicted in Fig. 22.

3.2.1 Tangential abrasion

Contact and relative motion between two solid surfaces always generates tangential abrasion, a common condition that liquid-repellent surfaces often encounter during real use. Dynamic friction between the contact points causes material removal, leading to gradual flattening of the rough textures and/or depletion of the infused liquid, which finally gives rise to the loss of the liquid repellence with abrasion-dependent extent. Various methods and setups have been reported to perform tangential abrasion test of liquid-repellent surfaces, such as simple finger wiping, manual sandpaper abrasion, automatic tribometer abrasion, scratch by hard tips, *etc*.

Finger wiping (Fig. 22a) is reported in the literature to simulate rubbing on liquid-repellent surfaces,[54,269,343-345] and Fig. 22b shows a finger rubbing induced surface morphology damage on a spray-coated superhydrophobic coating.[345] Although natural secretions like sweat and oil exist on fingers,[43,346] they can be neglected or eliminated by wearing a glove in the wiping test. Finger wiping is a simple method where no special requirements are needed, but it is difficult to control the applied pressure and to evaluate the mechanical durability quantificationally.

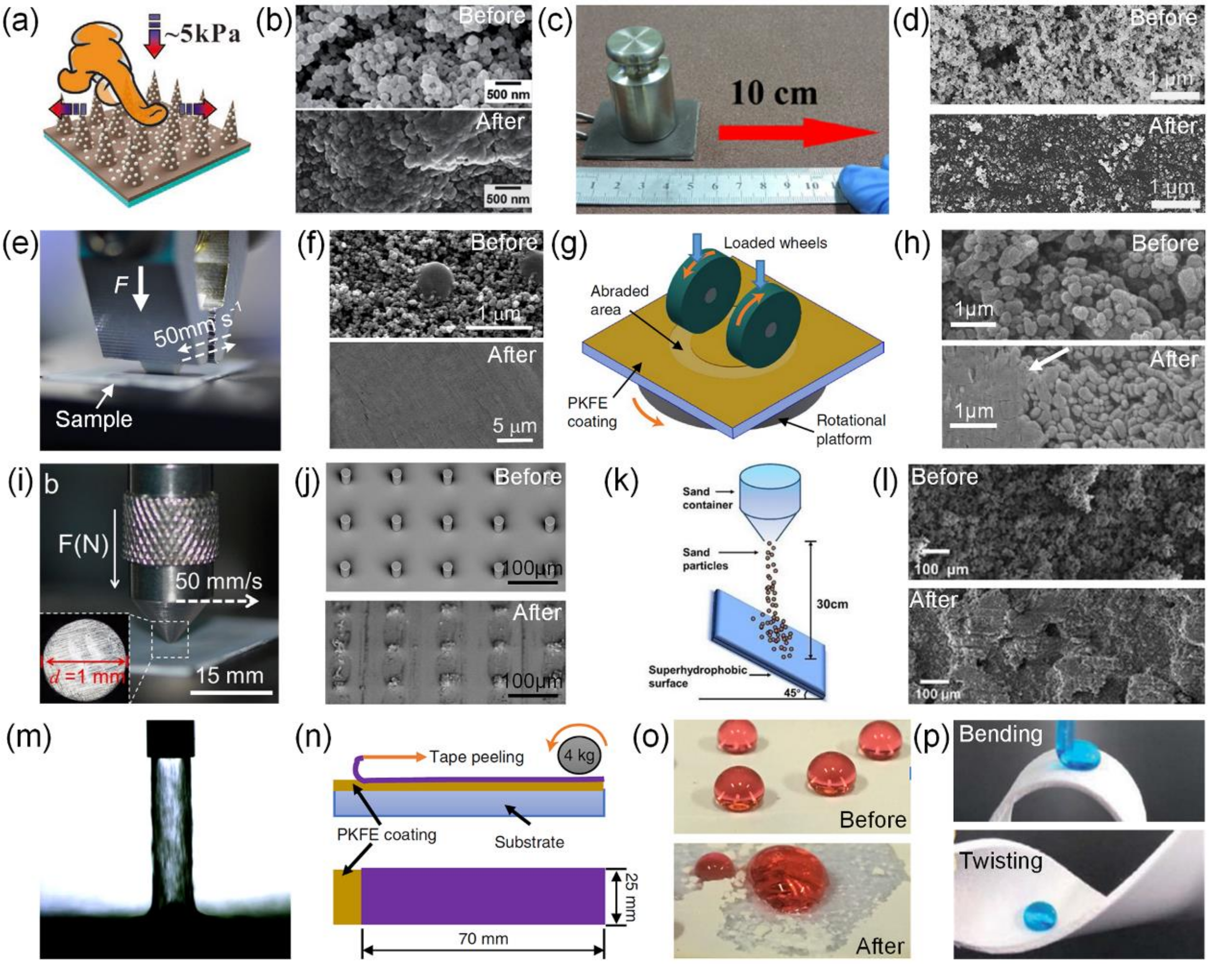

Fig. 22 Typical methods to test the mechanical durability of liquid-repellent surfaces. (a) Finger wiping. (b) SEM images of a superhydrophobic coating before and after finger wiping. (c) Sandpaper abrasion. (d) Surface morphology of a commercial superhydrophobic coating (Neverwet) before and after sandpaper abrasion. (e) Linear abrasion. (f) SEM images of a commercial superhydrophobic coating (Ultra-Ever Dry) before and after linear abrasion. (g) Circular abrasion. (h) Intensive Taber abrasion induced obvious plastic deformation of the surface structures. (i) Scratch by indenter. (j) Normal load of 10 N caused severe microstructures damage on a superhydrophobic pillar surface after scratching. (k) Falling sand impacting. (l) SEM images of a superhydrophobic coating before and after falling sand impacting. (m) Water jet impacting. (n) Tape peeling test. (o) Superhydrophobic coating with poor robustness could be easily destroyed by tape peeling. (p) Substrate deformation. (a) Reproduced with permission from ref. 347. Copyright (2021) WILEY-VCH Verlag GmbH & Co. KGaA, Weinheim. (b) Reproduced with permission from ref. 345. Copyright (2015) The Royal Society of Chemistry. (c) Reproduced with permission from ref. 348. Copyright (2019) American Chemical Society. (d) Reproduced with permission from ref. 52. Copyright (2021) Dong *et al*. (e, f, i, j and m) Reproduced with permission from ref. 47. Copyright (2020) Nature Publishing Group. (g, h and n) Reproduced with permission from ref. 291. Copyright (2018) Nature Publishing Group. (k, l) Reproduced with permission from ref. 349. Copyright (2020) Elsevier B.V. (o) Reproduced with permission from ref. 350. Copyright (2019) Elsevier B.V. (p) Reproduced with permission from ref. 351. Copyright (2019) The Royal Society of Chemistry.

Sandpaper abrasion (Fig. 22c) is probably the most widely selected mechanical durability testing method in the literature,[43,54,67,244,352-357] as it does not require specialized or professional equipment, and can offer quantitative analysis of the robustness. Typically, the liquid-repellent surface is placed face-down to a sandpaper, and a loading is applied on the solid substrate to provide normal pressure, then the substrate is moved along the tangential direction with a certain speed and distance. Longitudinal and then transverse abrasion or *vice versa* is suggested to be defined as one abrasion cycle.[54] Abrasion degree from the sandpaper can be adjusted by the grit number (*i.e.*, granularity) of sandpaper, the mass of applied loading (*i.e.*, pressure), and the speed and distance of each abrasion cycle. Fig. 22d illustrates the SEM images of a spray-coated commercial superhydrophobic coating (Neverwet) before and after sandpaper abrasion under a pressure of 10 kPa for 4.0 m, showing obvious surface textures damage and thus a CA decreasing from 156° to 92°.[52] However, sandpaper abrasion is sometimes time-consuming when too many abrasion cycles are required, especially for those abrasion-tolerant surfaces. Moreover, sandpaper abrasion is a full-manual testing process and is thereby susceptible to operator error, making it difficult to compare the robustness of different liquid-repellent surfaces.

Linear and circular abrasions by tribometer (Fig. 22e, g) are recently popular in mechanical durability testing of liquid-repellent surfaces due to their advantages in automation and qualitative analysis.[43,47,269,291,349,354,356,358] For example, Wang *et al*. showed that superhydrophobic surfaces coated with commercial Ultra-Ever Dry coating lost their super water repellence after 100 cycles linear abrasions due to nearly complete removal of the surface micro/nano structures (Fig. 22f).[47] Peng *et al*. performed the circular abrasion of an all-organic superhydrophobic nanocomposite coatings using an ASTM standard (D4060) Taber abrasion technique, and found that the area under drastic abrasion (100 cycles) suffered from obvious plastic deformation (Fig. 22h), leading to the partial loss of their superhydrophobicity.[291] These tests are generally conducted as follows: the testing surface is fixed upward on the sample platform of a standard equipment (*e.g.*, Taber abrasion machine), and then the abradant (*e.g.*, steel ball, indenter and abrasive wheels) makes contact with the surface under a normal loading, following which the abrasion testing starts automatically under to-and-fro feed movement of the abradant or rotation of the platform with the pre-set loading and speed. Linear and circular abrasions by tribometer could reduce operator error, enabling them to be preferable in evaluation of robustness towards tangential abrasion, especially in multiple abrasion cycles testing.

Scratch by hard tips (*e.g.*, blade, knife, screwdriver, indenter, *etc*.) is another common testing method for mechanical durability of liquid-repellent surfaces.[47,54,56,269,352,356-359] For example, Wang *et al*. showed that indenter scratch under normal load of 10 N (Fig. 22i) could severely damage the micropillars of a superhydrophobic surface (Fig. 22j), resulting in the decrease of water CA from ~ 160° to ~ 120° and droplet pinning,[47] while knife scratch has little influence on the liquid repellence of SLISs due to their self-healing ability.[56,269] Though this method is easy to be operated, it can hardly provide quantitative evaluation of the robustness, and the density of the scratches (*i.e.*, the scratched area) is rarely considered in previous publications.

3.2.2 Dynamic impacting

Rain, sand and wind storms are typical harsh conditions in outdoor application scenarios for liquid-repellent surfaces. For example, the raindrops in a thunderstorm have maximum diameters of 4–5 mm, and the impacting speed reaches up to 7–9 m s^{-1} on a solid surface with a frequency of 3.88×10^5 drops m^{-2} h^{-1}.[360] Intensive impacting could cause fracture of the surface textures and/or removal of the infused-liquid of the liquid-repellent surfaces, which could negatively affect their liquid repellence. Therefore, much attention has to be paid to the dynamic impacting induced potential fragility, and some artificial impacting methods are proposed to address this issue, including falling sand, liquid droplet, liquid jet, *etc*.[43,44,284]

Falling sand impacting is often employed to study the influence of solid particles impacting on liquid-repellent surfaces.[217,218,270,349,353,361-363] As depicted in Fig. 22k, in this testing, the liquid-repellent surface is fixed with a tilting angle (usually 45°), and the pre-collected sand is placed in a container and located above the surface, then the sand is dropped down, accelerated by gravity and finally impacts on the surface. As reported by Wu *et al.*, one of their superhydrophobic coatings lost its superhydrophobicity (water CA decreased from ~ 164° to ~ 140°, while SA increased from < 10° to 24°) after falling sand impacting, due to obvious flattening of the surface rough structures (Fig. 22l).[218] Wu *et al.* showed that falling sand impacting invalidated the liquid repellence and biofouling resistance of a SLIS (perfluoropolyether oil infused porous PTFE membranes),[270] which probably originated from the cooperative effect of rough structures change and lubricant depletion. Impacting energy (*i.e.*, velocity) of the falling sand is mainly affected by the falling height,[217,218] which partly determines the impacting force and thereby the damage degree to the liquid-repellent surfaces. However, the hitherto reported maximum falling height is 1.1 m,[349] corresponding to an impacting velocity of ~ 4.7 m s^{-1}, which is far below the typical sand speed in a sandstorm (> 10 m s^{-1}).[364]

High speed liquid droplet/jet impacting is also frequently used for the mechanical durability testing of liquid-repellent surfaces (Fig. 22m). As discussed in Section 3.1, liquid droplet/jet impacting can trigger thermodynamic instability of super liquid-repellent surfaces *via* cushions removal induced Cassie-Baxter to Wenzel transition,[299,302-306] as well as the drainage of the infused-liquid due to commonly observed meniscus and cloaking.[341] It should be emphasized that the interaction between dynamic liquids (including droplet, jet, and flow) and liquid-repellent surfaces could have a negative effect on their surface textures and/or infused-liquid due to the generated shear force, which sometimes leads to the loss of liquid repellence.[47,217,291,355,363,365-368] Notably, this is different from the meniscus and cloaking induced infused-liquid depletion of SLIS, which should be, more precisely, considered as a thermodynamic process.

3.2.3 Tape peeling

Binding strength is of great significance for the longevity of liquid-repellent surfaces fabricated by additive strategies like spray-/dip-coating and 3D printing, because external force action could cause mechanical peel-off of the coatings and thereby invalidate the liquid repellence. Tape peeling is a common approach used to assess the bonding strength between liquid-repellent coatings and solid substrates.[291,349,350,355,363,367,368] As depicted in Fig. 22n, the substrate is placed horizontally to the liquid-repellent coating upward, then adhesive tape is applied and uniformly pressed (usually by using a cylindrical block as a roller) for a while to adhere to the underneath coating, following which the tape is peeled off. Based on this testing, both the coating removal rate (*e.g.*, according to the ASTM standard D3359-17) and wettability change of the surface can be obtained. For example, Qing *et al*. showed that when a superhydrophobic 1,1,2,2-tetrahydroperfluorodecyltrimethoxysilane-TiO_2/PDMS coating was directly deposited on glass substrate, it could be easily removed by tape peeling, which obviously decreased its water repellence (Fig. 22o).[350]

Tape peeling can quantitatively evaluate the resistance of liquid-repellent coating towards mechanical peeling-off, and its result is significantly affected by the adhesive ability of the tape, and the pressing force. Peng *et al*. used Elcometer 99 tape (with adhesion to steel value of 642 $\mathrm{N\ m^{-1}}$) and VHB tape (with adhesion to steel value of 2600 $\mathrm{N\ m^{-1}}$) to test the peeling-off resistance of a robust superhydrophobic coating, and found that the two tapes had little influence on the superhydrophobicity, but it should be noted that the former one did not remove any coatings, whereas a small part of the coating (less than 5%) was removed onto the later one.[291] However, these influencing factors are rarely considered comprehensively throughout the literature, making the tape peeling indication of robustness of liquid repellence incomparable and even sometimes unconvincing.

3.2.4 Substrate deformation

Substrates with liquid-repellent surfaces often undergo deformation like stretching, compressing, twisting and bending (Fig. 22p), especially those employed in flexible electronics and wearable devices,[190,196,369,370] making it necessary to test their robustness against mechanical deformation. Generally, rigid substrates (*e.g.*, metals) are extremely sensitive to deformation due to their poor plasticity and elasticity, so little attention has been paid to the robustness of liquid-repellent surfaces on rigid substrates towards mechanical stretching or compressing, except some publications on bendable superhydrophobic metallic matrix.[371,372] By contrast, soft substrates (*e.g.*, silicone elastomer and fabric) often possess excellent flexibility, enabling them to be preferably selected to create liquid-repellent surfaces that are used in conditions with complex mechanical deformation. Typically, reconstruction (*e.g.*, sparsification and densification), rupture, or even peeling-off of the rough structures could be observed during the deformation of flexible substrates, which may sometimes lead to the loss of liquid repellence depending on the deformation.[373-376] For example, Zang *et al*. prepared superhydrophobic crumpled graphene layer on an elastic film of VHB acrylic 4905, and the water CA decreased from 152° to 103° when the substrate was biaxially stretched with a tensile strain of 400% due to the reduced surface roughness during graphene unfolding.[373]

3.2.5 Others

Besides the above-discussed testing methods, other techniques can also be found in the literature for the mechanical durability testing of liquid-repellent surfaces. Laundering in detergent or water is often used in mechanical durability testing of liquid-repellent fabrics,[346,355,377] as it represents the most common mechanical interaction of fabrics during their use. Laundering can create composite testing conditions containing solid-solid abrasion, solid-liquid abrasion, liquid impacting, substrate deformation, detergent adsorption, *etc.*, indicating that a relatively overall evaluation of the mechanical durability can be obtained. Ultrasonic processing can physically damage fragile surface structures or even break off the coatings that have poor adhesion with substrates, thereby making it an alternative candidate for mechanical durability testing of liquid-repellent surfaces.[378,379] Some groups also tested the mechanical durability of liquid-repellent surfaces by hammer punching,[66,359] which can roughly evaluate the robustness towards transient and huge impact pressure. In addition, spinning is always used to apply vigorous centrifugal/shear force to the infused lubricant on SLISs, so as to accelerate the lubricant depletion, which can be therefore employed to test the robustness of SLISs.[338-340]

3.3 Chemical Durability

Potential chemical processes have to be prudently considered for the real applications of liquid-repellent surfaces, especially under some harsh conditions, since they could cause a change in surface textures and/or surface chemistry, resulting in deterioration of the liquid repellence. For example, building walls with Lotus leaf-like self-cleaning ability are often exposed to direct sunlight and acid rain, ship hulls with drag-reduced surfaces are always immersed in corrosive seawater, superhydrophobic transmission lines may suffer from extremely low temperature, and so on. Chemical durability here refers to the resistance of liquid-repellent surfaces towards various chemical invasions, and it is vitally important to be emphasized.

3.3.1 Acid/alkaline/salty solutions corrosion

Artificial chemical corrosion by aqueous solutions, including acid (*e.g.*, HCl, H_2SO_4 and aqua regia), alkaline (*e.g.*, NaOH and KOH) and saline (*e.g.*, NaCl), are widely employed to test the chemical durability of liquid-repellent surfaces. Depositing corrosive liquid droplets on liquid-repellent surface and measuring their CAs on the surface is a simple method to estimate the chemical durability, but the results are sometimes unconvincing since the time interval during the droplet deposition and CA measurement is always too short to trigger the possible chemical processes between the corrosive liquids and the surfaces. Additionally, when chemical corrosion occurs between the corrosive liquid droplets and the surfaces, the measured CAs are always time-dependent, making it difficult to evaluate the chemical stability. Therefore, this method is advisable for the proof of highly chemical instability or transitory stability, but not for the chemical resistance assessment of long-term stable surfaces. By contrast, immersing the liquid-repellent surfaces into corrosive solutions for a certain period and then depicting their wettability could be a relatively reliable way to evaluate the chemical resistance. For example, Cheng *et al*. fabricated superhydrophobic fabrics by enzyme etching and subsequent methyltrichlorosilane modification, and tested their chemical durability *via* the two methods.[380] They showed that no obvious CA change was observed when HCl (pH = 2), NaCl (pH = 7) and NaOH (pH = 12) droplets were deposited on the superhydrophobic fabrics, but drastic water CA decrease was displayed after the fabrics were immersed in

HCl (pH = 2) and NaOH (pH = 12) for 24 h. Additionally, it has to be noted that the chemical resistance of underwater superoleophobic surfaces could be well characterised by oil CA measurement in corrosive aqueous solutions, because the samples are pre-immersed in and totally soaked by the corrosive solutions.

Another technique to test the chemical resistance of liquid-repellent surface is accelerated electrochemical corrosion in corrosive solutions (*e.g.*, 3.5 wt% NaCl solution) on an electrochemical workstation, during which potentiodynamic polarization (PDP) curve and electrochemical impedance spectroscopy (EIS) can be obtained.[48,296,381] Generally, a three-electrode configuration, with liquid-repellent surface as the working electrode (WE), a platinum electrode as the counter electrode (CE), and a saturated calomel electrode (SCE) as the reference electrode (RE), is used in this testing. Corrosion current density (I_{corr}) and corrosion potential (E_{corr}) obtained from the PDP curve can directly reflect the corrosion resistance of the tested sample, and the corresponding corrosion rate (CR, mm a^{-1}) could be obtained by the formula below:

$$CR=\frac{3725\times I_{\mathrm{corr}}\times M}{\rho\times V} \tag{31}$$

where M, ρ, and V is respectively the molar mass, density, and valence state of the tested substrates. In general, samples with better corrosion resistance show lower I_{corr} and CR but higher E_{corr} values. Based on the EIS results, many useful data can be collected to evaluate the corrosion behavior of the tested samples, such as the Nyquist plots and corresponding equivalent circuit models, Bode plots of impedance modulus (|Z|) *vs* frequency and phase angle *vs* frequency, *etc*. For example, it was demonstrated that the larger diameter of capacitive loop in the Nyquist plot and bigger value of |Z| at low frequency (*e.g.*, |Z| at f = 0.01 Hz, termed as $|Z|_{f\,=\,0.01\,\mathrm{Hz}}$) in the Bode plot revealed the better corrosion resistance. Moreover, the Bode phase angle plots indicated that the samples with the better corrosion resistance had higher and more stable phase angle maxima across a wider range of frequency. For example, Yang *et al*. studied the anticorrosive performance of superhydrophobic and slippery coatings on 316L stainless steel *via* accelerated electrochemical corrosion.[382] Laser textured 316L steel surface was functionalized by 1*H*,1*H*,2*H*,2*H*-perfluorodecyltriethoxysilane to obtain superhydrophobic surface, which was subsequently infused by silicon oil to construct SLIS. The PDP test results (Fig. 23a) showed that the SLIS possessed the lowest I_{corr} (1.61×10^{-8} A cm^{-2}), which was about 30-fold smaller than the superhydrophobic surface (4.70×10^{-7} A cm^{-2}) and 300-fold smaller than the original surface (4.56×10^{-6} A cm^{-2}), and the polarization resistance of SLIS (2327.42 kΩ cm^2) > superhydrophobic surface (83.16 kΩ cm^2) > original surface (13.23 kΩ cm^2). The EIS testing results showed that compared with the original steel substrate (Fig. 23b), the SLIS presented the best corrosion resistance due to its largest capacitive loop, followed by the superhydrophobic surface (Fig. 23c). In addition, as shown in Fig. 23d, the Bode plot of |Z| *vs* frequency showed that in the low frequency the SLIS had the |Z| of $10^{5.58}$ Ω cm^2, which was larger than the superhydrophobic surface ($10^{4.76}$ Ω cm^2) as well as the original surface ($10^{3.19}$ Ω cm^2). Overall, the accelerated electrochemical corrosion testing could provide more quantifiable data based on PDP and EIS, enabling us to evaluate the chemical durability of liquid-repellent surfaces quantificationally and convincingly.

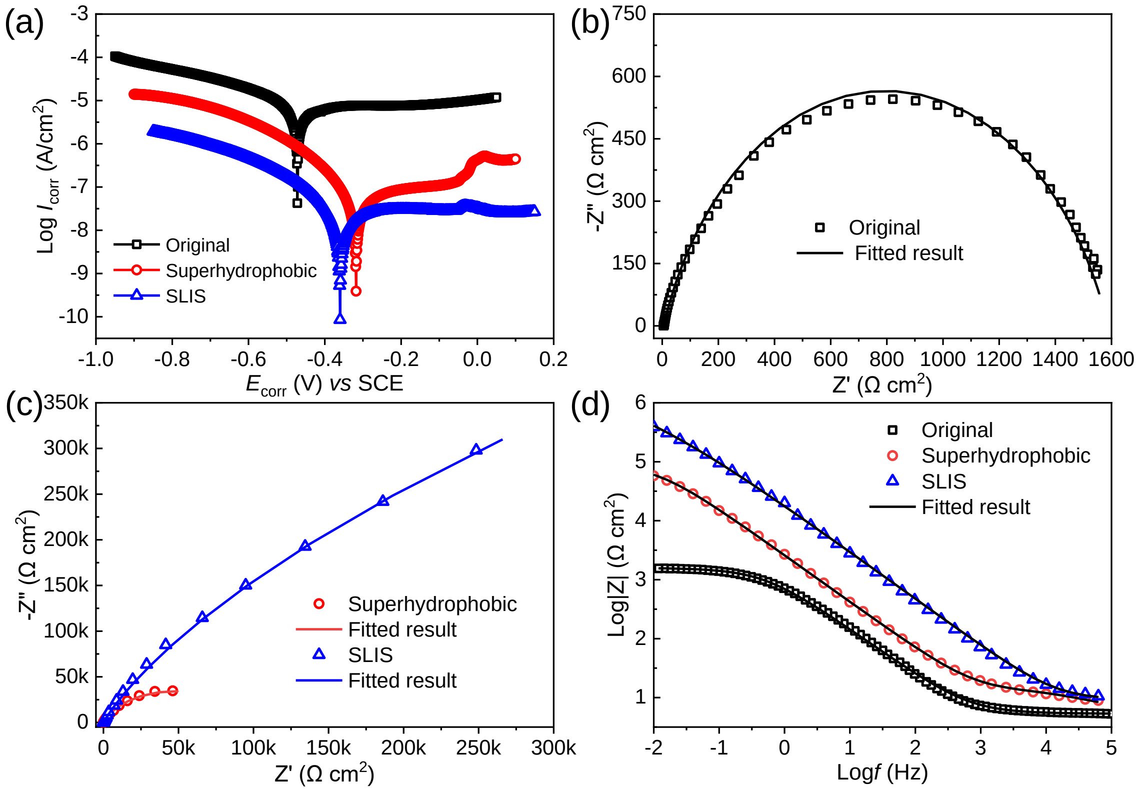

Fig. 23 Accelerated electrochemical corrosion testing of 316L stainless steel with original surface, superhydrophobic surface and SLIS: (a) PDP test results, (b–c) Nyquist and (d) Bode plots. Reproduced with permission from ref. 382. Copyright (2019) Elsevier B.V.

3.3.2 Exposure to UV and active species

Exposing to UV is an extensive method to evaluate the chemical durability of liquid-repellent surfaces in the literature. Direct irradiation by UV lamp or sunlight is employed to conduct the evaluation of UV-resistance for liquid-repellent surfaces.[72,218,271,383] Testing parameters, such as wavelength and intensity of the UV light, exposure duration, and the distance between UV source and surface, are generally considered. If the matrix materials and/or surface functional groups of liquid-repellent surfaces are degradable towards UV, the surfaces will lose their liquid repellence after UV treatment.[384-386] For example, thiols, which are widely used to lower surface energy, tend to be oxidized over short timescales when exposed to UV radiation, turning into disulfides and sulfonates that can be washed away easily by polar solvents such as water.[387] Kong *et al.* fabricated superoleophobic/superhydrophilic coatings on cotton fabric and sponge by liquid-phase deposition of TiO_2 nanoparticles that were subsequently decorated with perfluorooctanoic acid (PFOA).[385] Upon exposure to UV, TiO_2 with ·OH radicals and holes (h^+) could oxidize the adsorbed PFOA long chains *via* defluorination cycle reaction, which finally turned the surface to be both superoleophilic and superhydrophilic. By contrast, Kim *et al.* prepared superhydrophobic coatings on various pre-roughened metals by depositing PDMS that was vaporized with the aid of ammonium bicarbonate.[388] Although the surfaces retained their superhydrophobicity after

5 days of UV irradiation, they became superhydrophilic upon treatment by UV-ozone, which might be attributed to the strong oxidation effect of ozone. Therefore, reactive gas can also cause chemical damage for liquid-repellent surfaces. Recently, a superamphiphobic surface composed of Ti–O–Ti networks, hydrophobic titanium–carboxylate coordination complexes, and fluorinate-rich molecular chains was reported to be partially damaged by NH_3 exposure.[389] Due to the cleavage of a titanium–carboxylate coordination complex and the generation of ammonium carboxylate by NH_3-triggered surface reactions, the polar component of the surface free energy (γ_s^d) decreased while the polar component (γ_s^p) increased, and the dipolar-dipolar interaction between water molecules and formed ammonium carboxylate was enhanced, driving the water droplets to quickly spread on the treated surface.

As ionized gases, plasmas contain various energetic particles and highly reactive species, such as electrons, ions, excited groups, and metastable atoms/molecules, which enables them to be versatile sources to trigger interfacial physiochemical processes including physical/chemical etching, deposition, oxidation, *etc*. The specific plasma-target interfacial reactions heavily depend on the properties of plasmas. Generally, plasmas containing oxygen-based active species can oxidize liquid-repellent surfaces by incorporating oxygen-containing polar groups, such as –OH and –COOH, which thereby deteriorate their liquid repellence.[225,330,356,390] Oxygen, air or water vapor are often used as working gas directly or an additive to carrier gas (*e.g.*, nitrogen, helium, and argon) to generate oxygen-containing plasmas *via* gas discharge.

Additionally, polydopamine, a well-known substrate-independent adhesive that can attach to various materials through strong coordinative interactions, can also change the wettability of liquid-repellent surfaces due to the radicals generated during the oxidative polymerization of dopamine.[391,392] For example, Prieto-López *et al*. reported that when silicon-based SLISs prepared by swelling PDMS with silicon oil were placed in dopamine buffer solution containing NaOH, the surface hydrophobicity was changed and a polydopamine coating was observed on the damaged surface.[391] The authors found that the alkaline pH, the presence of Na^+ cations in the coating solution together with the active sites present in the polydopamine structure (*i.e.*, –OH, =O, –NH, and $–NH_2$), and especially various radical species generated during oxidative polymerization of dopamine, enabled the penetration of polydopamine particles through the lubricant layer, which further promoted the cleavage of the Si–O bond or C–H bond of the PDMS matrix and the subsequent anchoring of the dopamine/polydopamine species.

3.3.3 Others

Besides the aforementioned frequently-used testing methods, some other methods, such as organic solvents invasion and high/low temperature exposure, are also employed to evaluate the chemical durability of liquid-repellent surfaces. When organic solvents make contact with liquid-repellent surfaces, complete repelling or potential physicochemical processes may occur, such as adsorption of the solvents, dissolution or swelling of the substrate and/or the surface coating, *etc*., making it necessary to test the durability of liquid repellence towards organic solvents.[346,372,393] If the liquid-repellent surfaces possess complete repellence towards the testing organic solvents, they would be insusceptible to the invasion of the solvents.[17,20,188,231] For example, Pan *et al*. prepared hierarchically structured surfaces by using an electrospun coating of cross-linked PDMS + 50 wt% fluorodecyl polyhedral oligomeric silsequioxane on top of stainless steel wire meshes.[231] The resultant surface showed superamphiphobicity with virtually all liquids - organic or inorganic, polar or nonpolar, Newtonian or non-Newtonian, and jets of a range of different liquids could easily bounce on the surfaces. The super repellent surface with doubly re-entrant structures reported by Liu *et al*. showed excellent repellence to almost all available liquids, which enabled the surface to be chemically stable towards the invasion by even completely wetting organic solvents.[188] By contrast, when the tested surfaces can be (partially) wetted by or react with the testing organic solvents, their liquid repellence would be damaged. For example, Wang *et al*. prepared a superamphiphobic surface on cotton fabric by dip-coating a mixed suspension of fluorodecyl polyhedral oligomeric silsesquioxanes, TiO_2 and PTFE particles, and showed that the water CA of the fabric decreased from 164° to 128° after being contaminated by oleic acid.[346] Cross-linked PDMS, which is typically used as a coating with low surface energy for superhydrophobic surface or a versatile matrix for SLIS, has been demonstrated to be unstable upon organic solvents (*e.g.*, toluene, chloroform, and silicon oil) invasion.[231,280,281,347] In addition, for a SLIS with infused lubricant (Liquid A) and a testing organic solvent (Liquid B), if their surface tensions cannot meet eqns (12) and (14), the SLIS will be seriously damaged.[85,86]

Most liquid-repellent surfaces are characterised at room temperature, but the practical service conditions of these surfaces often involve high/low temperature. Extreme temperature exposure can lead to changes in surface morphology and/or chemistry, and thereby bring a potential threat to the stability of their liquid repellence.[372,394] For instance, Chandekar *et al*. studied the thermal stability of self-assembled thiol and silane monolayers, and found that these monolayers would be decomposed at evaluated temperatures, *e.g.*, self-assembled 1-octadecanethiol and 1*H*,1*H*,2*H*,2*H*-perfluorodecyltriethoxysilane monolayers started to decompose at ~ 110 °C and 350 °C, respectively,[395] indicating that the durability of thiol or silane functionalized liquid-repellent surfaces under high temperatures have to be well considered. Therefore, it is also important to study the stability of the wettability under high/low temperature treatment. Generally, a high and low temperature environment test chamber or hot platform can be used to provide continuously variable temperatures typically ranging from dozens of degrees below zero to a few hundred degrees above zero. Liquid nitrogen is always used to create extremely low temperature (−196 °C), while flame burning is sometimes employed to simulate high temperature source. After exposing the liquid-repellent surfaces in pre-set testing temperature for a certain period of time, the samples are then restored to room temperature, after which the changes of surface wettability are measured to evaluate their stability towards high/low temperature treatment. For example, Li *et al.* prepared a superhydrophobic coating by spraying the suspension containing epoxy resin modified silicone resin and its curing agent, multilayer graphene oxide, lamellar mica powders, and octadecyltrichlorosilane functionalized SiO_2 nanoparticles.[296] The obtained superhydrophobic coating could retain its excellent water repellence even after 12 cycles of storage in liquid nitrogen for 10 min and subsequently on a hot platform at 200 °C for 10 min, which was attributed to the durable surface structures and compositions during extremely large and rapid temperature changes. Notably, extreme temperature treatment induced chemical instability is different from vapor condensation caused thermodynamic instability (*i.e.*, flooding).

In addition, chemical degradations of the hydrophobic coatings of super liquid-repellent surfaces during water vapor condensation have also drawn much attention in recent years.[315,396-399]. For example, Wang *et al*. studied the condensation-induced chemical degradation and failure of organofunctional silane (including trichloro(octadecyl)silane and trichloro(1*H*,1*H*,2*H*,2*H*-perfluorooctyl) silane) self-assembled monolayer coatings on Si/SiO_2 substrate.[399] The authors found that silane-uncoated defects within the coatings were generated during the synthesis of the coatings in uncontrolled environments with unregulated water/moisture content, and these defects favored the condensed water to dissolve and hydrolyze the Si−O−Si bonds at the coating-solid interface, leading to partial detachment of the cross-linked silane agglomerates from the surface, which thereby acted as nucleation sites for degradation of the silane functionalized liquid-repellent coating. By conducting the silane coatings in an anhydrous/moisture-free environment, the authors effectively improved the chemical durability of the coatings under condensation conditions, and realized enhanced condensation heat transfer over an extended period of time.[399,400]

Although plentiful of liquid-repellent surfaces have been reported and their robustness and durability have also been evaluated skillfully, most of the tests are only conducted on lab-scale with limited testing intensity (*e.g.*, immersion under static water for several hours, or gentle sandpaper abrasion for dozens of cycles) that are far from the requirements for real-world applications, making it necessary to emphasize that long-term and repeated testing (*e.g.*, 80 days immersion under water, or 25000 cycles Martindale abrasion according to ASTM D4966)[47,288,401-404] that are in good accordance with practical application requirements, which are urgently demanded to promote the development of “real” robust and durable liquid-repellent surfaces.

4 Design and Fabrication of Robust and Durable Liquid-Repellent Surfaces

To apply liquid-repellent surfaces in daily life, their enhanced robustness and durability are urgently required in order for such surfaces to survive under complex conditions. Consequently, the past few years have witnessed a rapidly increased attention to the robustness and durability of liquid-repellent surfaces. By focusing on their thermodynamic, mechanical and chemical durability, significant breakthroughs have been achieved.[11,13,14,45,259,405] This section of the review will summarize the recently developed strategies in designing and fabricating robust and durable liquid-repellent surfaces, including choosing rational substrate/surface chemistry, designing special surface structures, enhancing the bonding strength between liquid-repellent coatings and substrate, and developing self-healable liquid repellence.

4.1 Optimizing Matrix/Surface Chemistry

As for liquid-repellent surfaces, the chemistry of the underneath solid substrate is sometimes unrelated to the surface wettability, but they are important to the robustness and durability of the liquid repellence. Intuitively, using intrinsically hard/wear-resistant material can allow for construction of mechanically robust liquid-repellent surfaces, while materials with naturally chemical inertness can be helpful to get chemically durable liquid-repellent surfaces. For example, Ye *et al*. synthesized amphiphilic vitrimer *via* base-catalyzed ring-opening between pristine and epoxy-modified biobased malic acid, which were then transformed into superhydrophilic vitrimer membrane after dry-pressing and sintering.[406] Similar to classical epoxy resins, the vitrimer epoxy resin possessed excellent mechanical durability and chemical inertness, which further endowed the resultant membrane with robust and durable underwater superoleophobicity towards sandpaper abrasion (Fig. 24a, b) and immersion in corrosive media (such as aqua regia and NaOH solutions). Concrete, a widely-used engineering materials with exceptional strength and good durability, has been used to construct a robust and durable superhydrophobic surface, which could tolerate various testing under harsh conditions, such as sandpaper abrasion, knife scratch, hammer beat, sand impacting, tape peeling, and concentrated acid/alkali/salt immersion.[66,407,408] Chen *et al*. proposed a multi-fluorination strategy to prepare all-organic superhydrophobic coatings consisting of fluorinated epoxy resin, perfluoropolyether and polytetrafluoroethylene nanoparticles (Fig. 24c).[291] The addition of the perfluoropolyether improved the mechanical flexibility of the coating, which imparted the coating with impalement resistance to high-speed droplets and turbulent water jets at least up to ~ 35 m s^{-1} and a Weber number of ~ 43,000 due to the flexibility-induced cushioning of pressure peaks. In addition, the choice of the all-organic raw materials with inherent chemical stability imparted the coating with excellent chemical durability, and the coating maintained a water CA of > 150° after 60 min immersion in aqua regia (Fig. 24d) and 12 h corrosion in 1 M NaOH (Fig. 24e). By mimicking natural nacre which exhibited exceptional mechanical and chemical performance due to biomineralization-induced hierarchical organization of organic matrix and inorganic aragonite component, Chen and co-authors reported a mechanically robust underwater superoleophobic film *via* superspreading and biomineralization strategies (Fig. 24f, g).[67,409,410] The prepared film was composed of aragonite platelets as the inorganic component and chitosan derivative as the organic framework, and showed outstanding robustness and durability in terms of long-term immersion in high salt solution or seawater, and intensive impingement by falling sands (Fig. 24h).

Surface chemistry is one of the dominant factors that determines the wettability of materials.[411,412] Silanes, thiols, and fatty acids containing CH- and CF-based groups are always employed to reduce the surface energy of a roughened surface to fabricate super liquid-repellent surfaces. Silanes are more stable due to their covalent bonding with the underlying surface, but thiols are generally less stable under ambient conditions, UV exposure or thermal treatment.[387,395] In addition, it was demonstrated that the surface free energy of these groups decreased in the order $-CH_2-$ > $-CH_3$ > $-CF_2-$ > $-CF_2H$ > $-CF_3$, and that increasing the chain length could further decrease the surface energy.[413,414] Samanta *et al*. studied the influence of surface chemistry on wettability of a laser-textured aluminum alloy.[415] They found that fluorinated groups ($-CF_2-$ and $-CF_3$ with very low dispersive and nondispersive surface energy) anchored the rough surface resulting in both water and diiodomethane repellence; polar nitrile group ($-C\equiv N$ with very high nondispersive and high dispersive surface energy) attachment leads to both superhydrophilicity and superoleophilicity; anchoring fluorinated groups ($-CF_2-$ and $-CF_3$) and polar sodium carboxylate ($-COONa$) together created very low dispersive and very high nondispersive surface energy components, resulting in the coexistence of water affinity and diiodomethane repellence. Wang *et al*. modified laser-roughened stainless steel surfaces respectively with stearic acid ($CH_3(CH_2)_{16}COOH$) and 1*H*,1*H*,2*H*,2*H*-perfluorodecyltrichlorosilane ($CF_3(CF_2)_7CH_2CH_2SiCl_3$) to fabricate superhydrophobic surfaces, and they found that the two surfaces possessed similar water repellence, but the fluoroalkylsilane modified one showed better chemical durability towards aqueous solution corrosion.[48]

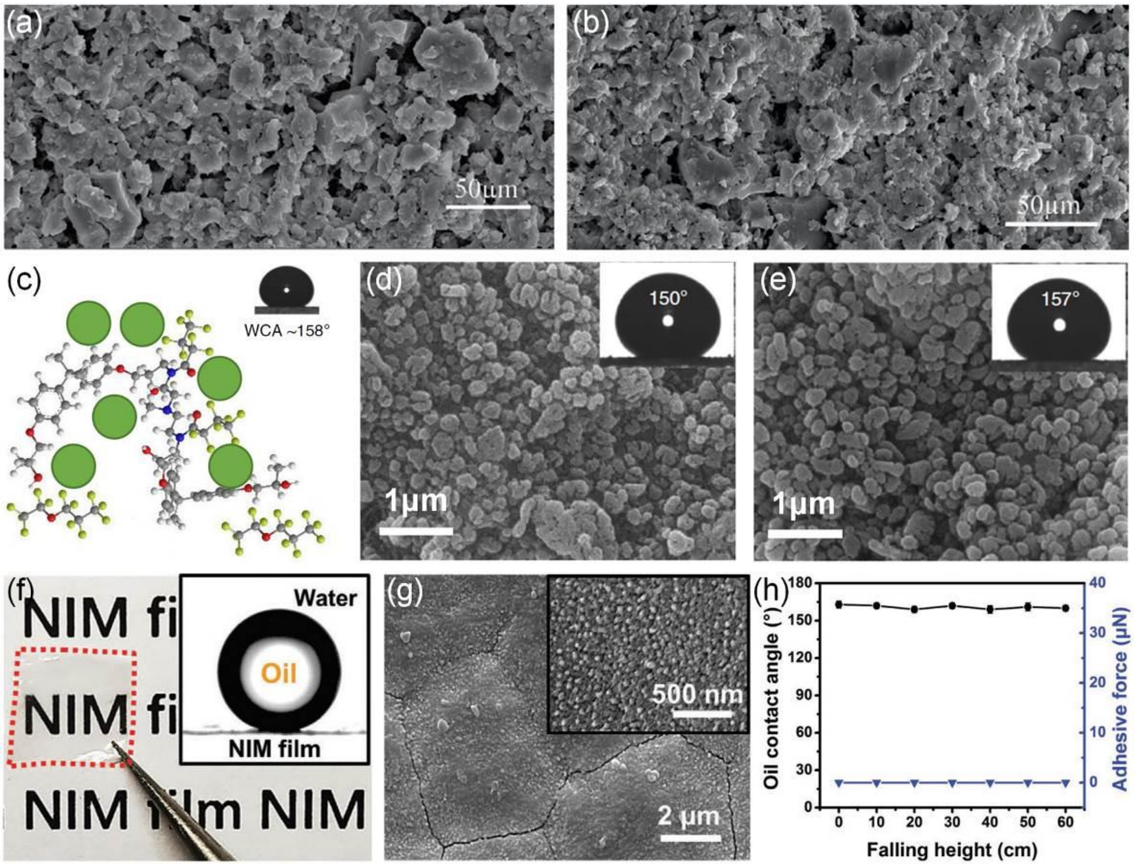

Fig. 24 SEM images of the superhydrophilic vitrimer membrane (a) before and (b) after 40 cycles sandpaper abrasion. (c) Illustration of the all-organic superhydrophobic coating, and its SEM images (d) after 60 min in aqua regia corrosion and (e) after 12 h in 1 M NaOH solution. (f) Photograph of the nacre-inspired mineralized (NIM) film. The inset image showed its underwater superoleophobicity. (g) SEM images of the NIM film. (h) Mechanical durability of the NIM film under falling sand impacting with different heights. (a, b) Reproduced with permission from ref. 406. Copyright (2021) Ye *et al*. (c–e) Reproduced with permission from ref. 291. Copyright (2018) Springer Nature. (f–g) Reproduced with permission from ref. 67. Copyright (2020) WILEY-VCH Verlag GmbH & Co. KGaA, Weinheim.

In addition, the use of CF-based compounds results in massive release of fluorine-compounds in natural environment, which has caused serious and recurrent threats to human health, such as the causation for cancer, disruptions of immune systems, and reproductive problems.[416] Consequently, fluorine-compounds are going to be banned in the European Union shortly,[417] indicating extremely timely and significant demand to realize liquid repellence with non-fluorinated surface chemistry. Materials with

CH-based groups that possess low surface tensions (*e.g.*, PDMS, polypropylene, silicone oligomer and stearic acid) are thereby promising candidates for the fabrication of fluorine-free liquid-repellent surfaces.[292,418-421] Wu *et al*. reported a fluorine-free superhydrophobic coating prepared by spray-coating copper alkylcarboxylates, $Cu(CH_3(CH_2)_{10}COO)_2$.[422] When the emulsion solution of $(CH_3(CH_2)_{10}COO)_2Cu$ with a concentration of 0.04 M in a mixed solvent of ethanol and water (volume ratio 1:1) was sprayed on various substrates and dried completely, the obtained coatings showed water CA of 158 ± 2° and SA of 5 ± 1.4° due to the resultant binary micro/nanostructures (microscale papillas and nanoscale rods) and the CH-based groups induced low surface energy. Cao *et al*. prepared a fluorine-free superhydrophobic fabric by depositing organically modified silica aerogel (ormosil) thin film onto the fabric and subsequently coating PDMS.[423] The PDMS layer not only increased the binding strength between the hierarchical ormosil film and fabric, but also lowered the surface energy of the sample, resulting in a mechanically robust and chemically durable superhydrophobic fabric. In addition, materials with CH-based groups can also be used to build 3D blocks with liquid repellence. For instance, Zhang *et al*. reported a press-in-mold method to fabricate non-fluorinated superhydrophobic blocks *via* dispersing hydrophobic SiO_2 nanoparticles in polymers.[46] Hydrophobic SiO_2 nanoparticles functionalized by hexamethyldisilazane were dispersed in various polymers including polyhexamethylene adipamide, polystyrene, polypropylene, and methyl silicone resin. After drying and then pressing in a mold, hard free-standing blocks were obtained, which became superhydrophobic after removing the outermost layer by sandpaper abrasion. The whole fabrication process did not include any fluorinated materials, and the superhydrophobic blocks could retain their super water repellence after knife/file scratching, liquid nitrogen testing, severe sand/water impacting, acidic/alkali corrosion and 20 m sandpaper abrasion. However, it is still a challenge to prepare fluorine-free superoleophobic surface in air, unless special doubly/triply re-entrant microstructures are employed,[188,191,424] which can be found in Section 4.2.2.

The underwater superoleophobicity can also be influenced by surface chemistry. Cheng *et al*. studied the underwater oil wettability of nanostructured copper that was modified by mixed thiols containing both $HS(CH_2)_9CH_3$ and $HS(CH_2)_{11}OH$, and the results showed that surfaces with controlled oil wettability from underwater superoleophilicity to underwater superoleophobicity could be achieved by simply changing the concentration of $HS(CH_2)_{11}OH$ in the mixed solution.[425] Zhao *et al*. further reported under-oil superhydrophobicity and underwater superoleophobicity coexisted copper surface by designing conformational transitions of surface self-assembled molecules.[246] The authors modified $Cu(OH)_2$ nanowire structured Cu plate in the ethanol solution of 1 mM different hydroxythiol ($HS(CH_2)_nOH$, where n is the number of methylene groups) for 5 h to prepare superwettable surface. The authors selected the following hydroxythiol: *β*-mercaptoethanol (n = 2), 3-mercapto-1-propanol (n = 3), 4-mercapto-1-butanol (n = 4), 6-mercapto-1-hexanol (n = 6), 9-mercapto-1-nonanol (n = 9), and 11-mercapto-1-undecanol (n = 11). Owing to the solvation effects, self-assembled hydroxythiol molecules underwent conformational reorientations in response to the external solvent environments. When the sheet was placed in water, the −OH groups exposed on the surface could form hydrogen bonds with water to form a stable solid-water composite interface, meaning that the surfaces modified with different hydroxythiol showed underwater superoleophobicity (Fig. 25a). In oily environments, the solubility of oil in hydrocarbons allowed it to penetrate into the ordered self-assembled molecule structure and triggered molecular conformation transition, which resulted in the mask of the hydrophilic groups ($-\mathrm{OH}$) by hydrophobic $-\mathrm{CH_2}-$ groups (Fig. 25b). When $n < 4$, the short $-\mathrm{CH_2}-$ chain could not completely block the $-\mathrm{OH}$ groups, so water molecules could still combine with the remaining hydrophilic groups, and the surface showed under-oil superhydrophilicity. By contrast, when $n \geq 4$, the chain bending caused the $-\mathrm{OH}$ groups to be completely covered by the $-\mathrm{CH_2}-$ groups, and the surface exhibited under-oil superhydrophobicity. Recently, by controlling the surface hydrophobic-hydrophilic heterogeneous chemistry, programmable super-antiwetting evolutions in oil-water-air system from single to quadruple super repellence have also been reported.[389]

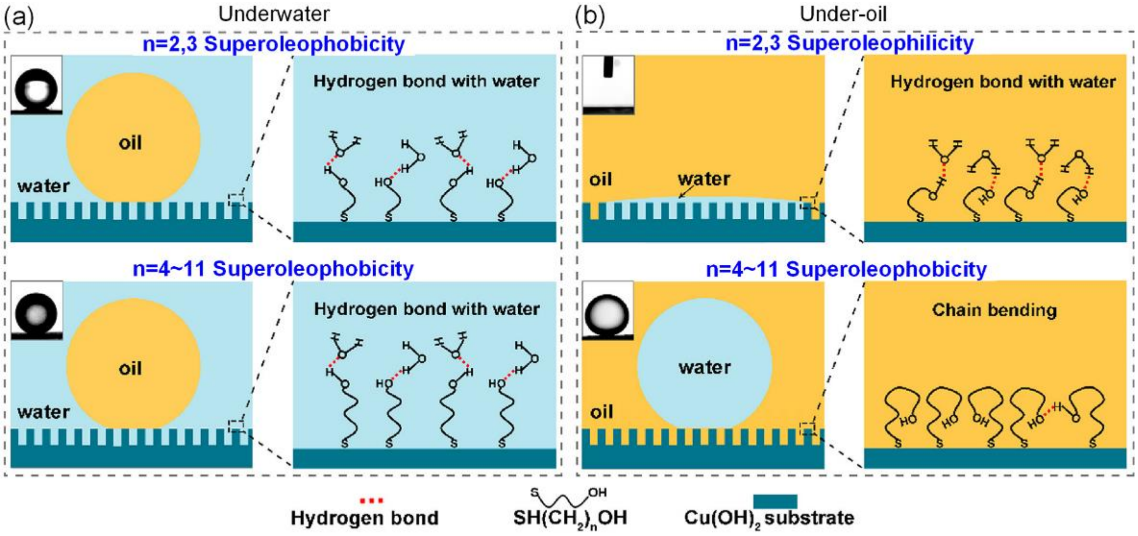

Fig. 25 Underlying mechanism of (a) underwater superoleophobicity and (b) under-oil superhydrophilicity and superhydrophobicity with different chain lengths. Reproduced with permission from ref. 246. Copyright (2020) American Chemical Society.

Alterations in the chemistry of superhydrophobic surfaces is a strategy to stabilize lubricants in porous structures of SLIS. Hydrophobically modified substrates show high chemical affinity towards oils, and therefore lubricants are able to wet surfaces completely and also could be stably locked into porous structures. Liu *et al*. reported a robust SLIS by infusing perfluoropolyether (PFPE) into porous PTFE nanostructures *via* a spin-coating method.[426] In this study, nanoscale PTFE coatings were used as porous structures, and PFPE was used as the lubricating oil. A uniform and dense PTFE layer exhibited similar chemical affinity towards PFPE, which was beneficial to stabilize lubricants into PTFE nanostructures. After being subjected to different mechanical damages, including wiping, sandpaper abrasion (Fig. 26a) and knife scratch, the SLIS remained repellent to water (Fig. 26b) and *n*-decane, exhibiting excellent mechanical stability. Different from the above remarkable work, Maji *et al*. reported that SLIS with hydrophilic porous layers were capable of stabilizing infused lubricants as well.[383] The hydrophilic porous interfaces (water CA of ~ 20°) were prepared by depositing chemically reactive nanocomplexes with acrylate groups onto glass substrates. After infusing silicone oils (AR20) into the porous layers, the inherently hydrophilic surfaces immediately became slippery with a water CA of ~ 83° and a tilting angle of ~ 4°. In this design, the residual hydrophobic acrylate groups played an important role in stabilization of the oil phase and compatibility with other kinds of oils, though chemically reactive nanocomplexes showed hydrophilicity. The as-prepared SLIS remained highly robust after exposure to physical or chemical damages, such as tape peeling, sandpaper abrasion, UV irradiation and corrosive solutions.

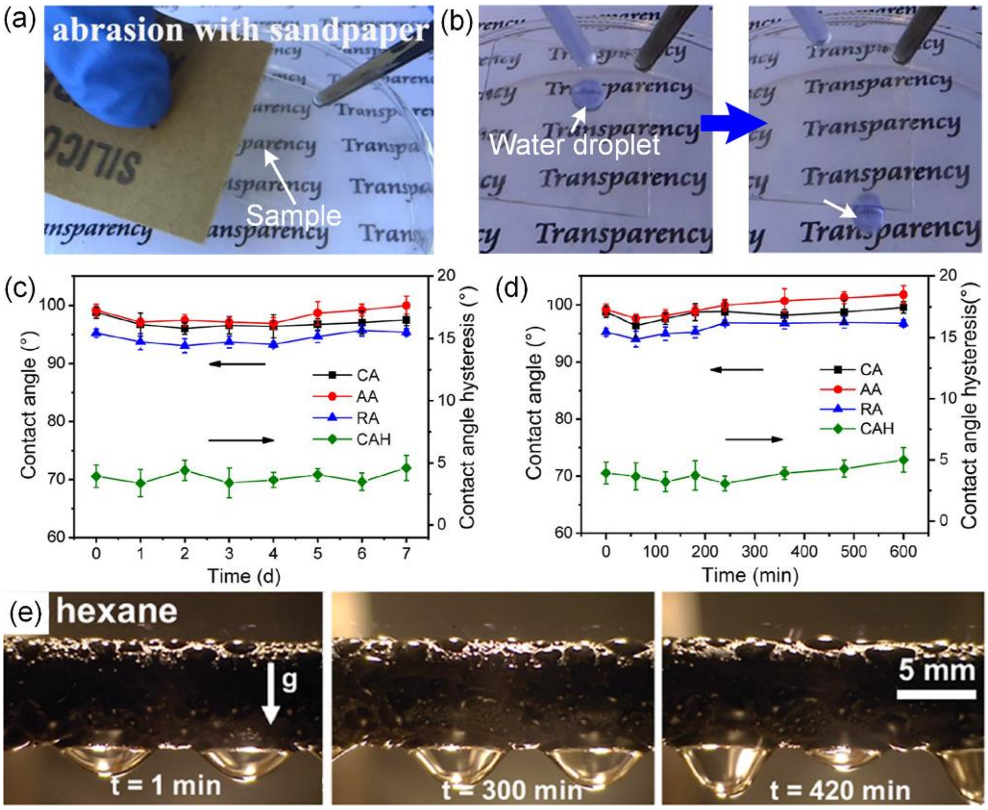

Fig. 26 Photographs showing (a) sandpaper abrasion of the PFPE infused porous PTFE film and (b) the liquid repellence of the film after the abrasion. Lubricants with low volatility enabled the SLIS with long-term durability during (c) evaporation at temperature of 75 °C and (d) continuous water-flow shear. (e) SLIS with highly viscous lubricant shows impressive durability during hexane steam condensation. (a, b) Reproduced with permission from ref. 426. Copyright (2017) Elsevier B.V. (c, d) Reproduced with permission from ref. 427. Copyright (2017) Elsevier B.V. (e) Reproduced with permission from ref. 428. Copyright (2019) American Chemical Society.

On the other hand, the surface chemistry of SLISs was primarily determined by the infused lubricant layer. Besides the consideration of surface tensions to prepare SLISs as described in eqns (12) and (14), some other physical properties of the lubricants (vapor pressure, viscosity, *etc*.) should also be considered. For example, Zhao *et al*. investigated the effect of volatility of infused lubricant oils towards the robustness of the SLIS.[427] For oils that were infused into hydrophobic nanostructured underlayers, such as pump oil (vapor pressure: 6.72×10^{-6} kPa), silicone oil (0.7 kPa) and perfluoropolyether (Krytox GPL105, ~ 10^{-8} kPa), they were of low volatility. When slippery surfaces infused with these lubricants were exposed to evaporation at temperature of 75 °C for 7 days (Fig. 26c) and continuous water-flow shear for 600 minutes (Fig. 26d), these surfaces still exhibited remarkable liquid repellence. Conversely, after hydrophobic porous layers were filled with high-volatility oils, such as petroleum ether (7.99 kPa), cyclohexane (10.31 kPa), and toluene (2.9 kPa), lubricants were prone to be evaporated from the SLIS in a short time even at room temperature. Finally, these slippery surfaces were transformed into hydrophobic surfaces, showing unstable performance of oils retention. Ouyang *et al.* discussed the effects of dimethyl silicone oils with different viscosities towards anti-corrosion and anti-biofouling performances.[429] High-viscosity dimethyl silicone oils (viscosity: 350 mPa·s) were demonstrated to possess better corrosion and biofouling inhibition performance than that of low-viscosity oils (50100 mPa·s) for a long term. Sett *et al.* prepared a robust nanostructured fluorinated SLIS for vapor condensation of ethanol and hexane.[428] They demonstrated that low-viscosity oils (Krytox GPL 100, 23 mPa·s) were quickly depleted from the slippery surfaces during steam condensation and high-viscosity lubricants (Krytox 1525, 496 mPa·s) were stable and durable for 7 h (Fig. 26e). Wang *et al.* fabricated robust SLIS by utilizing phase transformable peanut oil, and compared its stability with traditional SLIS.[430] Phase transformable SLIS (PTSLIS) was synthesized by infusing peanut oil in porous PDMS substrates. Subsequently, in the freezing condition, the solid peanut oils in PTSLIS were well retained in porous PDMS substrates while liquid oils in SLIS were easily drained from the pores by capillary force from nucleation of icicle. In addition, phase transformable lubricants were capable of self-healing bulk damage. At a temperature of above 3 °C, liquid-phase lubricants could spontaneously flow to the damage regions to form a homogenous lubricant layer *via* surface-energy-driven-capillary forces. At freezing temperature, liquid-phase oil was converted into solid-phase oil, which possessed greater intermolecular force and was beneficial for self-repair of damaged areas.

Stoddard *et al.* studied the effect of surface chemistry on the durability of superhydrophobic surfaces and SLISs.[431] Copper tubes were firstly roughened *via* chemical etching and electrodeposition methods, and then modified by six different functionalizing agents (including PFTDS, stearic acid, octylphosphonic acid, *n*-hexadecyl mercaptan, and DOW Sylgard-184) to obtain the superhydrophobic surfaces, after which five different lubricants (including Krytox 103 and 104, Dowsil 510 with viscosity of 50 and 100 cSt, Santolube OS-105) were infused to prepare the SLISs. Results showed that the superhydrophobic surfaces with different functionalizing agents performed well in cold water immersion (≤ 20 °C), but only *n*-hexadecyl mercaptan coating and curing-based Sylgard-184 exhibited significant durability in heated water immersion (70 °C) and under water jet impingement. In addition, a lubricant with high surface tension (Santolube OS-105, 36.1 mN m^{-1} at 23 °C) imparted the SLIS with the best durability in heated water immersion since the strong intermolecular interactions reduced the spreading of the lubricant in water, while high dynamic viscosity lubricant (Krytox 104, 243.5 mPa·s at 25 °C) showed the best durability towards water jet impingement due to its lowest susceptibility to shear degradation.

4.2 Designing Special Micro/Nano Structures

Apart from the chemical composition of the outermost surface, rough structure is another key element to render a solid substrate liquid-repellent. Therefore, designing special micro/nano structures is also of interest to improve the robustness and durability of the liquid repellence.

4.2.1 Micro/nano structures with optimized geometries

It is well-known that the geometries of rough structures are crucial for liquid repellence of a solid surface, as well as their own mechanical strength which mainly influenced the mechanical durability of the surface, but the requirements for liquid repellence and mechanical durability are conflicting from both theoretical and experimental perspectives.[45,47,432-434] Taking micro/nano pillars or needles featured superhydrophobic surface as an example, a high height-to-pitch aspect ratio of the features is required to decrease the liquid-solid contact area (*i.e.*, f_1 in eqn (6)) so as to increase superhydrophobicity, but the low contact area also results in high contact pressure and makes the pillars or needles fragile towards external force action, which thereby lowers the mechanical durability of the liquid repellence.[434] Therefore, the geometries of micro/nano structures have to be optimized in order to develop robust and durable liquid-repellent surfaces.

Compared with pillar-like open-cell structures, those closed-cell micro geometries (such as brick or honeycomb structures) are demonstrated to be more effective in constructing robust and durable liquid-repellent surfaces.[435] For example, Mishchenko *et al*. showed that a superhydrophobic surface with closed-cell brick structures (features of $15 \times 39\ \mu m^2$) could effectively repel water droplets impacting from a height of 10 cm, while that with posts array architectures failed at half that feature spacing.[435] They also demonstrated that the CA of a water droplet on superhydrophobic surface with closed-cell structures changed little even at pressures up to 40–60 atm, which implied that such surface was durable towards dynamic impacting by droplets with speed of 90–135 m/s. Park *et al*. reported a mechanically durable superhydrophobic surface with dual hole patterned hexagonal arrays (Fig. 27a).[436] A conventional photolithography process was employed to prepare a nickel stamp to imprint superhydrophobic pattern on the composite of carbon nanotubes and PDMS. By moving a rubber tip horizontally under applied normal loading of 1.5 N on the superhydrophobic surfaces with micro pillars or dual hole patterns, it could be observed that the pillars were severely damaged after 100 cycles wear test causing degradation of hydrophobicity, while the dual hole arrays maintained their morphology and hydrophobicity after even 600 cycles wear demonstrating their mechanical durability (Fig. 27b).

To improve the mechanical durability of superhydrophobic surface with nanocones, Kim *et al*. proposed a self-reinforcing egg-crate-like inverted-nanocones (*i.e.*, nanoholes).[437] When 4 N external force was applied on the two nano structures with pitch of 200 nm and aspect ratio of 4, the stress of the nanocone was clearly concentrated at the conical tip, and the calculated shear/normal stresses were 50.4/44.8MPa, while that of the inverted-nanocone evenly distributed over the entire top surface area, and the maximum shear/normal stresses were only 1.34/1.23 MPa (Fig. 27c). The enhanced mechanical stability of the interconnected inverted-nanocone arrays was attributed to the improved redistribution of the shear/normal mechanical loading compared with the nanocone arrays.

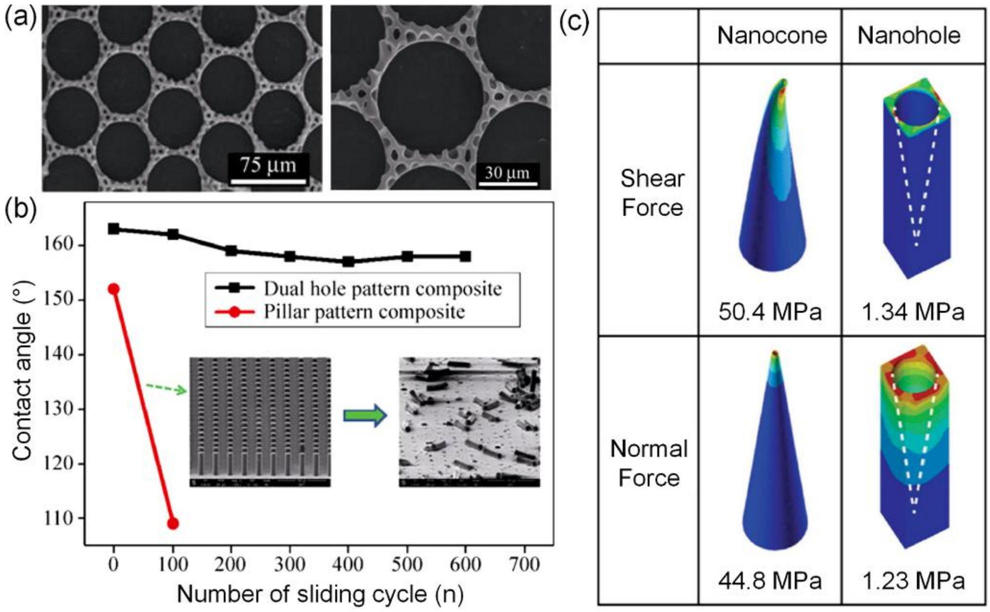

Fig. 27 (a) SEM images of the dual hole patterned superhydrophobic composite. (b) Mechanical durability of the dual hole patterned and pillar patterned superhydrophobic composites. The inset images show the severely damaged pillars after 100 cycles wear tests. (c) Stress distribution in a nanocone and a nanohole structure. (a, b) Reproduced with permission from ref. 436. Copyright (2013) Tsinghua University Press and Springer-Verlag Berlin Heidelberg. (c) Reproduced with permission from ref. 437. Copyright (2014) Wiley-VCH Verlag GmbH & Co. KGaA, Weinheim.

Wang *et al*. further studied the mechanical stability of interconnected microstructures (Fig. 28a) by changing the angle between the sidewall and the substrate of the microstructures ($\alpha_{\mathrm{sidewall}}$) while keeping the top contact area constant.[47] As shown in Fig. 28b, multipurpose finite-element analysis results showed that the third principal stress of the features decreased markedly as $\alpha_{\mathrm{sidewall}}$ increased, demonstrating that increasing $\alpha_{\mathrm{sidewall}}$ was an effective way to improve the mechanical stability of the interconnected microstructures. Conversely, the f_1^{before} increased to f_1^{after} after mechanical abrasion fracture reduced the height in half, and the increment ($\Delta f_1 = f_1^{\mathrm{after}} - f_1^{\mathrm{before}}$) increased with $\alpha_{\mathrm{sidewall}}$, which indicated larger liquid adhesion force and thereby poorer water repellence. Consequently, the $\alpha_{\mathrm{sidewall}}$ was optimized to be around 120° in which both superhydrophobicity and mechanical stability could be balanced and guaranteed. Moreover, the authors compared the mechanical stability of interconnected inverted-pyramidal ($\alpha_{\mathrm{sidewall}}$ = 125 °), pillar and pyramidal microstructures with the same f_1 of 3% (Fig. 28c). The breakpoints in the displacement-load curves of microindentation testing indicated the fracture of the microstructures (points I, II, and III in Fig. 28d), and it was found that the inverted-pyramidal structures could resist the highest loading and thereby showed the best mechanical stability. Based on the interconnected inverted-pyramidal with optimized geometries, the authors designed robust and durable armoured superhydrophobic surfaces, which will be discussed in Section 4.2.4.

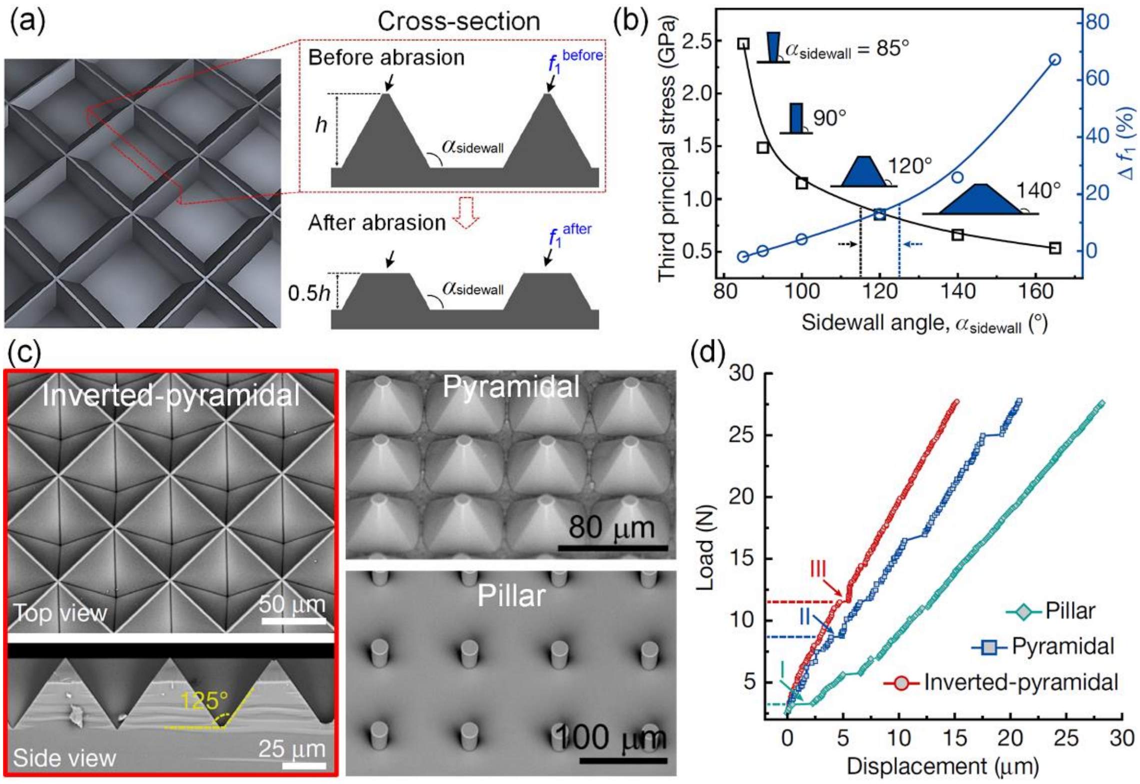

Fig. 28 (a) Schematic diagram of the interconnected microstructures and their cross-section that showed the change of contact area on the top of the structures before and after abrasion. (b) Influence of the sidewall angle on the mechanical stability and change of liquid-solid contact fraction ($\Delta f1$). (c) SEM images and (d) displacement-load curves under microindentation testing of the inverted-pyramidal, pyramidal, and pillar structures. (a–d) Reproduced with permission from ref. 47. Copyright (2020) Springer Nature Limited.

Re-entrant geometry was introduced to improve the mechanical durability of liquid-repellent surfaces against shear loading by scratching.[438] By mimicking the omniphobic skin of springtails, Hensel *et al*. prepared omniphobic polymer membranes with comb-like patterned cavities with re-entrant structures *via* reverse imprint lithography (Fig. 29a and b). Wear tests of the polymer membranes with the re-entrant structures in comparison to that with pillar structures were conducted by an oscillating steel ball in combination with a load. Results showed that membranes with re-entrant structures deformed plastically during loading dissipation and delaminated from the substrates, while the pillars broke at their bottom where the highest bending stress occurred (Fig. 29c). The re-entrant geometry provided a continuous and self-supporting surface that could resist normal loads of 200 to 500 mN depending on the comb wall width, while the pillar structures withstood much lower normal loads (1 to 75 mN) (Fig. 29d). Therefore, re-entrant structures featured surfaces showed significantly higher mechanical durability than pillar arrays covered ones. Furthermore, Hu *et al*. designed a flexible superhydrophobic surface comprising mesoscale heads and microscale spring sets (Fig. 29e) that was similar to the mushroom-like re-entrant geometry on springtail cuticles. Compared with mushroom-like units with rigid supports, the units with spring-like flexible supports showed mechanical durability against ubiquitous normal and shear compress (Fig. 29f), as well as tribological friction.[50] Moreover, these micro structures with re-entrant geometries can also be used to improve the thermodynamic durability of liquid-repellent surfaces, which will be discussed in section 4.2.2.1.

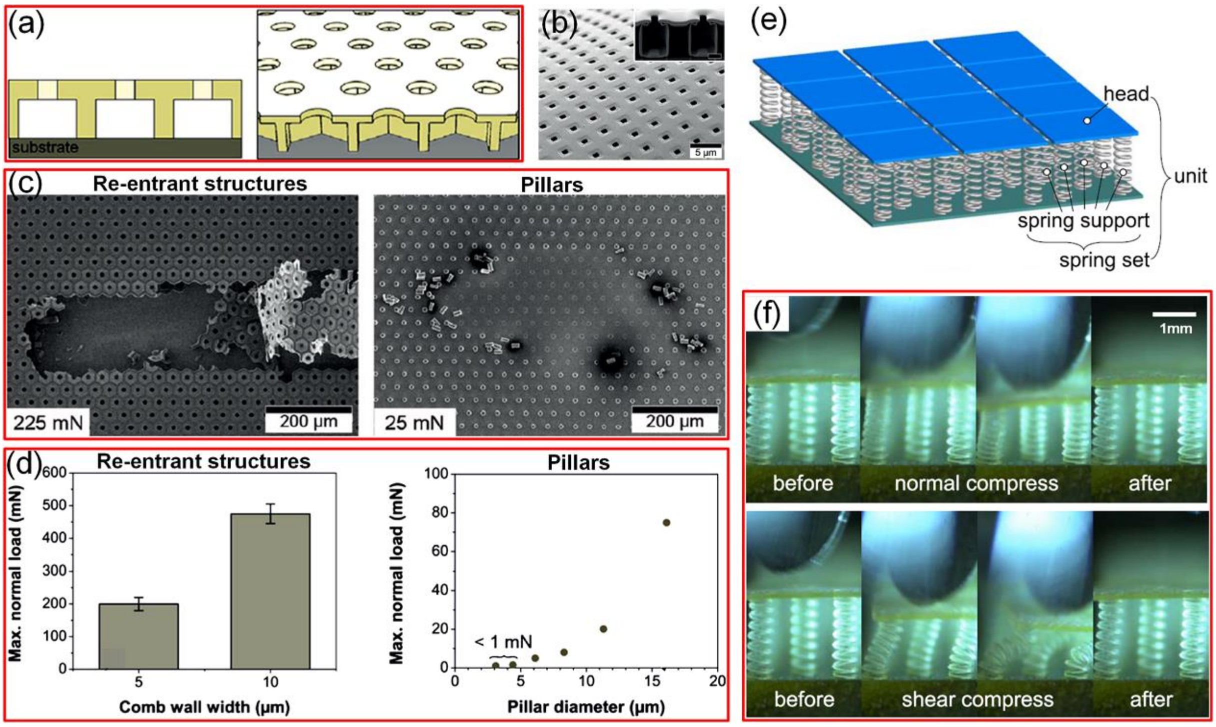

Fig. 29 (a) Schematic diagram and (b) SEM images of the comb-like patterned cavities with re-entrant structures. (c) SEM images of the polymer membranes after wear tests. (d) Maximal normal loads the surfaces could resist without being damaged. (e) Schematic diagram of the mushroom-like re-entrant geometry comprising mesoscale heads and microscale spring sets. (f) Images showing mechanical durability of mushroom-like flexible structures against normal and shear compress. (a–d) Reproduced with permission from ref. 438. Copyright (2013) WILEY-VCH Verlag GmbH & Co. KGaA, Weinheim. (e, f) Reproduced with permission from ref. 50. Copyright (2021) American Chemical Society.

4.2.2 Special structures stabilizing the “cushion”

As discussed above, superhydrophobicity and superoleophobicity in air relies on the retained air pockets, superoleophobicity underwater originates from the locked water layer, and the liquid repellence of SLIS depends on the infused lubricant layer. Consequently, the stability of these micro/nano structure enabled “cushion” determines the thermodynamic durability of the liquid-repellent surfaces, which further influences the chemical durability of these surfaces in terms of immersing in corrosive liquids or exposing to corrosive vapors. Closed-cell micro geometries show much higher pressure stability than open-cell structures due to the confinement of the air underneath the droplet in closed wells, rendering them capable of stabilizing the “cushion” and durable towards droplet impacting.[435] Besides, re-entrant structures and nano structures have been extensively designed to stabilize the “cushion”.

4.2.2.1 Re-entrant structures. Compared with traditional typical pillar microstructures, re-entrant structures have proved to be capable of increasing the breakthrough pressure of the liquid (P_{break}, namely the hydrostatic pressure value at which the "cushion" collapses upon immersion in the liquid), thereby stabilizing the air cushion to improve the durability of the super liquid-repellent surfaces. The springtail skin inspired polymer membranes with re-entrant structures (Fig. 29a and b) were shown to obviously increase the stability of the air cushion upon long-term immersion in water or hexadecane (Fig. 30a).[438] It could be found that the opening diameter of the cavity, 2*a*, had significant influence on the P_{break} (Fig. 30b). For $2a < 1$ μm, the P_{break} significantly increased up to ~ 350 kPa for water and ~ 60 kPa for hexadecane. Shi *et al*. fabricated re-entrant micropillar arrays by using a top-restricted self-growth strategy, through which the structural parameters of the re-entrant micropillar array (center-to-center distance *P*, microdisk diameter *D*, and height *H*) could be easily adjusted.[214] By studying the dynamic deformation of ethylene glycol droplet deposited on the surface by applying external vertical vibration, they found that the re-entrant micropillar with *P* of 650 μm, *D* of 500 μm and *H* of ~ 700 μm showed better dynamic pressure resistance. Recently, Hu *et al*. designed new super liquid-repellent surfaces with re-entrant heads atop spring-like flexible supports by 3D direct laser writing lithography (Fig. 30c), and trampoline-inspired extra horizontal springs to link adjacent mushroom-like heads was further proposed to resolve the structural instability owing to stress concentration and large aspect ratio (Fig. 30d).[215] In contrast to the re-entrant heads with rigid supports, the spring-like flexible supports were proved to contribute a 15.60% improvement of droplet impalement resistance, and even reached a 50.98% enhancement with the aid of trampoline-inspired horizontal springs.

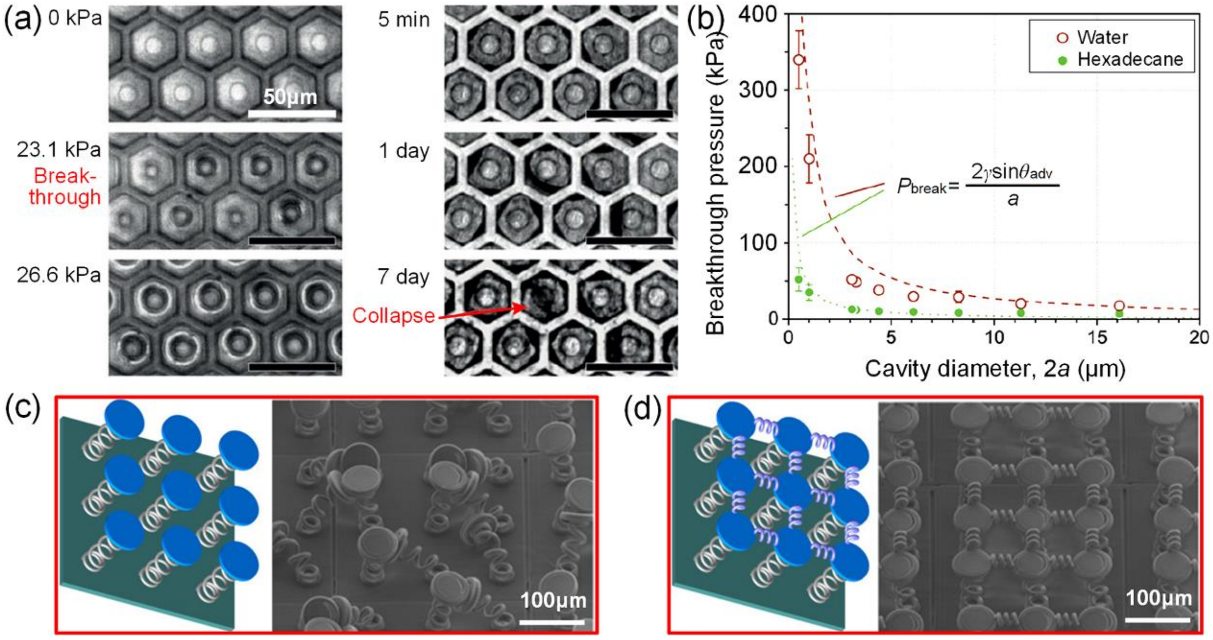

Fig. 30 Optical image series of (a) pressure-dependent and time-dependent collapse of the air "cushion" inside the cavities. (b) Breakthrough pressures of the re-entrant structures featured polymer membranes with different opening diameters. Illustration and corresponding SEM images of re-entrant heads atop spring-like flexible supports (c) with and (d) without extra linking springs. (a, b) Reproduced with permission from ref. 438. Copyright (2013) WILEY-VCH Verlag GmbH & Co. KGaA, Weinheim. (c, d) Reproduced with permission from ref. 215. Copyright (2020) Hu *et al*.

Although singly re-entrant structures increased the breakthrough pressure of liquids, and thus improved the stability of the air cushion, it was subsequently demonstrated that doubly or triply re-entrant structures could further minimize the break-in force by the liquid pressure and maximize the surface tension force that favored the beading up of the liquid even without the requirement of surface fluorination.[188,191] For example, Domingues *et al*. studied the stability of entrapped air on coating-free Si/SiO_2 surfaces with different micro-textures, including simple cavity, re-entrant cavity and doubly re-entrant cavity (Fig. 31a), under wetting liquids.[424] Results showed that the breakthrough pressures of intruding water on simple cavities were 0 kPa, while those on (doubly) re-entrant cavities were typically larger than 100 kPa. In addition, while the air entrapped in circular or non-circular simple cavities immersed in hexadecane was lost within 0.2 s, the air entrapped in various (doubly) re-entrant cavities showed much better stability, and the circular (doubly) re-entrant cavities even stabilized the intruding menisci such that the trapped air remained almost intact even after 27 days (Fig. 31b), a duration that was over 7 orders of magnitude longer than for the simple cavity. Recently, it was demonstrated that a surface with nanoscale doubly re-entrant structures could repel impacting water droplets with a Weber number as high as 10^3 at room temperature due to its extremely high breakthrough pressure.[305] Sun *et al*. designed robust super liquid-repellent surfaces by depositing hydrophobized silica nanoparticles onto multilayered doubly re-entrant micro structures (Fig. 31c) that could generate stepwise wetting resistance.[439] Three layers of doubly re-entrant posts with increasing diameter from top to bottom provided multiple energy barriers for intrusive liquid due to stepwise sagging of the liquid-air interface. The maximum Laplace pressure difference and theoretical P_{break} across the liquid-air interface at the third layer (respectively referred as P_{max3} and P_{break3} in Fig. 31d and e) reached up to ~ 1.6 kPa and ~ 2.3 kPa, respectively, which were approximately 2–3 times of those of single layered doubly re-entrant posts. This endowed the engineered surfaces with durable super liquid repellence against droplet evaporation, dynamic impact by ethylene glycol droplets with Weber number of 35, and random vibration underwater.

Furthermore, Liu *et al*. prepared triply re-entrant microstructures by adding a small overhang at the bottom of the inner vertical overhang doubly re-entrant microstructure *via* two-photon polymerization-based 3D printing (Fig. 32a–c), and demonstrated that the triply re-entrant structures showed higher P_{break} in comparisons with traditional microscale pillars, singly re-entrant structures, and doubly re-entrant structures (Fig. 32d).[191] The printed surface possessed super-repellence to water and various organic liquids with surface tensions of 12.0–27.1 mN m^{-1}, which could even be retained after oxygen plasma treatment.

4.2.2.2 Nano structures. Compared with microscale structures, nano structures can enhance the durability of superhydrophobic and superoleophobic surfaces in air by generating larger anti-wetting pressure. By introducing effective water hammer pressure of impinging droplets on superhydrophobic surfaces, Deng *et al*. demonstrated that sub-100-nm textures could generate large enough anti-wetting pressure for impinging droplets with high speed, which favored the durability of the air cushion under liquid impacting and thereby improved the thermodynamic durability of super liquid-repellent surfaces.[322]

Shieh *et al*. further revealed that a nanograss (diameter of ~ 20 nm, length of ~ 200 nm) or nanopillar (diameter of 100 nm, height of 1 μm, and pillar-to-pillar distance of 200 nm to 50 μm) structure alone did not result in an improvement, while the nanograss decorated nanopillar structures remarkably improved the robustness of the superhydrophobic surface towards liquid impingment.[440] Recently, it was also verified that a nanostructurally-densified superamphiphobic coating possessed enhanced durability during long-term immersion in mixed synthetic and vegetable oils.[441]

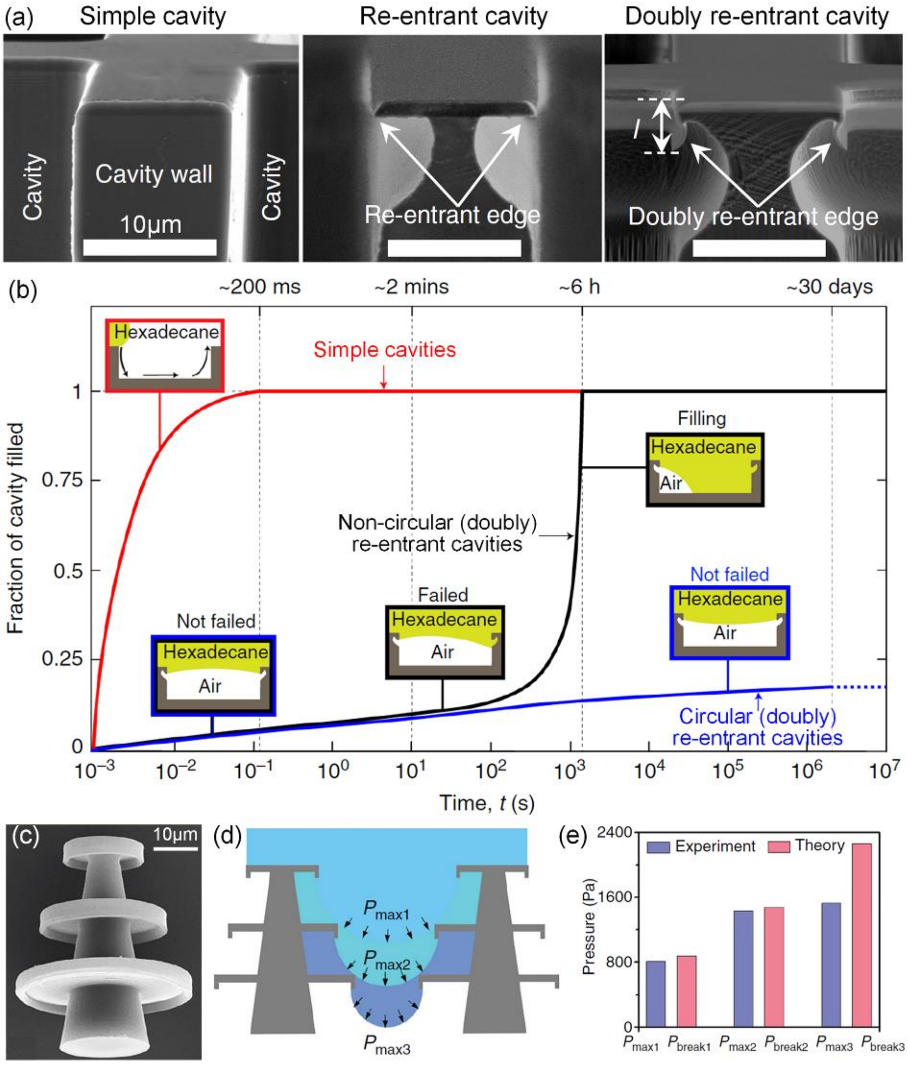

Fig. 31 (a) SEM images of the cross sections and (b) efficacy in sustaining trapped air of simple, re-entrant, and doubly re-entrant cavities. (c) SEM image and (d, e) breakthrough pressure of three layers of doubly re-entrant posts. (a, b) Reproduced with permission from ref. 424. Copyright (2018) Domingues *et al*. (c–e) Reproduced with permission from ref. 439. Copyright (2021) AIP Publishing.

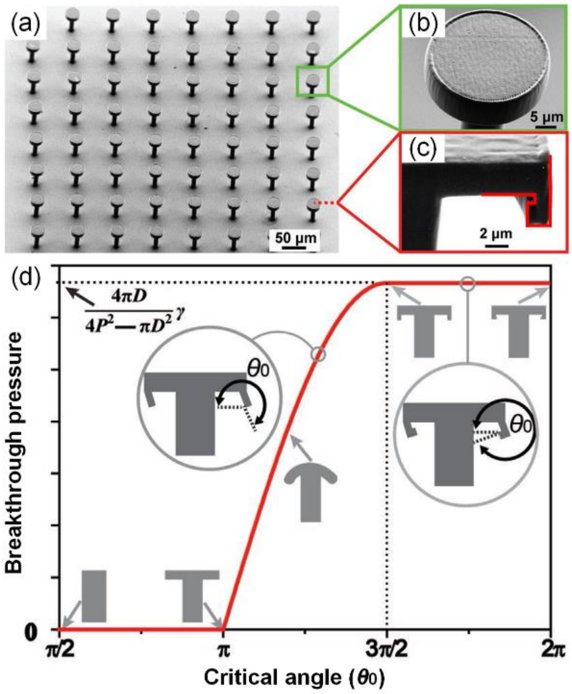

Fig. 32 (a–c) SEM images of the triply re-entrant microstructures. (d) Breakthrough pressures of different surface topologies, including pillars, singly, doubly, triply re-entrant structures, and springtails' skins. Reproduced with permission from ref. 191. Copyright (2018) WILEY-VCH Verlag GmbH & Co. KGaA, Weinheim.

It is well-known that the air cushion trapped in microscale structures can be easily penetrated by vapor, resulting in the loss of superhydrophobicity during condensation. Superhydrophobic surfaces with dense nanocone arrays were demonstrated to be much superior in antifogging,[442] which highlighted the role of nanoscale textures in stabilizing the air cushion towards vapor condensation. Meanwhile, condensate micro droplets on liquid-repellent surfaces with nanostructures could be self-propelled since the coalescence-released excess surface energy was much larger than the interface adhesion-induced energy dissipation.[51,183,443-448] For example, as shown in Fig. 33, Wang *et al*. demonstrated that condensate micro droplets on a superhydrophobic surface with closely packed aligned ZnO nanoneedles could be self-removed by mutual coalescence-induced jumping, and the surface thereby maintained long-term water repellence in extreme vapor conditions.[449] They also showed that the geometric parameters of the nanoneedles (*i.e.*, tip size, height, and interspace) influenced the vapor condensation and micro droplet departure: decreasing the interspace could increase nucleation density of condensate droplets and reduce their departure diameters. Reducing the tip size and height favored the reduction of the departure diameters of the droplets, all of which were beneficial to improve the durability of superhydrophobic surface towards condensation.

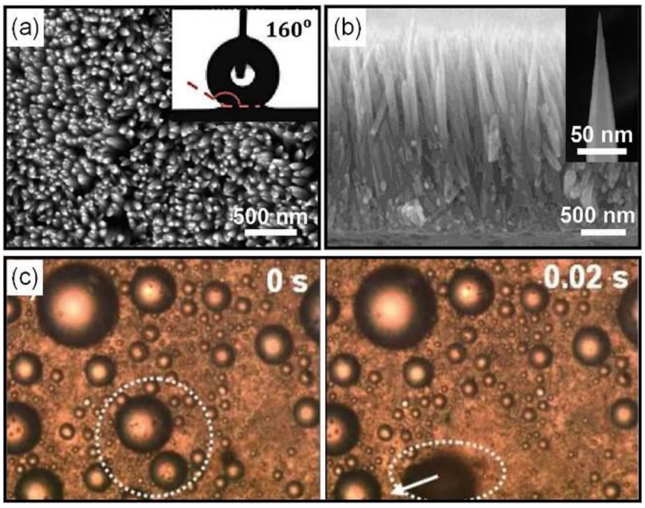

Fig. 33 Nanostructures enhanced durability of superhydrophobic surface towards vapor condensation. (a, b) SEM images of closely packed aligned ZnO nanoneedles on copper surface. (c) Optical images showing typical coalescence-induced self-propelling of vapor condensed micro droplets. Reproduced with permission from ref. 449. Copyright (2018) WILEY-VCH Verlag GmbH & Co. KGaA, Weinheim.

Besides the simple one-tier nanoscale structures, the role of nanostructures in designing super liquid-repellent surfaces with hierarchical structures has also been demonstrated. McCarthy *et al*. experimentally demonstrated that the micro and nanoscale structures of hierarchical superhydrophobic surfaces played distinct, but complementary, roles in endowing the surface with durable water repellence under droplet impacting.[450] The nanostructures provided a large anti-wetting capillary pressure, while the micro features hindered the development and propagation of pressures due to liquid compression. Verho *et al*. studied pressure-induced wetting states transition of superhydrophobic surfaces with one-tier (*i.e.*, microscale) and two-tier (*i.e.*, micro-nano hierarchical) topographies.[451] Results showed that positive Laplace pressure caused an irreversible transition from the Cassie to the Wenzel wetting state for the superhydrophobic surface with single-level topography (Fig. 34a). However, the nanostructures on the surface with hierarchical textures effectively suppressed the transition to the Wenzel state and instead to a so-called nano-Cassie state due to the trapped air in the nanostructures, demonstrating reversible and durable Cassie state superhydrophobicity (Fig. 34b). Similar work was reported by Li *et al.*, who demonstrated a so-called monostable superhydrophobic surface with hierarchical textures, where the transitions from the Cassie state to the Wenzel state became spontaneously reversible.[301] By considering nanotextures enhanced durability, Mouterde *et al*. proposed structural recipes of superhydrophobic surface for repelling hot water: rough features with small radial size (*e.g.*, radius of top, ~ 100 nm) and relatively large axial dimensions (*e.g.*, height of ~ 10 μm).[312] The nanometric top limited the size of vapor-condensation-induced water bridges and thus miniaturized the droplet sticking, while the tall features dynamically prevented the formation of water bridges between the hot droplets and the solid surface during contact.

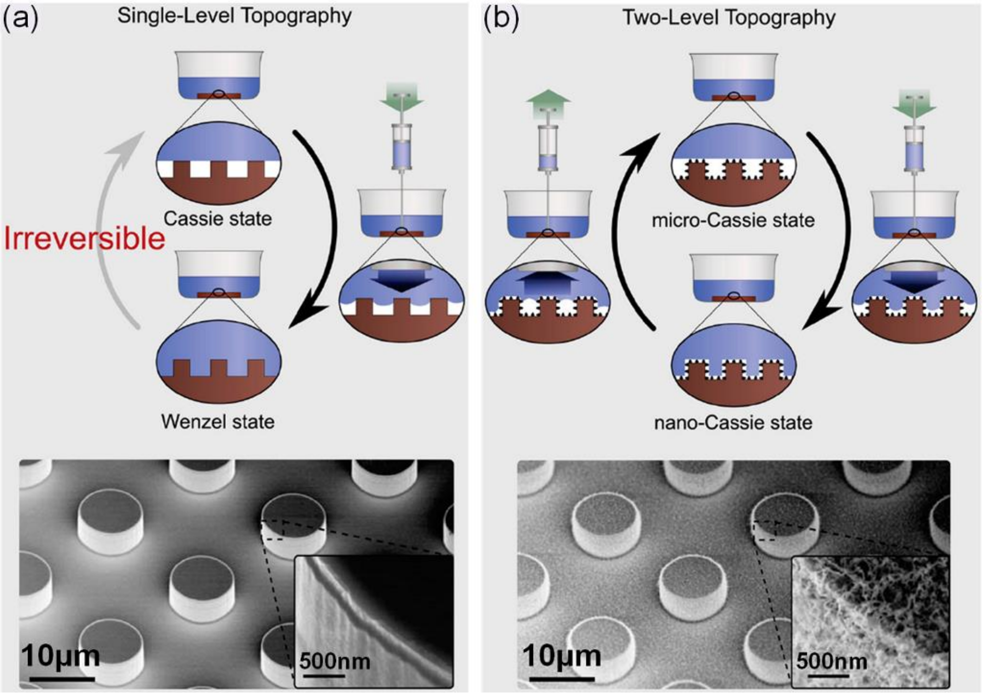

Fig. 34 Durability of superhydrophobic surfaces with single- and two-level topographies under pressure. (a) Single micro structures show irreversible transition from the Cassie to the Wenzel state, while (b) nanostructures of hierarchical topography suppress the transition and create nano-Cassie state instead. Reproduced with permission from ref. 451. Copyright (2012) Verho *et al*.

For underwater superolephobic surface and SLIS, nano structures stabilize the water or lubricant layer *via* superior capillary forces.[249,342] Kim *et al*. discussed the performance of retaining oils on four types of lubricant-infused substrates, such as flat, microtextured, nanostructured and hierarchically structured substrates, and demonstrated that the substrates with nanotextures possessed the best ability of oil retention (Fig. 35a).[261] Microtextured, nanostructured and hierarchically structured roughness on aluminum substrates were synthesized after sandblasting, boehmite and both of sandblasting and boehmite, respectively. For flat substrates, it was difficult to hold lubricants due to a lack of capillary force when exposed to practical conditions (Fig. 35a, i). On microtextured substrates, lubricants easily leaked from valleys between the microscale structures when the length scale of the microtextured features was larger than the capillary length of the lubricant (Fig. 35a, ii). In terms of hierarchically structured substrates consisting of nanostructured and micro-structured textures, nanoscale roughness provided a large capillary force to retain lubricants, but there was still the loss of lubricant from valleys of microscale topographies (Fig. 35a, iii). Lubricants were stabilized in SLIS with nanostructures when the thickness of the lubricant layer matched well with the height of nanostructured textures (Fig. 35a, iv). Therefore, SLISs with nanostructured roughness were demonstrated to possess the best performance in oil retention compared with the other three kinds of substrates under high shear conditions. Wang *et al*. fabricated robust tungsten oxide (WO_3)-based slippery surfaces, and proved that oil retention and durability of the obtained SLIS had a close relationship with the diameter and specific surface area of the WO_3 nanostructures.[452] WO_3 nanoparticles with smaller diameter and larger specific surface area were favorable for the immobilization of the lubricants, which improved the long-term stability of WO_3-based SLIS under high shear force and flowing water impact. Adera *et al*. studied the lubricant depletion from horizontal copper tube with SLIS, and found that the closely spaced nano-florets helped to immobilize and retain the lubrication film *via* capillarity, which made nearly half of the lubrication film to remain on the surface after 10 h of continuous steam condensation at ambient pressure, 23 °C, and 60% relative humidity.[342]

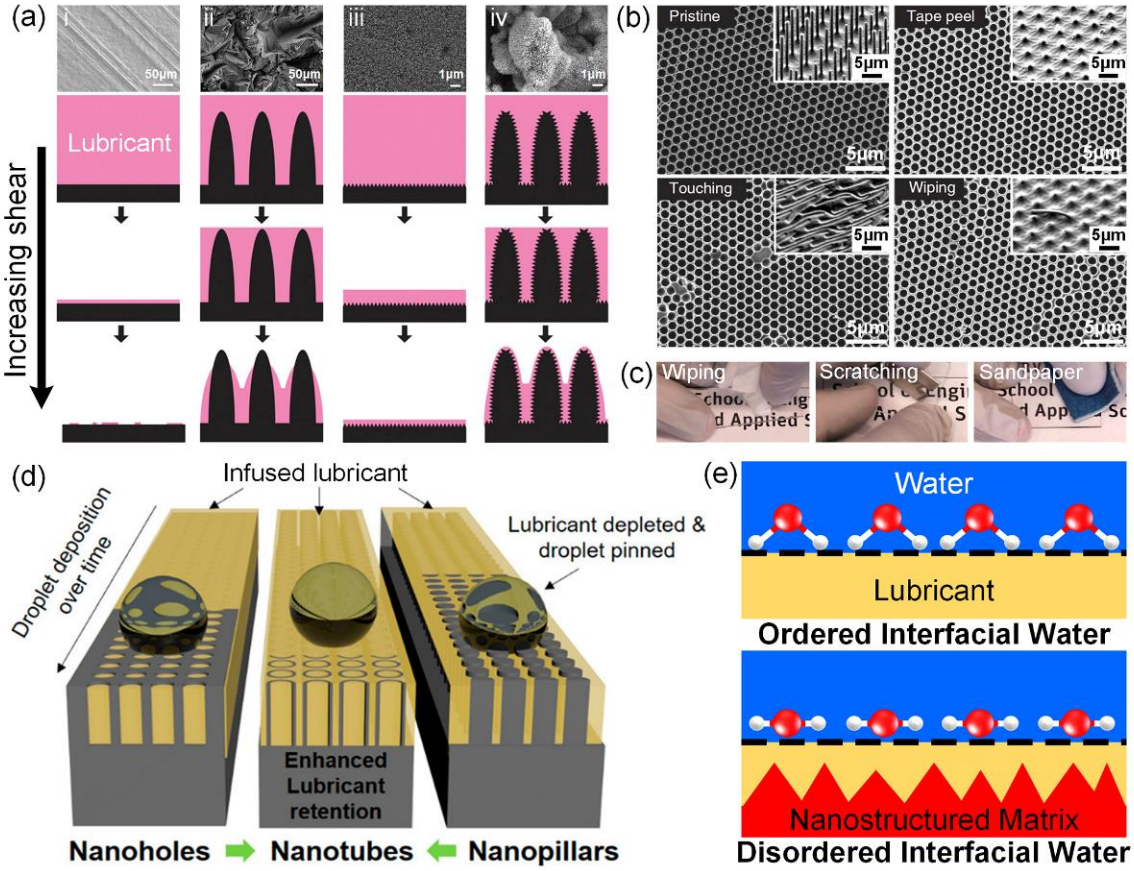

Fig. 35 Nanostructures enhanced lubricant retention for SLIS. (a) SEM images and schematic diagrams of lubricant retention for (i) flat surface, (ii) micro-structured surface, (iii) nanostructured surface, and (iv) hierarchically structured surface. (b) SEM images of the closed- and open-cell nanostructures (insert images) under mechanical testing, such as tape peeling, touching, and wiping. (c) Mechanical durability testing of the SLIS. (d) Schematic of lubricant depletion and liquid repellence of SLISs with different nanostructures. (e) Schematics of interfacial water molecule orientation at the water-lubricant interface. (a) Reproduced with permission from ref. 261. Copyright (2013) American Chemical Society. (b, c) Reproduced with permission from ref. 357. Copyright (2013) Macmillan Publishers Limited. (d) Reproduced with permission from ref. 453. Copyright (2021) American Chemical Society. (e) Reproduced with permission from ref. 454. Copyright (2021) American Chemical Society.

Vogel *et al*. designed well-ordered honeycomb wall nanostructures in which lubricants could be strongly locked and flow freely, even when exposed to strong shear forces or long-term storage.[357] The SLISs were prepared as follows: a homogeneous and interconnected porous layer was synthesized by using a silica precursor solution to backfill colloidal monolayer on a glass substrate and then the colloids were removed at high temperature, which was followed by infusing the porous intermediate with fluorinated oil. When the SLIS was damaged partly (damaged region was 33%), it retained outstanding octane repellent property with a SA of < 5° under spin-coating at 10000 r.p.m. This could be attributed to the interconnected nanoscale pore structures that favored the formation of intact surface *via* re-filling of the lubricant. The as-prepared SLIS retained remarkable octane repellency with SAs of below 10° after being stored more than 9 months without replenishment of the lubricants. In addition, SEM images shown in Fig. 35b demonstrated complete structural integrity of the closed-cell architectures after various mechanical testing including tape peeling, touching, and wiping, while the open-cell samples were completely destroyed by any of the testing (Fig. 35b, insets). These results demonstrated the excellent robustness and durability of the SLIS with closed-cell nanopores array, the coated glass slides showed efficient repellency to dyed octane droplet after mechanical wiping, scratching with a razor blade and sandpaper (Fig. 35c). Furthermore, Laney *et al*. reported delayed lubricant depletion of SLIS with nanotube texture in comparison to nanohole and nanopillar textures (Fig. 35d).[453] The authors fabricated an array of silicon nanotubes and equivalent arrays of nanoholes and nanopillars (pitch, 560 nm; height, 2 μm), and obtained the corresponding SLISs after surface hydrophobic treatment and subsequent infusion with lubricant Krytox 1525. Shear tolerance test revealed that all nanostructures were able to retain the lubricant *via* capillary action up to 10000 rpm, but harsh water droplet shedding test showed 2-fold and 1.5-fold enhancements of lubricant retention in nanotubes in comparison to nanopillars and nanoholes, respectively, demonstrating a prolonged lifetime of the SLIS with nanotube textures.

Recently, Zhang *et al*. proposed a new mechanism of nanostructures enhanced lubricant retention for SLIS during its contact with water.[454] By using surface-sensitive sum frequency generation vibrational spectroscopy, the authors characterised the water-lubricant interface of a water droplet depositing on a lubricant-infused nanostructured surface and the same lubricant layer without the underlying nanostructures. The results demonstrated that due to the strong interaction between the infused lubricant and underlying nanostructures, water droplets deposited on nanostructured SLIS preferred a molecular orientation that was predominantly parallel to the water-lubricant interface (Fig. 35e), which weakened the hydrogen bonding interactions between the water droplets and lubricant, imparting the SLIS with excellent water repellence and reduction of lubricant depletion during contact with water.

4.2.3 Self-similar micro/nano structure

Many of the durability problems of liquid-repellent surfaces arise from the fact that the outermost layer cannot survive through mechanical and chemical destruction, and the thin functional layer may be easily removed or destroyed so as to lose their liquid repellence. If the rough structures and chemistries are self-similar throughout the coating/matrix, the freshly exposed area after damage will be similar in wettability and functionality with the top or undamaged layer, which thereby can be used to design robust and durable liquid-repellent surfaces.[455-459] Based on this strategy, liquid-repellent coatings with self-similar structures can be used to render the underlying substrates robust and durable liquid repellence until the coatings are completely damaged or removed. For example, Deng *et al*. deposited a porous layer of candle soot on a glass slide and then coated the soot with a silica shell, after which the coating was calcinated and subsequently silanized to prepare a superamphiphobic surface (Fig. 36a, b).[217] The surface retained its superamphiphobicity after 5 min of falling sand abrasion from a height of 25 cm (the corresponding impacting velocity was ~ 2 m s^{-1}). The silica shells were not sufficiently robust to completely resist the sand abrasion, and an eroded cave was observed at the impacted area (Fig. 36c). However, the exposed area showed similar sub-micrometer structure with the original surface (Fig. 36d), which enabled the impacted surface to be oil-repellent until the coating's thickness was reduced to < 2 μm by extended sand abrasion. The proposed candle soot-templated porous silica shell with self-similar micro/nano structures was followed in many subsequent works that focused on the fabrication of various robust and durable liquid-repellent surfaces.[47,223,460-464] Additionally, fluorosurfactant-coated silica aerogels have also been demonstrated to create self-similar nanoporous frameworks with re-entrant surface topography that rendered the surface mechanically robust superamphiphobicity.[465] Kong *et al*. prepared a robust and durable sprayable superhydrophobic coating by designing polydivinylbenzene nanotubes interweaved fluorine-containing SiO_2 nanoparticles.[197] The authors firstly prepared post cross-linked polydivinylbenzene nanotubes with abundant mesopores *via* a Friedel-Crafts reaction, and then mixed the nanotubes with industrial paraffin wax, ethyl α-cyanoacrylate, and 1*H*,1*H*,2*H*,2*H*-perfluorodecyltrimethoxysilane functionalized SiO_2 nanoparticles, which were finally sprayed on wood substrates to create superhydrophobic surfaces. The combination of polydivinylbenzene nanotubes and fluorinated SiO_2 nanoparticles formed self-similar hierarchical structures, which enabled the superhydrophobic surface to tolerate various chemical and mechanical durability testing, such as immersion in corrosive solutions for 24 h, UV illumination for 70 h, ultrasonic processing for 1 h, finger rubbing, circular abrasion (500 g loading, 1000 cycles), and scratching by box cutter.

Besides these coated liquid-repellent materials on substrates, free-standing 3D blocks with self-similar structures between the exterior surface and internal space have also been widely developed to create liquid-repellent monoliths.[46,458] Li *et al*. reported a robust superhydrophobic PDMS/SiO_2 thick film prepared by thiol-ene photopolymerization of PDMS/hydrophobic SiO_2/cyclohexane suspension and subsequent solvent evaporation (Fig. 36e).[351] The formed self-similar hierarchical structures (Fig. 36f) enabled the film to retain its superhydrophobicity even after 500 cycles of abrasion by sandpaper, as well as "plasma + sanding" treatment. Based on a simple 1,4-conjugated addition reaction, Chen *et al*. prepared superhydrophobic nanocomplexes bulk by a facile gelation process involving dipentaerythritol penta-/hexa-acrylate (5Acl) and branched polyethylenimine ethylenediamine (BPEI) (Fig. 36g), and subsequent modification with octadecylamine.[466] Due to its self-similar microstructures (Fig. 36h), the bulk material retained the superhydrophobicity after cutting (Fig. 36i), water jet impacting, rubbing, and sandpaper abrasion. Recently, 1,4-conjugated addition reaction between selected small molecules, *i.e.*, [3-(2-aminoethylamino)propyl]trimethoxysilane and octadecyl acrylate, in the presence and absence of crosslinker molecules [pentaerythritol triacrylate (3-Acl) or 5-Acl], were reported to develop "tolerant and hard" superhydrophobic coatings on polyurethane fabric and melamine formaldehyde sponge.[467] The self-similar micro/nano structures enabled the resultant superhydrophobicity to be highly robust and durable towards sandpaper abrasion for 30 m, various chemical invasion (including acid, alkali, salt, and organic solvents) for 30 days, and washing test for 250 cycles. Recently, Dong *et al*. developed a method to print superhydrophobic objects with bulk nanostructures by combining 3D printing with photopolymerization-induced phase separation based on a specific printing ink composed of hydrophobic (meth)acrylate monomers and porogen solvents.[52] Owing to the self-similar bulk nanostructures, the printed object showed superhydrophobicity both on the surface and on the cross-section. As shown in Fig. 36j, when the bulk material was abraded on sandpaper under a pressure of 10 kPa for 10 cm per cycle, it remained superhydrophobic even after 40 abrasion cycles owing to the exposed surface underneath after abrasion was structurally similar to the original surface.

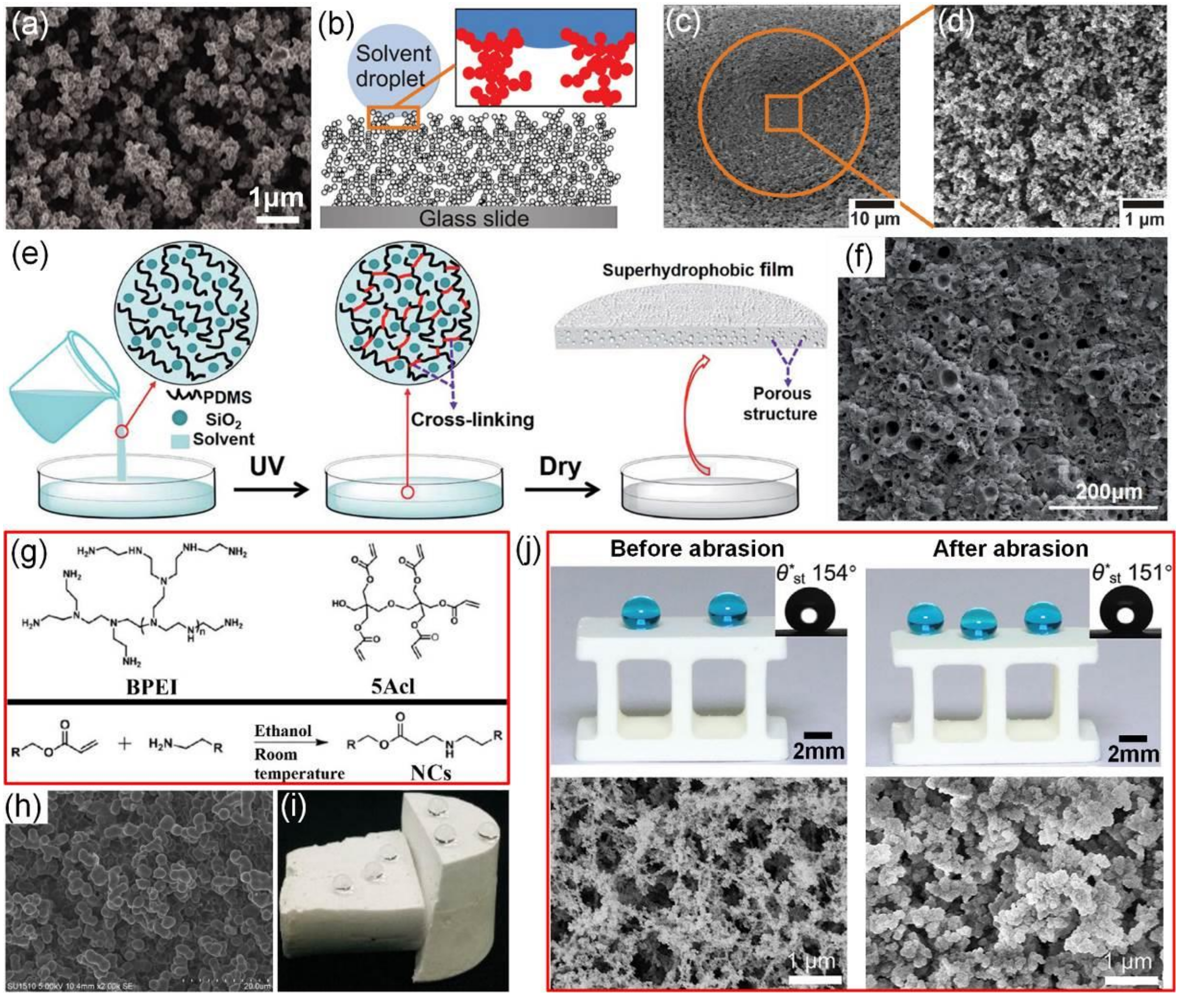

Fig. 36 Self-similar rough structures enhanced robustness and durability of liquid-repellent surfaces. (a) SEM image and (b) schematic of the prepared superamphiphobic coating. (c, d) SEM images of the superamphiphobic surface after falling sand impacting. (e) Preparation process and (f) cross-sectional SEM image of the superhydrophobic PDMS/SiO2 film. (g) 1,4-conjugated addition reaction between BPEI and 5Acl. (h) SEM image of the superhydrophobic nanocomplexes bulk whose (i) cross-section also showed super water repellence. (j) Self-similar bulk nanostructures enabled robust superhydrophobicity towards sandpaper abrasion. (a–d) Reproduced with permission from ref. 217. Copyright (2012) American Association for the Advancement of Science. (e, f) Reproduced with

permission from ref. 351. Copyright (2019) The Royal Society of Chemistry. (g–i) Reproduced with permission from ref. 466. Copyright (2020) Elsevier B.V. (j) Reproduced with permission from ref. 52. Copyright (2021) Dong *et al*.

4.2.4 Self-protective structure

Rough topographies are almost indispensable to achieve liquid-repellent surfaces. As discussed above, nanoscale structures can enhance the liquid repellence *via* special capillarity, but these structures are intrinsically extremely fragile towards mechanical force and can be easily destroyed even by rather low mechanical stress. By contrast, microscale features possess much higher resistance to external forces induced destruction. However, owing to the considerable contact line pinning at the edges of the microstructures, liquid-repellent surfaces with microstructures alone always exhibit large CAH and low liquid mobility. Therefore, hierarchical structures, combination of micro and nano structures, have been widely employed to improve the mechanical durability of liquid-repellent surfaces.[45,53,405,468] When hierarchical structures are exposed to mechanical stress, the microstructures bear much of the loading, which thereby protects the fragile nanostructures from being damaged. For example, Zimmermann *et al*. reported a gas phase coating procedure to deposit a polymethylsilsesquioxane nanofilaments layer on various textile fabrics, by which robust superhydrophobicity was created.[156] As illustrated in Fig. 37a, a superhydrophobic poly(ethylene terephthalate) (PET) fabric retained its water repellent property after 1450 cycles skin-simulating abrasion under a contact pressure of 7.8 kPa, and it could be easily seen that the 3D microstructure of the fabric protected the majority of the nanofilaments from being damaged during abrasion (Fig. 37b). Xiu *et al*. compared the mechanical durability of several superhydrophobic surfaces, including hierarchically structured silicon, nanostructured polyurethane, PTFE, silica and silicon.[53] After abrasion by polyester/cellulose Technicloth II wipes (pressure of 3.45 KPa and abrasion length of 25 cm), the superhydrophobic silicon surface with two-scale micro- and nano-structures showed robust water repellence with nearly constant water CA (> 165°) and small CAH increase (from 2° to 13.6°), while all other surfaces lost their superhydrophobicity (water CA < 140° and CAH > 60°). Surface morphology characterisation showed that the nanostructures alone were easy to damage, as well as those on the tops of the micro pyramids, but the nanostructures close to the base of the micro pyramids were well protected and retained, which largely improved the robustness of water repellence towards mechanical abrasion. Verho *et al*. proposed a model to explain the hierarchical architectures induced mechanical durability of super liquid repellence, as shown in Fig. 37c.[286] If the surface was composed of one-tier structures (either micro or nano scale), abrasion caused the structures to wear off, leading to a rupture of the Cassie-Baxter wetting state. By contrast, if nanostructures were decorated on microstructures, most of the nanoscale architectures could be protected by the microstructures during abrasion, except the ones on the top of the microstructures that were directly exposed to abrasion, which favored the stable Cassie-Baxter wetting state.

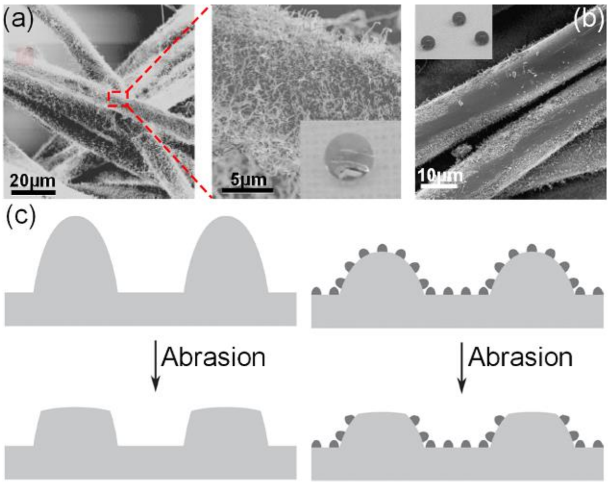

Fig. 37 SEM images of superhydrophobic PET fabrics (a) before and (b) after 1450 cycles of skin-simulating abrasion. Insets show water droplet deposited on the respective fabrics. (c) Self-protective effect of hierarchical structures. (a, b) Reproduced with permission from ref. 156. Copyright (2008) WILEY-VCH Verlag GmbH & Co. KGaA, Weinheim. (c) Reproduced with permission from ref. 286. Copyright (2011) WILEY-VCH Verlag GmbH & Co. KGaA, Weinheim.

Lin *et al*. designed a robust superhydrophobic carbon nanofiber-polydimethylsiloxane (CNFs-PDMS) network inlay-gated stainless-steel mesh (SSM).[469] They deposited CNFs into the pores of SSM to form network fillers *via* vacuum filtration, which became superhydrophobic after being coated with PDMS layer (Fig. 38a). The wires of the mesh acted as protective supports to the embedded CNFs-PDMS composites during abrasion (Fig. 38b and c), which enabled the mesh to retain its superhydrophobicity after 15 cycles abrasion by sandpaper under pressure of ~ 1.7 kPa and abrasion length of 5 cm per cycle. Based on this, they proposed a concept of discrete or partial superhydrophobicity, indicating that although the protective structures were partially damaged and lost the water repellence due to physical abrasion, the protected areas were well preserved and thereby retained the overall superhydrophobicity of the surface.

Recently, Qing *et al*. proposed a microskeleton-nanofiller composite to form an excellent mechanically robust superhydrophobic film against abrasion and impact.[354] They filled phosphorizing liquid roughened porous iron with inorganic/organic medium composed of fluorinated epoxy resin, hydrophobic SiO_2 nanoparticles and γ-aminopropyltriethoxysilane, and the resultant composite film showed superhydrophobicity (Fig. 38d). Due to the protectiveness of the microskeleton, the nanofiller could be well retained during knife scratch, cyclic tape peeling, and continuous sandpaper/Taber abrasion (Fig. 38e and f), thereby reserving superhydrophobicity before complete wearing of the film. Additionally, the tight composite filler protected the microskeleton from being collapsed during bearing ball impacting (Fig. 38g), which enabled robustness to heavy impact at least up to a kinetic energy of ~ 40.2 J.

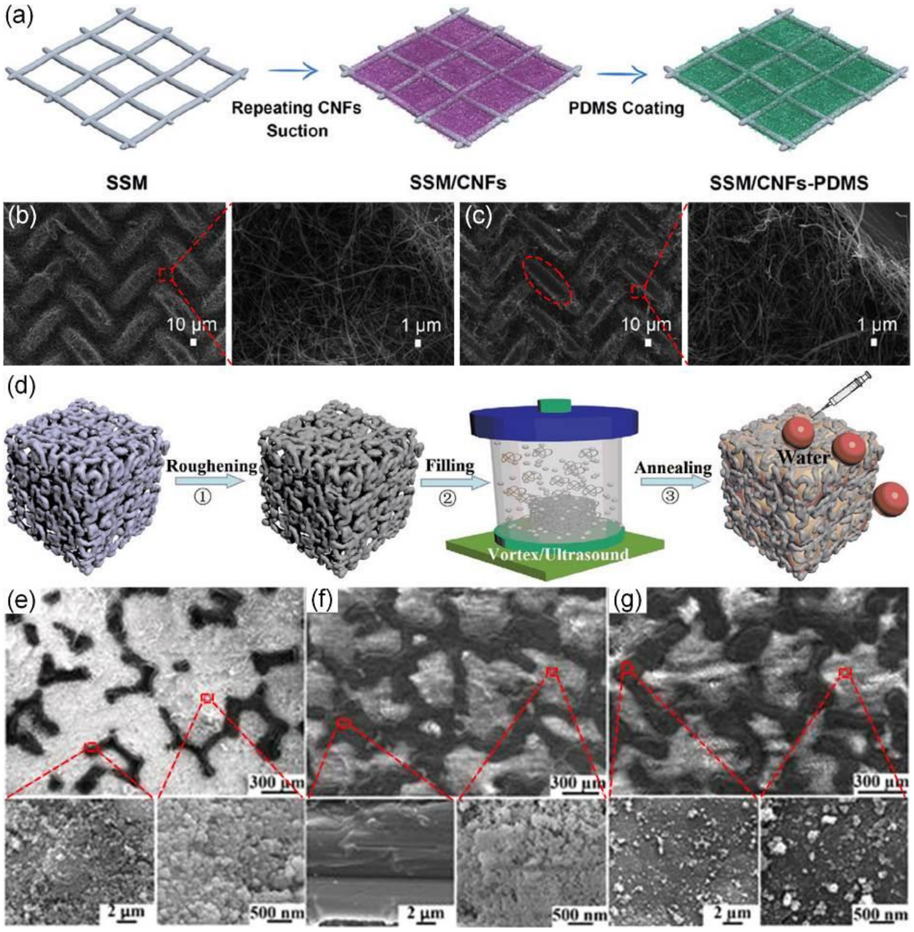

Fig. 38 (a) Fabrication of the superhydrophobic CNFs-PDMS network inlay-gated SSM. SEM images of the mesh (b) before and (c) after 20 cycles of sandpaper abrasion testing. (d) Fabrication of the superhydrophobic microskeleton-nanofiller composite. (e) SEM images of the as-prepared superhydrophobic composite. SEM images of the composite after (f) 2500 cycles of abrasion by sandpaper and (g) impacting by a bearing ball from a height of 1 m. (a–c) Reproduced with permission from ref. 469. Copyright (2016) The Royal Society of Chemistry. (d–g) Reproduced with permission from ref. 354. Copyright (2020) WILEY-VCH Verlag GmbH & Co. KGaA, Weinheim.

Wang *et al*. further demonstrated that when the liquid-solid contact fraction (f_1) is small enough, the surface could still repel water even if the contact areas were altered from hydrophobic to hydrophilic during mechanical abrasion (Fig. 39a).[47] Based on this, they reported a mechanically durable water-repellent surface with skillfully designed “armoured” micro/nano structures. They deposited nanoparticles into interconnected microstructures that contained crater-like “pockets”, and the nanostructures were used to provide water repellency while the microstructures were designed to protect the mechanically fragile nanoparticles (Fig. 39b). Benefiting from the protection of mechanically robust microstructure armour, the housed superhydrophobic nanoparticles could be well preserved during abrasion, which endowed the surface to be water-repellent before f_1 increased to a critical value upon abrasion (Fig. 39c). For example, they fabricated inverted-pyramidal microstructures on silicon substrates with different open cavity widths L and liquid-solid contact fractions f_1, and then filled the microstructure frameworks with soot-templated silica nanostructures, finally yielding water-repellent surfaces after fluoridation. Repeated scraping by steel blade gradually removed materials (both the fluorosilane layer and the matrix) from the top of the microstructures (Fig. 39d), which changed the local wetting properties of the surface from hydrophobic (θ_Y = 115°) to hydrophilic (θ_Y = 45°) and increased the liquid-solid contact fraction f_1, but the surfaces retained their super water repellence after abrasion if f_1 was lower than 8% (Fig. 39e and f). Linear abrasion testing (vertical pressure of 12 MPa and abrasion speed of 50 mm s^{-1}) of the armoured superhydrophobic surfaces showed that more than 1000 cycles of abrasion could be tolerated, which was 10 times higher than that of conventional superhydrophobic surfaces (Fig. 39g). The remarkable mechanical durability of the armoured water-repellent surfaces was also confirmed by other testing, including scratching, tape-peeling, Taber abrasion and high-speed water jet impacting.

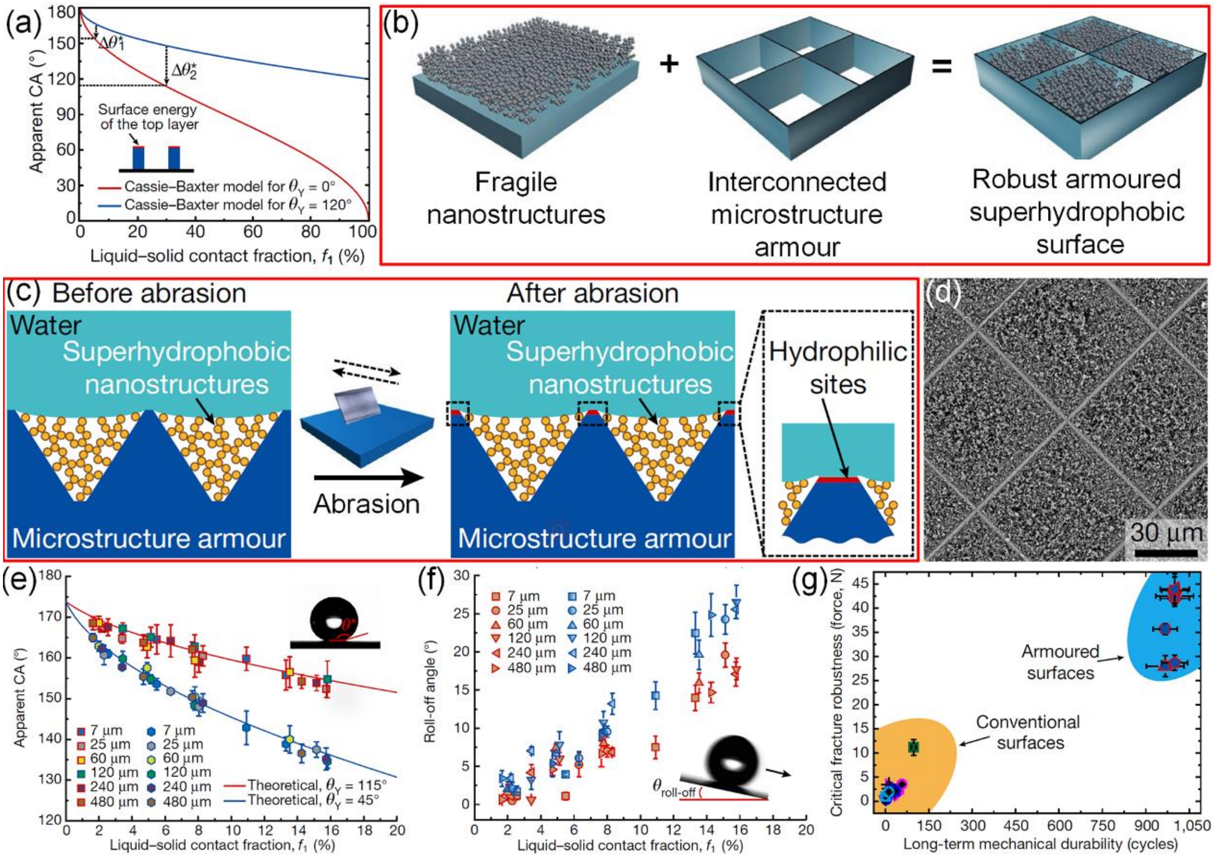

Fig. 39 . (a) Relationship between the apparent CA and the liquid-solid contact fraction f_1 for an ideal Cassie-Baxter state at two different Young's CA. (b) Schematic showing the design strategy for the armoured superhydrophobic surface. (c) Mechanism of the water repellence of the armoured surface before and after abrasion. (d) SEM images of the silica nanostructures housed within the silicon microstructure frame after abrasion. (e) Apparent CAs and (f) RAs of the armoured surfaces before and after abrasion. (g) Comparison of the mechanical durability of different superhydrophobic surfaces under linear abrasion. (a–g) Reproduced with permission from ref. 47. Copyright (2020) Springer Nature Limited.

4.3 Strengthening the Bonding between Coating and Substrate

Compared with roughening the substrates and tailoring the surface free energy, coating is regarded as a universal, easy-to-commercialize, and substrate-independent solution to construct liquid-repellent surfaces. Therefore, strengthening the bonding between the coating and the substrate becomes significant to improve their robustness and durability. Different from the weak physical adsorption induced by van der Waals forces, chemical bonding *via* covalent bonds, cross-linking, adhesive layer assistance, *etc*. are much stronger to tolerate mechanical and chemical damage, which are thereby widely developed to enhance the bonding strength at the coating-substrate interface of liquid-repellent surfaces.[45,344,405]

4.3.1 Covalent bonding

In general, covalent bonds can be generated between substrates and coatings *via* reactions of chemical reactive groups. Surfaces with abundant hydroxyl groups (*e.g.*, cellulose-based fabrics, filter paper, *etc*.) can directly react with silanol, epoxide groups, *etc*. to form covalent bonds. Deng *et al*. soaked a cotton fabric into a methanol solution containing 1*H*,1*H*,2*H*,2*H*-nonafluorohexyl-1-acrylate monomer and then initiated graft polymerization under γ-rays irradiation in a nitrogen atmosphere, which resulted in covalent connection of fluorinated compounds onto the cotton fiber at the molecular level.[377] When the degree of grafting was higher than 10%, the obtained fabric showed stable superhydrophobicity. Due to the strong binding between the cotton fiber and the fluorinated groups, the grafted fabric retained its superhydrophobicity after 50 accelerated laundering cycles, which was equivalent to 250 commercial or domestic launderings. Zou *et al*. prepared a highly durable and robust superhydrophobic cotton fabrics based on covalent bonding by using diblock copolymers consisting of poly(glycidyl methacrylate) (PGMA) and poly(2,2,2-trifluoroethyl methacrylate) (PTFEMA) blocks.[290] The block copolymers self-assembled into micellar aggregates to form nanoscale roughness, and the PTFEMA block lowered the surface free energy, while the PGMA block was covalently bonded to the surfaces of cotton fibers through a ring-opening reaction between the epoxy groups of the PGMA chains and the hydroxyl groups of the cotton fiber, and the self-crosslinking of the epoxy groups from PGMA chains. The covalently bonded PTFEMA chains favored the robustness and durability of the superhydrophobic fabrics towards various testing, including sandpaper abrasion, laundering, ultrasonication and boiling in tetrahydrofuran or trifluorotoluene, soaking in organic solvents and acidic/basic aqueous solutions, and exposure to UV irradiation. Fang *et al*. modified fabric with mercaptopropyltriethoxysilane to incorporate thiol groups, which was then used to anchor methacryloxypropyltrimethoxysilane modified $SiO_2@Fe_3O_4$ (MPS-$SiO_2@Fe_3O_4$) nanoparticles *via* UV-assisted thiol-ene click chemistry (Fig. 40a).[470] The obtained superhydrophobic fabric showed excellent robustness against tape-peeling, sandpaper abrasion, and corrosive solutions, which were attributed to the strong interactions between the MPS-$SiO_2@Fe_3O_4$ nanoparticles and fabric by thiol-ene click reaction-induced covalent bonding.

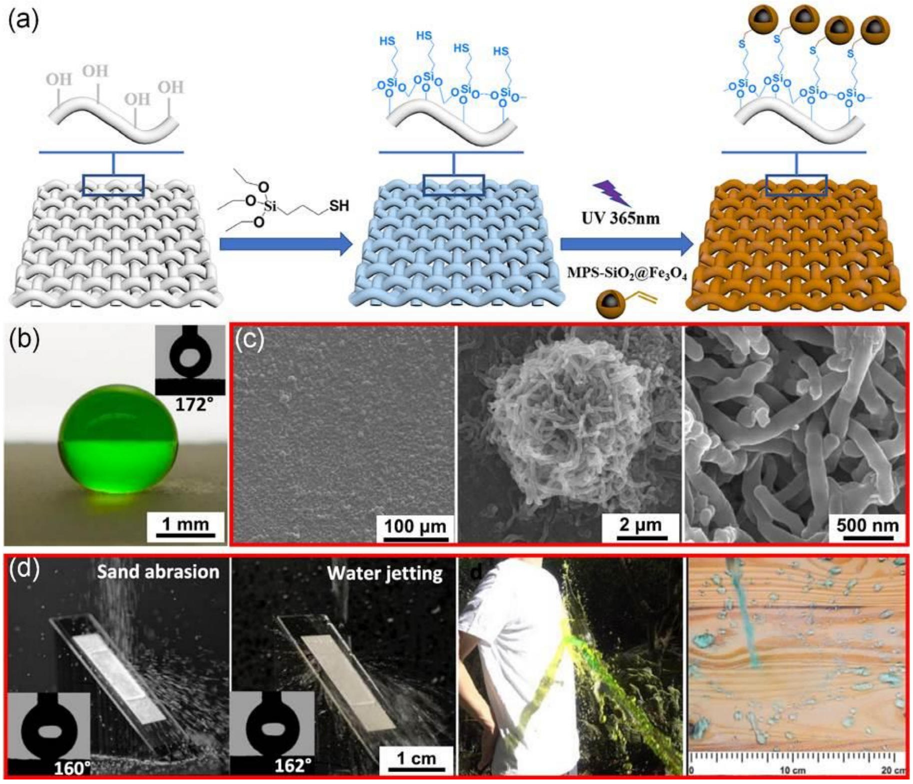

Fig. 40 (a) Preparation steps of superhydrophobic fabric with MPS-SiO_2@Fe_3O_4 nanoparticles *via* UV-assisted thiol-ene click chemistry. (b) Optical image showing a water droplet on the superhydrophobic coating treated glass slide, and (c) the corresponding SEM images. (d) Robustness testing of the superhydrophobic coating, including sand abrasion, water jetting, and water splashing. (a) Reproduced with permission from ref. 470. Copyright (2020) American Chemical Society. (b–d) Reproduced with permission from ref. 414. Copyright (2021) Zhang *et al*.

For those surfaces with insufficient reactive groups (*e.g.*, glass), pre-treatments by UV, ozone, plasma, or chemical solutions are required. For example, Zhang *et al*. reported a method to prepare robust superhydrophobic coatings *via* stoichiometric silanization (Fig. 40b–d).[414] The authors mixed pure octadecyltrichlorosilane (OTS) with water by vortex and sonication, which was then incubated for 2 h under ambient conditions before being diluted with hexane. The solution could be used to treat various substrates directly to obtain superhydrophobic surfaces, such as cotton fabric, filter paper, and PET, but pretreatment by UV-ozone cleaner was required for glass slides (Fig. 40b). During the solution preparation procedure, stoichiometric silanization reaction between long-chain organosilanes and water occurred and created micro- and nano-scale hierarchical siloxane aggregates (Fig. 40c). Owing to the incomplete silanization reaction after 2 h, reactive sites (−Si−OH or −Si−Cl) still existed on the aggregated particles, which facilitated the formation of covalent bonding between these hierarchical particles and the substrates covered with −OH groups during the coating treatment. The covalently bonded coating showed robust superhydrophobicity towards falling sand abrasion, water jetting, water splashing and tissue wiping, *etc*. (Fig. 40d). Additionally, the coating could tolerate abrasion by sandpaper under a pressure of 2.5 kPa and a distance of 50 cm, since only the top layer of the coating was partially removed while the remaining micro/nano structures were similarly rough to retain the super water repellence.

Besides the covalent bonding of liquid-repellent coatings as discussed above, the lubricant layer of SLIS can also be stabilized *via* covalent bonding to improve its durability and stability.[266,275] For example, Chen *et al.* fabricated robust ionic liquid-infused slippery surfaces *via* enhancement of the interaction between substrate and lubricant using a covalent half-polymerization strategy.[471] Anodic aluminum oxide (AAO) with homogeneous pore size (~ 200 nm) was utilized as the porous substrate, and ionic liquid (1-vinyl-3-hexylimidazolium bis(tri-fluoromethanesulfonyl)imide) was employed as the infusing lubricant. Silane couplers with alkene terminated groups were firstly anchored on the AAO surfaces with abundant hydroxyl groups *via* chemical bonding (Fig. 41a), and then the intermediates with alkene groups were chemically linked with vinyl groups of ionic liquid *via* alkene polymerization (Fig. 41b). In this case, both the porous nanostructures-induced capillarity and the covalent half-polymerization-enhanced interaction between the substrate and ionic liquid contributed greatly to the stabilization of the lubricant layer, which rendered the resulted SLIS with excellent underwater durability, high temperature stability, shear-resistance and corrosion-resistance. Liu *et al*. reported a liquid-repellent PDMS coating on silicon or glass slide prepared by spontaneous and fast polymerization of dichlorodimethylsilane under the assistance of water hydrolysis.[273] The grafted liquid-like PDMS brushes enabled the surface to be slippery and droplets of a variety of liquids could slide off at the tilting angles below 5°. Due to the strong covalent attachment of the PDMS brushes to the substrates, the prepared slippery liquid-repellent surface showed outstanding durability against long-term sonication washing, tape peeling, scouring pad wiping, high temperature treatment, and water vapor exposure.

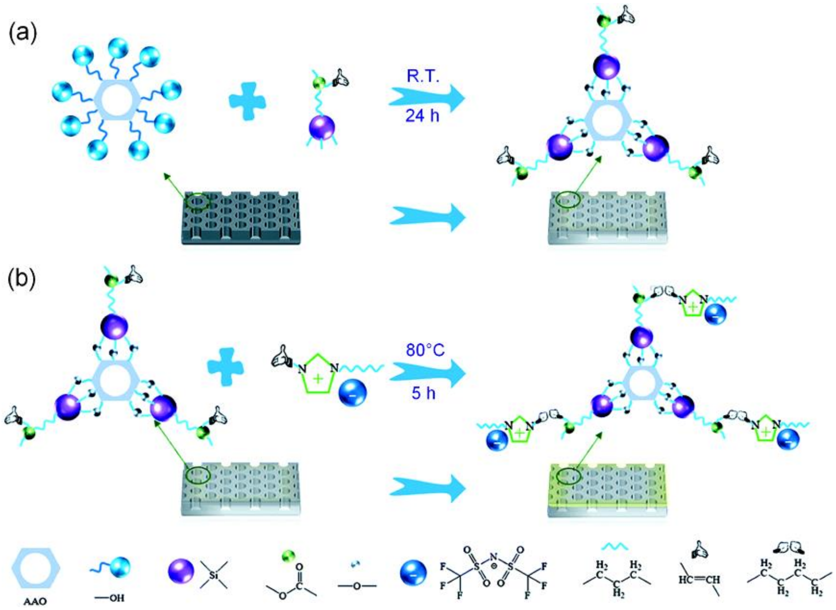

Fig. 41 Schematic of (a) silane couplers anchored on the AAO surfaces and (b) then the intermediates were chemically linked to ionic liquid *via* alkene polymerization. Reproduced with permission from ref. 471. Copyright (2020) The Royal Society of Chemistry.

4.3.2 Cross-linking

In addition to directly forming covalent bonds, cross-linking has also been introduced to increase the bonding density, which can further improve the bonding strength between liquid-repellent coatings and substrates. Cross-linking reactions can be triggered by adding cross-linking agents/catalysts, exposing to UV/plasma, *etc*. For example, Ye *et al*. synthesized 3-aminopropyltriethoxysilane functionalized hydrophobic SiO_2 nanoparticles (NPs) first, and then incorporated hexamethylene diisocyanate tripolymer (N3375) as a cross-linking agent into their mixture with hydroxyl acrylic resin, which was finally sprayed onto a glass slide and cured to prepare a superhydrophobic surface.[418] Owing to the formed cross-linked network structure (Fig. 42a), the resultant superhydrophobic surface could retain its water repellence after 30 cycles of sandpaper abrasion and 240 h of immersion in acid solution (pH = 1). Li *et al*. reported a method to prepare robust superhydrophobic surface by rapid UV cross-linking of superhydrophobic PDMS/SiO_2 coating onto a stretchable polyurethane acrylate (PUA) substrate.[472] As shown in Fig. 42b, pre-polymer of PUA was cured *via* UV irradiation to form stretchable matrix, while its surface remained uncured due to the oxygen inhibition when exposed to air during the photopolymerization. The uncured PUA surface provided abundant reactive sites for cross-linking of the sprayed superhydrophobic PDMS/SiO_2 coating under UV irradiation. The formed covalent cross-linking greatly enhanced the interface adhesion between the coating and substrate, which obviously improved the mechanical durability of the resultant superhydrophobic surface towards sandpaper abrasion and stretching-releasing.

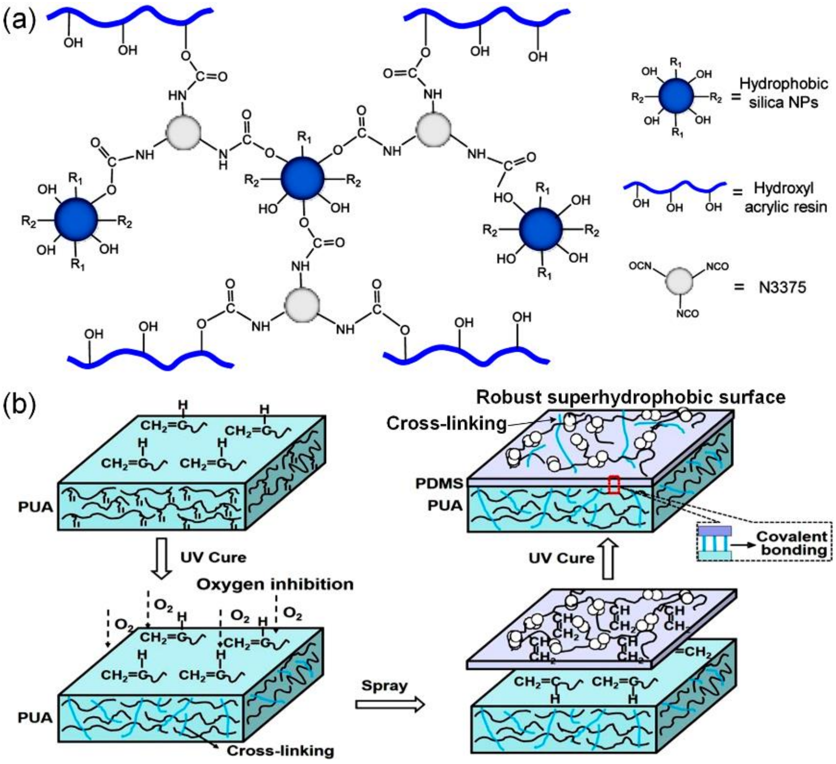

Fig. 42 (a) Cross-linked network structure among hydrophobic SiO_2 NPs, hydroxyl acrylic resin, and N3375. (b) Illustration of preparing a robust superhydrophobic coating by UV cross-linking. (a) Reproduced with permission from ref. 418. Copyright (2017) American Chemical Society. (b) Reproduced with permission from ref. 472. Copyright (2018) Elsevier B.V.

Chen *et al*. fabricated robust superhydrophobic cotton textile by a simple two-step dip-dry strategy.[473] The authors firstly dipped cotton fabric into homogeneous mixture of spherical SiO_2 particles with different diameters (100, 200 and 400 nm), and 3-aminopropyltriethoxysilane (APTES) in ethanol for 10 min. After drying at room temperature, the fabric was immersed into the mixture of PDMS prepolymer and its curing agent (mass ratio of 10:1) and 3-isocyanatomethyl-3,5,5-trimethylcyclohexyl isocyanate (IPDI) in *n*-hexane for 2 min, and then obtained the superhydrophobic cotton after curing at 120 °C for 2 h. The surfaces of the SiO_2 particles and cotton fabric were rich in −OH groups, enabling them to be easily cross-linked together *via* the assistance of the silane coupling agent. During the first dip-coating, the −OH groups generated by the hydrolysis of the C_2H_5O- groups of APTES acted as the linkage point and the −OH groups on the surface of SiO_2 particles were firstly bonded to the −OH groups of the silanol surface and then connected to the −OH groups of the cotton surface. The −OH groups dehydrated and condensed during high-temperature curing, making the SiO_2 particles combine with the cotton textile closely. In the second dip-coating procedure, IPDI was used as the cross-linking agent and its −NCO group was introduced into the condensation reactions with the −OH groups. During the heating assisted curing, the −NCO group reacted with the −OH group to form −NHCOO− group, enabling the formation of covalent bonds among the PDMS, the SiO_2 particles and the cotton textile. The covalent bonds imparted the superhydrophobic surface with outstanding mechanical durability (130 sandpaper abrasion cycles and 40 washing cycles) and chemical durability (immersion in strong acid, alkali, ethanol, toluene, hexane, acetone and boiling water for 24 h).

4.3.3 Adhesive layer assistance

Besides direct covalent bonding and cross-linking, an adhesive layer has also been widely employed to enhance the bonding strength between liquid-repellent coatings and substrates. The mechanisms of adhesive enhanced bonding are complicated, including intermolecular forces, chemical bonds, mechanical interlock, *etc*. Both commercial and lab-synthesized adhesives, such as epoxy resin,[343,474] PDMS,[363,475] and even glues and double-sided tapes,[54,218] have been reported to bond the coatings to improve the robustness and durability of the liquid-repellent surfaces. Zhou *et al*. prepared a robust superamphiphobic coating on fabric by immobilizing nanoparticles in the coating layer with a binding agent (Fig. 43a).[403] Two coating solutions, a nano particulate silica sol that was co-hydrolyzed from tetraethylorthosilicate and 1*H*,1*H*,2*H*,2*H*-perfluorodecyltriethoxysilane (PFDTS) in ethanol under alkaline condition, and a poly(vinylidene fluoride-*co*-hexafluoropropylene) (PVDF-HFP)/dimethylformamide solution containing PFDTS, were applied in sequence onto the fabric by the dip-coating method. The PVDF-HFP not only lowered the surface energy of the coating, but also served as a binder to immobilize the SiO_2 particles, hence rendering the superamphiphobic coating with impressive durability towards 600 cycles of standard machine laundry, 800 cycles of abrasion, 1 h of boiling water soaking, and 7 days of immersion in strong acid and base solutions. Recently, PVDF-HFP and polyethersulfone were used as adhesive layer to bond fluorinated palygorskite@SiO_2 composite to create a robust superamphiphobic surface.[476] Wu *et al*. reported robust superhydrophobic surfaces that were prepared by forming Ag nanoparticles (NPs) coated with the copolymer (polystyrene-*block*-poly(ethylene-*co*-butylene)-*block*-polystyrene: SEBS) *via* Ag precursor reduction and synchronous nonsolvent induced phase separation (Fig. 43b).[378] The SEBS significantly strengthened the interaction among individual Ag NPs and the bonding between Ag NPs and the substrate, thereby making the superhydrophobic surfaces robust against ultrasonic treatment, bending, and sandpaper abrasion. Later, SEBS was used to enhance the bonding between dimethyloctadecyl [3-(trimethoxysilyl) propyl] ammonium chloride modified SiO_2 nanoparticles and various flat substrates, which endowed the resultant superhydrophobic surfaces with outstanding robustness and durability to cyclic tape-peeling, falling sand impacting, sandpaper abrasion, scrubbing, concentrated acid/alkaline, high/low temperature and UV irradiation.[477]

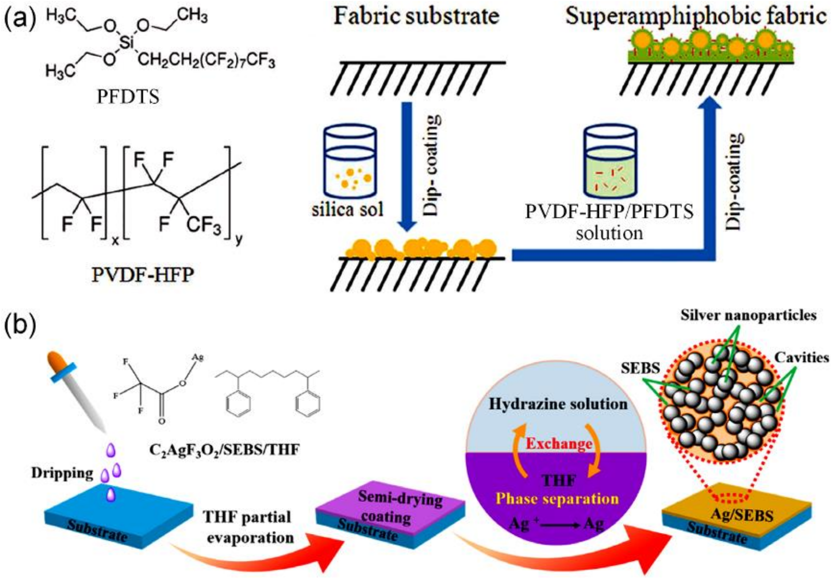

Fig. 43 Scheme of the preparation of (a) superamphiphobic fabrics with PVDF-HFP/PFDTS/SiO_2 coatings and (b) superhydrophobic SEBS/AgNP coatings. (a) Reproduced with permission from ref. 403. Copyright (2013) WILEY-VCH Verlag GmbH & Co. KGaA, Weinheim. (b) Reproduced with permission from ref. 378. Copyright (2019) American Chemical Society.

Lu *et al*. first proposed to promote the mechanical durability of superhydrophobic coatings by commercial adhesive enhanced bonding between the coatings and substrates.[54] A paint-like ethanolic suspension of perfluorosilane-coated TiO_2 nanoparticles was prepared and then sprayed, dipped, or extruded onto both hard and soft materials (*e.g.*, glass, steel, cotton wool, and filter paper) to create superhydrophobic surfaces (Fig. 44a, for example). The authors developed a method to enhance the bonding strength between the coatings and substrates by using commercial adhesives (*e.g.*, double-sided tape, spray adhesive), from which the weak inherent robustness of the superhydrophobic coatings was significantly overcome. The "paint + adhesive + substrate" strategy enabled the resultant superhydrophobic surfaces to retain their water repellency after finger wiping, knife scratching, and 40 abrasion cycles with sandpaper (Fig. 44b). Enlightened by this work, commercial adhesive or glue have been frequently used to construct robust and durable liquid-repellent surfaces.[295,478] For example, Chen *et al*. prepared mechanically robust superamphiphobic surfaces by bonding perfluorooctanoic acid modified copper particles onto various substrates (*e.g.*, glass, aluminum, rubber, scouring pad, filter paper and sponge) with double-sided tape or commercial spray adhesive.[218] Intensive falling sand abrasion (150 g of sand impacted on the coating from the height up to 70 cm) had little influence on the superamphiphobicity of the as-prepared surfaces, and a coated rubber could even retain both water and oil repellency after 50 stretch/release cycles.

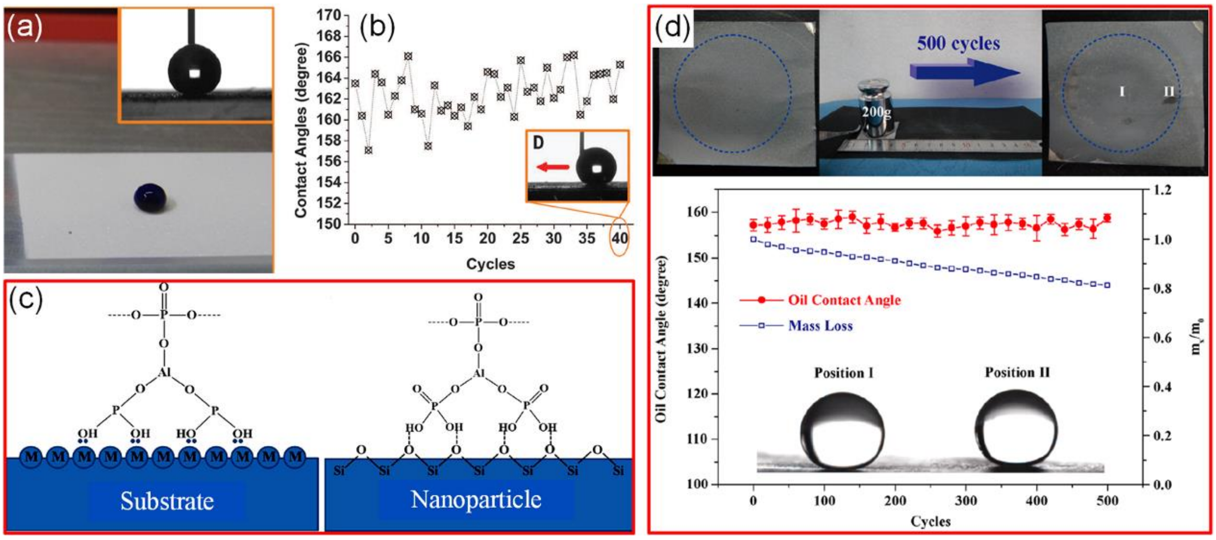

Fig. 44 (a) Superhydrophobic coating on glass slide, and (b) its robustness towards sandpaper abrasion. (c) Schematic of the interaction forces between the AP binder and substrate/nanoparticles. (d) Robustness of the underwater superoleophobic TiO_2-AP-treated SSM towards sandpaper abrasion. (a, b) Reproduced with permission from ref. 54. Copyright (2015) American Association for the Advancement of Science. (c, d) Reproduced with permission from ref. 244. Copyright (2019) American Chemical Society.

Besides the above-mentioned organic adhesives, inorganic adhesives have also been employed to enhance the bonding strength between liquid-repellent coatings and substrates. For example, Liu *et al*. developed robust underwater superoleophobic surfaces by spraying a composite suspension of nanoparticles and aluminum phosphate (AP) binder.[244] The spraying solution was prepared by mixing AP with nanoparticles in ethanol/water cosolvent. During heating-assisted curing process, the hydroxy groups of the AP binder favored condensation-polymerization reaction *via* intermolecular and intramolecular dehydration to form continuous network structures, and the hydrogen (or coordination) bonds between the functional groups of the AP binder and oxygen (or metal) atoms on the surfaces of the substrates created strong molecular attractive forces to increase the adhesion (Fig. 44c). This strategy was available for various nanoparticles (such as TiO_2, SiO_2, and Al_2O_3) and substrates (SSM, ceramic, and glass) to construct robust underwater oil-repellent surfaces. As shown in Fig. 44d, after 500 abrasion cycles by sandpaper, the underwater oil CAs of the TiO_2-AP-treated SSM retained above 150° and the mass loss of the TiO_2-AP coating was only ~ 20%. Sun *et al*. prepared a superamphiphobic coating by spray-coating of the suspension containing PFDTS-modified SiO_2 nanoparticles and AP. The coating showed remarkable mechanochemical robustness due to the adhesive layer enhanced bonding between the inks and substrate, and neighboring SiO_2 particles.[479] Xue *et al*. bound polystyrene nanoparticles onto cotton fibers with AP and then coated them with PDMS layer, finally yielding superhydrophobic cotton fabrics.[393] Due to the improved bonding strength between the fibers and nanoparticles, the prepared fabric surfaces showed excellent stability to acid, alkali, salt, organic solvents and UV exposure, and could tolerate 2000 cycles of abrasion by nylon fabric cloth under loading pressure of 45 kPa, or 35 cycles of intensive laundering.

Mussel-inspired adhesion that is mediated by 3,4-dihydroxyphenylalanine opens a new avenue for enhancing the bonding strength between coating and substrate,[480] and has also been frequently applied to fabricate robust and durable liquid-repellent surfaces.[481] By taking advantages of the self-polymerization of dopamine and dehydration polymerization of aluminum orthophosphate (AOP) binder, Lin *et al*. reported a robust and durable superhydrophobic coating with reinforced composite interfaces.[358] As depicted in Fig. 45a, they firstly coated polydopamine layer on carbon nanotubes (CNTs) under the assistance of tris(hydroxymethyl) aminomethane hydrochloride. The polydopamine provided active hydroxyl groups for the *in situ* grows of $Mg(OH)_2$ on CNTs when Mg^{2+} were introduced under alkaline conditions, and CNTs-polydopamine&MgO (CP&MgO) composite particles with improved interfacial compatibility were obtained after calcination at 500 °C for 2 h under nitrogen atmosphere. Finally, the CP&MgO suspension, AOP binder solution and PTFE emulsion were well-mixed and sprayed on various cleaned substrates and then cured at 380 °C for 20 min to yield superhydrophobic PTFE-CP&MgO-AOP coating. As shown in Fig. 45b, during the dehydration polymerization reaction between the CP&MgO particles and AOP binder, phosphate networks (CP&MgO-AOP) were formed through cross-linking and hydrogen bonding interactions, which not only enhanced the interfacial interaction among CP&MgO particles but also strengthened the interfacial binding force between the PTFE-CP&MgO coating and the substrates. Owing to the improved composite interfacial strength, the superhydrophobic PTFE-CP&MgO-AOP coating showed excellent mechanical durability, which could withstand more than 1.27×10^5 cycles Taber abrasion with a 1000 mesh friction wheel and a loading of 100 kPa, as well as knife-scratching, finger wiping, and tape peeling. Additionally, the AOP binder enabled reticular/coral-like composite structures and the chemical inert PTFE layer imparted the superhydrophobic surfaces with excellent chemical durability and long-term stability under water.

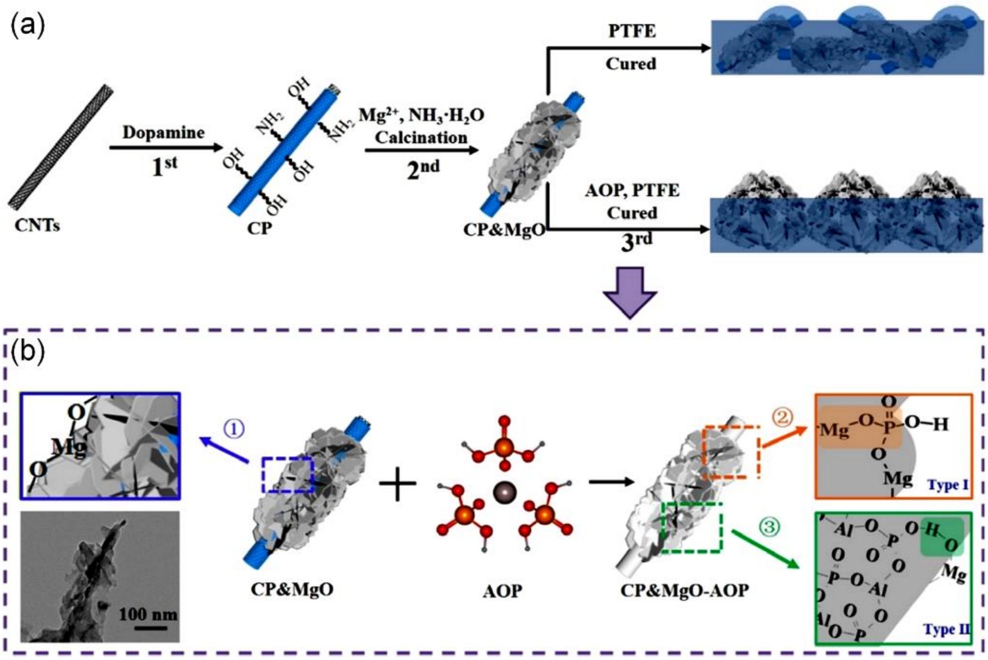

Fig. 45 Schematic illustration of (a) preparation and (b) molecular interaction of the superhydrophobic PTFE-CP&MgO-AOP coating. Reproduced with permission from ref. 358. Copyright (2019) American Chemical Society.

Apart from the consideration of adhesives themselves, optimizing the bonding between the adhesive layer and micro/nano particles has also been proposed in recent years to further improve the robustness of the liquid-repellent surfaces.[349,474] For example, Wu *et al*. proposed an inverse infusion method to construct extremely robust superhydrophobic hierarchical structures by using hydrophobic epoxy resin and Al_2O_3 nanoparticles (Fig. 46a).[349] They drop-casted an uncured fluorinated epoxy layer first on the substrate and then sprayed a nanocomposite coating containing fluorinated epoxy and Al_2O_3 nanoparticles, after which the uncured epoxy inversely infused into the micro/nanostructure and constructed a tougher microstructure on the top as well as a continuous nanocomposite layer throughout the coating after curing. Compared with the coating without inversely infused epoxy (*i.e.*, the drop-casted epoxy layer was fully cured before spraying the nanocomposite coating, as depicted in Fig. 46b), the inverse infusion processed hierarchical structures showed more robust superhydrophobicity, which could tolerate 600 cycles of tape peeling tests, 20 m sandpaper abrasion, 115 cycles of Taber abrasion, and 600 g of sand impact from a height of 110 cm. Zhao *et al*. proposed to improve the adhesive bonding and hierarchical textures of the spin-coated superhydrophobic coating by using hydrophobic/hydrophilic dual-sized SiO_2 nanoparticles (Fig. 46c).[474] Hydrophilic SiO_2 nanoparticles (200 nm) synthesized *via* Stöber method[482] and commercially available hydrophobic SiO_2 nanoparticles (55 nm) functionalized with $-O-Si-(CH_3)_3$ groups were mixed and coated on the substrate by epoxy resin bonding. They found that the combination of the hydrophobic SiO_2 and hydrophilic SiO_2 was essential in creating hierarchical structures, and the strong adhesion of hydrophilic SiO_2 (bottom of the coating film) to the substrates and porous structures of hydrophobic SiO_2 (top of the coating film) were crucial to form robust superhydrophobicity towards droplet impacting and tape peeling (Fig. 46d–f).

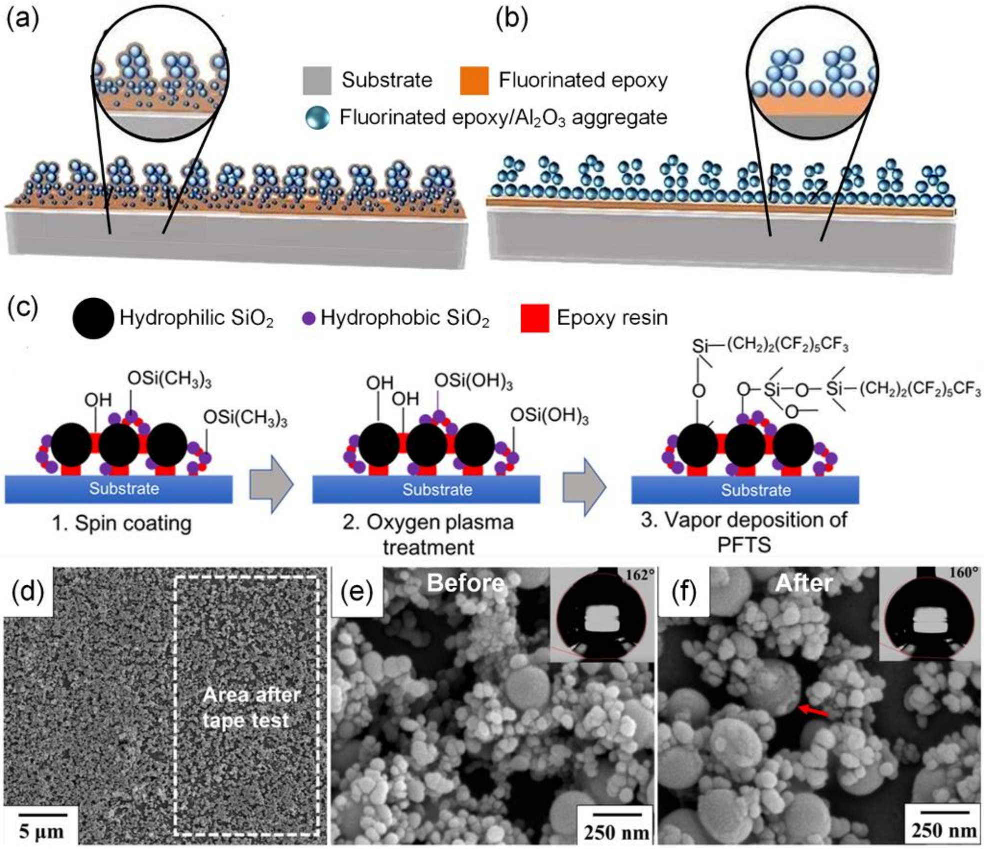

Fig. 46 Fabrication of the superhydrophobic epoxy resin/Al_2O_3 coating (a) with or (b) without inverse infusion process. (c) Schematic showing the fabrication of superhydrophobic coating with dual-sized hydrophilic/hydrophobic SiO_2 particles. (d–f) SEM images and corresponding water CA of the coating before and after tape-peeling. (a, b) Reproduced with permission from ref. 349. Copyright (2020) Elsevier B.V. (c–f) Reproduced with permission from ref. 474. Copyright (2020) Elsevier Inc.

4.4 Imparting Surface with Self-Healing Property

The aforementioned strategies extend the lifespan of liquid-repellent surfaces by improving their own robustness and durability; however, it is very challenging to withstand the continuously complex and intensive external damages. Endowing liquid-repellent surfaces with intelligent self-healing properties could be a promising method to address this issue. Taking the advantage of the self-healing property, robust and durable liquid repellence can be gained even the surfaces themselves are vulnerable to some damages. Up to now, self-healable surface chemistry, restorable microstructure, and their combination, have been reported to realize self-healing of liquid-repellent surfaces.[11,45,405]

4.4.1 Self-healable surface chemistry

When liquid-repellent surfaces are damaged mechanically or chemically, healing the surface chemistry may restore the lost liquid-repellence provided that the surface textures are adequate, which is inspired by those natural plants like Lotus leaves that can release new wax film to recover the damaged liquid repellence.[483] Subsequently, endowing liquid-repellent surfaces with self-healable chemistry that mainly depends on surface reorganization or chemical agents releasing is popular to improve both their mechanical and chemical durability.[220,330,484,485] In addition, this thermodynamically-driven process occurs spontaneously under most conditions and can be accelerated by heating, increasing air humidity, *etc*.[330] As illustrated in Fig. 47a, Li *et al*. prepared polymeric porous coatings with hierarchical structures by layer-by-layer assembly of polyelectrolyte complexes of poly(allylamine hydrochloride) (PAH) and sulfonated poly(ether ether ketone) (SPEEK) with poly(acrylic acid) (PAA), and finally obtained superhydrophobic coatings after chemical vapor deposition (CVD) of 1*H*,1*H*,2*H*,2*H*-perfluorooctyltriethoxysilane (POTS) layer.[486] Upon exposure to oxygen plasma, the deposited POTS layer was etched away and oxygen-containing hydrophilic groups were generated on the coating surface, leading the coating to be superhydrophilic. The interfacial surface energy difference between the plasma treated surface and the surrounding air would drive the covalently bonded hydrophobic POTS molecules underneath the treated area to migrate to the outer surface through rearrangement of polyelectrolyte chains, which enabled the coating to restore its superhydrophobicity after aging for only 4 h under a relative humidity of 40%. Later, Jin *et al*. reported robust superamphiphobic silica aerogels that could retain their liquid repellence after 100 mechanical abrasion cycles, which was attributed to the combined effect of the self-similar re-entrant topography of the silica aerogels and the self-healing of the fluorinated surfactant (Fig. 47b).[465] Liu *et al*. reported a mechanical stimuli induced self-healing of chemically damaged superhydrophobicity.[487] They prepared superhydrophobic textiles by coating polydopamine nanocapsules that were filled with hydrophobic agents such as octadecylamine and octadecanethiol. These trapped hydrophobic agents could be released under mechanical stimuli (*e.g*., stretching, compression, friction, and even mechanical washing), which favored the self-healing of the superhydrophobicity when it was damaged by plasma treatment (Fig. 47c).

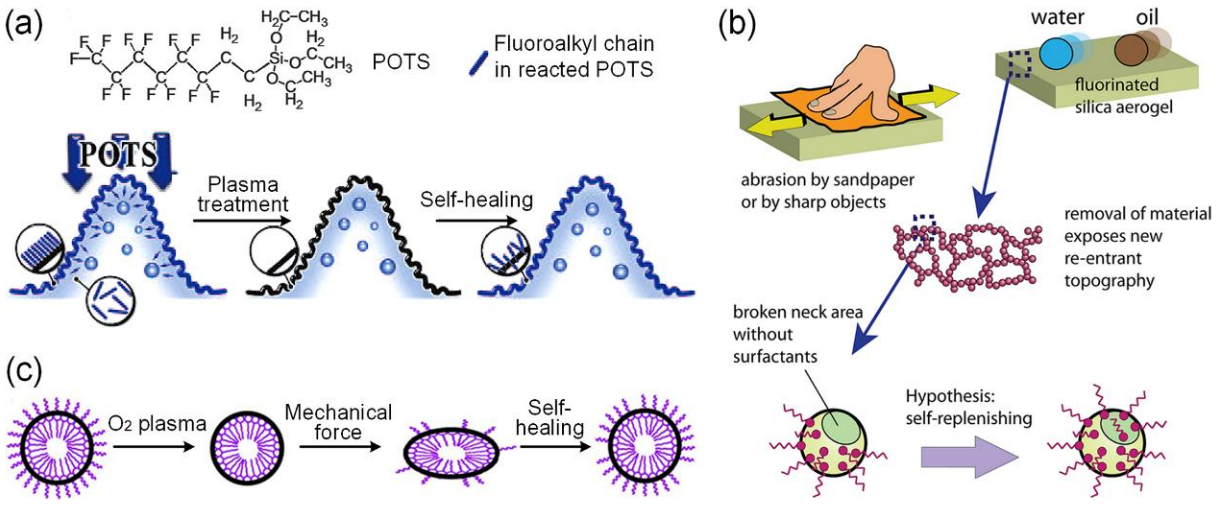

Fig. 47 (a) Self-healing mechanism of a plasma treated superhydrophobic coating. (b) Replenishing of fluorinated surfactant healed superamphiphobic surface. (c) Mechanical force enabled self-healing of a chemically damaged superhydrophobic surface. (a) Reproduced with permission from ref. 486. Copyright (2010) WILEY-VCH Verlag GmbH & Co. KGaA, Weinheim. (b) Reproduced with permission from ref. 465. Copyright (2013) American Chemical Society. (c) Reproduced with permission from ref. 487. Copyright (2015) American Chemical Society.

Compared with superhydrophobic and superoleophobic surfaces, SLISs are naturally self-healable due to the mobility of the infused lubricant.[20] However, lubricants are easily depleted or removed under some conditions like continuous water flow impacting or evaporation, even if the surface structures of the SLIS are well-designed.[275] In order to further improve the longevity and durability of SLIS, incorporating self-replenishable lubricant by using internal oil reservoirs could be a good choice.[488] Once lubricant layers are damaged, oils can continuously migrate from internal oil reservoirs to refill the damaged regions, and thus the self-healing function of SLIS is realized. For example, Liu *et al.* prepared robust and self-replenishing slippery lubricant-infused porous network surface (SLIPNS) for anti-icing applications.[56] The key structures of the SLIPNS were the microchannels and nanosheets, which worked as internal oil reservoirs and vessels, respectively. As a comparison, SLIS with only nanosheets was also synthesized. During multiple icing/de-icing cycles, it was found that more lubricant retained on the SLIPNS, which exhibited more stable performance than the SLIS. When oil depletion occurred on SLIS, only the interfacial lubricant film flowed into the damaged areas (Fig. 48a). By contrast, in terms of the SLIPNS, the lost oil could be supplemented by both top oil layer and interconnected microchannels (Fig. 48b). Similarly, owing to the self-healable lubricant layer, the water repellence of the SLIPNS retained almost unchanged after knife scratch, repeated icing/de-icing, and water flow impact. Yu *et al*. fabricated robust and self-healing SLIS by using modified hollow silica spheres as oil reservoirs *via* a spray-coating method.[271] The modified mesoporous silica particles were synthesized after vinyl-terminated PDMS was grafted on the external and internal sulfhydryl-modified hollow spheres *via* a thiol-ene click reaction. Consequently, lubricants could be locked or stored in hollow silica spheres due to its hollow cavity. When the lubricant layer was damaged, a certain amount of silicon oil could directly migrate from the inner wall to the surface of the modified hollow sphere to repair the defects under heat treatment. Li *et al*. reported another self-healing SLIS with superior self-replenishable lubrication by combining microstructured SLIS and nanostructured SLIS together (Fig. 48c), in which the square PDMS microwell was used as a reservoir to store sufficient lubricant and the PTFE nanofilm was employed as a skin to stabilize the thin lubricant layer.[489] Through the collaborative effect of capillary corner filament inside the microwell and wettability gradient between the microwell and the nanofilm, the lubricant stored in the microwells could be directionally and timely transported to replenish the nanofilm when the lubricant within the nanofilm was depleted. Therefore, compared with the square microwell SLIS or nanofilm SLIS alone, the combined SLIS possessed lower oil depletion and more stable water repellence towards long-term cooling, heating, and water droplets impinging, and thereby showing robust and durable liquid repellence. Additionally, they found that the corner structures of the square microwell were indispensable for complete oil self-replenishment from a single microwell to the upper nanofilm, while most oil would stay at the bottom of the circular microcavity (Fig. 48d), which lead to a much higher self-replenishing ratio of the lubricant in square microwell (> 95%) than that in circular microcavity (~ 50%).

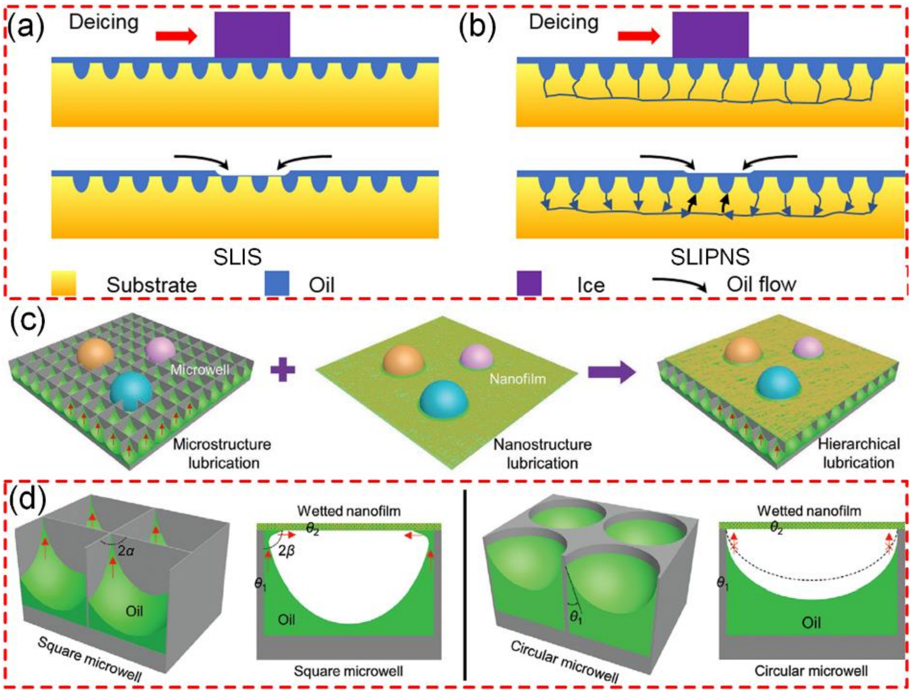

Fig. 48 Schematics for the replenishment mechanism of stored oil on (a) SLIS and (b) SLIPNS after oil depletion by de-icing. (c) Design scheme of the hierarchical self-replenishing SLIS that combines microstructured LIS and nanostructured LIS together. (d) Mechanism of oil self-replenishment in square microwell and circular microcavity. (a, b) Reproduced with permission from ref. 56. Copyright (2020) American Chemical Society. (c, d) Reproduced with permission from ref. 489. Copyright (2021) WILEY-VCH Verlag GmbH & Co. KGaA, Weinheim.

4.4.2 Restored topographic morphology

The surface morphologies of liquid-repellent surfaces can be changed under the action of mechanical force and chemical media, which lead to the loss of liquid repellence of different degrees. When the surface textures of liquid-repellent surfaces are distorted but not removed from the underlying substrates by external force, strategies like using elastic materials (*e.g.*, PDMS) and shape memory polymers (SMPs) can be used to recover the textures, and thereby restores the liquid repellence.

Elastic materials can deform actively when mechanical forces are applied on (*e.g.*, impacting, bending, twisting, compressing, and stretching), which avoids the fracture and removal of micro/nano structures; once the forces are withdrawn, the materials recover their original surface morphologies owing to the reversible deformation. Therefore, endowing the liquid-repellent coating and/or the underneath substrate with elasticity becomes a general method to improve their mechanical durability.[58,153,196,294,375,490] It was demonstrated that compared with rigid superhydrophobic surface, a water droplet impacting an elastic superhydrophobic surface showed a two-fold reduction in the contact time between the droplet and surface.[491] This was attributed to the distinct post-impacting kinetic-to-elastic energy conversion between the droplet and elastic substrate, which enabled the substrate to oscillate upon impacting, and then applied vertical momentum back to the droplet with a springboard effect during the droplet retraction, resulting in a rapid droplet bouncing with reduced contact time and an improved durability towards droplet impacting.

By mimicking the exoskeleton of insects, Hoshian *et al*. proposed a robust hybrid PDMS/TiO_2 superhydrophobic surface.[490] The authors firstly deposited a protective TiO_2 layer on a pre-roughened aluminum template by atomic layer deposition, which was then transferred to an elastic PDMS scaffold *via* sacrificial release etching. Without any further surface treatment, the resultant hybrid PDMS/TiO_2 replicas showed robust and durable superhydrophobicity towards mechanical abrasion, knife scratch, rubbing, bending, tape peeling, high temperature annealing, UV exposure, water jet impinging and long-term underwater storage (90 days). The robustness and durability resulted from a thick nanostructured elastic substrate that was conformally covered by a TiO_2 layer instead of a monolayer hydrophobic coating. As shown in Fig. 49a, the pure TiO_2 nanostructure was likely to be broken under mechanical stress, while the elastic PDMS structure alone would stick to itself due to self-adhesiveness. By contrast, for the hybrid PDMS/TiO_2 coatings, the TiO_2 nanostructures bended during mechanical contact and the elastic PDMS part allowed their recovery after unloading, while the TiO_2 film prevented the PDMS self-adhesiveness. Although TiO_2 film might break down into small pieces due to mechanical stress in the abrasion test, the elastic PDMS scaffold kept these pieces in place as the TiO_2 film was strongly adhered to the elastomer. Based on the similar strategy, they reported a robust PDMS/Cu superhydrophobic composite material that could withstand 1000 cycles of mechanical abrasion and 10,000 cycles of stretching and bending recently.[294]

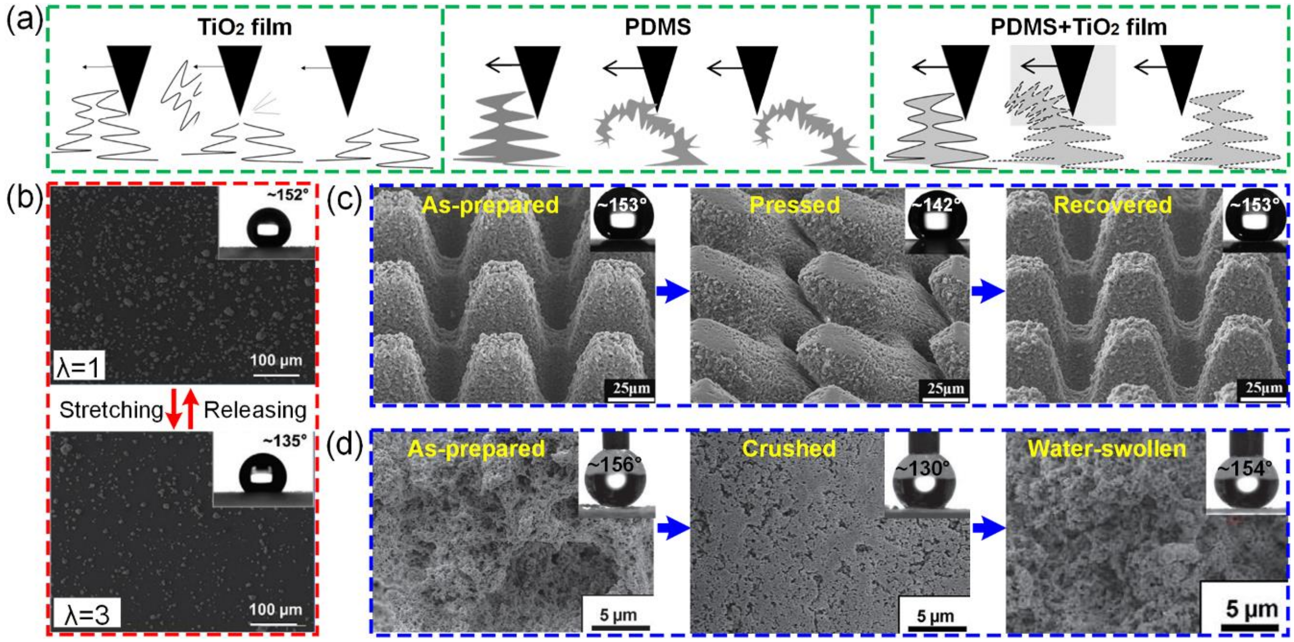

Fig. 49 (a) Schematic of elasticity enhanced robustness of superhydrophobic surface towards mechanical abrasion and knife scratching. (b) Micro/nanostructured elastomer film enhanced superhydrophobicity. (c) Recovery of the water repellence of SMP-based superhydrophobic surfaces. (d) Self-healing of the water repellence of superhydrophobic polymer coating *via* water-induced swelling. (a) Reproduced with permission from ref. 490. Copyright (2016) The Royal Society of Chemistry. (b) Reproduced with permission from ref. 153. Copyright (2020) Li *et al*. (c) Reproduced with permission from ref. 492. Copyright (2019) Elsevier B.V. (d) Reproduced with permission from ref. 493. Copyright (2013) WILEY-VCH Verlag GmbH & Co. KGaA, Weinheim.

As shown in Fig. 49b, when a hydrophobic TiO_2 nanoparticles coated elastic VHB 4910 film was equi-biaxially stretched with stretch ratio $\lambda = 3$, the micro/nanostructured TiO_2 clusters were diluted and the film thereby lost its superhydrophobicity, which could be easily recovered by releasing the film ($\lambda = 1$) due to its excellent elasticity.[153] Dai *et al*. fabricated a robust superhydrophobic film based on magnetic field-assisted *in situ* formation of PDMS microcilia arrays and subsequent swelling-assisted decoration of silica nanoparticles.[347] Due to the elasticity of the PDMS matrix and the robust adhesion of the silica nanoparticles, the as-prepared film showed robust super water repellence towards finger rubbing, ultrasonic treatment, cyclic compression, high-speed water jet impacting, tape peeling, sandpaper abrasion, as well as periodical linear stretching, bending, twisting and squeezing.

SMPs have been employed to construct self-healing liquid-repellent surfaces based on the shape memory effect originating from external-stimulus-dependent molecular chain configuration and mobility.[494,495] For example, Bai *et al*. prepared superhydrophobic surface on various thermal-responsive SMPs by femtosecond laser texturing and subsequent fluoroalkylsilane treatment.[492,496] After being heated and pressed, the surface lost its superhydrophobicity due to the surface topography deformation, which could be regenerated through a simple reheating at 80 °C for ~ 3 min (Fig. 49c).

Besides, Manna *et al*. reported a healable superhydrophobic surface based on liquid water-induced swelling of polymer coating.[493] They deposited porous rough polymer multilayers by layer-by-layer assembly of branched poly(ethyleneimine) (PEI) and the amine-reactive polymer poly(vinyl-4,4-dimethylazlactone) (PVDMA), and the coating became superhydrophobic (water CA of 156°) after treating with *n*-decylamine (Fig. 49d). After being crushed with a glass slide under a pressure of ~ 6.4 MPa for 1 min, the micro/nano-scale features were completely damaged, and the water CA decreased to ~ 130°. However, when the crushed sample was immersed in deionized water for 1 h and then dried under vacuum, the topographic features were almost completely regenerated and superhydrophobicity was restored. Moreover, this recovery process was substantially faster when the crushed films were incubated at low pH (*e.g.*, a complete recovery was realized within 60 s in 200 mM acetate buffer with pH of 3), which was probably due to the protonation of the amines of the PEI component speeding up the swelling of the polymer coating.

However, if the surface textures are removed (*e.g.*, by abrasion), regeneration of the rough structures under suitable external stimuli may be effective in healing the liquid repellence. For instance, Wang *et al*. reported thermo-induced self-healing of superhydrophobic coating prepared by using self-assembled flaky micro/nano structures of cellulose-derived phase-change nanocrystals.[497] The authors firstly hydrolyzed microcrystalline cellulose by using hydrochloric acid to extract cellulose nanocrystals (CNCs), which were then modified with 10-undecenoylchloride in pyridine under heterogeneous reaction conditions to synthesize undecenoated cellulose nanocrystals (UCNCs), and then 1-octadecanethiol was grafted in the shell layer of the UCNCs containing terminal vinyl groups *via* thiol-ene reaction to prepare 1-octadecanethiolated UCNCs (C18-UCNCs) (Fig. 50a). The C18-UCNCs possessed a distinct core-shell structure: the cellulose crystalline core retained the basic structure and the soft shell containing octadecyl chains allowed phase transition. During the evaporation from its tetrahydrofuran suspension, the phase transition of the C18-UCNCs shell led to the formation of self-assembled flaky micro/nano structures with superhydrophobicity (Fig. 50b), by which both self-standing C18-UCNCs films and coatings on other substrates with super water repellence could be obtained. The assembled flaky hierarchical structures showed limited mechanical durability towards abrasion by 800 mesh sandpaper under loading of 50 g and an abrasion length of 20 cm, and the damaged structures decreased the water CA of the self-standing film from ~ 160° to ~ 115° (Fig. 50c). After heating the damaged films at 80 °C for 30 min, cooling down, and aging at room temperature for 24 h, the flaky hierarchical structures regenerated and the films restored their superhydrophobicity (Fig. 50d), and the abrasion-healing process could be repeated for more than 10 cycles.

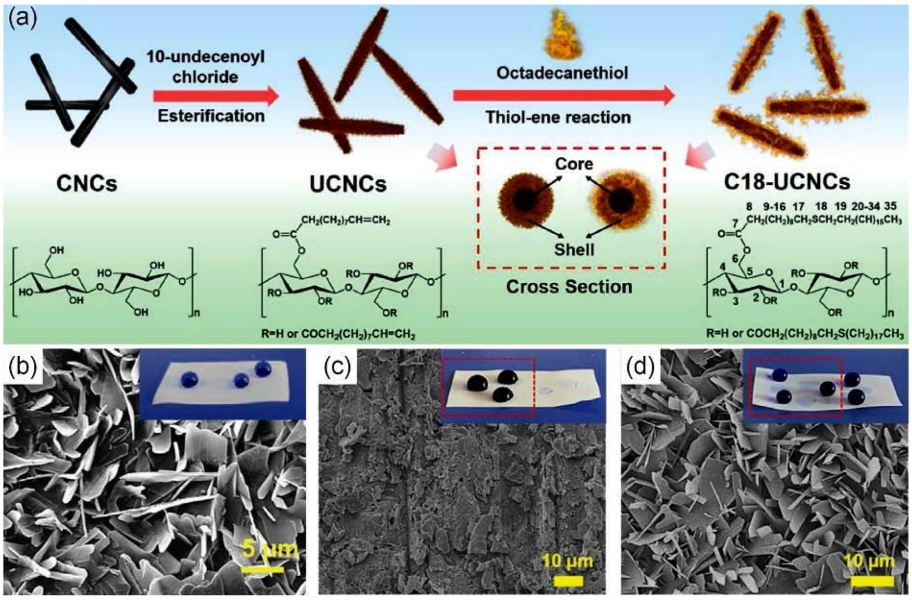

Fig. 50 (a) Schematic of the synthesis of C18-UCNCs from UCNCs *via* the thiol-ene reaction with 1-octadecanethiol. SEM images of (b) the as-prepared, (c) sandpaper abrasion damaged, and (d) self-healed C18-UCNCs film. The insets showed dyed water droplets on the corresponding film. Reproduced with permission from ref. 497. Copyright (2020) Wang *et al*.

Moreover, in terms of macroscopic ruptures (*e.g.*, by knife cutting) on liquid-repellent materials, the reforming effect of coordination bonds could be used to heal the cracks and subsequently the liquid repellence.[198,498,499] Jin *et al*. prepared a self-healing SLIS *via* cross-linking of dopamine-armed Fe_3O_4 nanoparticles, diethylenetriamine, and glycidyl methacrylate-*co*-polydimethylsiloxane propyl ether methacrylate, and subsequent silicone oil swelling.[500] As depicted in Fig. 51a, owing to the photothermal effect of Fe_3O_4 nanoparticles, reversible Fe-catechol coordination, and reconfigurable lubricant layer, the cracked SLIS could be recovered after being irradiated with sunlamp for 2 h and sequentially healed for 10 h under ambient conditions (Fig. 51b). Shan *et al*. prepared a self-healing superhydrophobic surface by spraying polystyrene (PS) and SiO_2 particles on a layer of cross-linked PDMS-based silicon elastomer containing imidazole-zinc coordination bonds.[499] The imidazole group had strong coordination ability towards metal ions (*e.g.*, Zn^{2+}), and the pendant structure imparted the imidazole group and PDMS chains with high mobility, which enabled the coating to recover its topographic structures and thus super water repellence within 20 min at room temperature when it was damaged by knife-induced ruptures (Fig. 51c).

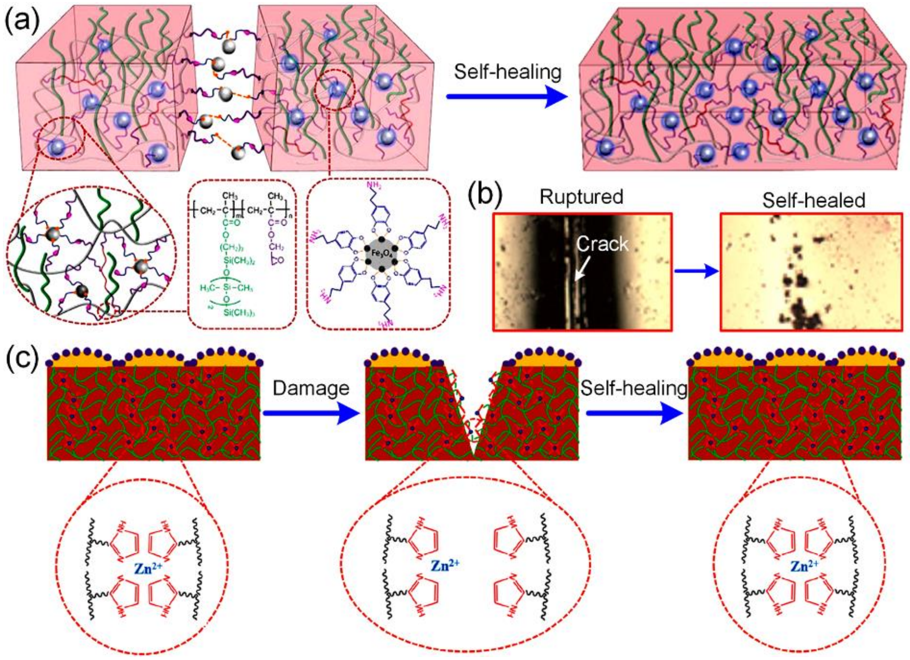

Fig. 51 (a) Schematic of the self-healing of the ruptured SLIS. (b) Images of the ruptured and self-healed SLISs. (c) Self-healing mechanism of the superhydrophobic coating *via* bond reforming. (a, b) Reproduced with permission from ref. 500. Copyright (2017) American Chemical Society. (c) Reproduced with permission from ref. 499. Copyright (2020) The Royal Society of Chemistry.

4.4.3 Self-healing of both surface chemistry and morphology

Based on the above two aspects, liquid-repellent surfaces with both self-healable surface chemistry and restorable microstructure have also been developed to address their robustness and durability.[501-503] For example, Pan *et al*. reported a self-healable superhydrophobic surface that composed of SMP micropillars decorated by pH-responsive capsules encapsulated with fluoroalkylsilane (Fig. 52).[503] As shown in Fig. 52a, they firstly prepared pH-responsive dodecafluoroheptyl-propyl-trimethoxysilane (FAS12, $C_{13}H_{18}F_{12}O_3Si$) encapsulated microcapsules by polymerizing milky emulsion containing 2-(diethylamino)ethyl methacrylate (DEAEMA), 1,6-hexanediol diacrylate (HDDA), benzoin isobutyl ether (BIE), FAS12 and sodium dodecyl sulfate (SDS) under UV exposure. Then the microcapsules decorated epoxy-based SMP micropillars were fabricated *via* mold replication method, which showed super water repellence with water CA of 153° and SA of 7°. Owing to the shape memory effect of the micropillar and the encapsulated agent of FAS12, the prepared superhydrophobic surface could not only restore the crushed surface textures by heat, but also heal the damaged surface chemistry under the assistance of acid stimuli (Fig. 52b).

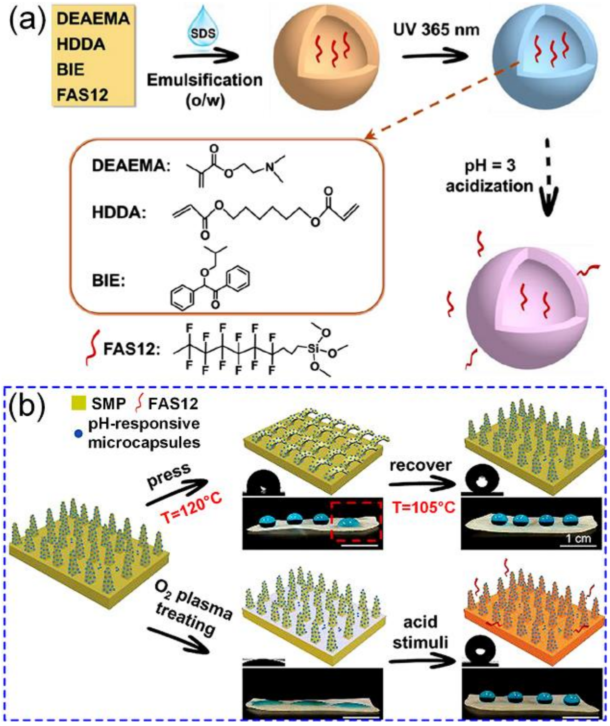

Fig. 52 (a) Synthesis of pH-responsive microcapsules encapsulated with FAS12. (b) Superhydrophobic surface with self-healing property on both surface chemistry and morphology. Reproduced with permission from ref. 503. Copyright (2020) American Chemical Society.

Recently, Yu *et al*. prepared a robust and durable slippery film with lubricant self-replenishing and morphology self-healing properties by encapsulating silicone oil into thermoplastic elastomers.[504] As shown in Fig. 53a, polysiloxane-polyurea elastomer composite silicone oil (PDMS-IPDI@Oil) was firstly synthesized by a polycondensation reaction between aminopropyl-terminated polydimethylsiloxane (NH_2-PDMS-NH_2) and isophorone diisocyanate (IPDI) in tetrahydrofuran solution containing silicone oil. Then, the terminal −NH_2 groups of the PDMS-IPDI@Oil further reacted with the −CHO groups of the chain extender terephthalic aldehyde (TPAL) to yield PDMS-IPDI@Oil with dynamic imine bond (named as PDMS-IPDI-TPAL@Oil). Due to the reversible cleavage and reconstruction of the imine and hydrogen bonds, the damaged crack could be restored *via* bonds recombination (Fig. 53b). In addition, as shown in Fig. 53c, when the oil film was wiped off the surface by paper towel, the lubricant stored in the oil storage capsules could be easily released by applying 500 g of pressure on the surface, which enabled quick replenishing of the lubricant layer to recover the liquid repellence.

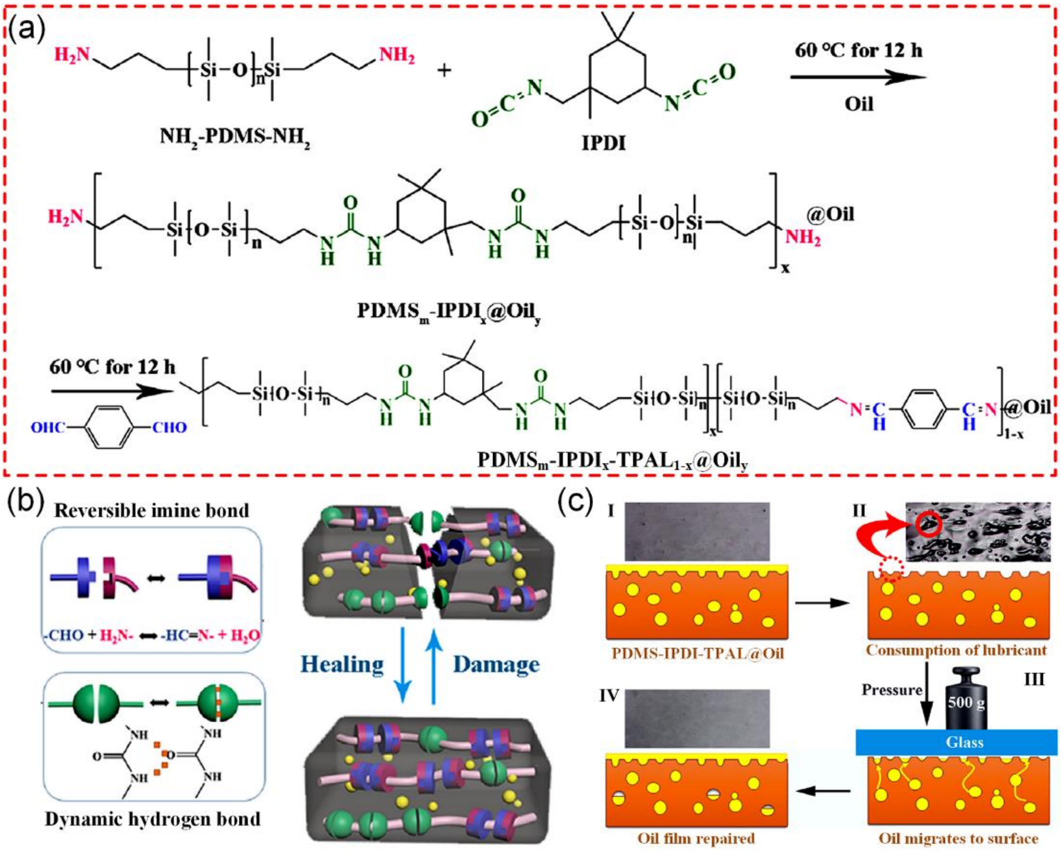

Fig. 53 (a) Synthetic routes, (b) matrix self-healing, and (c) lubricant self-replenishing of the slippery PDMS-IPDI-TPAL@Oil. Reproduced with permission from ref. 504. Copyright (2021) American Chemical Society.

5 Applications of Robust and Durable Liquid-Repellent Surfaces

As the research of liquid-repellent surfaces has rapidly developed in the past two decades, the application of these surfaces has also been greatly broadened to various fields like aviation, navigation, chemical industry, biomedicine, energy and environment. In this section, some typical applications of robust and durable liquid-repellent surfaces, including protection of substrate, liquid/gas harvesting/transport/manipulation, immiscible liquids separation, electricity generation, and enhanced heat transfer are introduced.

5.1 Protection of Substrate

Liquid-repellent surfaces can always decrease solid-liquid contact area and contact time, which enables the surfaces to be capable of protecting the underneath substrate from being contaminated, fouled, corroded, or covered with ice. Here we firstly focus on the application of robust and durable liquid-repellent surfaces towards anti-corrosion, anti-fouling, and ice-phobicity.

5.1.1 Anti-corrosion

Corrosion of metallic substances and their alloys in humid or hypersaline environments has caused waste and unsatisfactory strength of materials, environmental contamination and tremendous economic loss.[32,505] Casting a robust physical barrier between substrates and corrosive medium (*e.g.*, H_2O, O_2 and chloride ions) has been recognized as an effective strategy to inhibit corrosion at the interface.[32,506] Superhydrophobic surfaces, superoleophobic surfaces and SLISs have attracted great interests because they can effectively protect metal surfaces from being corroded.[32,506,507]

In terms of superhydrophobic and superamphiphobic surfaces, the anti-corrosion mechanism is where the air trapped in micro/nanostructures of superhydrophobic or superamphiphobic substrates protect surfaces from external environments. For example, Wang *et al.* endowed a magnesium alloy with robust hydrophobicity and corrosive resistance through chemical etching, zinc deposition and hydrophobic modification of ethanolic stearic acid solution.[508] On exposure to corrosive saline solution (3.5 wt% NaCl solution) and humid atmosphere (relative humidity of ~ 90%), superhydrophobic samples were hardly corroded until 12 hours and 96 hours, respectively. The anti-corrosion mechanisms include (1) air film prevents interaction of corrosive ions and substrates (Fig. 54a), and (2) superhydrophobic surfaces restrain the formation of an electrolyte film (Fig. 54b). After a tape peeling test, superhydrophobic surfaces retained their robustness and exhibited no delamination or detachment. Su *et al.* prepared superhydrophobic coatings on copper substrates as effective corrosion barriers through a nickel electrodeposition approach and subsequent hydrophobization.[509] The as-prepared superhydrophobic surface remained robust after mechanical damage (hardness and mechanical abrasion) and chemical erosion (acid and alkaline). Li *et al.* reported the corrosion resistance of a superhydrophobic layer on aluminum alloy substrates *via* a hydrothermal treatment in a $La(NO_3)_3$ solution and subsequent hydrophobic modification by dodecafluoroheptyl-propyl-trimethoxylsilane.[510] The superhydrophobic surfaces showed little change after being immersed in 3.5 wt% NaCl solution for 48 h and the water CA remained above 150°. The water CAs of the as-prepared surfaces were almost unchanged after being placed in air for 80 days, being exposed to a 250 °C atmosphere or being under UV irradiation for 24 h, and were above 150° after NaCl corrosion and abrasion. The strong bonding between lanthanum hydroxide and hydrophobic molecules formed during hydrothermal process, and hydrophobic lanthanum oxide contributed to sustaining the robustness of the resulting surfaces in harsh environments. Li *et al.* developed hydrophobic coatings with passivation ability for corrosion resistance of carbon steel using polyether sulfone (PES), potassium titanate whisker (PTW), nanoscale SiO_2 and 1*H*,1*H*,2*H*,2*H*-perfluorooctyltriethoxysilane *via* a spraying method.[511] Atomic oxygen was produced by oxygen vacancies on the surface of reduced potassium titanate whisker (RPTW) and then reacted with iron to generate passive films on carbon steel. Corrosive medium permeated micro-defects, voids, and cavities to the surface of carbon steel and then led to the corrosion of substrates (Fig. 54c). Despite of the existence of passive films, the electrolyte could still pass though the coatings and subsequently damage the passive film after long-term immersion (Fig. 54d). With the cooperative effect of passive film and air cushion, superhydrophobic layers were able to prevent the permeation of corrosive solution containing water and chloride ions (Fig. 54e).

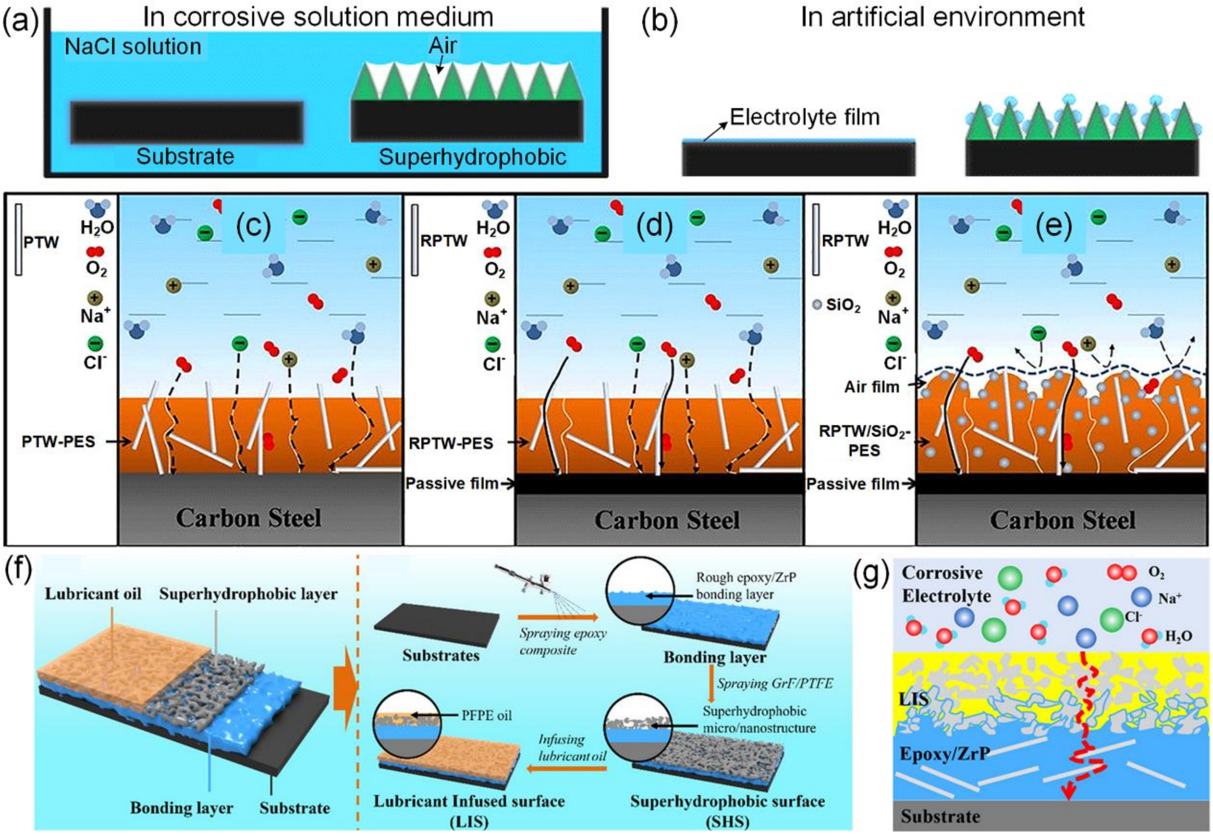

Fig. 54 (a, b) The scheme of anti-corrosion mechanisms of superhydrophobic surfaces in corrosive solution and artificial environments. (c–e) Corrosion protection mechanism of superhydrophobic coatings. (f) Schematic of the preparation and (g) anti-corrosion mechanism of SLIS. (a, b) Reproduced with permission from ref. 508. Copyright (2013) Elsevier B. V. (c–e) Reproduced with permission from ref. 511. Copyright (2019) American Chemical Society. (f, g) Reproduced with permission from ref. 512. Copyright (2021) American Chemical Society.

With similar water-repellent property to superhydrophobic surfaces, superamphiphobic surfaces are used as a durable barrier film for protecting metal surfaces from corrosion.[64,204] For example, Wei *et al.* revealed different anti-corrosion properties of superhydrophobic and superamphiphobic coatings for metal protection under different volumes of NaCl droplets.[367] Superhydrophobic hexadecyl polysiloxane modified SiO_2 nanoparticles (HD-POS@SiO_2) and superamphiphobic perfluorodecyl polysiloxane modified SiO_2 nanoparticles (PF-POS@SiO_2) were coated on magnesium alloy that was pretreated with epoxy paint (EP) *via* a spray-coating method, respectively. For water droplets larger than 0.9 μL, superhydrophobic and superamphiphobic coatings displayed the same wettability; hence superamphiphobic coatings showed better water repellent properties when water droplets were smaller than 0.9 μL. This was attributed to the lower surface energy of C−F in PF-POS@SiO_2 nanoparticles than that of C−H groups in HD-POS@SiO_2 nanoparticles. When small NaCl droplets adhered stably on the superhydrophobic coating, water (or vapor), oxygen and chloride ions diffused through the coating and then seriously eroded the metal substrates. However, affected by low-surface-energy C−F groups in PF-POS@SiO_2 coatings, NaCl micro-droplets rolled off from the surface easily, the limited contact time and area between the NaCl droplets and superamphiphobic surface contributed to restricting the diffusion of corrosive medium effectively. In addition, robust superamphiphobic coatings could retain remarkable anti-corrosion performance after long-term immersion and neutral salt spray test.

For SLISs that are applied in metal corrosion protection, the mechanism was similar to that of superhydrophobic surfaces, the air cushion trapped in hierarchical surfaces is replaced by a lubricant film.[32] For example, Sun *et al.* reported robust SLIS with excellent anti-corrosion performance *via* mimicking *Nepenthes* pitcher plant.[512] The SLIS were prepared as follows: α-zirconium phosphate (ZrP)/epoxy suspensions were coated on different substrates, followed by construction of superhydrophobic PTFE/graphite fluoride (GrF) micro/nanostructure layer, and perfluoropolyether (PFPE) infusion (Fig. 54f). The water CA and SA were respectively ~ 118° and ~ 2.3°, and the cetane CA was ~ 61°, and thus the oil layer possessed water resistance as well as resisted liquids with low surface tension. The impedance modulus of SLIS-coated steel ($|Z|_{f\,=\,0.01\ \mathrm{Hz}} = 9.96 \times 10^{7}\ \Omega\cdot\mathrm{cm}^{2}$) was much higher than pure steel ($|Z|_{f\,=\,0.01\mathrm{Hz}} = 8.89 \times 10^{2}\ \Omega\cdot\mathrm{cm}^{2}$), demonstrating a good anti-corrosion property. The corrosion protection mechanisms of the SLIS are (i) chemically inert and low-surface-energy hydrophobic layer (PTFE/GrF) prevented the invasion of corrosive medium, (ii) ZrP plates prolonged the pathway of the corrosive medium to the substrate (Fig. 54g). Besides, SLIS coatings kept robust and still displayed water CA of > 110° and SA of < 10° even after 30-day immersion in acidic and alkali solutions. Chen *et al.* developed slippery surfaces coated on porous aluminum oxide for corrosion resistance using environmentally friendly ionic liquid *via* a polymerization process.[471] With the assistance of capillarity and intermolecular interaction, low-surface-energy ionic liquid and porous surfaces were interacted firmly, leading to the stability of solid-liquid interfaces. The as-prepared surfaces (E_{corr} = –0.701 V, I_{corr} = –8.71 A cm^{-2}) exhibited a better corrosion resistance than pristine aluminum oxide surfaces (E_{corr} = –0.764 V, I_{corr} = –6.897 A cm^{-2}). Additionally, slippery ionic liquid-infused surfaces exhibited outstanding temperature stability and stability of resistance to shear stress.

Generally, owing to better stability of the infused lubricant layer in comparison with the air cushion, SLISs have been demonstrated to be more effective in anti-corrosion than superhydrophobic and superoleophobic surfaces.[513-515] For example, Zhang *et al*. compared the anti-corrosion property of superhydrophobic surface and SLIS.[514] Chemical etching of an aluminum alloy in aqueous $FeCl_3$ solution and PFDTS modification enabled the preparation of the superhydrophobic surface, and subsequent perfluoropolyethers lubricant infusion yielded the SLIS. Corrosion inhibition evaluation showed that the SLIS retained its original anti-corrosion ability after immersing in 3.5 wt% NaCl aqueous solution for 7 days, while the superhydrophobic surface almost lost its corrosion resistance.

5.1.2 Anti-fouling

Anti-fouling surfaces show significant roles in a wide range of areas, such as medical devices, maritime industries, and food packaging.[516] Nature inspired liquid-repellent surfaces, including superhydrophobic surfaces, underwater superoleophobic surfaces, and SLISs have been employed to protect the underlying substrates from being contaminated by foulants such as protein, bacterial, algae, and blood, enabling liquid-repellent surfaces to be potentially employed in biomedical and marine applications, *etc*.[517] This section introduces the application of liquid-repellent surfaces in anti-fouling.

Superhydrophobic surfaces have been successfully used for inhibition of foulants due to the trapped air "cushion" prevents intimate contact between the surfaces and aqueous solutions containing foulants.[517-519] For example, Leibner *et al*. found that a superhydrophobic expanded PTFE surface showed negligible adsorption towards human serum albumin, which was, however, totally changed after being evacuated to remove the trapped air prior to contact with protein solutions.[520] Similarly, the effect of air "chshion" on preventing protein adsorption was also verified on a superhydrophobic/superhydrophilic patterned surface with TiO_2 nanotubes.[521] Dou *et al.* investigated wettability regulated Gram-positive bacteria adhesion on bioinspired hierarchical structures duplicated from rose petal structures whose surface wettability were then tuned from superhydrophilicity to superhydrophobicity by changing the interfacial chemical composition of the self-assembled films from supramolecular gelators.[522] Results demonstrated that the Gram-positive bacteria adhesion was crucially mediated by peptidoglycan (PGN) due to its different interaction mechanisms with the surfaces (Fig. 55a). Owing to the tightly bound water layer on the superhyrophilic surface, weak H-bonded driving force between PGN and the surface enabled a 0.32 ng cm^{-2} adsorption of PGN. Increased H-bonding interaction on hydrophilic surface and hydrophobic interaction on hydrophobic surface resulted in 1.86 ng cm^{-2} and 2.12 ng cm^{-2} adsorption of PGN on hydrophilic surface and hydrophobic surface, respectively. By contrast, the trapped air "cushion" on superhydrophobic surface minimized the hydrophobic interaction area between PGN and the surface, leading to the best bacteria adhesion resistance with PGN adsorption of only 0.11 ng cm^{-2}. Wang *et al*. prepared micro/nanoscale diamond films on different substrates *via* CVD and self-assembly seeding method, and showed that compared with flat diamond coatings, the superhydrophobic hierarchical diamond coatings showed better anti-fouling performances towards bacterial and marine algae.[179]

Superhydrophobic surfaces also showed enhanced anti-blood-adhesion ability, making them promising in enhancing the hemocompatibility of blood-contacting devices and implants (*e.g.*, wound dressing, catheter, endoscopes and stents).[39,523-527] Blood is a challenging liquid to repel due to its easily-activated intrinsic hemostatic mechanisms, induction of coagulation, and platelet activation upon contact with foreign incompatible surfaces.[39] Jiang *el al*. prepared superhydrophobic TiO_2 coatings on biomedical Ti-6Al-4V alloys *via* micro-arc oxidation technique and subsequent surface fluorination by 1*H*,1*H*,2*H*,2*H*-perfluorooctyl-trichlorosilane, by which the *in vitro* hemocompatibility of the alloy was greatly improved since the superhydrophobic coatings reduced the hemolysis ratio and platelets adhesion effectively.[523] Nokes *et al*. investigated the blood coagulation on superhydrophobic plastics that were constructed by roll-to-roll shrinking of a pre-stressed thermoplastic.[524] Results showed that the superhydrophobic surface minimized blood adhesion, leading to significantly reduced blood coagulation compared to flat surface (> 5 times reduction after 50 min testing) without the need of anticoagulants, as depicted in Fig. 55b. Bartlet *et al*. prepared superhydrophobic TiO_2 nanotube array surfaces by anodization, annealing, and low surface energy modification, and evaluated their hemocompatibility.[525]

Results showed that compared with original Ti and unmodified TiO_2 nanotube arrays surfaces, the superhydrophobic nanotube arrays surfaces effectively reduced albumin and fibrinogen adsorption, human platelet rich plasma cell adhesion, and platelet activation. By focusing mainly on platelet anti-adhesion, Jokinen *et al*. proposed that superhydrophobic surfaces repel blood because they can (i) reduce the effective area exposed to platelets, (ii) reduce the adhesion area available to individual platelets, (iii) reduce platelet adhesion *via* hydrodynamic slip effects, and (iv) reduce or alter protein adsorption in a way that is not conducive to thrombus formation.[39] However, most of the above-mentioned results are obtained from *in vitro* studies, and the *in vivo* testing of the anti-blood-adhesion property and medical safety aspects of superhydrophobic surfaces are rarely focused on,[375,527,528] and more in-depth *in vivo* studies are required to fill the largely unknown area in the future.

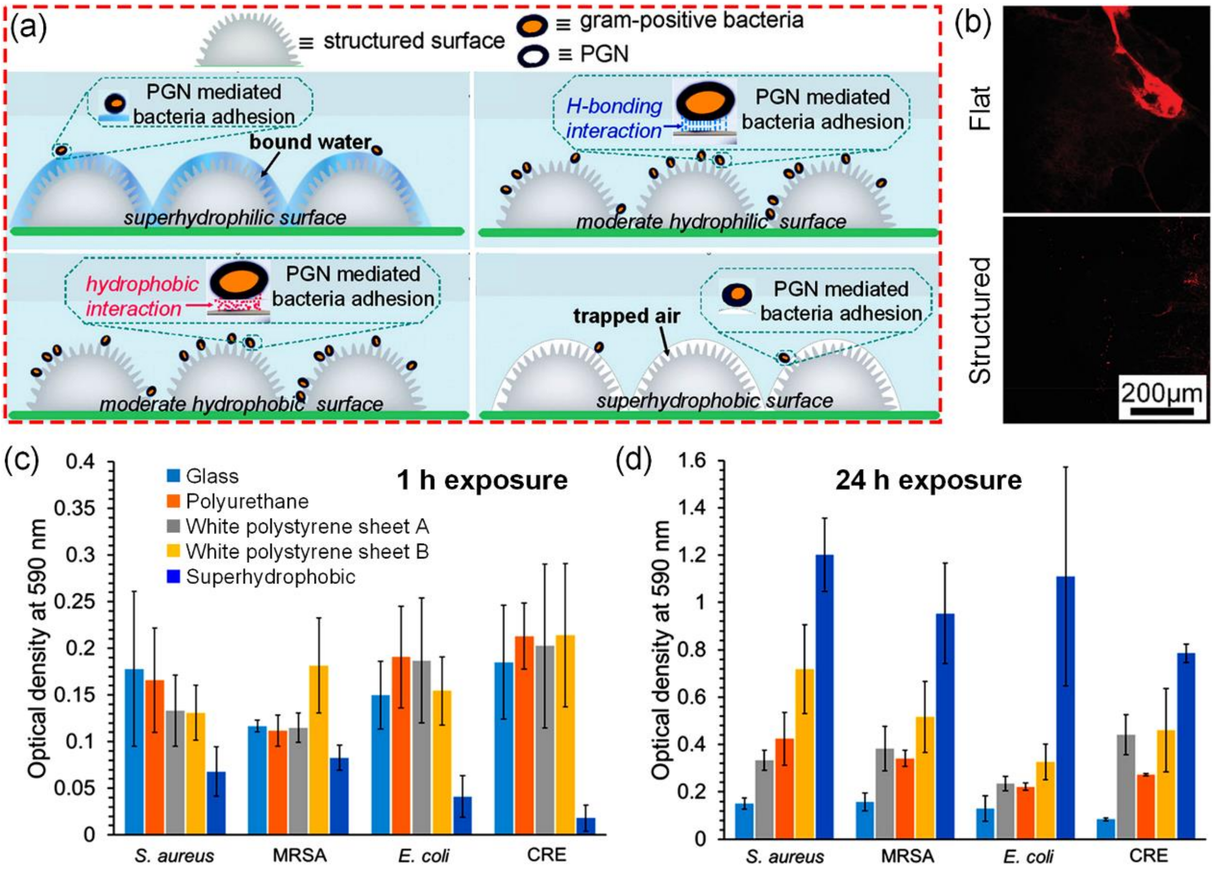

Fig. 55 (a) The mechanism of peptidoglycan (PGN) mediated Gram-positive bacterial adhesion on superhydrophilic, superhydrophobic, and moderate hydrophilic and hydrophobic surfaces. (b) Fluorescently labeled fibrinogen shows blood coagulation on the flat and structured superhydrophobic surfaces for 50 min, indicating significantly reduced blood coagulation on the superhydrophobic surfaces. Comparison of bacterial attachment to various surfaces after (c) 1 h and (d) 24 h exposure to BHI broth. (a) Reproduced with permission from ref. 522. Copyright (2015) American Chemical Society. (b) Reproduced with permission from ref. 524. Copyright (2016) WILEY-VCH Verlag GmbH & Co. KGaA, Weinheim. (c, d) Reproduced with permission from ref. 529. Copyright (2018) American Chemical Society.

The durability of the anti-fouling ability of superhydrophobic surfaces during long-term usage remains challenging, as the air "cushion" tends to disappear. For example, Hwang *et al.* investigated the bacterial adhesion on various substrates including glass slide, polyurethane, white polystyrene sheet, and superhydrophobic surface.[529] Results showed that the superhydrophobic surface exhibited obvioulsy reduced bacterial adhesion compared to the control surfaces after 1 h of exposure to a bacterial suspension in either brain-heart-infusion (BHI) broth or phosphate buffered saline (PBS), as exampled in Fig. 55c. However, the anti-fouling of superhydrophobic surface was short-lived and that the bacteria attachment increased greatly after 24 h exposure in either BHI or PBS. As depicted in Fig. 55d, compared to glass, there was a 9-fold increase in the density of adherent bacteria to the superhydrophobic surface for clinical strain of *E. coli* expressing a carbapenemase enzyme (CRE 1030) in BHI. This was attributed to the loss of the air layer on superhydrophobic surface after prolonged immersion in liquids (*e.g.*, BHI), and the rough structures unexpectedly functioned as reservoirs to enhance bacterial colonization over the longer term. Therefore, it is of great importance to improve the durability of the air "cushion" of superhydrophobic surfaces in order to realize long-term anti-fouling (Section 4). In addition, superhydrophobic surfaces combined with anti-fouling agents have been used to resist foulants aiming to improve the anti-fouling performance and long-term anti-fouling efficiency.[530,531]

Similar to the trapped air "cushion" on superhydrophobic surfaces, the tightly adsorbed and locked water layer on pre-wetted superhydrophilic/underwater superoleophobic surfaces can prevent direct contact between the surfaces and foulants, which thereby protects the substrates from being contaminated by foulants.[522,532] For example, Chen *et al.* developed robust superhydrophilic/underwater superoleophobic and anti-biofouling coatings on glass substrates based on the assembly of hierarchical microgel spheres.[533] The hierarchical microgel spheres were prepared by coating SiO_2 particles on microgel spheres *via* complexing interaction. Subsequently, the hierarchical structures were hydrophilized using a hydrophilic block copolymer, which were then coated on glass *via* a self-assembly method, followed by coating a thermoset resin layer, washing using ethyl acetate and curing. The as-prepared coatings effectively protected the substrates from being fouled by bovine serum albumin protein (Fig. 56a), a significantly decreased protein adsorption (~ 3 μg cm^{-2}) was found on the coating. Moreover, after sandpaper abrasion and 30 days incubation, the coatings still exhibited excellent anti-fouling performance (Fig. 56a) with extremely low protein adsorption (<10 μg cm^{-2}), suggesting long-term anti-fouling ability of the superhydrophilic coatings. In addition, superhydrophilic/underwater superoleophobic surfaces also show anti-oil-adhesion property when they are immersed in water.[240] For example, Chen *et al.* synthesized nacre-inspired hydrophilic mineralized films coated on different substrates using inorganic aragonite and chitosan derivatives.[67] The oil CA and SA of the obtained films were $162.3 \pm 2.7°$ and $1.6 \pm 0.2°$, indicating their low-oil-adhesion property. For a mineralized film coated swimming goggles, the oil stain could be easily removed and became clean immediately after being immersed in water (Fig. 56b), and a coated lens of camera remained its high transparency and high-quality observation in oil-water environment (Fig. 56c).

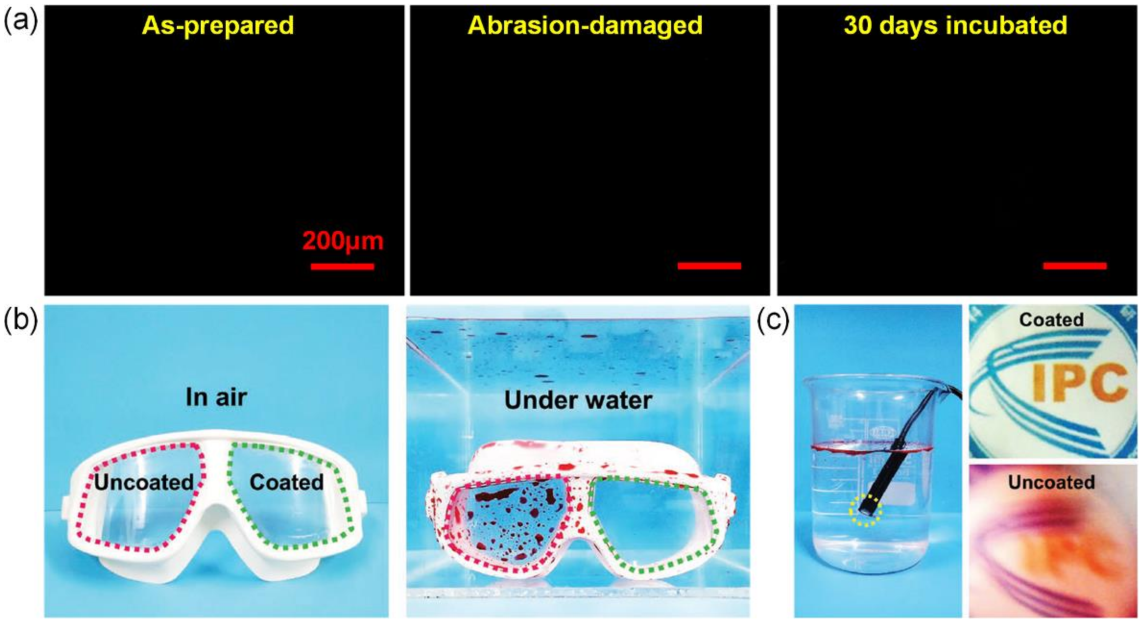

Fig. 56 (a) Fluorescence imaging of bovine serum albumin attached onto the as-prepared, sandpaper abrasion damaged, and 30 days incubated coatings, indicating that no fluorescence (*i.e.*, protein adsorption) could be observed. (b) The image of swimming goggles coated with hydrophilic mineralized film in air (left), and coated area became clean while the uncoated area was stained with mineral oil (right). (c) The hydrophilic mineralized coated lens of camera remained its high transparency underwater and high-quality observation. (a) Reproduced with permission from ref. 533. Copyright (2015) American Chemical Society. (b, c) Reproduced with permission from ref. 67. Copyright (2020) WILEY-VCH Verlag GmbH & Co. KGaA, Weinheim.

Continuous and stable lubricant films locked on SLISs can effectively prevent the contact between foulants and substrates, enabling the SLISs to be capable of resisting fouling adhesion.[11,20,279,357] Epstein *et al*. investigated the anti-fouling performance of SLISs by using lubricant infused porous PTFE substrate or microstructured fluoro-silanized Si wafer.[534] They showed that the SLISs could prevent 99.6% of *Pseudomonas aeruginosa* biofilm attachment over a 7 days period, as well as *Staphylococcus aureus* (97.2%) and *Escherichia coli* (96%), while superhydrophobic control surfaces attached biofilms within hours, under both static and physiologically realistic flow conditions (10 mL min^{-1}). As evidenced in Fig. 57a, after 48 h of room temperature growth in static culture, uniform biofilm coverage was observed on the superhydrophobic surface, while only sparse and isolated cells were seen on the SLIS. Similar results were observed on the two surfaces after 7 days' growth in 10 mL min^{-1} flow condition (Fig. 57b). Manabe *et al*. reported an anti-thrombogenic slippery film composed of chitosan and alginate.[535] The film was prepared *via* a combination of electrostatic interactions between chitosan and alginate and hydrogen-bonding between alginate and polyvinylpyrrolidone *via* layer-by-layer self-assembly method. After cross-linking of the chitosan and alginate, the hydrogen-bonding component was removed by immersing in buffer solution with pH of 10 to generate a porous film, which was then hydrophobized and infused with almond oil to construct a SLIS. Blood could easily flow off the SLIS without leaving any stains, and blood coagulation on the surface was significantly delayed, demonstrating anti-blood-adhesion and anti-thrombogenicity of the SLIS. Lee *et al*. prepared fouling resistant SLISs on endoscope lens by femtosecond laser texturing, a fluorinated monolayer self-assembly, and infusion of medical-grade perfluorocarbon lubricants.[536] The resultant SLISs showed excellent blood repellence and anti-protein adsorption properties. After immersing bare glass and the SLIS in aqueous protein solutions (blood mixed with either albumin or fibrinogen) and incubated for 24 h, the fluorescence imaging clearly demonstrated that significant amounts of protein were attached on the bare glass surface, whereas negligible attachment was observed on the SLIS, as shown in Fig. 57c and d. By incorporating SLISs, various medical devices, such as scalpels,[272,537] endoscope lens,[536] intranasal splints,[538] and silicone rubber tubes,[539] with enhanced anti-fouling ability have been manufactured and tested *in vitro*.

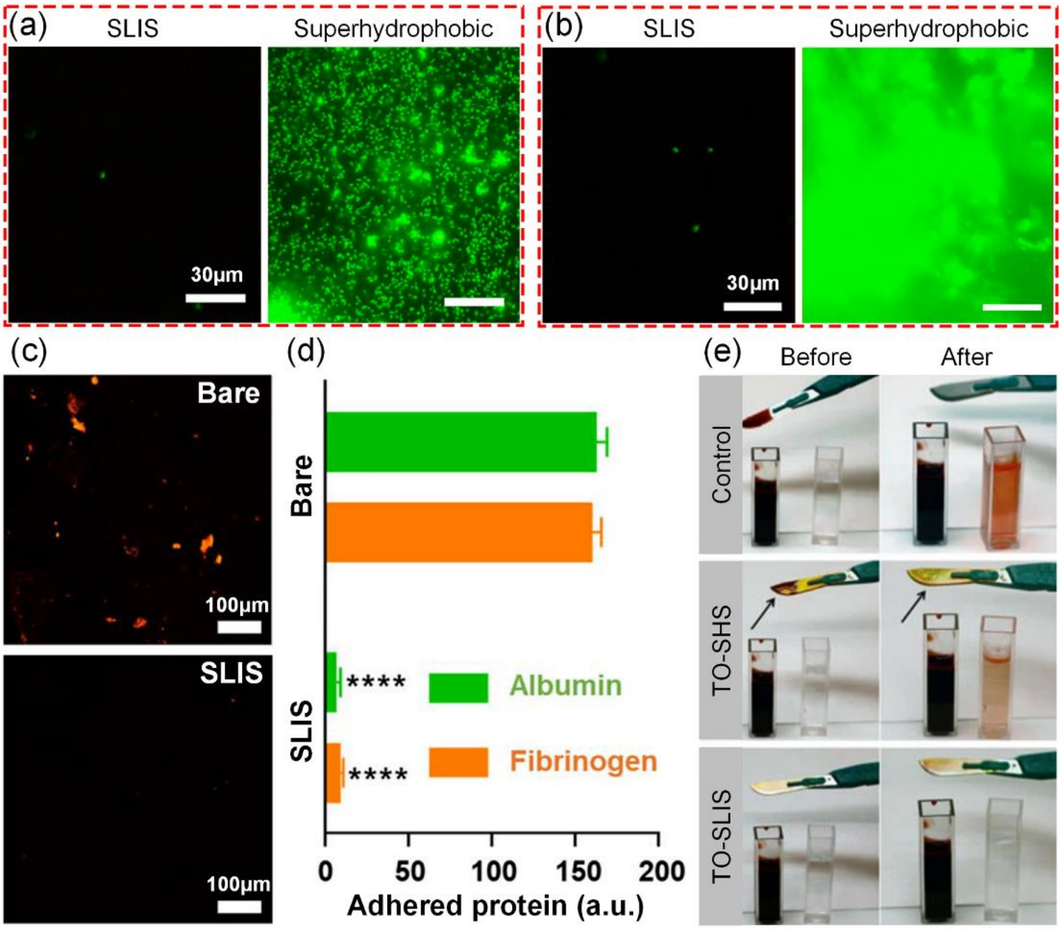

Fig. 57 Fluorescence imaging of attached *Pseudomonas aeruginosa* biofilm after (a) 48 h incubation and (b) 7 days' growth in 10 mL min^{-1} flow condition on SLIS and superhydrophobic PTFE surface. (c) Fluorescence imaging of attached fibrinogen and (d) relative amount of protein (albumin and fibrinogen) adhesion on bare glass surface and SLIS. (e) Images of the blood-stained untreated, TO-SHS and TO-SLIS scalpels before and after immersing in water. (a, b) Reproduced with permission from ref. 534. Copyright (2012) Epstein *et al*. (c, d) Reproduced with permission from ref. 536. Copyright (2020) Lee *et al*. (e) Reproduced with permission from ref. 537. Copyright (2015) Macmillan Publishers Limited.

Durability of the lubricant "cushion" greatly influences the long-term liquid repellence and anti-fouling performance of SLISs, which could be well addressed by the strategies discussed in Section 4. For instance, Tesler *et al.* developed slippery tungstite oxide (TO) films on steel surfaces with excellent anti-fouling properties *via* an electrodeposition method.[537] Hydrophilic TO covered steel surfaces became superhydrophobic (termed as TO-SHS) after being modified with perfluoroalkyl-bearing phosphate. Subsequently, TO-SLIS was prepared by infusing TO-SHS with perfluoropolyether lubricants. When the untreated, TO-SHS and TO-SLIS scalpels were immersed into blood and then washed by water, TO-SLIS scalpels exhibited remarkable blood-repellent property (Fig. 57e). Besides, TO-SLIS possessed more outstanding resistance performance towards reducing bacterial and green algae adhesion than that of the untreated and the TO-SHS. The TO-SLIS coatings retained their liquid repellence after being damaged by abrasion due to their self-healing property. Wei *et al*. synthesized slippery hybrid coatings with long-term stability for biofouling resistance.[339] Low-surface-energy surface with nanostructures on glass or aluminum substrates were fabricated by using methyltriethoxysilane, tetraethyl orthosilicate and *n*-octyltriethoxysilane *via* a polycondensation method, and then were infused with silicon oil to obtain slippery coatings. The prepared coatings could protect the substrates from being contaminated by blood and bacteria, and even inhibited protein adsorption. Owing to the abundant internal cross-linked networks and nanostructures of the hybrid coatings, the SLISs could store the silicon oil stably and maintain excellent long-term slippery properties even under accelerated lubricant depletion conditions, such as evaporating at 70 °C for 7 days and immersing in flowing aqueous systems for 7 days. Recently, Hong *et al*. investigated the optimization of perfluorinated SLISs for blood-contacting applications.[540] The authors prepared tethered-perfluorocarbon layers containing large bumpy aggregates (300 ± 200 nm thick) on top of an underlying uniform coating (35 ± 15 nm thick) by a vapor phase silanization reaction, which were then infused with perfluoroperhydrophenanthrene or perfluorodecalin to create SLISs. Although the two lubricants were similar in preventing fibrin adhesion from human whole blood, the higher viscosity of perfluoroperhydrophenanthrene than perfluorodecalin (28.2 mPa·s *vs* 5.1 mPa·s) made it the preferred lubricant for reducing thrombosis in medical applications under blood flow condition due to its greater resistance towards shear-flow induced depletion.

Superhydrophobic surfaces could effectively reduce foulants adhesion in a short time, but their anti-fouling performance was barely satisfactory towards liquids/foulants with low surface tensions[541] or when the air “cushion” was lost during long-term repelling.[529] For superhydrophilic/underwater superoleophobic surfaces, most studies mainly focus on their oil repellence rather than their anti-fouling property. SLISs show more remarkable and long-lasting anti-fouling performance than superhydrophobic surfaces,[20,534,537,539] but the problem of lubricant depletion is still challenging. Moreover, *in vivo* study of the anti-fouling of liquid-repellent surfaces are urgently required so as to promote their practical applications.

5.1.3 Ice-phobicity

Undesired ice accumulation on solid surfaces causes tremendous damage to commercial and residential activities.[542,543] For example, countries in northern latitudes usually face enormous economic losses and various safety hazards when their infrastructures or devices are covered with ice, such as power lines, ships, aircrafts and roads in winter.[544] Traditional methods, such as cracking ice by inflating, melting ice by thermal/chemical induction, and chemicals incorporated protective coatings, could be used to mitigate ice threats, but these techniques are energy consuming, environmentally harmful, or not reliably up to the goal.[435,545] To overcome these challenges, liquid-repellent surfaces possessing passive anti-icing ability to significantly suppress ice nucleation, to impede frosting and to lower ice adhesion force have been widely developed recently.[30,545-548] In this section, the application of superhydrophobic surfaces and SLISs in ice-phobicity are introduced.

Ice accumulation often occurs when water droplets come into contact with solid surfaces that are at temperatures below the freezing point. For an ice phase to be initiated and grow, favorable conditions for stable nucleation must be fulfilled, *i.e.*, the Gibbs free energy barrier for ice embryo formation must be overcome.[549] Classical nucleation theory is frequently employed to describe the formation of ice. Fig. 58a shows the condition required for homogeneous ice nucleation to proceed, which is depicted by the relationship between the change in Gibbs free energy (ΔG) and the radius of ice embryo (r_i), and the ΔG could be decomposed into the ice-liquid interface contribution (ΔG_S) and the volumetric contribution (ΔG_V). Fig. 58a also shows that at a given temperature an ice nucleus must reach a critical radius, $r_\mathrm{i,c}$, for freezing to initiate and propagate, indicating an energetically favorable growth of the ice embryo when r_i exceeds $r_\mathrm{i,c}$. Spatially, nucleation can occur within a liquid droplet at the free gas-liquid interface (*i.e.*, homogeneous nucleation, Fig. 58b) or the liquid-solid interface (*i.e.*, heterogeneous nucleation, Fig. 58c).[550] Meanwhile, the ΔG is shown to be a function of surface temperature and ice-water interfacial energy, and the ΔG for heterogeneous nucleation is lower than that for homogeneous nucleation at a given temperature.[549] Also, it was suggested that surface-based approaches are effective in preventing heterogeneous nucleation.[551] Therefore, the ice-phobicity of liquid-repellent surfaces could be attributed to the two following strategies: minimizing the contact time between droplets and surface to accelerate the shedding of droplets before ice nucleation occurs, and delaying heterogeneous nucleation through the optimization of surface roughness, chemistry and topography.[30]

Minimized contact time are commonly observed when water droplets impinging on superhydrophobic surfaces due to the trapped air and extremely low CAH of the surfaces,[552-554] which enables them to prevent ice formation effectively even under temperatures below freezing point.[435,546,555-557] For example, Mishchenko *et al*. compared the dynamic droplet freezing behaviors on hydrophilic, hydrophobic, and superhydrophobic surfaces.[435] As shown in Fig. 58d, the authors demonstrated that the impinging droplets attached and froze on hydrophilic and hydrophobic surfaces due to incomplete retraction (*i.e.*, the contact time was long enough for nucleation and freezing), while that on superhydrophobic surface rapidly bounced away (*i.e.*, extremely short contact time) before freezing occurred at surface temperatures above −25 °C, which rendered the superhydrophobic surface ice-phobic. Bahadur *et al*. developed a model to predict ice formation on cooled superhydrophobic surfaces under impact of super-cooled water droplets.[558] The model showed that when a droplet impacted a super-cooled surface and the contact time was long enough to initiate ice nucleation at the tips of the posts, the retraction force responsible for de-wetting of the impacting droplet was thereby decreased, which eventually resulted in incomplete retraction, pinning and complete freezing of the droplet; if the contact time was less than the time required to induce pinning, the droplet would rebound completely and there was no ice formed. Meanwhile, a reduction in temperature increases the viscosity of water, for example, the viscosity shows a 5-fold increase at −27 °C compared to room temperature (23 °C).[304] The resulting stronger viscous dissipation effects significantly influences the impacting dynamics of the water droplet, causing partial meniscus penetration and retarding/preventing droplet retraction, which thereby increases the contact time and facilitates icing.[304,559] Consequently, ensuring stable Cassie-Baxter wetting state and minimized contact time of the impacting droplets, particularly of those extremely supercooled ones, are crucial for the ice-phobicity of superhydrophobic surfaces. However, if a droplet impacts a superhydrophobic surface with sufficient kinetic energy, it may penetrate the surface textures and displace the trapped air "cushion", and finally become pinned in the Wenzel state, resulting in the loss of superhydrophobicity and thereby the ice-phobicity. As discussed in section 4.2.2, micro/nano structures, such as closed-cell features[435] and closely packed nanostructures,[560] can be created or integrated to increase the capillary pressure of the surface textures and to resist the transition from the Cassie-Baxter state to the Wenzel state, thereby improving the anti-icing capacity of superhydrophobic surfaces.[30]

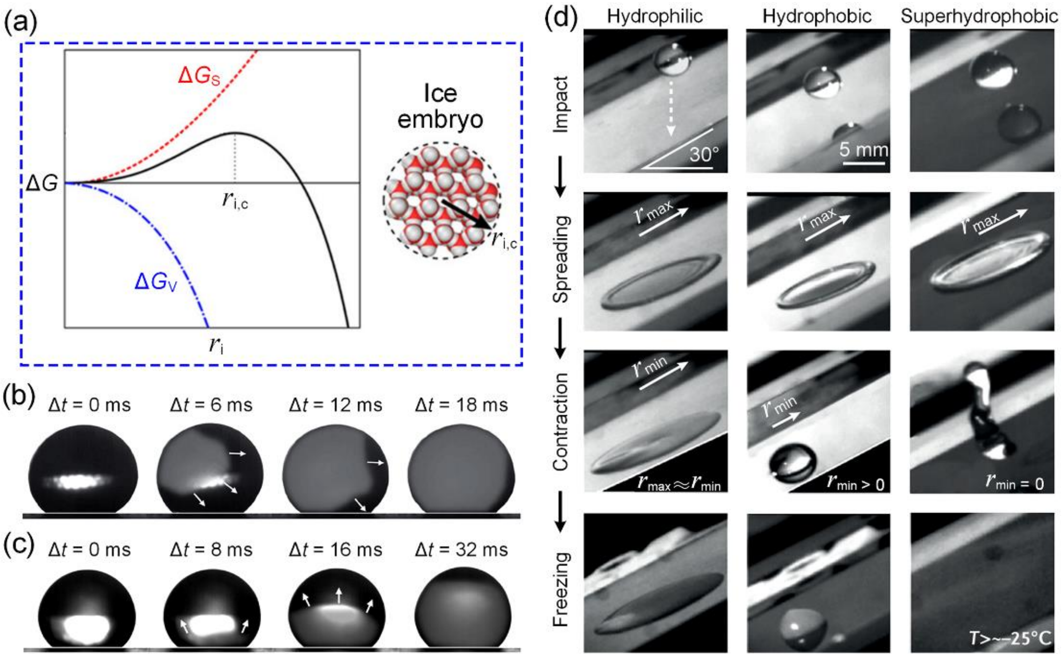

Fig. 58 (a) Plot of ΔG vs r_i. The inset image is a schematic of an ice embryo with critical radius ($r_{i,c}$). Origin and propagation of (b) homogeneous nucleation at the gas-liquid interface and (c) heterogeneous nucleation at the liquid-solid interface. The arrows indicate the propagation directions of the ice front. (d) Impacting and subsequent freezing of water droplets on a hydrophilic, a hydrophobic and a superhydrophobic surface. (a) Reproduced from with permission from ref. 549. Copyright (2014) American Chemical Society. (b, c) Reproduced from with permission from ref. 550. Copyright (2012) Macmillan Publishers Limited. (d) Reproduced from with permission from ref. 435. Copyright (2010) American Chemical Society.

Although dynamic bouncing and rapid shedding of impinging droplets can significantly enhance the anti-icing property of superhydrophobic surfaces, it becomes important to delay heterogeneous nucleation when the contact time is long enough to trigger ice nucleation (*e.g.*, freezing of a static droplet).[30,561,562] Generally, minimized liquid-solid contact area is crucial for the nucleation delay on superhydrophobic surfaces, which can be attributed to the reduced heat transfer between liquid and subcooled substrate, and an increased free-energy barrier for heterogeneous nucleation at the water-substrate interface.[30,435,544,551] For example, Guo *et al*. investigated the anti-icing performance of fluorinated stainless steel surfaces with different topographies, including micro/nano structures, micro structures, nano structures and smooth structures.[546] According to the delay time of ice formation on different surfaces at −10 °C (Fig. 59a), the micro/nanostructured superhydrophobic surfaces (CA ~ 150°) possessed the longest delay time (~ 7200 s), while nano structured surface (CA ~ 120°) and smooth/micro structured surfaces (CA < 90°) showed much shorter delay time to resist water droplets freezing (< 1740 s). Qualitative analysis showed that the liquid-solid contact area of micro/nanostructured surfaces was much lower than the other three surfaces, so less heat transfer occurred upon contacting, which resulted in higher net heat gain in unit time on the micro/nanostructured surfaces and smaller decrease in the temperature of the droplet, thereby delaying the ice nucleation.

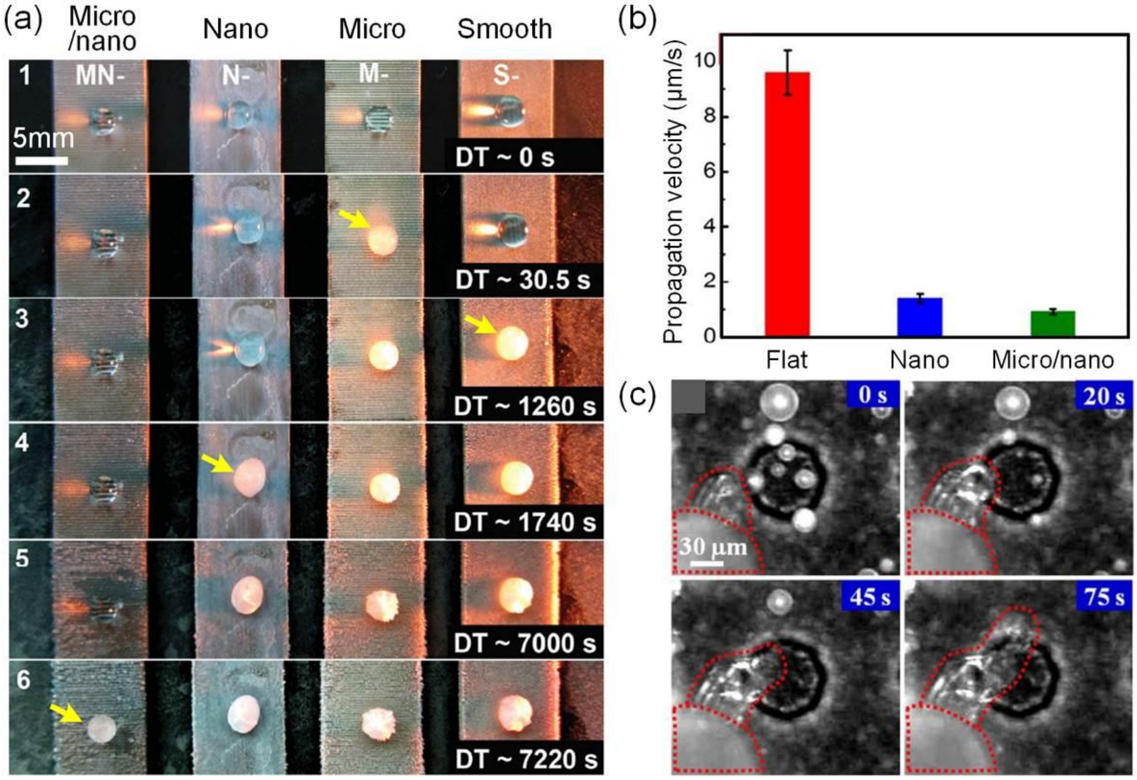

Fig. 59 (a)Image showing delay time (DT) for ice formation on different surfaces. (b) The interdroplet freezing wave propagation velocities on the flat hydrophobic, nanograssed and micro/nano structured superhydrophobic surfaces. (c) Geometric barrier imposed by the micro structures during freezing front propagation. (a) Reproduced with permission from ref. 546. Copyright (2012) WILEY-VCH Verlag GmbH & Co. KGaA, Weinheim. (b, c) Reproduced from with permission from ref. 563. Copyright (2013) Chen *et al*.

When the temperature of a superhydrophobic surface falls below the dew point, water condensates and coalesces indiscriminately within the rough structures under supersaturated condition, which gradually results in the trapping of the growing water droplets in the Wenzel state.[300,560,564] Moreover, when the temperature is lower than the freezing point, frost can form either directly from the water vapor through desublimation or *via* freezing of the condensed water droplets. Water vapor condensation and frosting significantly enhance ice nucleation and increase ice adhesion on superhydrophobic surfaces, which thereby impedes the ice-phobicity of the surfaces under high humid atmosphere.[30,549,564,565] To address these challenges, one feasible strategy is nanoscale features enabled self-propelled jumping of condensed water microdroplets, which could be observed on superhydrophobic surfaces with closely packed nanostructures or micro/nano hierarchical structures.[546,560,566-571] The spontaneous jumping of microdroplets that powered by the surface energy releasing upon smaller droplets coalescence can remove the condensed droplets from the surface before heterogeneous ice nucleation occurs, which thereby improves the anti-icing property of the surfaces under high humid condition. For example, Chen *et al*. showed that although frosting over the entire surface was inevitable due to undesired interdroplet freezing wave propagation initiated by edge corners of the substrate, the propagation velocity of the front was up to an order of magnitude slower on superhydrophobic surfaces with nanostructures than on a flat hydrophobic surface (Fig. 59b).[563] The authors also found that owing to the microscale edge effect of the hierarchical structures, the energy and structural barriers for the interdroplet freezing wave propagation were increased (Fig. 59c), which resulted in slower condensation frosting for superhydrophobic surface with hierarchical micro/nano structures compared to that with nanostructures alone. Wang *et al.* reported a durable ice-phobic superhydrophobic surface composing of heptadecafluorodecyl tri-propoxy silane coated PDMS micropapillae and ZnO nanohairs.[556] The surface remained dry and possessed a water-rebounding ability after being placed at a temperature of −20 °C and a relative humidity of 90% for 3 months, which were attributed to the ZnO nanostructures repelling condensed droplets, and the PDMS micropapillae suspending droplets and cushioning the pressure from droplets impacting.

Another strategy is to replace the trapped air “cushion” of superhydrophobic surfaces with lubricant “cushion”, namely, to create SLISs to enhance the ice-phobicity of solid substrates, particularly in highly humid conditions.[29,30,548,572-574] Kim *et al*. investigated the ice formation process of various Al surfaces, including superhydrophobic surface and SLIS, under a prolonged exposure to freezing temperature of −2 °C and relative humidity of 60%.[572] As can be seen from Fig. 60a, after 100 min of freezing, the superhydrophobic sample had > 99% of its surface covered with ice, while only ~ 20% of the SLIS experienced ice coverage that mainly originated from the edge effect and the bulk of the SLIS remained ice-free. Benefitting from the extremely low CAH of SLISs, condensed water microdroplets as small as 100 μm in diameter became highly mobile and moved continuously at speeds that were several orders of magnitude higher than those on identically textured superhydrophobic surfaces, and finally departed the surface before freezing.[572,573] Meanwhile, SLISs exhibited significantly decreased nucleation temperature of supercooled water, reduced heterogeneous nucleation, and lowered frost propagation velocity, which further improved the ice-phobicity of SLISs.[575,576] However, the migration and depletion of the lubricant during icing and de-icing have to be considered since they would inevitably weaken the liquid repellence as well as the ice-phobicity of SLISs.[547,577,578] Optimized selection of lubricant and underlying surface chemistry can stabilize the infused lubricant firmly through enhanced chemical affinity (section 4.1), and nanostructured surface textures can improve the retention of the lubricant "cushion" of SLISs *via* increased capillary pressure (section 4.2.2), all of which contribute to the durability of their ice-phobicity during repeated icing/de-icing.[30,573] Wong *et al*. put forward a method of preventing lubricant depletion during anti-icing of SLIS, involving the capillary pressure provided by nanostructures being greater than the capillary-induced suction pressure caused by frost dendrites.[547] Both microstructured and nanostructured SLISs were constructed on the same micropillar array, but differences occurred between them when both surfaces were infused with silicone oil with or without the addition of epoxy-amine nanoparticles. Nanostructured SLIS possessing smaller interstitial spacing (30 nm) than microstructured SLIS (18 μm) and provided much stronger capillary retentive forces, resulting in reduced lubricant depletion during icing (Fig. 60b, c). As a result, the lubricant film of microstructured SLIS was damaged while that of nanostructured SLIS remained unchanged during condensation-frosting process. After 50 de-icing cycles, there was no obvious lubricant loss in the nanostructured SLIS, indicating its exceptional durability. In addition, imparting SLISs with self-healing property (section 4.4) can also be an alternative method to improve their ice-phobicity for long-term icing/de-icing applications.[56,579]

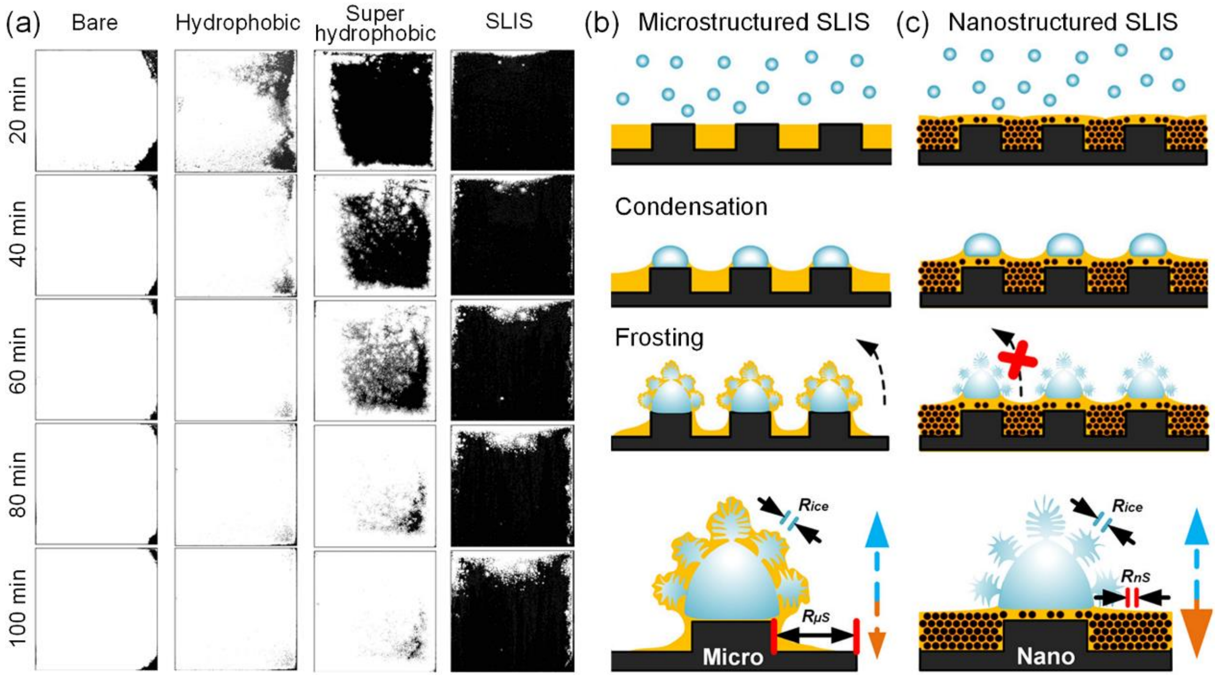

Fig. 60 (a) Time lapse images of ice formation on various Al substrates. The white and black represent ice-covered and ice-free areas on the surface, respectively. (b) The process of water condensation and frosting on microstructured SLIS, and the damage of lubricant layer. (c) The process of water condensation and frosting on nanostructured SLIS, and the prevention of lubricant layer loss. (a) Reproduced with permission from ref. 572. Copyright (2012) American Chemical Society. (b, c) Reproduced from with permission from ref. 547. Copyright (2020) American Chemical Society.

Although liquid-repellent surfaces show remarkable anti-icing property, ice eventually forms on even the best liquid-repellent surfaces under extreme conditions, making de-icing a key consideration for the evaluation of ice-phobicity. Typically, shearing the ice from a surface using a force probe, or removing the ice using centrifugation are two most widely used techniques to measure ice adhesion strength. Owing to the minimized direct contact between ice and solid substrates, superhydrophobic surfaces siginificantly decrease the ice adhesion strength.[564,580-583] For example, Song *et al*. prepared superhydrophobic concrete with excellent anti-icing property by a metal mesh covering and hydrophobic modification of fluoroalkylsilane.[66] When the sloping angles of the prepared superhydrophobic surfaces were larger than their SA, water droplets easily rolled off from the as-prepared surfaces while droplets firmly adhered on unmodified surfaces and were then frozen into ice. By placing the samples horizontally and forming ice on them, de-icing test by using a force gauge showed that the ice adhesion strength on untreated concrete was about 1496.9 kPa, while that on superhydrophobic concrete was only 113.3 kPa. It has to be noted that the ice-phobicity of superhydrophobic surfaces may deteriorate due to the rough morphologies can be destroyed during de-icing process.[56,564,584-586] SLISs can effectively prevent the direct contact between condensed water droplets and solid substrate, thereby exhibiting ultra small ice adhesion strength as low as several kPa.[56,572,578,586] However, this will gradually lose when the lubricant layer was depelted during cyclic icing/de-icing,[56,578,587] emphasizing the importance of stabilizing the lubricant “cushion” of SLISs. For example, Long *et al*. put SLIS and superhydrophobic surfaces in water with a tilting angle of 30° at −15 °C for 24 h and then compared their anti-icing performance.[588] Results showed that both the SLIS and superhydrophobic surface could be easily drawn out from the ice after freezing, but the ice adhesion strength on SLIS (6.2 kPa) was much lower than that on the superhydrophobic surface (35.2 kPa). After 12 icing/drawing cycles, the water CAs of the superhydrophobic surface decreased from 156.1° to 108.9° due to the gradually damaged micro/nanostructures during de-icing, while that of the SLIS remained almost unchanged (~ 106.3°) as the lubricant layer kept homogeneous and smooth, demonstrating that the ice-phobicity of the SLIS was robust and durable.

5.2 Liquid/Gas Harvesting, Transport and Manipulation

The manipulation of liquid or gas in air or under water has aroused great interest in many fields, such as water purification/collection,[160,589-593] controllable chemical microreactors,[594-596] gas bubbles capture and transport,[597-600] droplet-based actuators,[601,602] and so on. In this part, liquid/gas harvesting, transport and manipulation by liquid-repellent surfaces are introduced. Additionally, advantages and disadvantages of these surfaces applied in the same fields will be discussed and summarized.

To date, two strategies have been used for water manipulation on superhydrophobic surfaces in air, (a) utilization of different water adhesion on different superhydrophobic surfaces for no-loss water transportation in a programmable way; (b) loss-free water motion in one direction on superhydrophobic surfaces with the help of external driving forces.[603] Theoretically, whether two methods can be applied for water manipulation is primarily related to water wetting states on superhydrophobic surfaces. For example, inspired by rose petals, Tan *et al*. regulated superhydrophobicity and adhesive force of as-prepared interfaces for microdroplets manipulation.[595] The highly folded graphene oxide papillae/latex bilayer films were prepared *via* a three dimensional shrinking method, and subsequently modified with (heptadecafluoro-1,1,2,2-tetrahydrodecy) trichlorosilane. The resulting graphene-based surfaces not only exhibited superhydrophobicity, but also showed strong water adhesion due to the existence of oxygen-containing groups, even after the modification of hydrophobic agents. Through the optimization of microstructures of papillae (microfolds or microwinkles), papillae numbers and the arrangement of papillae arrays, superhydrophobicity (water CA > 170 °) with different adhesive forces (39.2 μN to 129.4 μN) became tunable. These properties enabled the loss-free manipulation of microdroplets with different sizes. As shown in Fig. 61a, when a microdroplet with a volume of 3 μL was placed on the triangle array, it could be captured and then transferred to the hexagon array through a manipulator with square array. In contrast, the same microdroplet could not be transferred from square array to triangle array because of poor reversibility. Furthermore, these obtained films remained robust after external damages including stretching, folding, twisting and rubbing. These stable performances were attributed to the strong chemical bonding between the graphene oxide film and the latex substrate.

In addition to programmable manipulation of microdroplets, using external driving forces may be another strategy for precise control of microdroplets moving or stopping in any directions on superhydrophobic surfaces. For instance, Dai *et al*. utilized an electrostatic field to manipulate the motion of water droplets in different wetting states on a superhydrophobic PDMS surface.[154] The as-prepared superhydrophobic surface possessed a water CA of 157.2 ± 1.6° and an adhesive force of 9.8 ± 0.8 μN. After dynamic friction on the superhydrophobic surface, microdroplet acquired positive charges and showed a water CA of 151.1 ± 2.4° and a higher adhesive force of 59.8 ± 2.6 μN, with offset Cassie-Wenzel transition state. Exposed to an electric field, a positively charged droplet moved upward on the superhydrophobic surface, and then the air cushion trapped in the micro/nanostructures returned to its original state. Its adhesive force also recovered from 59.8 μN to 9.2 μN and the water CA increased to 156.4 ± 1.2°. Therefore, a droplet of charged water exhibited an onset Cassie wetting state. Under electrostatic repulsion, the water droplet displaying onset Cassie wetting state travelled for a distance of 8.2 mm in 0.3 s without any loss while the water droplet at a Cassie-Wenzel transition state pinned on the superhydrophobic surface. Wu *et al*. reported multimode (rolling, bouncing/reverse bouncing, converging/diffusing, climbing, 90° turning, and sequential transport), large-volume-range, and high-speed unidirectional manipulation of microdroplets by horizontal vibration on femtosecond laser engineered slant microwall arrays (Fig. 61b), and the unidirectional transport mechanism was attributed to the variance of viscous resistance induced by the difference of contact area between the microdroplet and the slant microwalls (Fig. 61c).[70] The no-loss transport/manipulations of liquids on superhydrophobic surfaces promote the development of droplet-based chemical mixing microreactors (Fig. 61d), which can guarantee the safety of experimenters, reduce the consumption/cost of chemical regents, and improve reaction rates.[604] In terms of water harvesting, hydrophobic cactus spine was effectively used to collect water.[605] Due to the difference of toughness and hydrophobicity on the tip and the base of cactus spines, driving forces derived from the gradient of surface-free energy directionally drive water collection from the tip to the base. Laplace pressure also contributes to the water harvesting process. Bai *et al*. fabricated artificial cactus spines with nanogroove-based structures for water collection using micrometer silver needles and the imidization reaction of polystyrene and poly(amic acid).[606] Hierarchical nanogrooves facilitated water harvesting and transportation, and the water transportation velocity was ~ 360 μm/s.

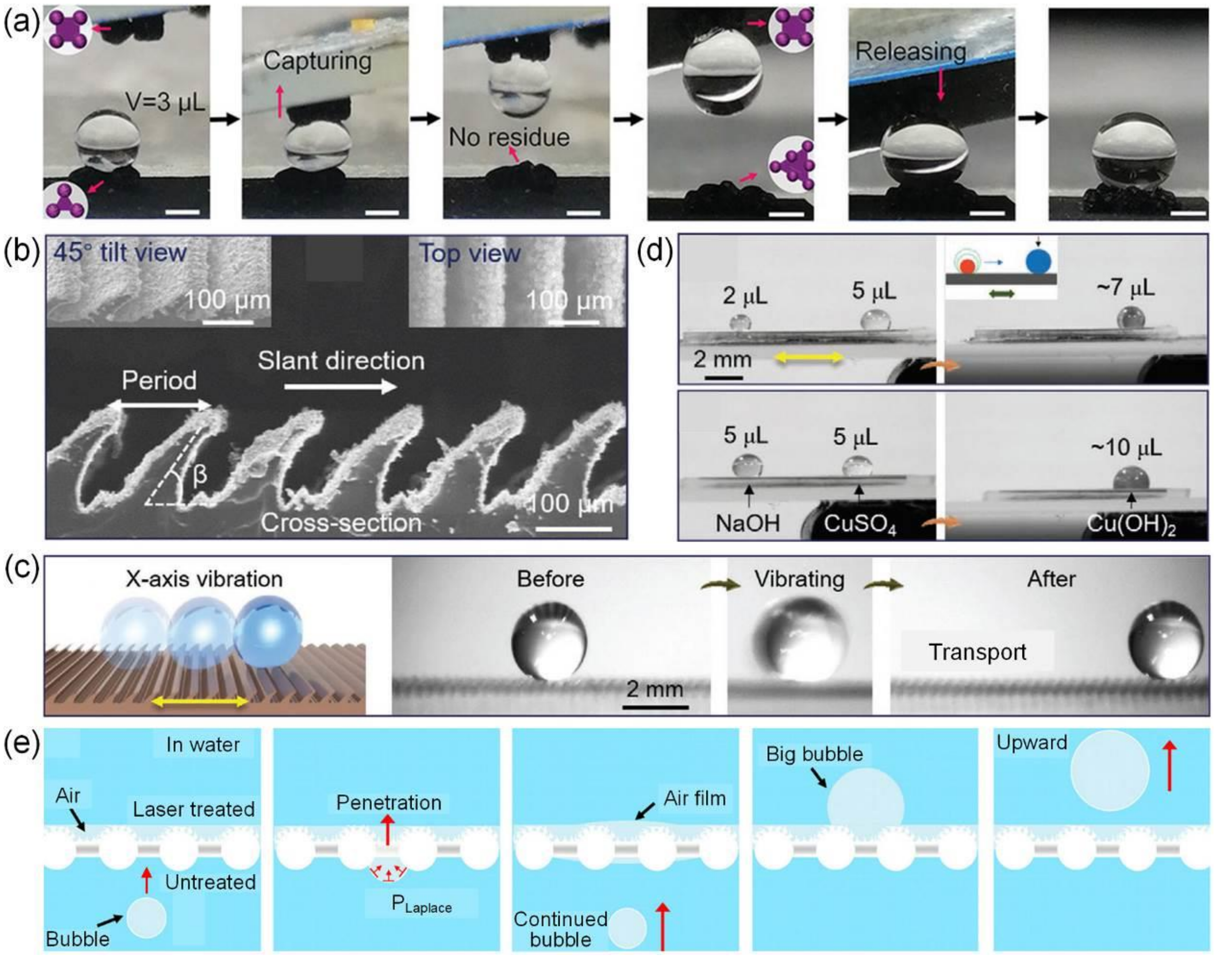

Fig. 61 (a) The loss-free water transfer process from triangle array to hexagon array in a programmable way. (b) SEM images of superhydrophobic PDMS with slant microwall arrays. (c) Water droplet transport by asymmetrical superhydrophobic slant microwalls under the X-axis vibration. (d) Controllable droplets mixing and reaction of NaOH solution and CuSO4 solution. (e) The schematic of PTFE mesh for the directional transportation of underwater gas bubbles. (a) Reproduced with permission from ref. 595. Copyright (2019) WILEY-VCH Verlag GmbH & Co. KGaA, Weinheim. (b–d) Reproduced with permission from ref. 70. Copyright (2020) WILEY-VCH Verlag GmbH & Co. KGaA, Weinheim. (e) Reproduced with permission from ref. 607. Copyright (2018) American Institute of Physics.

Superhydrophobic surfaces exhibit underwater superaerophilicity and possess high bubble adhesive force, which are used for underwater gas bubbles capture and transportation.[599,608] In this process, when a superhydrophobic surface was immersed in water, a continuous layer of gas film was firstly formed on the superhydrophobic surface and then captured underwater gas bubbles. Finally, the collected bubbles were released from the as-prepared surface *via* Laplace pressure.[607] For example, Yin *et al*. fabricated robust superhydrophobic PTFE meshes to transport and collect underwater gas bubbles continuously.[607] The hierarchical micro/nanostructures of one-sided PTFE meshes were constructed *via* a femtosecond laser ablation. The laser-treated side of PTFE mesh was superhydrophobic in air (water CA of 152 ± 2°) and superaerophilic in water (bubble CA of 0°). The other side of the PTFE mesh was untreated, exhibiting hydrophobicity in air and aerophobicity in water. When the as-prepared mesh was immersed in water, the laser-treated side was covered with air layer while the untreated side was filled with water. Driven by its buoyancy and the Laplace pressure, air bubbles penetrated through the resulting mesh freely and continuously (Fig. 61e). However, air bubbles spread horizontally over the laser-treated side and were not allowed to pass from the laser-treated side to the untreated side. Additionally, these modified superhydrophobic PTFE meshes remained robust and stable even after corrosion and abrasion tests. In the same group, they synthesized a robust cross-shaped superaerophilic trapezoidal platform for carbon dioxide (CO_2) bubbles harvesting in CO_2-saturated water.[600] When a superaerophilic platform was immersed in water, underwater CO_2 bubbles were captured and coalesced together, and were then transferred to the center of the cross-shaped platform *via* self-driven forces. Finally, bubbles were detached away from the platform due to the buoyancy. After being damaged by corrosive solutions and abrasion tests, the resulted superaerophilic trapezoidal platform remained stable and durable. Xue *et al*. fabricated superhydrophobic cones to continuously collect and transport CO_2 bubbles with the assistance of the gradient of Laplace pressure and surface-free energy.[597] The cones were prepared *via* gradient electrochemical corrosion using $CuSO_4$ solution and superhydrophobic modification using SiO_2 nanoparticles. The highest efficiency of CO_2 bubbles collection was achieved when the apex angle was 9°. As for oils capture or harvesting, oils are normally adsorbed or filtered by superhydrophobic adsorbents or membranes. However, such superhydrophobic materials cannot be reused easily, because the oils with low surface tensions and viscous properties are extremely difficult to be removed from the superhydrophobic substrates.

Superhydrophobic surfaces can usually be wetted by low-surface-tension liquids (*e.g.*, hexadecane or ethanol).[609] Superamphiphobic surfaces may be a better choice than superhydrophobic surfaces in terms of the manipulation of a wide range of oils with different surface tensions.[610] For example, Yao *et al*. fabricated $Cu(OH)_2$ nanostructures by immersing Cu foils in 0.03 M ammonia solution at 5.0 °C for 36–48 h, which were then reacted with 1*H*,1*H*,2*H*,2*H*-perfluorodecanethiol in its ethanol solution (~ 0.01 M) for 1–36 h to prepare superoleophobic surface in air. By controlling the reaction time (Fig. 62a) and preload force to hexadecane droplet (Fig. 62b), the adhesion between the droplet and superoleophobic surface could be well regulated.[152] Depending on the tunable adhesive force, transport of hexadecane droplet was realized on the prepared superoleophobic surface in air (Fig. 62c). Chao *et al*. fabricated superamphiphobic Cu surfaces by nanosecond laser directly writing, followed by alkali assistant oxidation reaction, and fluoroalkylthiolate modification, whose oil adhesion performance in air could be tuned by changing the grid spacings of laser ablation.[611] As the grid spacings changed from 60 μm to 480 μm, the surface roughness factor got smaller and the wetting behaviors of oils were correspondingly transformed from the Cassie-Baxter state to the Wenzel state, which enabled loss-free transportation of oils by using different interfaces with programmable oil adhesion behaviors.

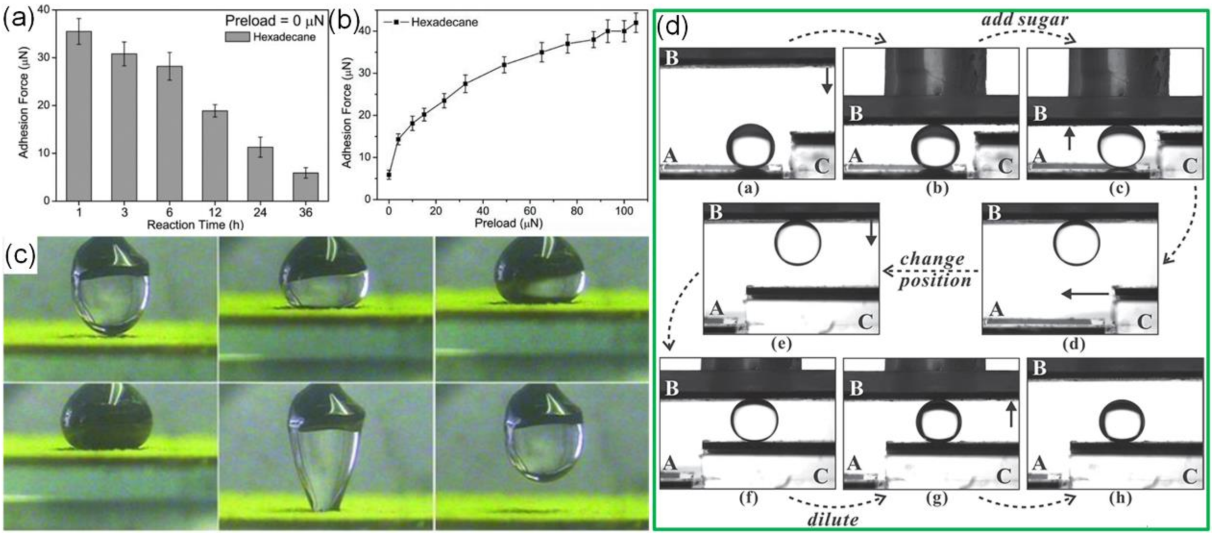

Fig. 62 Regulating adhesive force between hexadecane droplet and superoleophobic surface in air *via* (a) reaction time and (b) preload force. (c) Digital image of loss-less hexadecane droplet transport by the superoleophobic surface. (d) Lossless oil droplet transport on underwater superoleophobic surface with ultralow oil-adhesion by adding sugar into the water solution. (a–c) Reproduced with permission form ref. 152. Copyright (2011) WILEY-VCH Verlag GmbH & Co. KGaA, Weinheim. (d) Reproduced with permission form ref. 612. Copyright (2015) WILEY-VCH Verlag GmbH & Co. KGaA, Weinheim.

Compared with the superoleophobic surfaces in air, oil droplet manipulation on underwater superoleophobic surfaces have drawn more attention due to their feasibility to control the adhesion between oil droplet and surfaces.[64,613] For example, Huo *et al*. adjusted surface adhesive forces of different types of glass plates to manipulate oil droplets in water in a programable routine.[614] By changing the ratios of flat and rough areas of glass using a femtosecond laser ablation, adhesive forces became controllable. A droplet of oil (1,2-dichloroethane, 7 μL) could be transferred from ultralow adhesive surface and then pinned on the ultrahigh adhesive surface without any oil loss in a designed routine. The same group further realized lossless oil droplet transport on underwater superoleophobic surface with ultralow oil-adhesion by changing the buoyancy of oil droplet in water solution (Fig. 62d).[612] They irradiated silicon surface with femtosecond laser to construct periodic rough micro-mountain array with a period of ~ 10 μm, which showed superhydrophilicity in air and superoleophobicity underwater with ultra-low oil adhesion. As shown in Fig. 62d, the pre-deposited oil droplet on Sample A could float up when the density of water solution was increased by adding sugar, and then the droplet was captured by Sample B due to the increased buoyancy. Then Sample C was moved below the oil droplet, and the water solution was diluted to decrease the floatage on the oil droplet, which finally resulted in the transport of the oil droplet to Sample C. In practical applications, no-loss manipulation of oil microdroplets is of great importance in chemical or biological reactions.[251] Additionally, superhydrophilic membranes that are assembled into membrane devices for oil/water separation[615] or advanced funnel-like device for oils collection[592] have emerged in order to transport/collect a large scale of underwater oils with high efficiency.

SLISs have also been widely applied to liquid harvesting and manipulation due to extremely high mobility of liquid droplets deposited on them.[616,617] For instance, Yang *et al*. reported a rice leaf inspired 3D topological SLIS with anisotropic slippery state on copper sheet that was composed of laser-ablated sub-millimeter groves, alkaline oxidizing nanotextures, and infused silicon oil.[618] The nanostructures were crucial for the durability of the SLIS, while the micro textures were necessary for the anisotropy. The sliding resistance anisotropy of water droplet on this surface reached up to ~ 109.8 μN, which endowed the surface with precise directional transport of water droplets under the assistance of gravity (Fig. 63a). Additionally, as shown in Fig. 63b, by mimicking the shore bird feeding water using beak with wedge-shaped opening, the authors fabricated wedge-shaped nanotextured SLIS that could confine the droplet footprint and squeeze droplet to produce a Laplace pressure gradient, which enabled the surface to realize continuous self-driven droplet transport. Recently, inspired by rice leaves, butterfly wings and Pitcher plants, Cai *et al*. report a tridirectionally anisotropic slippery surface (TASS) with periodic step-like micro grooves for programmable droplet transport in three directions.[619] The authors employed a two-round femtosecond laser ablation technique to construct periodic step-like micro grooves on copper plate, and then NaOH-assisted chemical oxidation was used to create nanostructures on the surface, which were followed by surface fluorination and spin-coating-assisted silicon oil infusion. The resultant TASS showed a tridirectional droplet sliding behavior, *i.e.*, the ultra-slipperiness along the grooves with a SA of ~ 2°, and the bidirectionally anisotropic sliding perpendicular to the grooves with difference of SA up to ~ 50°, which was demonstrated to be caused by the pinning effect of the step edge. The tridirectional anisotropy of the TASS allowed unidirectional droplet transport under assistance of vertical vibration, and the transport could be controlled *via* the groove features, the droplet volume, and the vibration frequency, based on which programmable droplet transports, including merging/separation of droplets, sequential droplet-based chemical micro-reactions, and synthetic motion of droplets, were demonstrated on specially designed TASSs.

SLISs can also be used for water harvesting, and in order to improve the performance, micro/nanostructures and surface chemistry on slippery surfaces should be regulated. For example, Gou *et al*. reported the effects of two different kinds of morphologies of SLISs on water harvesting behavior.[620] The modified SLISs were prepared by etching of copper foils, morphologies control using cationic or anionic surfactants, surface hydrophobic modification, and hydrophobic lubricant infusion. SLISs with nanolamellas displayed better water collection performance (782.4 mg cm^{-2} h^{-1}) than that of needles-assembled surfaces (580.8 mg cm^{-2} h^{-1}) because of excellent retention of lubricant layer in nanolamellas-based structures. The as-prepared SLISs showed chemical and physical robustness under harsh environments, such as corrosive solutions, long-term storage, and ultraviolet light exposure, which was ascribed to surface textures on SLISs. Compared with plane SLIS, porous 3D frames with SLISs showed more remarkable water collection capacity. For instance, Pei *et al*. investigated the performance of water harvesting of 3D copper foams with superhydrophobic surface and hydrophobic SLIS.[69] Superhydrophilic surfaces of copper foams covered with dense nanospines were firstly prepared by an etching method using the mixed solution of NaOH and $(NH_4)_2S_2O_8$, and then became superhydrophobic after surface modification by CVD of fluoroalkyl silane. Hydrophobic SLISs were obtained after infusing the superhydrophobic surfaces with hydrophobic lubricant (PMX200/5cs). The modified slippery surfaces exhibited superior water collection performance (~ 800 mg cm^{-3} h^{-1}) than that of superhydrophobic surfaces (~ 500 mg cm^{-3} h^{-1}). This is because tiny fog droplets were captured by nanospines, grew larger and finally formed a layer of water film on superhydrophobic surfaces. In this case, the formation of water layer hindered water removal and new droplets capture on the superhydrophobic foam, resulting in unsatisfactory water collection performance. However, slippery interfaces were able to quickly capture tiny droplets and continuously promote the water transportation and removal under the synergistic effect of nanospines and low SAs, and thus the efficiency of water harvesting was improved. Additionally, these as-prepared slippery foams maintained stable fog harvesting efficiency at ~ 25% and fog harvesting rate of 15200 mg cm^{-3} h^{-1} for 30 consecutive cycles, and also retained low lubricant loss (~ 6.7%). The robustness was mainly attributed to nanospines on modified slippery foams which endowed strong capillary force, allowing lubricant to be trapped on resulted foams. In addition to hydrophobic SLISs, hydrophilic ones are developed and show exceptional water harvesting performance. For example, Dai *et al.* investigated water harvesting rates on different surfaces, and found that hydrophilic slippery rough surfaces (SRS) displayed faster water microdroplets nucleation and removal than those of hydrophilic or hydrophobic SLIS and hierarchical superhydrophobic surface (SHS, no lubricants) (Fig. 63c–e).[160] The as-prepared hydrophilic SRS were fabricated by combining the features of pitcher plants (SLIS) and rice leaves (directional and hierarchical structures) to facilitate water droplets harvesting and mobility. The performance of water harvesting on hydrophilic SRS, hydrophilic or hydrophobic SLIS and hierarchical SHS were about 500, 350, 200 and 175 mg cm^{-2} h^{-1}, respectively. By tuning surface chemistry and increasing surface roughness, water collection performance could be significantly promoted. After continuous 1000 droplet shedding, liquid repellency remained excellent, as the lubricants were maintained in the nano-textured surfaces. This is because the capillary force in nanostructures protected lubricants from being damaged. Additionally, lubricant detachment could be further reduced by using lubricants with higher viscosity.

Besides water harvesting, SLISs have also been designed to manipulate underwater bubbles dependent on buoyancy.[621,622] For example, Wang *et al*. prepared a slippery track with remarkable mechanical stability for underwater bubbles manipulation.[623] Superhydrophobic coatings were constructed on porous alumina ceramic substrates under UV irradiation using the mixtures of vinyl triethoxy silane, hydrophobic fumed silicas and photo initiator. Afterwards, SLISs were obtained when silicone oils were infused into the porous superhydrophobic substrates. The as-prepared slippery track exhibited underwater bubble CA of 72.8 ± 3.8° and possessed the ability to transport bubbles (10 μL) from lower to upper surface of an

S-shaped track (Fig. 63f). The mechanism of bubbles moving is as follows: driving forces originated from adhesion and buoyancy promoted the motion of bubbles when the slippery track was tilted at a certain angle (Fig. 63g). When the samples were soaked in water for 28 days, owing to the existence of hydrophobic fumed silica, the as-prepared surfaces retained excellent slippery performance and maintained the SA of below 10°, showing a stable and durable silicone oil layer. As discussed above, superhydrophobic surfaces are also able to capture and deliver underwater bubbles, primarily relying on Laplace pressure as a driving force, which was induced from asymmetric geometric structures of superhydrophobic surfaces, such as trapezoidal and cone or star-based shapes.[621] However, it may be ineffective for superhydrophobic surfaces under pressure or highly humid atmosphere because of the disappearance of the air cushion; while SLISs could always self-repair the lubricant once the layers are damaged.[620,624]

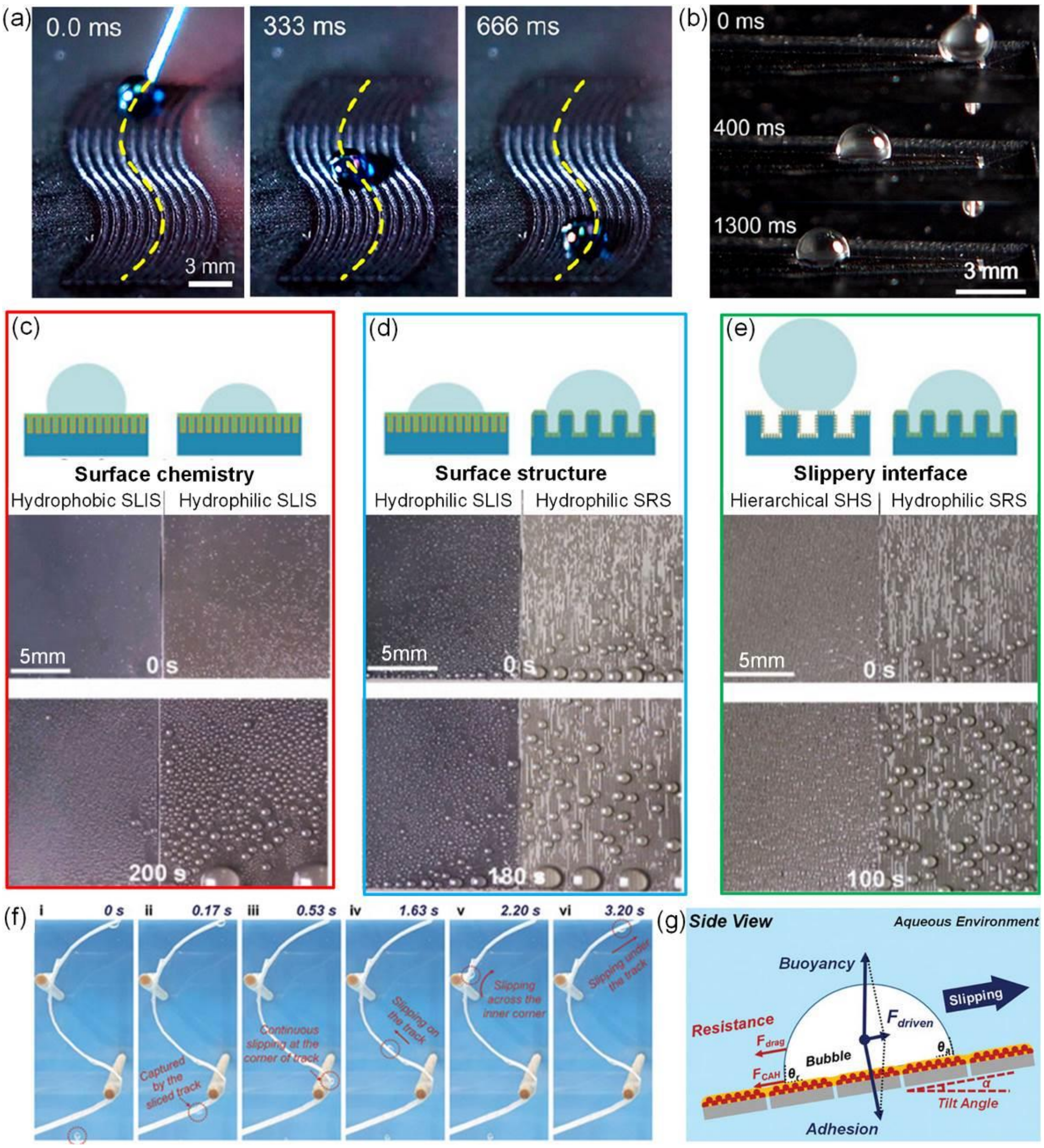

Fig. 63 (a) Directional droplet transport by SLIS with groove-shaped structures under the aid of gravity. (b) Shore bird feeding inspired wedge-shaped nanotextured SLIS for continuous self-driven droplet transport. The effect of (c) surface chemistry, (d) surface structure, and (e) slippery interface on the

performance of water harvesting of different surfaces. (f) Bubbles transport on S-shaped slippery track. (e) The mechanism of gas bubbles transport on SLISs titled at a certain angle *via* buoyancy. (a, b) Reproduced with permission from ref. 618. Copyright (2021) American Chemical Society. (c–e) Reproduced from with permission from ref. 160. Copyright (2018) Dai *et al*. (f, g) Reproduced with permission from ref. 623. Copyright (2021) WILEY-VCH Verlag GmbH & Co. KGaA, Weinheim.

A surface that combines both (super)hydrophilic and superhydrophobic areas is usually applied for water collection. In this combination, water microdroplets are absorbed and condensate on hydrophilic areas, and the superhydrophobic areas promote the efficiency of water removal. For example, in nature, desert beetle, *Stenocara,* with a hydrophilic/superhydrophobic patterned surface on its back, possesses a unique ability for water collection from fog-rich wind.[589,591] The elytra of the desert beetle are covered with an array of bumps, whose sizes are ~ 0.5 mm in diameter (Fig. 64a). The peaks of bumps are smooth and wax-free (hydrophilic) while troughs consist of microstructure covered with wax (Fig. 64b). These microstructures are flattened hemispheres in shape with the diameter of ~ 10 μm and exhibit superhydrophobicity (Fig. 64c).[589] Water microdroplets from moist atmosphere condensate and then coalesce on hydrophilic regions, which are viewed as nucleation sites. After reaching a critical size, water droplets are transported to the beetles' mouths through superhydrophobic areas (wax regions) when the beetles tilt their bodies.[625] According to this interesting natural phenomenon, Yin *et al*. reported a robust hybrid hydrophilic/superhydrophobic copper-based surface for efficient water harvesting.[626] They adhered copper mesh onto the top of a PTFE sheet and then scanned the resulting sample by femtosecond laser line-by-line, during which PTFE particles were deposited on the mesh due to the re-solidification of the ejected PTFE nanoparticles during laser exposure. The resultant PTFE-coated copper mesh showed super water repellence with water CA of 159 ± 2°, water SA of 3° and low water adhesion. By tightly assembling the superhydrophobic copper mesh with a naturally hydrophilic copper sheet, a hydrophilic/superhydrophobic fog collector was obtained. By tuning the mesh numbers (40–100) and inclined angles (15–90°), water collection rate of the as-prepared samples reached approximately 200 mg cm^{-2} h^{-1}. The process of water collection was shown in Fig. 64d, water microdroplets were firstly captured on the hydrophilic copper sheet, then grew larger than the pore size of the superhydrophobic copper mesh, and subsequently rolled off the modified copper mesh. Additionally, the as-prepared water collectors were durable and could retain a water CA of above 150° and a water collection rate of ~ 200 mg cm^{-2} h^{-1} after being immersed in corrosive solutions (such as 1 M HCl, 1 M NaOH and 10 wt% NaCl solution) for 2 hours.

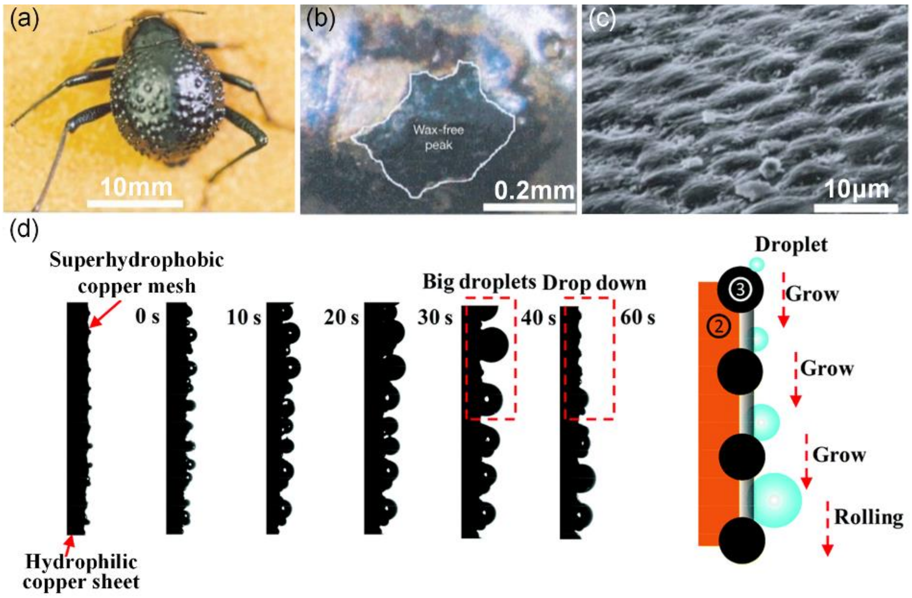

Fig. 64 (a) Digital images of a desert beetle, and (b, c) the corresponding surface features on its elytra. (d) Schematic diagram of water harvesting on a hydrophilic copper sheet and superhydrophobic copper mesh integrated surface. (a–c) Reproduced from with permission from ref. 589. Copyright (2001) Macmillan Magazines Ltd. (d) Reproduced from with permission from ref. 626. Copyright (2017) The Royal Society of Chemistry.

5.3 Immiscible Liquids Separation

Undesired liquids mixing, such as continuous discharge of industrial wastewater and domestic sewage, and frequent occurrence of marine oil spillage, poses huge threats to the environment, resources, public health and the economy.[627] For example, according to the statistics by the International Tanker Owners Pollution Federation (ITOPF), there were 181 oil spills of 7 tons and over in the 2000s, resulting in 196,000 tons of oil lost.[628] The *Deepwater Horizon* accident in 2010 spurted > 50,000 tons of crude oil into the Gulf of Mexico, which contaminated approximately 5,000 square kilometers of area, killed millions of seabirds and lost hundreds of billions of dollars. Therefore, it is of great significance to remediate these contaminated liquid resources.

Flocculant,[629] Fenton catalytic decomposition,[630] and physical separation[498,631] are several typical methods for remediation of mixed immiscible liquids. Among them, physical separation could simultaneously separate and recycle immiscible liquids with little negative environmental impact, enabling this method to be the most promising one. Porous particles, two-dimensional (2D) filters (*e.g.*, metallic meshes, fabrics or membranes) and three-dimensional (3D) monoliths (*e.g.*, sponges, carbon aerogels) are the three most commonly used substrates; however, some of these traditional filters and adsorbents have low separation efficiency, liquid selectivity and reusability.[25,632,633]

To separate immiscible liquids with a high separation efficiency, a filter or adsorbent is expected to be preferentially wetted by oil and repel water, or vice versa. Superhydrophobic-(super)oleophilic filters are usually applied for separation of immiscible liquids due to their selective wettability of water and oil/organic solvents. In terms of other types of liquid-repellent surfaces, *e.g.*, superamphiphobic surface and SLIS, they repel both water and oil/organic solvents and are not very applicable in the separation of immiscible liquids. In this section, superhydrophobic-(super)oleophilic materials will be discussed for immiscible liquids separation, in the forms of particles, 2D filters and 3D monoliths.

5.3.1 Particles

Superhydrophobic and oleophilic powder adsorbents can be effectively applied to remove large-scale oil spills, especially for the treatment of a thin oil film (0.04–50 µm of thickness) that is floating on the water surface.[634] When oil is spilled on sea water, it is easy to manipulate powder-formed oil adsorbents, which only need to be sprinkled on the region of the oil spill. The adsorption process is spontaneous with the aid of waves and tides. To design a high-performance particle adsorbent, three factors are taken into consideration, *i.e.*, surface chemical properties, porosity and the price of raw materials, which may directly affect their selectivity, oil adsorption capacities and extensively practical usage.

Dolomite and calcium carbonate are high-efficiency mineral oil adsorbents because of their low cost, high specific surface area, and ready availability.[635,636] However, pristine minerals can be wetted by oils and water at the same time, and thus find it difficult to separate oil and water. It is necessary to modify surface properties to obtain hydrophobicity and oleophilicity. For example, Shen *et al*. prepared powder-formed superhydrophobic and oleophilic calcium carbonate adsorbents for oil spill clean-ups.[635] After coating with a layer of hydrophobic fatty acid molecules, porous calcium carbonate particles were transformed from hydrophilic to hydrophobic. This approach created low-surface-energy and rough surface simultaneously, and provided superhydrophobic and oleophilic properties of calcium carbonate particles. The water CA of modified calcium carbonate particles was 152°. As a result, these powders floated on water surface and adsorbed oil contaminants autonomously. By quantitative study of calcium carbonate's oil adsorption performance under different ratios of oil and water, the removal efficiencies towards crude oil and diesel oil from water were all greater than 98%.

Conventional particle-typed oil adsorbents are easy to use; they can be simply spread and dispersed onto the spilled oil layer. However, these particles are very difficult to recycle after adsorbing spilled oil. Hydrophobic and oleophilic particulate adsorbents are combined with magnetic particles to fabricate highly efficient magnetic oil adsorbents, such as TiO_2 nanotubes, porous carbon and SiO_2 powders *etc*., which can be easily re-collected and separated by a magnetic separation process.[637-639] For example, Pathak *et al.* fabricated magnetic controllable superhydrophobic and oleophilic TiO_2 nanotubes for selective oil removal from water surface.[640] The magnetic TiO_2 nanotubes were fabricated *via* a hydrothermal method by using magnetite nanoparticles (Fe_3O_4) and TiO_2 nanotubes, and were subsequently post-modified with hydrophobic octadecylamine. The as-prepared TiO_2 nanotubes had a water CA of 166 ± 1° and could adsorb oil from water with a maximum adsorption capacity of 1.5 times of their own weight, and could be separated under an external magnetic force. However, bare Fe_3O_4 nanoparticles tend to be instable under acid conditions. Developing core-shell magnetic materials may be a good strategy to improve Fe_3O_4 stability under a harsh environment. For example, superhydrophobic core-shell $Fe_2O_3@C$ nanoparticles were synthesized for fast and selective adsorption of oils from water.[638] The Fe_2O_3@C nanoparticles were prepared after thermal decomposition of ferric benzoate precursor at 600 °C for 6 h, followed by coating with hydrophobic vinyl trimethoxysilane (Fig. 65a), endowing the as-synthesized Fe_2O_3@C nanoparticles with water CA of 162.9 ± 2°. The porous Fe_2O_3@C nanoparticles could selectively adsorb various oils with the capacity up to 3.8 times of their own weight while completely repelling water. After adsorption, magnetic materials along with oils could be separated by a magnet bar (Fig. 65b). In addition, Fe_2O_3@C nanoparticles exhibited outstanding chemical stability and retained water CA of > 150° under 0.1 M NaCl and solutions with pH ranging from 3 to 14. Jiang *et al.* reported vinyl trimethoxysilane-modified magnetic SiO_2 particles with core-shell structure for oil removal.[639] When the adsorption process was completed, magnetic SiO_2 particles could be removed by a magnetic bar, and the adsorption capacity of the resultant SiO_2 powders was 7.2 times of their own weight.

Superhydrophobic and oleophilic particle adsorbents are fabricated *via* a simple dip-coating method. Modified particulate oil adsorbents have a great potential to remove thin oil film *in situ* over a large scale, but their separation and secondary pollutants may hinder their further applications. Particulate oil adsorbents functionalized with magnetic materials may be promising in future applications, however, there are two challenges remaining to be overcome: (1) magnetic materials are unstable under acid conditions and (2) the adsorption performance of magnetic materials towards oils is still unsatisfactory. Therefore, developing highly efficient and stable magnetic oil adsorbents may be an important research direction in the future.

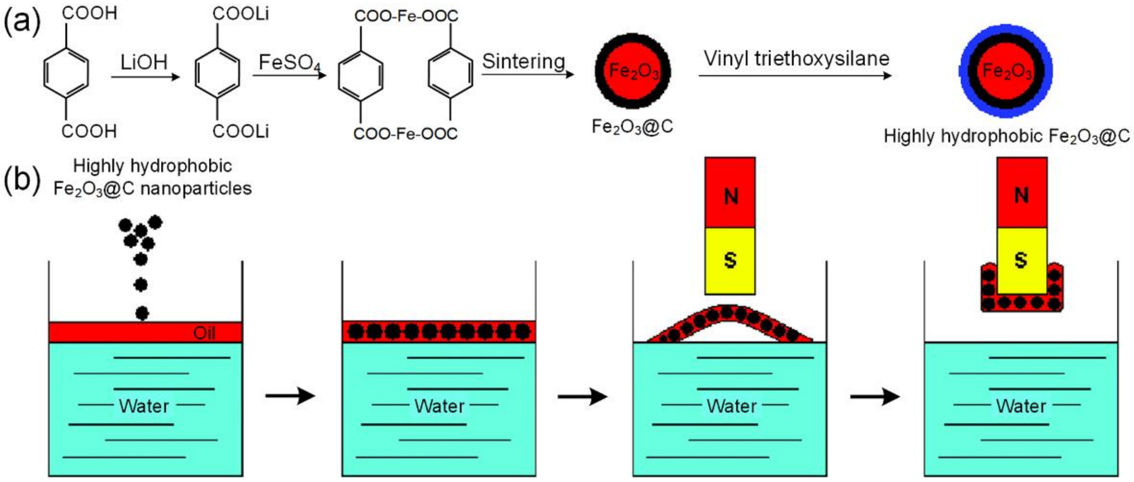

Fig. 65 (a) The preparation process of highly hydrophobic Fe_2O_3@C nanoparticles. (b) Separation of floating oil from water surface by the Fe_2O_3@C adsorbents with the assistance of a magnet. (a, b) Reproduced with permission from ref. 638. Copyright (2010) American Chemical Society.

5.3.2 Two-dimensional filters

Owing to their remarkable operability, excellent separation efficiency and high filtering flux, 2D filters (*e.g.*, stainless steel meshes, textiles and artificially prepared electrospun films) with selective liquid repellence are highly desirable in the separation of pre-collectable immiscible liquids. To evaluate the separation capacity of these 2D liquid-repellent filters, separation efficiency and filtering flux are always characterised. Separation efficiency (%) indicates the mass (or content) percentage of the separated liquid to that in the original mixtures, and filtering flux (L m^{-2} h^{-1}) means the average flow rate of the filtered liquid running through the filter during separation.

Stainless steel meshes are extensively used as substrates for selective oil/water separation owing to their high filtration flux, excellent mechanical strength and mass production.[641] For example, Zhang *et al*. utilized etching and *in situ* growth method to prepare superhydrophobic zeolitic imidazolate frameworks (ZIF-L) coated meshes for oil/water separation.[642] The stainless steel meshes were firstly etched by HCl for one hour followed by immersion in the precursor solutions of ZIF-L. Then a layer of hydrophobic ZIF-L with dagger-like structure was grown *in situ* on the surfaces of the meshes (Fig. 66a). The resulting meshes exhibited water CA of 155.4 ± 1.8°, and achieved isooctane flux of 1.75×10^5 L m^{-2} h^{-1} and separation efficiency of 99.7%. The hydrophobic modified meshes with long-term water resistance and stability possessed water CAs of above 150°. Moreover, the modified meshes displayed outstanding antibacterial performance, reducing the opportunity of the hydrophobic layer being destroyed by bacteria due to the existence of Zn ions and 2-methimidazole (Hmim). Li *et al*. reported superhydrophobic hybrid meshes with high stability under conditions of hot water and strong corrosive solutions through a spray-coating method (Fig. 66b).[643] The robust superhydrophobic meshes with water CA of 160 ± 1° were fabricated *via* sequential deposition of candle soot and SiO_2 particles. The modified stainless mesh could be made into a small box and put on a beaker. The kerosene could selectively permeate through the box and be collected into the beaker with the separation efficiency of higher than 99.0%. Furthermore, the as-prepared meshes were chemically stable and possessed robust hydrophobicity, showing water CA of above 150° under harsh conditions, for example, strong acidic, alkaline, salty solutions, and even hot water.

Commercial textiles, such as, cotton textiles and polymer-based textiles, are widely reported as porous substrates for oil/water separation.[631,644] For example, Zhou *et al.* used cyclic self-assembly and dip-coating method to synthesize superhydrophobic cotton fabrics for oil/water separation.[645] Phytic acid (PA) molecules were firmly anchored on cotton fabrics *via* covalent bonds and then coordinated with metal ions to create hierarchical micro/nanostructures on the fabrics. Subsequently, intermediate fabrics were hydrophobically modified *via* PDMS, the resulting fabrics with water CAs of 152.9 ± 1.8° were obtained after 8 cycles of self-assembly (Fig. 66c). The separation efficiencies of hydrophobic fabric for all tested oils were above 95%. After 30 cycles of abrasion tests and 300-cycle peeling tests, the water CAs of as-prepared fabric were 142.5 ± 2.5° and above 150°, respectively, retaining excellent hydrophobicity. In addition, superhydrophobicity of the modified fabrics exhibited no obvious change under UV radiation, high temperature and chemical solvents. The robustness of the resulting meshes was attributed to covalent bonds between the polymer and hydroxyl groups of the fabric. Zhou *et al.* modified cotton fabric with a hydrophobic layer comprising of $FeCl_3$/1*H*,1*H*,2*H*,2*H*-perfluorooctyltriethoxysilane (PTES) and polyaniline (PANI) micro/nanoparticles through a vapor phase deposition method (Fig. 66d).[646] A piece of cotton fabric was firstly coated with a layer of $FeCl_3$ and PTES. Subsequently, micro/nanoscale PANI granules were prepared onto the fabric surface by placing intermediates in a chamber filled with aniline *via* polymerization. Low-surface-energy material PTES molecules were linked with PANI granules *via* hydrogen bonding. When superhydrophobic fabrics were attacked by acidic and alkaline liquids, or damaged by abrasion and scratch, they still maintained microstructure and surface chemical compositions of the fabric. Under high humidity and temperature, they also kept highly hydrophobicity. After long-term separation, hierarchical nanostructures on the fabric surface were mostly retained. These remarkable performances of modified fabrics may be ascribed to hydrogen bonding between PANI and PTES. Additionally, the hydrophobic fabrics achieved separation efficiency of as high as 97.8%. In addition to stainless steel meshes and cotton fabrics, electrospun films as porous substrates have been studied in the past few decades. Zhang *et al*. prepared polyimide (PI) electrospun hybrid films with hydrophobicity.[647] The PI films were dipped in PDMS solutions and then decorated with ZnO particles *via* a hydrothermal reaction for 5 h at 110 °C, the hydrophobic hybrid films were prepared. The separation efficiencies towards oils or organic solvents were all above 90%. After exposure to different damages, such as acidic and alkaline solvents, high temperatures and chemical corrosion, the water CA of modified films remained unchanged. Additionally, the PI hybrid films were resistant to UV radiation for 24 h due to the presence of ZnO particles.

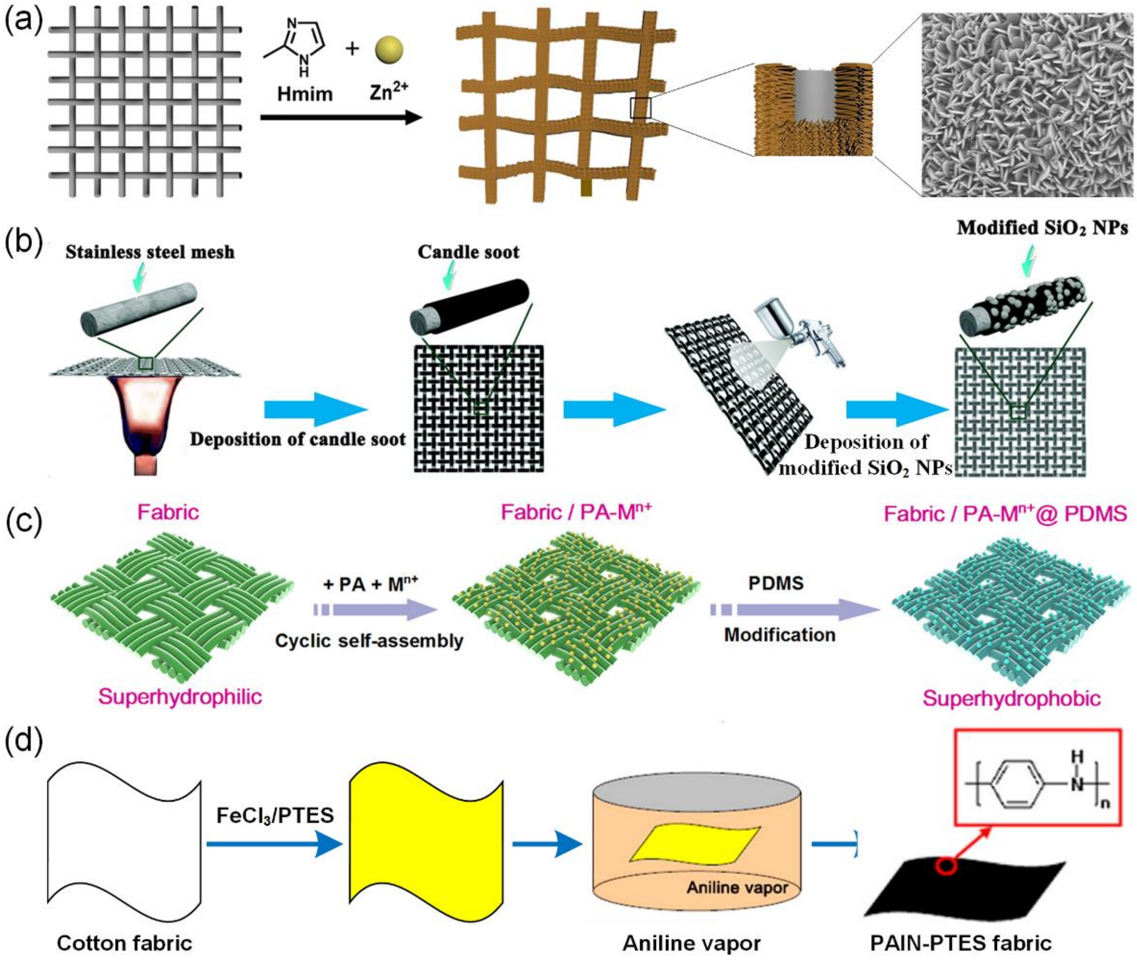

Fig. 66 (a) The fabrication of hydrophobic meshes *via* an *in-situ* growth of ZIF-L nanoparticles on mesh surfaces. (b) Deposition of candle soot and modified SiO2 nanoparticles on the mesh *via* a spray-coating method. (c) The fabrication of superhydrophobic PET fabric *via* cyclic self-assembly of metal ions and

PA molecules and subsequent PDMS modification. (d) Hydrophobic modification of cotton fabric by PTES and aniline *via* a CVD method. (a) Reproduced with permission from ref. 642. Copyright (2019) WILEY-VCH Verlag GmbH & Co. KGaA, Weinheim. (b) Reproduced with permission from ref. 643. Copyright (2016) The Royal Society of Chemistry. (c) Reproduced with permission from ref. 645. Copyright (2017) American Chemical Society. (d) Reproduced with permission from ref. 646. Copyright (2013) American Chemical Society.

To design excellent (super)hydrophobic filters for immiscible liquids separation, some criterions need to be considered. (1) Selection of a suitable substrates. It is known that fabric and electrospun films are easy to be modified hydrophobically due to their functional surface groups, but they may suffer from weak mechanical performance. Stainless steel meshes possessed excellent mechanical performance, but they can be easily damaged or corroded when used in acidic or salty solutions. Each substrate has advantages and disadvantages and needs different modification methods, they need to be balanced before use. (2) The combination modes between hydrophobic coatings and substrates, *e.g.*, chemical bonding is usually superior compared with interparticle interactions, and enables more robust hydrophobic coatings and further improves the lifespan of filters, especially in harsh environments. (3) The low preparation cost and easy modification methods may affect their scalability in practical applications.

5.3.3 Three-dimensional monoliths

The oil/water separation by 2D filters always need external driving forces (*e.g.*, gravity or pressure), making these materials unadoptable to remove large-scale oil spills on water surface. Clean-up of oil spills by 3D adsorbents may be a promising method and has received more attention in terms of *in situ* removal of spilled oil.[25,648,649] Adsorption capacity (g g^{-1}), which is defined as the mass ratio of the adsorbed oil and the adsorbent itself, can be used to assess the oil removal capacity of the 3D adsorbent. Compared with particulate adsorbents, 3D adsorbents show higher adsorption capacity, higher adsorption rate and easier recyclability.

Commercially available polymeric sponges or foams, such as polyurethane sponge and melamine sponge, have been widely used as ideal 3D porous substrates for the preparation of oil adsorbents because of their light weight, high adsorption capacity, as well as excellent recyclability and elasticity.[650] However, amphiphilic polyurethane sponges or melamine sponges are not suitable for oils adsorption due to the lack of selectivity towards oils and water. There are two effective ways to modify polymeric sponges or foams transforming from amphiphilicity to hydrophobicity. The first approach is to improve surface polarity *via* chemical reactions, *i.e.*, surface polarity of chemical groups is proportional to surface energy. Polyurethane or melamine sponges possess abundant polar groups, such as amine and triazine groups, which could bond with modifying agents or metal ions to endow polyurethane or melamine sponge hydrophobicity.[651] For example, Ding *et al*. developed metal ions-induced highly hydrophobic melamine sponges for oil adsorption *via* a dip-coating method.[651] The mechanism of melamine sponges transforming from hydrophilicity to hydrophobicity was that N atoms of amine and triazine groups were coordinated with metal ions (including Fe^{III}, Zn^{II}, Co^{II} and Ni^{II}) (Fig. 67a). The reduction of polar groups led to hydrophobicity of pure melamine foams. Therefore, as-synthesized sponges could selectively adsorb oil and repel water, and the adsorption capacity were 71–157 g g^{-1}. The resultant oil adsorbents kept robust after mechanical squeezing, and also showed remarkable resistance to flame. Pham *et al*. synthesized superhydrophobic melamine sponges with low-surface-energy material octadecyltrichlorosilane. The melamine sponges were contacted with hydrophobic modifying agent through (i) direct hydrogen bonding between secondary amine groups and silanol, and (ii) hydrogen bonding produced between amine groups and oligomers formed by condensation of the Si-OH (Fig. 67b).[652] After that, sponges turned from amphiphilicity into superhydrophobicity and showed water CA of 151.0 ± 1.1°. The as-prepared sponges could selectively adsorb oil or organic solvents and achieved the adsorption capacities of 82–163 g g^{-1}. Owing to the existence of hydrogen bonding, the hydrophobicity of modified sponges remained unchanged after repeated cycles of squeezing.

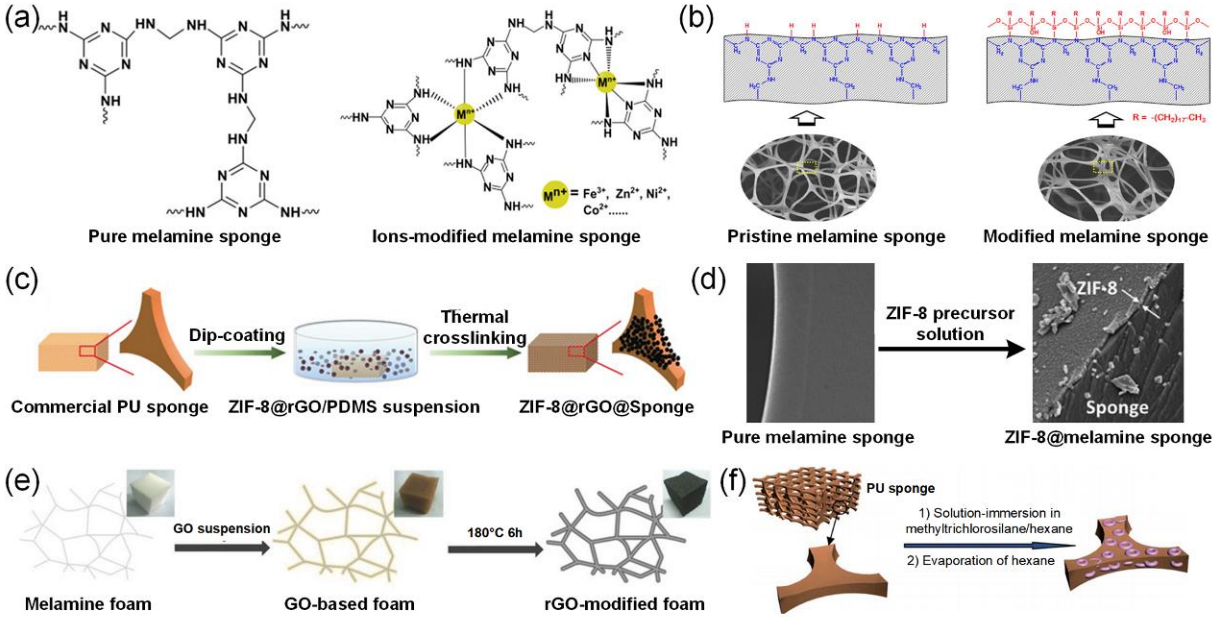

Fig. 67 (a) Metal ions-induced hydrophobicity of melamine sponge *via* a dipping method. (b) Superhydrophobic melamine sponges fabricated by hydrophobic modifying. (c) The synthesis process of hydrophobic polyurethane sponges *via* a dip-coating method. (d) Fabrication of ZIF-8 nanoparticles coated melamine sponge *via* an *in-situ* growth method. (e) The preparation process of hydrophobic rGO-modified foam *via* thermal reduction of GO on melamine sponges. (d) Polysiloxane-coated polyurethane sponges using methyltrichlorosilane though a one-step immersion method. (a) Reproduced with permission from ref. 651. Copyright (2018) American Chemical Society. (b) Reproduced with permission from ref. 652. Copyright (2014) American Chemical Society. (c) Reproduced with permission from ref. 181. Copyright (2019) WILEY-VCH Verlag GmbH & Co. KGaA, Weinheim. (d) Reproduced with permission from ref. 653. Copyright (2017) WILEY-VCH Verlag GmbH & Co. KGaA, Weinheim. (e) Reproduced with permission from ref. 654. Copyright (2015) WILEY-VCH Verlag GmbH & Co. KGaA, Weinheim. (f) Reproduced with permission from ref. 655. Copyright (2013) The Royal Society of Chemistry.

The second strategy is the construction of superhydrophobic nanomaterials onto the skeleton surfaces of sponges or foams, such as metal organic frameworks, graphene oxide or other nanoparticles that are post-modified by hydrophobic agents. For example, Gu *et al*. prepared robust superhydrophobic wrinkled microspheres-coated polyurethane sponges for efficient oil/water separation *via* a dip-coating method (Fig. 67c).[181] When a piece of polyurethane sponge used as a substrate was dipped in zeolitic imidazolate frameworks (ZIF-8)@reduced graphene oxide (rGO) and polydimethylsiloxane suspension, superhydrophobic ZIF-8@rGO microspheres-coated polyurethane sponge was fabricated. The as-prepared polyurethane sponges with water CA of 171° could remove oil from water selectively and achieved a high adsorption capacity of 14–29 g g^{-1} towards various oils and organic solvents. Robust sponges could retain excellent superhydrophobicity after repeated squeezing due to the firm adhesion of microspheres onto the interlaced branches of the sponge. Zhu *et al*. prepared hydrophobic ZIF-8-coated melamine sponges through an *in situ* growth reaction (Fig. 67d).[653] After a melamine sponge was immersed into the precursor solution of ZIF-8, sponge skeletons were completely covered with a layer of hydrophobic ZIF-8 nanoparticles, which improved chemical composition and roughness of the surfaces simultaneously. The thin wettable layer was robust and stable, and kept intact even after over ten cycles of compressive tests. In addition, the adsorption capacities of the resultant sponge were 74–145 g g^{-1}. Zhu *et al*. immersed a sponge into graphene oxide nanosheets solution, followed by chemical reduction of graphene oxide into rGO though a hydrothermal reaction (Fig. 67e).[654] Hydrophobic rGO nanosheets were anchored firmly on the sponge's skeleton *via* the van der Waals force, which created hierarchical roughness and lowered surface energy on surface of the sponge. The resulting sponges displayed a water CA of 151.4° and selectively adsorbed oils from water, with the adsorption capacity of 60–140 g g^{-1}. After 50 cycles of adsorption-squeezing process, adsorption efficiency did not decline significantly. Besides, the rGO-modified sponges possessed outstanding flame-retardant property. Zhu *et al.* fabricated polysiloxane-coated polyurethane sponges using methyltrichlorosilane though a one-step immersion method (Fig. 67f).[655] Polysiloxane was formed after the hydrolysis of methyltrichlorosilane, and was anchored firmly on the sponges' surface, leading to hierarchical surface roughness and low surface energy. The adsorption capacity of the obtained superhydrophobic adsorbents were 15–25 g g^{-1}. The superhydrophobic sponges exhibited remarkable chemical and thermal stability, and had a water CA of > 150° after immersing in strong acid or alkali solution and even exposed to a temperature range of 30–90 °C. In addition, superhydrophobicity and elasticity of the modified sponges showed no decline even after 300 consecutive compressions, possessing excellent mechanical stability.

Carbon-based materials with super water repellence are also one of the most used oil adsorbents. For example, Chen *et al*. prepared superhydrophobic poly(vinylidene fluoride) (PVDF)-based foams by using table salt as a sacrificial template.[72] As shown in Fig. 68a, PVDF, multiwalled carbon nanotube (MWCNT) and table salt were mixed together and then heated at the temperature of 200 °C for 30 min. After cooling and dissolution of the table salt, the porous superhydrophobic PVDF-MWCNT foams with water CAs of 152.6 ± 4.5° were obtained. The foams possessed adsorption capacities of 3–12 g g^{-1} to oils or organic solvents with different densities. Besides, the foams were highly resistant towards UV radiation, corrosive solutions, and turbulent conditions. Xia *et al*. synthesized carbon-based porous foam consisting of carbon-nanosheet (CNS) frameworks and iron/iron carbide (Fe/Fe_3C) nanoparticles *via* ferric nitrate assisted chemical blowing and carbonization of polyvinylpyrrolidone, and finally obtained superhydrophobic and magnetic CNS-based foam after PDMS treatment (Fig. 68b).[656] The foam showed low density, extremely high compressive strength, and selective oil cleanup ability with oil adsorption capacity of 5–27 g g^{-1}. The foam could remove oil selectively from water in non-open channels under magnet assistance due to its paramagnetic property, and could be easily recovered by heating or releasing in other solvents with stable adsorption capacity. The chemically stable CNS frameworks and PDMS coating enabled the foam to be durable towards high/low temperature and corrosive solutions (*e.g.*, 1 M NaOH and saturated NaCl solution). The 3D porous and self-similar micro structures of the foam enabled it to be mechanical abrasion resistant so as to retain its super water repellence and oil adsorption capacity after repeated and intensive abrasion by sandpaper. Compared with carbon-based sponges and foams, porous carbon aerogels derived from biomass show outstanding features of low density, high porosity, fire-resistance and chemical stability.[25,657,658] Wu *et al*. reported an ultralight, flexible, fire-resistant, and superhydrophobic carbon nanofiber aerogels for oils adsorption by pyrolyzing bacterial cellulose pellicles.[659] High porosity of carbon aerogel was beneficial for oil adsorption and its adsorption capacities for oily liquids were up to 106–312 g g^{-1}. In addition, it had an excellent fire-resistant property when being exposed to flame, enabling the recycling of carbon aerogels for oil adsorption by a direct combustion method. Besides these carbonized aerogel derived from biomass, hydrophobized nanocellulose-based materials have also been widely used as oil sorbents due to their abundant and sustainable resources, natural renewability, excellent biodegradability and mechanical properties.[660,661] Phanthong *et al*. fabricated a nanocellulose sponge *via* freeze-drying of nanocellulose aqueous suspension and following hydrophobic treatment with stearoyl chloride at 50 °C for 1 h.[662] The obtained porous nanocellulose sponge showed superhydrophobicity (water CA 160 °) and superoleophilicity, which enabled the sponge to selectively adsorb oils from water surface with absorption capacities of 25–55 g g^{-1}. The nanocellulose sponge could be easily recovered by squeezing, so it could be reused for selective oil removal at least 10 cycles with high separation efficiency. Shang *et al*. prepared a cross-linked nanocellulose aerogel through the freeze-drying of cellulose nanofibril (CNF) and 1,2,3,4-butanetetracarboxylic acid (BTCA) and subsequent esterification at high temperature (170 °C), which became superhydrophobic and superoleophilic after being modified by CVD of hexadecyltrimethoxysilane (HTMS) (Fig. 68c).[663] Ultra-low density (6.05 mg cm^{-3}) and high porosity (99.61%) enabled the aerogel to adsorb various oily liquids with adsorption capacity of 77–226 g g^{-1}. The chemical cross-linking reaction greatly enhanced the structural and thermal stability of the resultant aerogel, as well as the reusability towards repeated oil adsorption.

3D monoliths could selectively *in situ* adsorb oils, possess high adsorption capacity, and could be easily regenerated by squeezing or combustion after adsorption. However, it is ineffective for adsorbents to remove crude oils with high viscosity because the infusion of crude oils into porous structures is relatively slow compared with light oils. During desorption, porous structure and hydrophobic coatings may be damaged by consecutive squeezing and combustion, and thus selectivity and adsorption capacities are directly influenced. Besides, when adsorbents were affected by external harsh surroundings, such as wave or heavy rain, oils may be desorbed from the adsorbents.

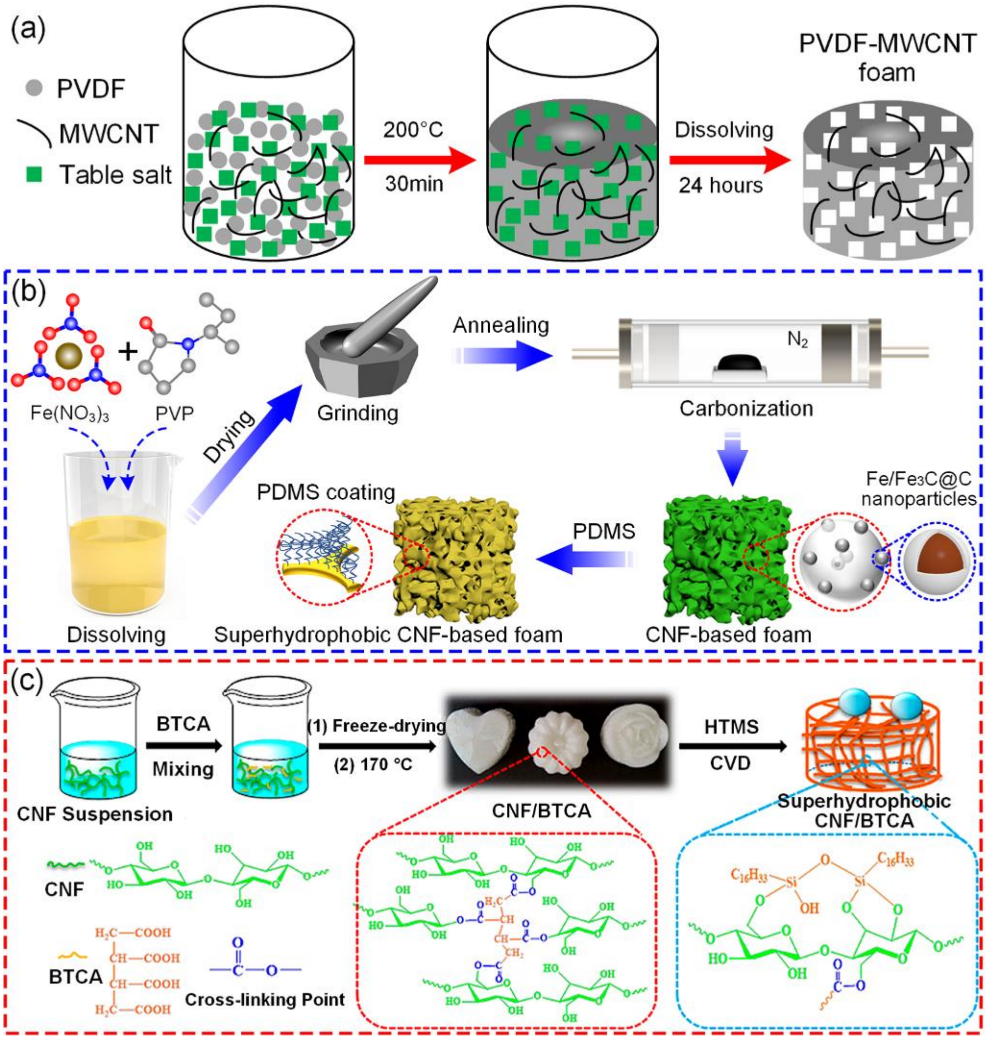

Fig. 68 Schematic illustration of (a) fabrication of porous PVDF–MWCNT foam by using table salt as a sacrificial template, (b) synthesis of superhydrophobic CNS-based foam by Fe(NO3)3 assisted chemical blowing and carbonization of PVP, and post-treatment by PDMS, (c) preparation of superhyrophobic nanocellulose aerogel *via* freeze-drying and esterification of CNF/BTCA and subsequent CVD of HTMS. (a) Reproduced with permission from ref. 72. Copyright (2017) Chen *et al*. (b) Reproduced with permission from ref. 656. Copyright (2021) Elsevier B.V. (c) Reproduced with permission from ref. 663. Copyright (2021) Shang *et al*.

Oil adsorbents, namely particulate adsorbents and 3D monoliths, exhibit some excellent features of *in situ* oil removal, easy operation and spontaneous adsorption. It was challenging to collect used adsorbents that spread over wide ocean surface in severe ocean weather, even though they possess magnetism and millimeter size. Furthermore, the complicated regeneration process and limited adsorption capacity may hinder further practical applications of powder-formed adsorbents. In some cases, the combination of particles and 3D monoliths may be an effective approach to adsorb oils from sea surface. 3D monoliths are applied to remove a large amount of oil and then particle adsorbents are used to remove thin residual oil layer. Super liquid-repellent 2D filters are capable of selective oils or organic solvents separation with high efficiency and continuous operation, but their usage may be impeded for separation of heavy oils (*e.g.*, tetrachloromethane). The cleaning and disposal of used filters is a great challenge because the eluting agents may be environmentally unfriendly and even damage the micro/nano structures required by liquid repellence. All oils adsorbents and filter materials face the problem of durability and stability in harsh environments, such as high temperature, corrosive solutions, UV exposure, mechanical disruption and turbulent surroundings. In short, lots of challenges need to be overcome for the design of next-generation adsorbents and filters with liquid repellence.

5.4 Electricity Generation

Energy issues have aroused worldwide and ever-lasting concerns from both academic and commercial circles. Developing advanced techniques to collect hydraulic power has become a promising and effective solution to address energy shortage.[36] Recently, liquid-repellent surfaces have been employed to collect the energy of liquid droplet and generate electricity based on triboelectrification and electromagnetic induction, which are discussed in this section.

5.4.1 Triboelectrification

The triboelectric nanogenerator (TENG), firstly introduced by Wang's group, is based on combined effects of contact electrification and electrostatic induction.[664] Recently, droplet based-TENGs have received extensive research interest because they could effectively convert low-frequency motion of water into electric energy, and the usage of the liquid itself as the triboelectric material overcomes the inevitable friction wear between two solid materials.[36,37,665-667] In this section, droplet based-TENGs with different types of interfaces are divided into liquid-solid TENG and liquid-liquid TENG.[36] For liquid-solid TENG, it is classified into single electrode mode and freestanding mode according to the numbers of electrodes.[668]

Liquid-solid TENG. Liquid-solid TENGs with liquid-repellent solid surfaces can timely shed droplets from the surface without forming liquid film even at high impact frequency, resulting in enhanced electrical output.[669] Cho *et al*. fabricated superhydrophobic TENGs with different surface structures (nanostructures and hierarchical structures) and investigated the effect of two types of morphologies towards electric output performance.[670] The as-prepared TENGs were composed of nanostructured and hierarchically structured $Al(OH)_3$, which were etched on aluminum using alkali or acid etching method and superhydrophobic treatment (heptadecafluoro-1,1,2,2-tetrahydrodecyl-trichlorosilane). As a result, a droplet of water impacting on the hierarchically structured surface rebounded from the surface while the water droplet tended to adhere on the nanostructured surface. The effect of water droplet release height and remaining water on both surfaces on energy harvesting were compared. When water droplets were sequentially released on two surfaces at the height of 1 cm, the output voltage from the nanostructured surface greatly decreased, but the voltage from hierarchically structured surface only slightly fluctuated.

Besides, it was easy for a thin water layer to generate on nanostructured superhydrophobic surfaces due to the disappearance of the air cushion. Therefore, the output voltage significantly reduced and then towards no electric output when the impact velocity of water droplets was low. However, in terms of superhydrophobic surfaces with hierarchical structures, water droplets at high impact velocity were split into different sizes, large droplets rebounded while small droplets got pinned on the hierarchically structured surface. Therefore, the energy harvesting performance was decreased. When another water droplet coalesced with the remaining small droplets, an improvement of output voltage resulted. In addition, superhydrophobic surfaces with hierarchical structures showed excellent resistance to low surface tension liquids and highly viscous liquids, and could generate stable output voltage as well. Differing from traditional TENGs whose electrodes were underlying dielectric layers, Zhang *et al*. synthesized single electrode droplet-based electricity generator (DEG), in which the Al electrode was arranged on the top of different artificial and natural dielectric materials, such as PTFE, silicon, aloe, cicada wing, stone, wood, paper and glass (Fig. 69a).[665] Among these surfaces, stone, wood, paper and glass were pre-modified *via* commercial hydrophobic spray (NeverWet). All the as-mentioned surfaces were demonstrated to be hydrophobic, leading to the rapid refreshment of liquid-solid surfaces after continuous water droplets impinging. When a water droplet impacted the solid surface and then spread to contact the Al electrode, the solid material and Al electrode was connected, and thus there was an electric output between Al electrode and ground. After the water droplet left the solid surface, the output disappeared. The as-prepared electricity generators can drive a calculator or store energy when PTFE or aloe/stone were selected as solid materials, respectively. Besides, the resulted electricity generator could be arranged on any surfaces to harvest kinetic energy of water droplets and then convert into electricity power. Recently, Zhao *et al*. proposed an oil-solid TENG by pasting an Al electrode with 80-μm-thick polyimide or PTFE films, which were then coated with a superamphiphobic SiO_2 layer.[671] The superamphiphobic SiO_2 coating was prepared by depositing 1*H*,1*H*,2*H*,2*H*-perfluorodecyltriethoxysilane on anionic fluorocarbon surfactant modified SiO_2 nanoparticles. Based on the contact and separation between oils and solid surfaces, the as-prepared oil-solid TENG generated an excellent electric output with an open-circuit voltage of 22.5 V, a short-circuit current of 50 nA, a charge density of 9.1 $\mu C\ m^{-2}$ and a power density of 1.23 $mW\ m^{-2}$, which was an order of magnitude higher than that of oil-solid TENGs made from commercial dielectric materials. In addition, the TENG showed excellent durability and retained 90% of the initial electrical output even after 30000 cycles.

In addition to single-electrode mode, Zhao *et al*. reported a freestanding mode TENGs with two electrodes under the dielectric layer.[672] A pair of silver electrodes with 5 mm interval were placed between the Nylon and PTFE, where Nylon was used as a support and PTFE worked as a dielectric material. The resulting freestanding mode TENGs were prepared after the intermediate was sealed by PDMS solution. The generation of electric output from freestanding TENGs relied on effective contact area, which was determined by the water spreading and shrinking on the PTFE surface. When installed on an umbrella, the as-prepared TENGs could generate the maximum power density of 1.838 $W\ m^{-2}$ and light up ~ 30 light-emitting diodes (LEDs) instantaneously. Hu *et al*. developed superhydrophobic TENGs, which consisted of a superhydrophobic layer and several Cu electrodes, for biomedical applications.[673] The resultant TENGs were fabricated after Cu electrodes with double-sided adhesive tapes were coated with hydrophobic fumed silicon *via* a dip-coating method (Fig. 69b). The TENGs exhibited excellent repellency towards various liquids with CAs of near 160° to droplets of HCl, NaOH, water, blood, urine and phosphate buffer. A water droplet impacted the superhydrophobic TENG, due to contact electrification, the water droplet and the solid surface were positively charged and negatively charged, respectively. As shown in Fig. 69c, when the as-prepared TENG was tilted at 20°, a water droplet with positive charges touched the superhydrophobic surface, the first electrode exhibited negative charge, the other electrode displayed positive charge, and thus a pulsed current was generated. When a droplet of water contacted solid surface above the second Cu electrode, this electrode was negatively charged, while the other was positively charged. These two obtained pulsed currents were opposite. The superhydrophobic liquid-solid TENGs can be used for medical application as droplet sensors *via* detecting the signal of pulsed currents. In addition, the device was robust due to the existence of sticky force between superhydrophobic fumed silicon particles and double-sided tapes. Recently, Zhang *et al*. proposed an efficient raindrop energy-based TENG by using a superhydrophobic polyethylene (PE) film as a negative triboelectric layer material.[674] As depicted in Fig. 69d, the outer surface of the PE film was firstly functionalized by plasma to gain superhydrophobicity and then a thin copper upper electrode was attached on, while the inner surface of the film was spin-coated with a thin layer of poly(3,4-ethylenedioxythiophene):poly(styrenesulfonate) (PEDOT:PSS) and was used as a lower electrode. Owing to electrostatic induction, at initial impacting stage between water droplet and the film surface, equal negative charges and positive charges were respectively generated on the film and lower electrode, and no current formed between the lower and upper electrodes. As the droplet spread and contacted with the upper electrode, the film acquired more electrons based on liquid-solid contact electrification, and electrostatically induced positive charges on the lower electrode were transferred to the upper electrode, which resulted in an electrical output. When the water droplet completely spread on the upper electrode, the two electrodes and PE film were connected to form a closed-loop electrical system, enabling the generation of triboelectric charges through the bulk effect between the lower/upper electrode and the film rather than through the traditional interfacial electrostatic induction between the lower electrode and the film. The interfacial screening effect was consequently avoided, and effective triboelectric charge transfer was thus realized. After the droplet rolled off from the film, the charges moved back from the upper electrode to the lower electrode, and the cyclic electricity generation process could thereby be realized by another water droplet impact. When the dripping frequency and height of simulated rain droplets were respectively set to 2 Hz and 15 cm, a 10 μF capacitor was charged to ~ 6 V after 3 min continuous droplets dripping, which could be used to drive a timer for ~ 12 s. Based on the same working mechanism, Chen *et al*. reported another droplet-based TENG by using laser-induced graphene (LIG) electrodes.[675] By using interfacial laser processing method, the TENG was constructed by *in situ* growth of fluorine-doped LIG (F-LIG) and LIG electrodes on the top and bottom sides of fluorinated ethylene propylene (FEP)-coated polyimide (PI) film, and the working mechanism of the assembled F-LIG-based TENG is illustrated in Fig. 69e. After water droplet impacted the FEP surface, charge accumulation at the LIG electrode occurred due to electrostatic induction. When the droplet spread and contacted with the F-LIG electrode, a closed-loop circuit was formed, which triggered rapid charges transfer from the LIG to F-LIG electrodes, leading to a large instantaneous electric power of ~ 53.2 mW due to the extremely short contact duration between the droplet and superhydrophobic F-LIG. The TENG showed high power conversion efficiency, generating a peak power of 15.2 mW with the power density of 47.5 W m^{-2} during the impacting and sliding of a water droplet with volume of 105 μL from a height of 25 cm. Moreover, the TENG possessed superior operational stability under various harsh conditions, maintaining 88% of the peak power at a high humidity level of 96%, 70% of the peak power density after 10000 cycles testing, and functioning well in aqueous solutions with pH values of 3–13.

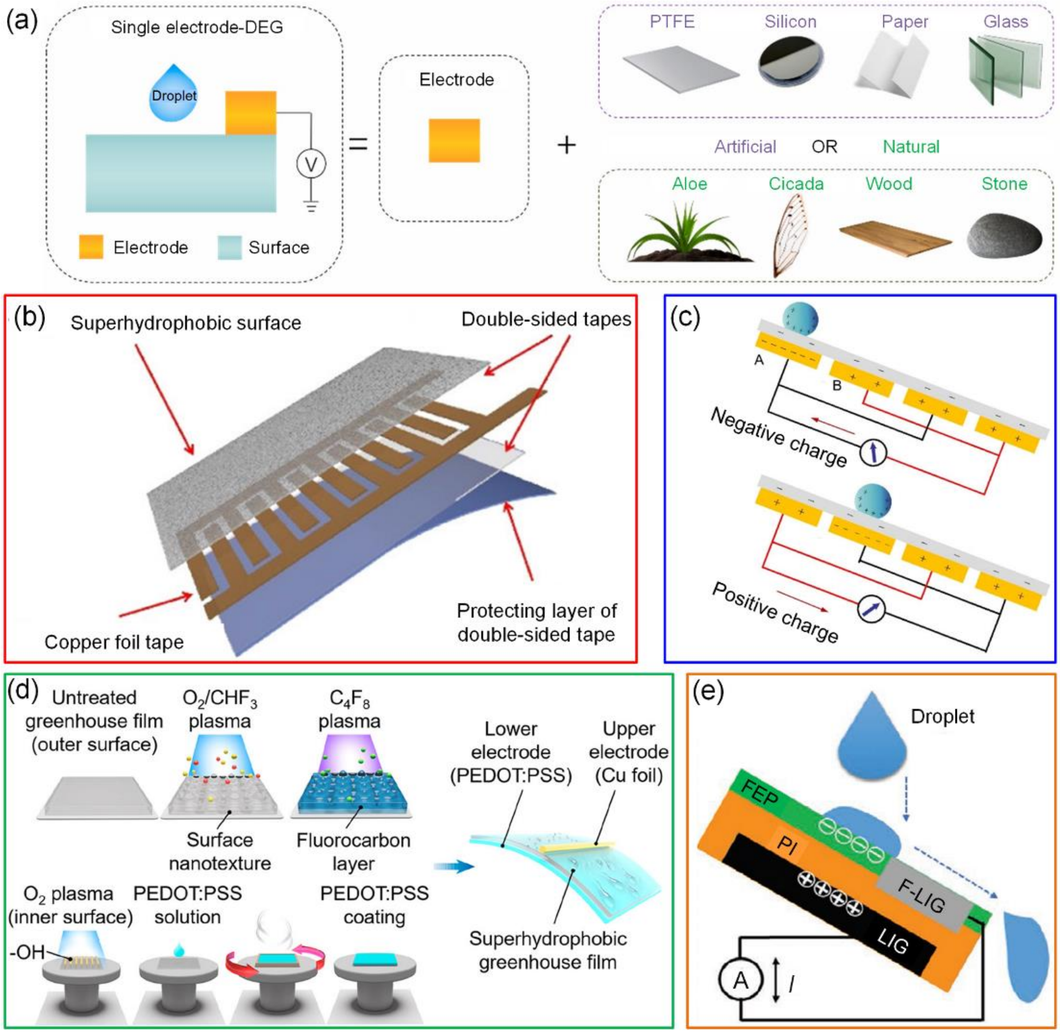

Fig. 69 (a) The schematic of the preparation of single electrode-DEG. Single electrode-DEG constitutes electrode and artificial or natural surfaces, including PTFE, silicon, paper, glass, Aloe, cicada, wood, and stone. (b) The structure diagram of superhydrophobic TENG and (c) the schematic diagram of the electricity generation when a water droplet impacted the as-prepared TENG. (d) Schematic illustration of the fabrication process for the rain droplet energy-based TENG. (e) Working mechanism of F-LIG-based TENG. (a) Reproduced with permission from ref. 665. Copyright (2020) Elsevier B. V. (b, c) Reproduced with permission from ref. 673. Copyright (2020) American Chemical Society. (d) Reproduced with

permission from ref. 674. Copyright (2021) American Chemical Society. (e) Reproduced with permission from ref. 675. Copyright (2021) WILEY-VCH Verlag GmbH & Co. KGaA, Weinheim.

Liquid-liquid TENG. Superhydrophobic TENGs reduced the effective contact area between liquid and solid surfaces, compromising energy conversion efficiency.[676] Besides, it is unsuitable for superhydrophobic TENGs to be applied in high humid surroundings and freezing temperature due to the disappearance of the air cushion, followed by the formation of unwanted wetting transition. As a result, charge generation and transport were screened, and the efficiency of energy harvesting was reduced.[677] Xu *el al*. reported a robust SLIS-based triboelectric nanogenerator and demonstrated charge generation primarily were from the triboelectricity between water and SLIS interface.[676] The as-prepared SLIS-TENG constituted indium tin oxide (ITO) electrodes and a perfluorinated liquid-infused porous PTFE layer (Fig. 70a). At a temperature of below 5 °C, water droplet could easily slide off the SLIS-TENG, but the water droplet was pinned on the superhydrophobic surfaces (*i.e.*, SHS-TENG or PTFE-TENG) (Fig. 70b). The SLIS-TENG retained stable output power of 200 nW and could light up bulbs in both room and freezing temperature (−3 °C). However, bulbs could not be lit up on the superhydrophobic surface at −3 °C (Fig. 70c). It is because the formation of ice/frost was delayed or suppressed on SILS-TENG, promoting droplet mobility on its surface and energy generation. However, there were ice crystals formed on PTFE-TENG owing to the disappearance of air pocket, preventing charge separation in the process of triboelectricity. In addition, the effect of scratches on energy generation performance of SLIS-TENG was negligible because of the self-healing property of SLISs. The SLIS-TENG was demonstrated to be robust and durable after 10,000 consecutive water droplets impact, with only 0.4% of lubricant loss.

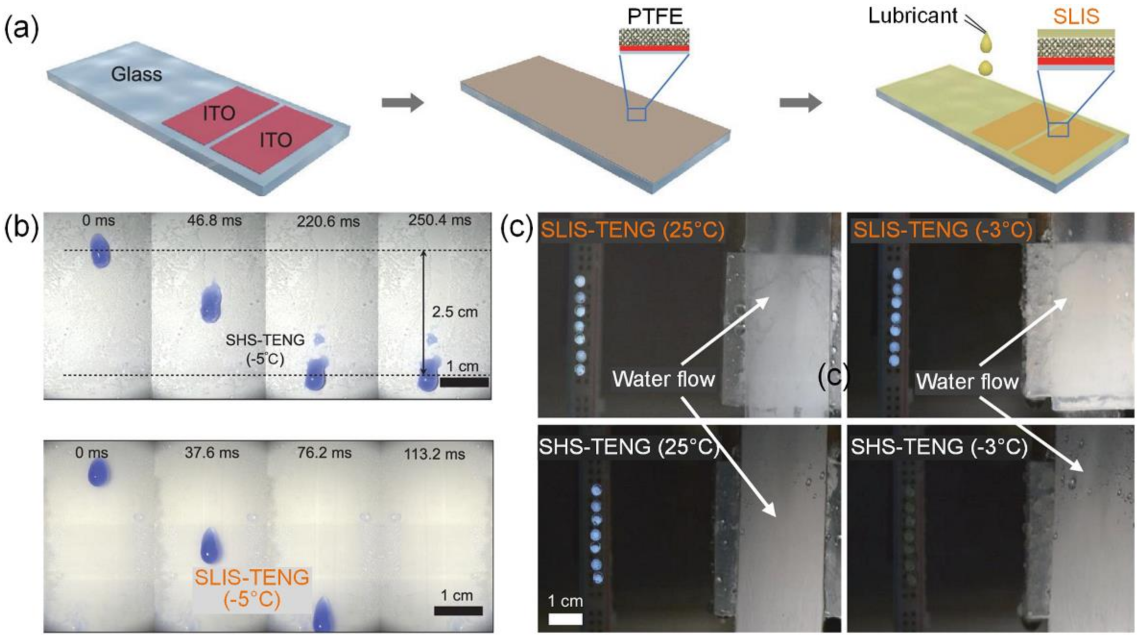

Fig. 70 (a) The schematic diagram of the preparation of SLIS-TENG. (b) A water droplet slides from SHS-TENG and SLIS-TENG at the temperature of −5 °C. (c) LEDs were lighted up by continuous water flow on SLIS-TENG at 25 and −3 °C, and on SHS-TENG at 25 °C, but could not be lighted up on

SHS-TENG at −3 °C. (a–c) Reproduced with permission from ref. 676. Copyright (2020) Xu *et al*.

5.4.2 Electricity generation *via* electromagnetic induction

Besides the above-discussed TENGs, electromagnetic induction on liquid-repellent surfaces has also been exploited to construct electricity generators.[678-680] As shown in Fig. 71a, Ma *et al*. proposed a superhydrophobic surface-based magnetoelectric system that could generate electricity from falling water droplets *via* mechanical-electrical conversion.[678] The system was composed of a superhydrophobic top surface containing a conductive coil, glycerin droplets, and a superhydrophobic magnetic $Nd_2Fe_{14}B$ powder/Ecoflex base. Falling water droplets impacted the upper part and rebounded from the superhydrophobic surface, during which the glycerin droplets sandwiched between two superhydrophobic surfaces were compressed to semi-Cassie state and then recovered to Cassie state. The deformation and recovery of the glycerin droplets changed the distance between the coil and the magnetic base, which changed the magnetic flux through the coil and thereby generated electricity. Multiple bouncing of the water droplet on the superhydrophobic surface enabled the magnetic flux passing through the coil to increase/decrease periodically, which resulted in a damping electric performance. When a 50 μL water droplet was released from a height of 10 cm, the first impacting generated electricity with peak power of 23.8 μW. Afterwards, they developed another superhydrophobic surface-based electricity generator by using water-based ferromagnetic liquid droplet sliding induced magnetic flux change (Fig. 71b).[679] As illustrated in Fig. 71c, upon tilting the superhydrophobic substrate, the ferromagnetic liquid droplet containing randomly distributed Fe_3O_4 nanoparticles started sliding on the surface and moved onto the magnetic field area, after which the nanoparticles were magnetized and thereby changed the magnetic flux passing through the conductive coil, allowing electricity generation in the coil. After the ferromagnetic liquid droplet rolled away from the magnetic field area, the magnetic flux recovered and electricity generated in the coil again. When a 100 μL ferromagnetic liquid droplet slid on the surface (tilting speed of 9.5° s^{-1}) under a 13 mT magnetic field, an electrical response with output power of 2.1 nW were recorded. Similarly, electricity generation under water by using oily magnetic nanofluid droplet sliding on underwater superoleophobic surface has also been reported.[680]

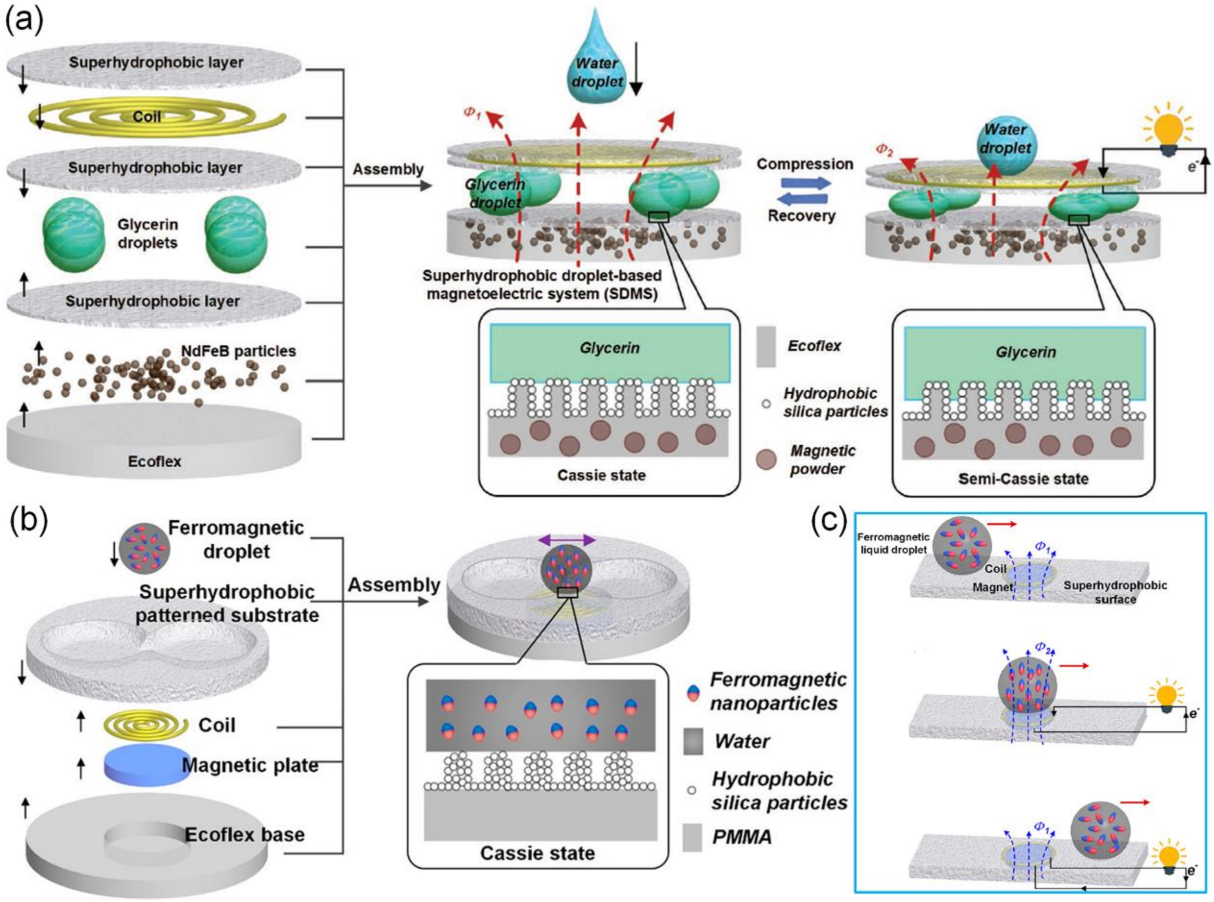

Fig. 71 Electricity generation *via* electromagnetic induction on liquid-repellent surfaces. (a) Schematic diagram of a superhydrophobic surface-based magnetoelectric system that generates electricity from falling water droplets. (b) Illustration and (c) mechanism of a superhydrophobic surface-based electricity generator by using water-based ferromagnetic liquid droplet sliding induced magnetic flux change. (a) Reproduced with permission from ref. 678. Copyright (2020) WILEY-VCH Verlag GmbH & Co. KGaA, Weinheim. (b, c) Reproduced with permission from ref. 679. Copyright (2021) American Chemical Society.

5.5 Enhanced Heat Transfer

With the rapid development of high-power electronic devices such as microprocessors, radars and advanced lasers, highly efficient heat dissipation and cooling by enhanced heat transfer is becoming increasingly important.[681-684] As a useful and efficient process to transfer energy, liquid-vapor phase change (*e.g.*, boiling and condensation) heat transfer has drawn great research interest in recent years, and critical heat flux (CHF) and heat transfer coefficient (HTC) are always employed to evaluate its heat transfer performance.[33-35,685-691] CHF is the maximum heat flux, beyond which a much less effective filmwise heat transfer or even a boiling crisis develops, and HTC is defined as the heat flux divided by the temperature difference (ΔT) between the surface and the bulk fluid (*i.e.*, superheat for boiling and supercooling for condensation). The liquid-vapor phase-change heat transfer involves recurrent nucleation, growth, coalescence, and departure of a new phase (that is, bubbles for boiling and droplets for condensation),[33-35,692] which is highly dependent on the wettability of the surface.[74,692-696] For boiling heat transfer, hydrophobicity promotes the nucleation, whereas hydrophilicity is preferred for the growth and departure of bubbles.[34,689] Meanwhile, hydrophilicity can also favor rapid liquid re-wetting of the surface during boiling, which restrains the formation of a vapor blanket between the surface and bulk liquid at high superheat, thereby delaying the boiling crisis that leads to significant increase of the surface temperature.[34,689] It is well verified that (super)hydrophobic surfaces offer better nucleate boiling heat transfer than hydrophilic surfaces at low superheat due to the siginificantly increased active nucleation site density, but their performance deteriorate sharply and become worse than hydrophilic surfaces at high superheat, as the high superheat results in high-density vapour bubbles which coalesce rapidly and form a relatively insulated evaporating vapor blanket on the (super)hydrophobic surface acting as a thermal barrier for heat transfer (*i.e.*, film boiling).[34,686,689,697-700] To delay the early transition into filmwise boiling and the formation of the insulating vapor layer that greatly decreases heat transfer efficiency, some strategies, such as decorating (super)hydrophobic patterns on (super)hydrophilic surface,[686,701-703] and boiling on a superhydrophobic surface in the Wenzel wetting state,[704,705] have been proposed to increase the CHF and/or HTC compared with their flat hydrophilic counterparts. Even so, the research on boliling heat transfer mainly focuses on those micro/nano structured (super)hydrophilic surfaces with high wickability rather than (super)hydrophobic surfaces. By contrast, condensation heat transfers on liquid-repellent surfaces (including superhydrophobic surfaces and SLISs) have drawn keen research interest in recent years, and much progress have been achieved.[34,35,74,315,446,449,573,687,689,706-716] Therefore, in this section, we emphatically discuss the condensation heat transfer on superhydrophobic surfaces and SLISs.

Heat transfer behavior of condensation can be described by the typical curve depicted in Fig. 72a where the heat flux (Q) is plotted as a function of surface subcooling (ΔT).[33] When the subcooling is very low, condensation is negligible and the heat is mostly transferred by convection (region A in Fig. 72a). As the subcooling increases continuously, liquid vapor starts to nucleate at the onset of droplet nucleation (ODN), and dropwise condensation mode occurs, which enables a monotonic increase of the heat flux due to the accelerated droplet nucleation, growth, and removal refresh the nucleation sites rapidly, until the maximum value of CHF is obtained (region B in Fig. 72a). Taking superhydrophobic surfaces as examples, Fig. 72b shows their typical dynamic processes of recurrent dropwise condensation, as well as the characteristic diameters at each stage.[34] The processes starts from the heterogeneous nucleation of droplets with critical diameters of several nanometers. After continuous condensation and growth, the droplets with diameters in the range of 2–500 μm coalense with each other, followed which the condensed droplets are removed from the surfaces through either surface energy release-induced jumping (~ 2–1000 μm in diameters) or gravity-driven sliding (1.5–2.5 mm in diameters). The removal of condensed droplets effectively refreshes the nucleation sites on the surfaces, which favors the heat transfer efficiency of superhydrophobic surfaces. As shown in the region C of Fig. 72a, further increase of the subcooling leads to too fast nucleation and the condensed droplets cannot shed off from the surface but tend to coalesce into a liquid film, and a transition heat transfer mode with sharply decreased Q occurs. At higher subcoolings, liquid film eventually formed on the surface and results in a filmwise condensation mode that is characterized by relactively low CHF and HTC. Liquid-repellent surfaces with low CAH towards droplets enable rapid removal (*via* jumping or/and sliding) of the condensed droples and significantly delay the transition to filmwise condensation even at high subcooling, which shows distinct advantages over hydrophilic surfaces with high CAH. Therefore, the droplet condensation heat transfer on liquid-repellent surfaces that functioned in region B (Fig. 72a) is widely explored.

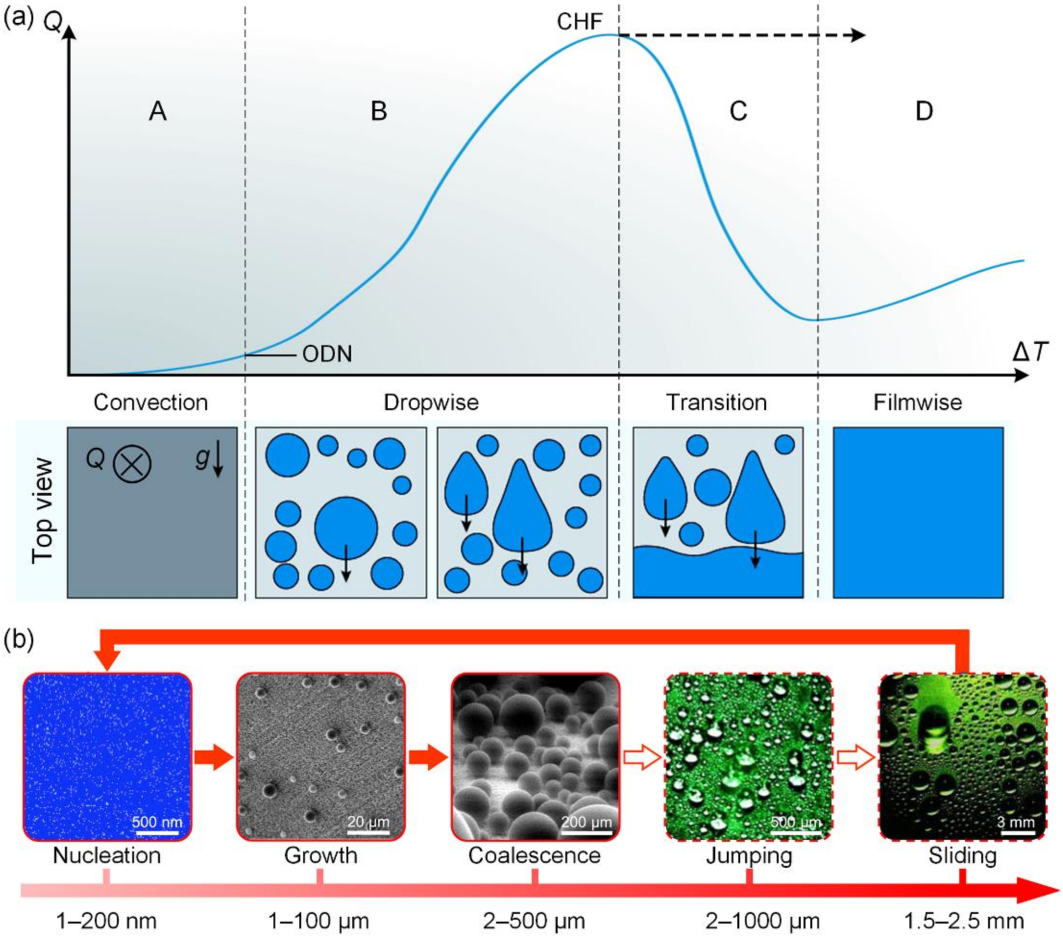

Fig. 72 (a) Schematic diagram of typical heat transfer curve of condensation. (b) Typical dynamic processes of the recurrent dropwise condensation on superhydrophobic surfaces with their corresponding characteristic scales in diameters. (a) Reproduced with permission from ref. 33. Copyright (2016) Macmillan Publishers Limited. (b) Reproduced with permission from ref. 34. Copyright (2018) Elsevier Inc.

It is well-known that nanostructured (either nanostructured alone or micro/nano hierarchical) superhydrophobic surfaces could potentially favor dropwise condensation, while microstructured ones often lead to highly pinned Wenzel droplets during short-term condensation,[717,718] making those nanostructured ones more appealing towards dropwise condensation enhanced heat transfer. Typically, when condensation develops on a nanostructured superhydrophobic surface characterizing with high CA and low CAH (*i.e.*, the Cassie-Baxter wetting state), three morphologies (Fig. 73a), including suspended, partially wetting, and pinned droplets, can be observed.[711,719-721] Miljkovic *et al*. demonstrated the critical effect of droplet morphology on droplet growth dynamics and heat transfer during condensation on superhydrophobic nanostructured surfaces.[706] They fabricated silicon nanopillar surfaces by using e-beam lithography and deep reactive ion etching of silicon wafer, which was then silanated by CVD of (tridecafluoro-1,1,2,2-tetrahydrooctyl)-1-trichlorosilane to obtain superhydrophobicity. *In situ* ESEM study showed that both suspended and partially wetting droplets underwent coalescence-induced jumping at identical length scales, but the initial growth rate of the partially wetting droplets was 6 times higher than that of the suspended ones due to the increased contact with the substrate. By using a thermal resistance-based droplet growth model, the authors found that the partially wetting droplets had 4–6 times higher heat transfer rates than that of the suspended ones, which was attributed to the siginificant thermal resistance caused by the air "cushion" under the suspended droplets. Furthermore, they showed that compared with a flat hydrophobic silicon surface, the superhydrophobic nanostructured surfaces had 56% heat flux enhancement for the partially wetting droplet morphology but 71% heat flux degradation for the suspended one. By contrast, under increased surface subcooling (heat flux) and/or saturation pressure, reduced nucleation size and increased nucleation site density result in the formation of highly pinned droplets that even develop into flooding condensation, which severely deteriorates the heat transfer efficiency of the surfaces.[687,711,722-724] Therefore, ensuring rapid droplet shedding and minimizing the negative effect of the air "cushion" by favoring partially wetting droplet morphology need sufficient consideration when design superhydrophobic surfaces for enhanced heat transfer.

The droplet wetting morphologies are highly depedent on the surface properties and condensation conditions. Enright *et al*. proposed that the local energy barriers was a key to the droplet growth during condensation, and the emergent droplet morphology was influenced by the droplet-droplet interactions that were governed by the nucleation density (*i.e.*, the average spacing between nucleation sites $\bar{L}$ relative to the structure length scale l, $\bar{L}/l$).[719] Suspended droplets with Cassie-Baxter state nucleating on the tips of the structures were unconditionally stable in the absence of droplet interactions and gravity. They showed that the droplet morphology was dictated by the intricate liquid/structure interaction dynamics, and it could be roughly estimated by an energy criterion that compared the energies of the non-equilibrium advancing Cassie-Baxter ($\cos\theta_{\text{adv,C-B}} = -1$) and Wenzel ($\cos\theta_{\text{adv,W}} = r\cos\theta_{\text{adv,flat}}$) states with a dimensionless energy ratio:

$$E^{*}=\frac{\cos\theta_{\text{adv,C-B}}}{\cos\theta_{\text{adv,W}}}=\frac{-1}{r\cos\theta_{\text{adv,flat}}} \qquad (32)$$

where $\theta_{\text{adv,flat}}$ is the advancing CA of a flat surface. As shown in the regime map depicting the dominant wetting behavior during condensation (Fig. 73b), Wenzel droplet morphologies were favored when $E^{*} \geq 1$, while partially wetting Cassie-Baxter droplets formed when $E^{*} \leq 1$. Meanwhile, the authors found that the droplet morphology was also influenced by the droplet nucleation density, and when $\bar{L}/l \geq 2$–5 and $E^{*} \leq 1$, the formation of partial wetting Cassie-Baxter droplets was favored, while when $\bar{L}/l$ was lower than the critical value, Wenzel droplets formed regardless of the energetically preferred wetting state. Wen *et al*. studied the wetting transition of condensed droplets on a nanostructured superhydrophobic surface with tapered nanogaps, and demonstrated that the surface wetting property, topography, and condensing condition played synergistic effect on the wetting state and dynamic behavior of the condensed droplets.[721] Copper plate was firstly nanostructured by chemical oxidation and then coated with (1*H*,1*H*,2*H*,2*H*-perfluorooctyl)silane layer *via* CVD, rendering the surface superhydrophobic (Fig. 73c). Results showed that the surface subcooling (ΔT) had significant effect on the nucleation size and nucleation site density (Fig. 73d). When ΔT was set to be 0.3 K, condensation started from the nucleation of droplets with large size and the condensed droplets tended to be in the suspended Cassie-Baxter state (Fig. 73e), enabling them to shed off the surface rapidly *via* spontaneous jumping with a maximum size of less than several tens of micrometers (Fig. 73f). By increasing the surface subcooling, more droplets nucleated on the surface but their critical nucleation size decreased (Fig. 73d), resulting in pining of the condensed droplets or even flooding of the surface. Taking $\Delta T = 0.8$ K as an example, the nucleated droplets with reduced size could stay at the bottom of the nanogaps and then easily merged within the nanogaps due to the spatial confinement effect (Fig. 73g), leading to the formation of pinned droplets with obviously increased size on the surface (Fig. 73h), and gravity-induced sliding dominated the subsequent shedding of the condensed droplets. These results demonstrated that the transition from suspended Cassie-Baxter and partially wetting states to pinned Wenzel state or even flooding could be effectively suppressed by decreasing the length scale of the surface structures. This was also verified by Seo *et al*. who showed that improving the nanoscale coating homogeneity and reducing the structure length scale favored effective anti-flooding during condensation on superhydrophobic surfaces and thereby enhanced the long-term heat transfer efficiency.[724] They deposited nanoscopically non-uniform and uniform coating by liquid-phase and vapor-phase depositions of 1*H*,1*H*,2*H*,2*H*-perfluorodecyltrimethoxysilane, respectively. As shown in Fig. 73i, the non-uniform coating consisted of solid-phase agglomerates around which a thin dilute-phase film of disordered molecules located, while the uniform coating had a well-ordered and highly uniform molecular film. Rough CuO structures with different length scales were prepared by chemical immersion methods (Fig. 73j). Relatively large CuO structures had height of ~ 1.0 μm, pitch of ~ 300 nm, solid fraction of ~ 0.023, roughness factor of ~ 10, while relatively small CuO structures showed height of ~ 200 nm, pitch of ~ 150 nm, solid fraction of ~ 0.020, and roughness factor of ~ 12. Condensation testing results showed that compared to superhydrophobic surface with large CuO structures and non-uniform coating, the one with small structures and uniform coating provided a ~ 130% enhanced average HTC with ~ 14% larger supersaturation range for droplet jumping.

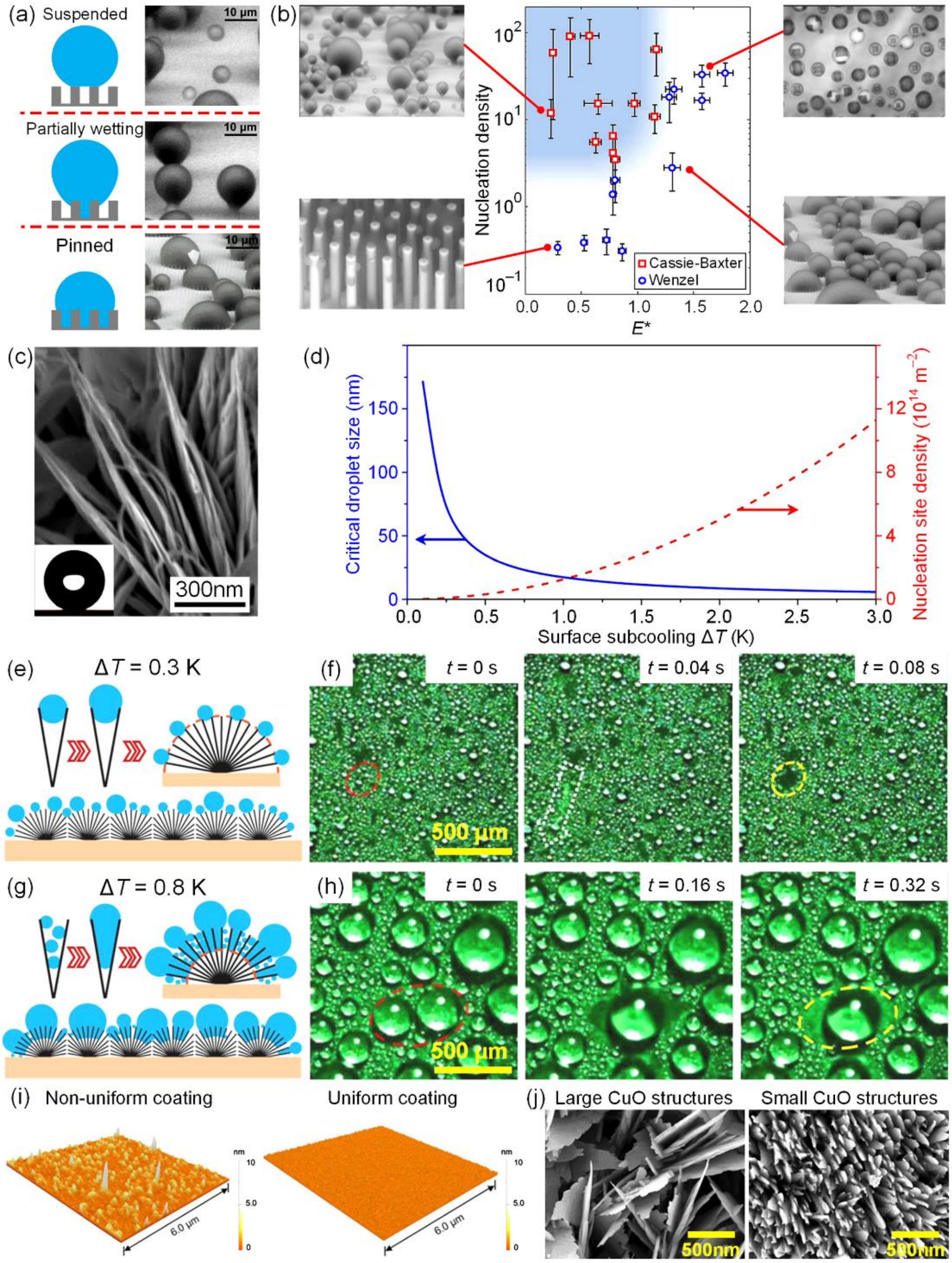

Fig. 73 (a) Schematic diagram and corresponding ESEM images of typical droplet morphologies (*i.e.*, suspended, partially wetting, and pinned) on a superhydrophobic surface during condensation. (b) Regime map showing the dominant wetting behavior observed during condensation, as well as the corresponding ESEM images. (c) SEM image of the nanostructured copper surface with tapered nanogaps. The inset shows the superhydrophobicity of the surface. (d) Critical droplet size and nucleation site density as a function of surface subcooling (Δ*T*). Schematic diagram of droplet growth under Δ*T* of (e) 0.3 K and (g) 0.8 K. Time-lapse images of condensation at Δ*T* of (f) 0.3 K and (h) 0.8 K. (i) AFM images of nanoscopically non-uniform and uniform coating. (j) SEM images of large and small CuO structures. (a) Reproduced with permission from ref. 720. Copyright (2013) ASME. (b) Reproduced with permission from ref. 719. Copyright (2012) American Chemical Society. (c–h) Reproduced with permission from ref.

721. Copyright (2017) American Chemical Society. (i, j) Reproduced with permission from ref. 724. Copyright (2020) American Chemical Society.

To avoid the failure of superhydrophobicity and to delay the transition to flooding during condensation, well-designed closely packed nanostructures that can stabilize the trapped air “cushion” and enhance droplets self-propelled jumping upon coalescence (Fig. 74a, also see Section 4.2.2) are desired for heat transfer enhancement.[33-35,51,443,444,446,448,687] For example, Miljkovic *et al*. prepared nanostructured CuO films on Cu tube surface by chemical oxidation in a hot alkaline solution composed of $NaClO_2$, NaOH, $Na_3PO_4 \cdot 12H_2O$, and deionized water (3.75:5:10:100 wt%), which were then functionalized by using CVD of a fluorinated silane (trichloro(1*H*,1*H*,2*H*,2*H*-perfluorooctyl)silane).[687] As shown in Fig. 74b, sharp, knife-like CuO nanostructures with heights of ~ 1 μm, solid fraction of ~ 0.023, and roughness factor of ~ 10 were constructed. Depending on the very efficient removal of the coalesced droplets (radius of ~ 8 μm) *via* self-propelled jumping (Fig. 74c and d), a 25% higher overall heat flux and 30% higher HTC were achieved on the nanostructured CuO superhydrophobic surfaces compared with conventional dropwise condensation on smooth Cu surfaces at low supersaturations (< 1.12). However, at high surface subcooling and/or supersaturations, the droplet nucleation density increased sharply and the interactions between droplets occurred on a similar length scale as the spacing among nanostructures (~ 1 μm), leading to the formation of highly pinned Wenzel droplets rather than the energetically favorable partially wetting Cassie-like droplets, which triggered the transition to flooding condensation (Fig. 74e).

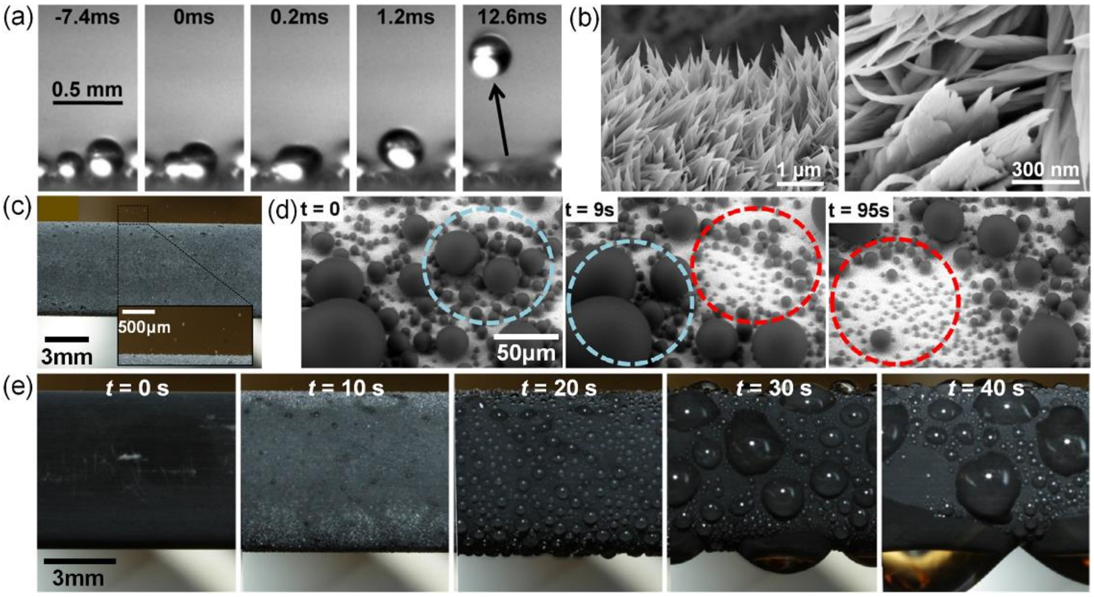

Fig. 74 (a) Side-view images of self-propelled droplet jumping powered by dynamic coalescence. (b) SEM images of knife-like CuO nanostructures. (c) Optical image of droplets jumping on the Cu tube with superhydrophobic nanostructured CuO films. The inserted image shows the magnified view of the jumping droplets. (d) Time-lapse ESEM images of droplets coalescing and jumping. (e) Flooding condensation on the the tube under high supersaturations. (a) Reproduced with permission from ref. 443. Copyright (2009) American Physical Society. (b) Reproduced with permission from ref. 687. Copyright (2012) American Chemical Society.

By reduceing the permeation of water vapor molecular into the intervals between nanowires on condensing surfaces (Fig. 75a), Wen *et al.* proposed to enhance their condensation heat transfer even under large surface subcooling (up to 24 K) *via* controlling droplet nucleation based on spatial confinement effect.[710] By using a two-step porous anodic alumina template-assisted electro-deposition method, the authors prepared closely packed copper nanowires on copper substrate with an average diameter of 200–240 nm, a height of 20 μm, and an average interval of 100–140 nm (Fig. 75b), which were then funationalized by *n*-octadecanethiol for hydrophobicity. When the surface subcooling was small (ΔT < 8 K), the condensed droplets were mostly removed by self-propelled jumping (Fig. 75c),[710,725] and both heat flux and HTC gained more than 100% enhancement over the dropwise condensation on a flat hydrophobic surface, and the CHF of ~ 136 kW m^{-2} was measured at surface subcoolings of 6 K.[710] However, as ΔT increased to 9 K, the condensed droplets grew rapidly and then merged to be larger, which resulted in droplet sliping and thereby surface refreshing by sweeping (Fig. 75d).[725] When ΔT further increased to 18 K, large condensed droplets with diameters up to > 2 mm sticked on the surface and highly pinned Wenzel droplets were observed (Fig. 75e), which led to the undesired flooding condensation and greatly degraded the heat transfer performance.[725] To delay the transition to flooding condensation on such surface with uniform nanowires under large ΔT, Wen *et al*. proposed to control the droplet nucleation, growth and departure by using superhydrophobic surface with micropatterned nanowire arrays (Fig. 75f).[725] It was found that the jumping droplet condensation could be well maintained when ΔT was increased from 2 K to 9 K (Fig. 75g and h), and although the sweeping droplet condensation was observed when ΔT increased to 18 K (Fig. 75i), the flooding condensation was avoided even when their testing ΔT was up to 28 K. As a result, compared with the uniform nanowired surface, the micropatterned one showed significantly enhanced heat transfer performance in the full tested surface subcooling range of 0–28 K, and the CHF was increased by 37% from 136 to 186 kW m^{-2} at ΔT of 14 K, which also indicated that the region of ΔT for self-propelled droplet jumping was expanded by 133% from 6 to 14 K. The ehhanced heat transfer was attributed to the combination of the spatial control of nucleation for mobile droplets using the closely packed nanowires (Fig. 75j) and the Laplace pressure-powered spontaneous outward moving of the droplets for rapid removal using micropatterned nanowire arrays (Fig. 75k). Tang *et al*. prepared a hierarchical micro-nanostructured superhydrophobic surface with tapered micro and nano gaps *via* electrodeposition and alkaline oxidation.[718] Condensation testing showed that the nanostructures enabled jetting of microdroplets *via* tapered nanogaps induced Laplace pressure and self-propelled jumping of submillimeter droplets upon coalescence, and the tapered microstructures favored to push the pinned droplets out of the microgaps *via* additional Laplace pressure generated by the tapered microtopology (*i.e.*, dislodging). The subsequent droplets coalescence on top of the microstructures triggered microdroplets navigation before finally shedding off from the surface, which prevented the pinning of the condensed droplets, and thereby delayed flooding and enhanced heat transfer performance. Compared with the superhydrophobic surface with nanostructures alone, the surface with hierarchical micro-nanostructures showed much longer duration for dropwise condensation (3 h *vs* 10 h), and the highest heat flux of 223 ± 9.8 kW·m^{-2} at ΔT = 10 K and the maximum HTC of 218 ± 29 kW·m^{-2}·K^{-1} at ΔT = 0.2 K were achieved.

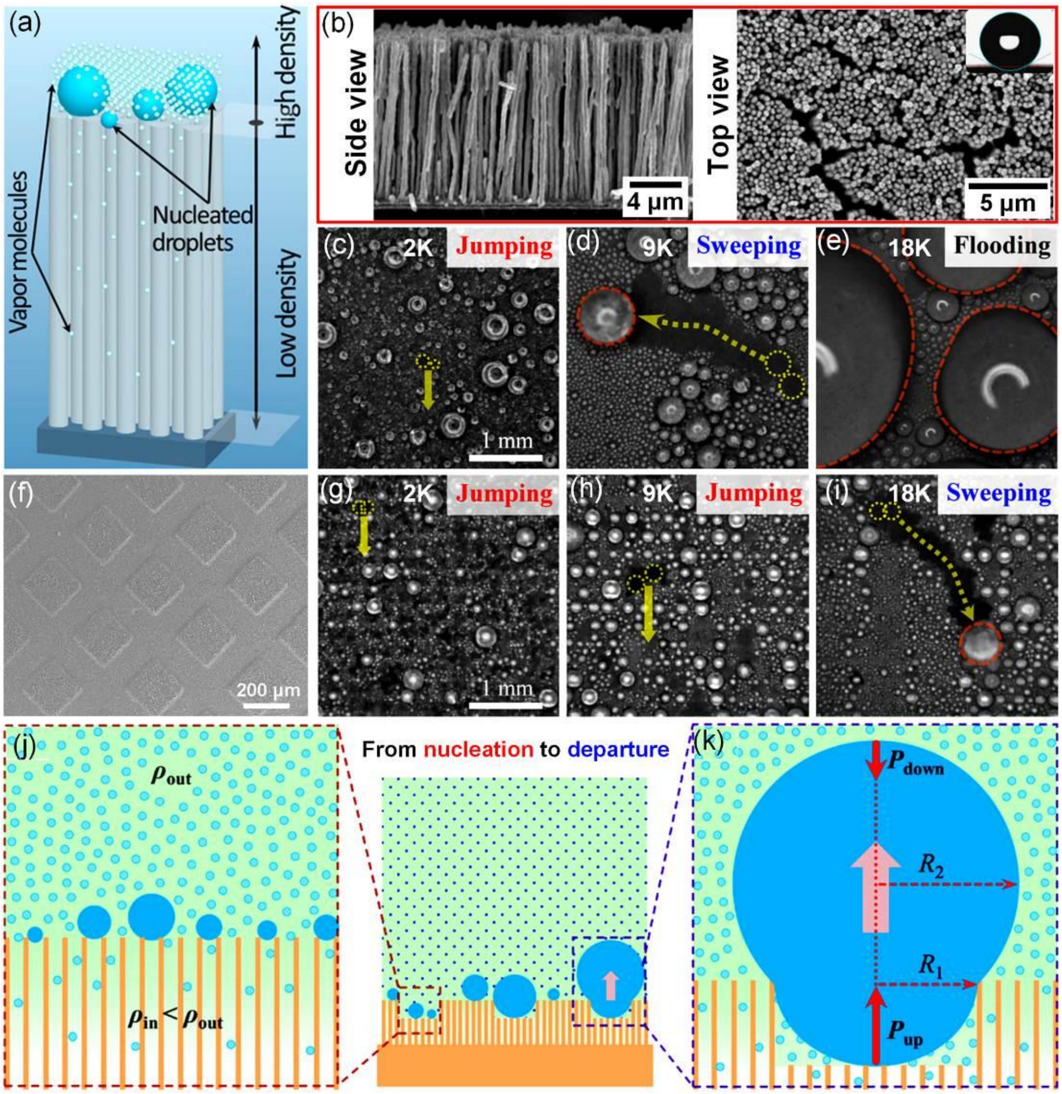

Fig. 75 (a) Schematic diagram showing the spatial confinement effect that prohibits droplet formation in the intervals between nanowires due to the reduced permeation of vapor molecules. (b) SEM images of the superhydrophobic surfaces with closely packed straight nanowires, and their condensations at surface subcoolings of (c) 2 K, (d) 9 K, and (e) 18 K. (f) SEM image of the hierarchical nanowired superhydrophobic surfaces, and their condensations at surface subcoolings of (g) 2 K, (h) 9 K, and (i) 18 K. Schematic diagram showing the (j) nucleation control and (k) rapid departure of condensed droplets on the hierarchical superhydrophobic surface with micropatterned nanowire arrays. (a, b) Reproduced with permission from ref. 710. Copyright (2017) Elsevier Ltd. (c–k) Reproduced with permission from ref. 725. Copyright (2017) American Chemical Society.

Meanwhile, it was found that during the fabrication of closely packed straight nanowires, they tend to agglomerate due to surface tension, leading to the formation of numerous micro-defects with size of 1–3 μm (Fig. 76a and b).[711] The micro-defects showed much smaller energy barrier (~ -5.7×10^{-12} J) compared with that required in the intervals between nanowires (~ -6×10^{-15} J) for droplet nucleation, enabling them to become preferred nucleate sites, which subsequently promote the formation of highly pinned droplets at large surface subcoolings (Fig. 76c).[711] To avoid the heat transfer deterioration caused by the agglomeration of straight nanowire arrays, Wen *et al*. proposed to construct superhydrophobic surface with 3D nanowire networks with interconnections among them.[711,726] The authors fabricated 3D porous anodic alumina template by anodizing impure (purity < 99.5%) Al foil, which was then used as a template to prepare 3D copper nanowire networks through a two-step electro-deposition method (Fig. 76d and e). Then a fluorinated silane (trichloro(1*H*,1*H*,2*H*,2*H*-perfluorooctyl)-silane) was uniformly deposited to render the resultant surface superhydrophobic. Compared with the straight nanowire arrays, the proposed 3D nanowire networks provided homogeneous surface morphologies without micro-defects, and the interconnections reduced the effective spacing between neighboring nanowires, which enabled spatially controlled nucleation at the top of nanowires for the formation of suspended or partially wetting droplets and thereby enhanced stable droplet jumping even at large surface subcoolings of up to 28 K (Fig. 76f). In addition, the interconnections reduced the effective thermal resistance of the nanowire layer, which favored the heat exchange between the droplets and condensing substrate. As a result, significant enhancement of heat transfer was observed on the superhydrophobic 3D nanowire networks (Fig. 76g and h), and a 100% higher heat transfer flux was obtained at large surface subcooling, for example, heat flux of ~ 280 kW·m^{-2} was realized when ΔT = 28 K.

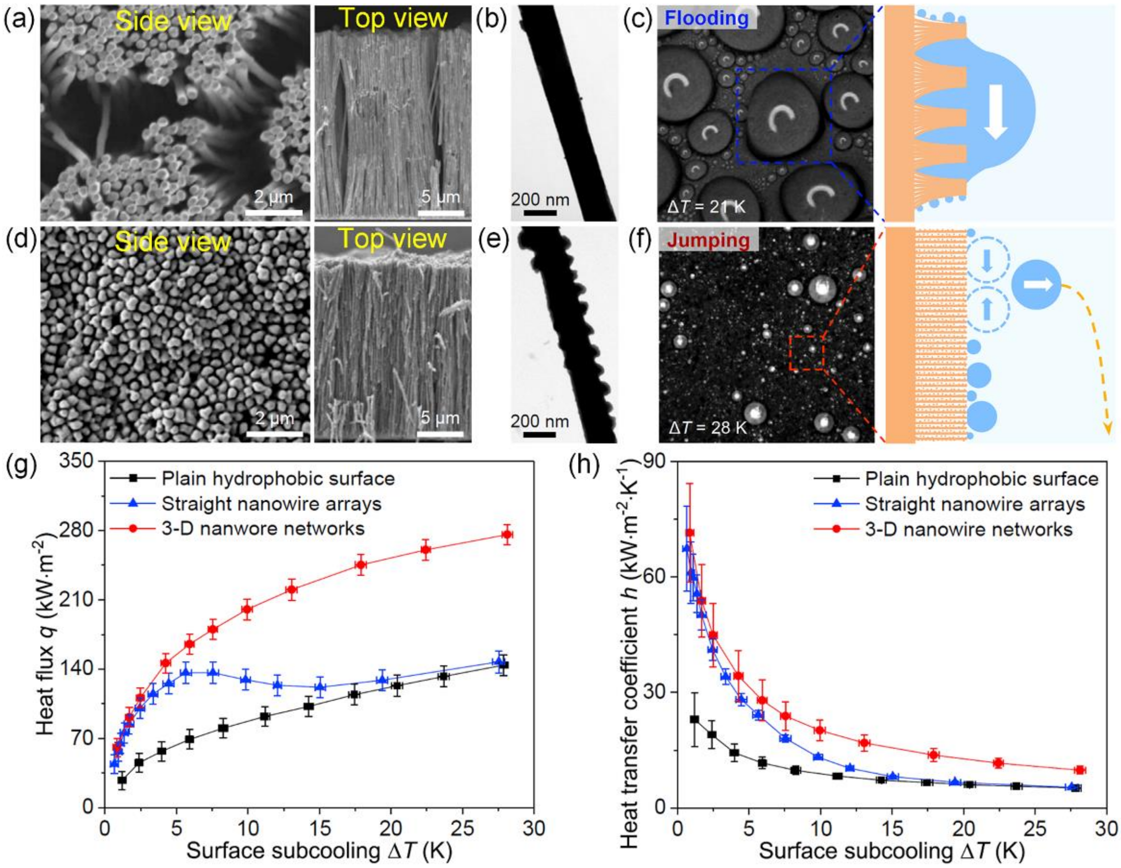

Fig. 76 (a) SEM images of straight nanowire arrays with micro-defects. (b) Transmission electron microscopy images of a single straight nanowire. (c) Flooding of the superhydrophobic straight nanowire arrays at ΔT = 21 K. (d) SEM images of 3D nanowire networks. (e) Transmission electron microscopy images of a single nanowire with nanoscale bumps from 3D nanowire networks. (f) Stable droplet

jumping condensation on the 3D superhydrophobic nanowire networks without flooding under large Δ*T* of 28 K. (g) Heat flux and (h) HTC as a function of surface subcooling Δ*T*. Reproduced with permission from ref. 711. Copyright (2017) Elsevier Inc.

Patterning superhydrophobic surfaces with wettability contrast (*i.e.*, designing biphilic surfaces) is also demonstrated to be capable of delaying the flooding phenomenon at high surface subcoolings so as to improve their heat transfer performance.[34,35,444,446,723,727-730] For example, Hou *et al*. reported enhanced heat transfer *via* recurrent filmwise and dropwise condensation on a beetle inspired superhydrophobic surface with hydrophilic patterns.[446] They fabricated micro-scale SiO_2 patterns on Si wafer using standard photolithography and oxide etching processes, and then obtained micropillars with SiO_2 tops by etching using tetramethylammonium hydroxide, which was followed by a modified deep reactive ion etching process to construct nanograss on the valleys of the micropillar arrays. After conformally coating a thin hydrophobic layer and then selectively removing the superficial SiO_2 layers and the fluoride polymer coating on the top of the micropillars by buffered oxide etching, the hydrophilic micropillars patterned superhydrophobic surface (Fig. 77a) was obtained. The hydrophilic tops of the micropillars facilitated fast droplet nucleation and initial growth (*i.e.*, filmwise condensation), while the valleys between the micropillars that were covered with superhydrophobic nanograss guaranteed the dropwise condensation and coalescence-induced self-propelled droplet jumping (Fig. 77b). Condensation testing under high concentration of noncondensable gas showed that the patterned superhydrophobic surface had much higher HTC (~ $1.5 \pm 0.3\ \mathrm{kW{\cdot}m^{-2}{\cdot}K^{-1}}$) than superhydrophobic surface with nanograss alone (~ $0.6 \pm 0.2\ \mathrm{kW{\cdot}m^{-2}{\cdot}K^{-1}}$) and flat hydrophobic surface (~ $0.9 \pm 0.2\ \mathrm{kW{\cdot}m^{-2}{\cdot}K^{-1}}$). Ölçeroğlu *et al*. prepared nickel nanostructures on Si surfaces *via* the self-assembly and metallization of *Tobacco mosaic virus*, and then functionalized the surfaces by using either CVD of a monolayer of trichlorosilane or spin coating of a nanoconformal PTFE film to render them superhydrophobic, which were then patterned using standard lithography techniques and oxygen plasma etching to construct superhydrophilic islands with diameters of 3 μm (Fig. 77c).[723] At low supersaturation (*e.g.*, 1.06), nucleation on the superhydrophobic surface was largely suppressed, while nucleation was significantly promoted on the superhydrophilic islands, enabling 250% larger nucleation density on the patterned surface than superhydrophobic surface without patterns, and both surfaces promoted continuous coalescence induced self-propelled droplets jumping. At high supersaturation (*e.g.*, 1.54), droplets nucleated randomly initially in a suspended morphology on both surfaces. The superhydrophobic surface without patterns subjected rapid transition to local flooding within 60 s. By contrast, the nucleated droplets on patterned surface gradually self-organized into an ordered array as they grew and coalesced laterally (Fig. 77d), enabling continuous formation of large droplets that were loosely bound to the islands and easy to shed off to refresh the suface, which prevented the transition to flooding. In addition, flooding occurred on the superhydrophobic surface when the Δ*T* was larger than 20 K, but the patterned surface only witnessed a transition from droplets jumping to shedding removal with no flooding occurred even when the Δ*T* increased up to the testing limit of 25 K

(Fig. 77e). Recently, Hoque *et al*. coupled individual droplet growth and condensation heat transfer with droplet-jumping dynamics to optimize the design of superhydrophobic nanostructured surfaces with wettability contrast patterns for maximum heat flux.[730] They reported that the wettability of the patterns should not be optimized to minimize droplet adhesion while maximizing individual droplet growth rates rather than toward minimizing droplet nucleation energy barriers. It was found that a higher RCA of the patterns minimized individual droplet adhesion, and lower pattern pitch ratio (*i.e.*, the ratio of the pitch between neighboring patterns to the diameter of the patterns) minimized individual droplet thermal resistance during condensation, which could favor a higher global jumping-droplet condensation heat transfer. For example, a patterned superhydrophobic surface with hydrophilic spots ($\theta_{\mathrm{RCA}} \leq 60$ °), pitch ratio of 8.35, and Ohnesorge number of 0.15 was expected to show a HTC of ~ 54 $\mathrm{kW \cdot m^{-2} \cdot K^{-1}}$, while that with hydrophobic spots ($\theta_{\mathrm{RCA}} = 120$ °) with a low pitch ratio of ~ 3 and Ohnesorge number of 0.15 increases to of ~ 260 $\mathrm{kW \cdot m^{-2} \cdot K^{-1}}$. In addition, they showed that superhydrophobic surface with smooth, low-surface-energy patterns had a 10 times higher HTC compared with superhydrophobic surfaces without patterns.

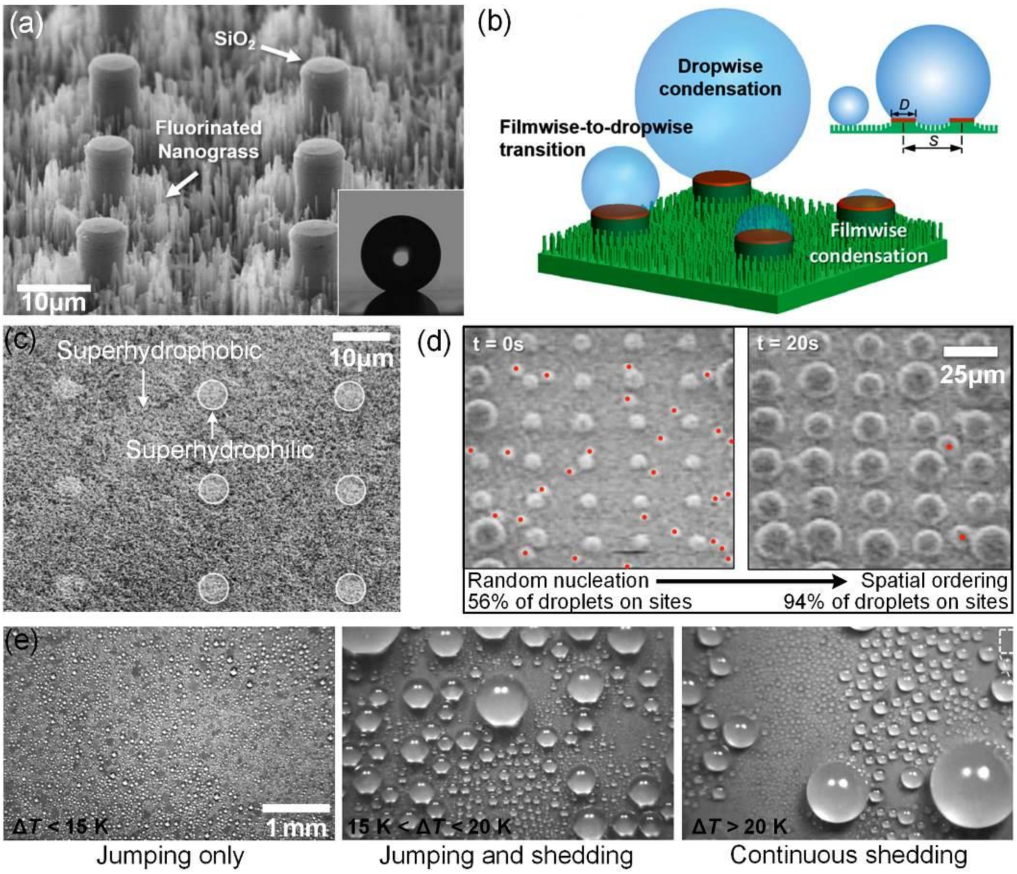

Fig. 77 (a) SEM image and (b) schematic diagram of the recurrent filmwise and dropwise condensation of the hydrophilic micropillars patterned superhydrophobic nanograss. (c) SEM images and (d) droplets self-organization of the superhydrophilic islands patterned superhydrophobic surface. (e) Condensed droplets showed a transition from droplets jumping to shedding removal with no flooding occurred on the patterned surfaces. (a, b) Reproduced with permission from ref. 446. Copyright (2014) American Chemical Society. (c–e) Reproduced with permission from ref. 723. Copyright (2016) American Chemical Society.

However, these (quasi) 2D patterned surfaces could not drain the condensed droplets away efficiently, and liquid-bridging phenomenon that eventually evolved into flooding was also observed at high surface subcoolings (Fig. 78a).[729,731] To address these problems, Lo *et al*. proposed a 3D patterned surface consisted of superhydrophobic Si nanowire arrays and hydrophilic microchannels to enhance the condensation at high surface subcoolings.[729] As shown in Fig. 78b–d, the microchannels with a depth of 50 μm were etched by deep reactive ion etching, and the nanowires with height of 15 μm were synthesized by an aqueous electroless etching technique and selectively coated with 60-nm-thick PTFE thin layer, yielding superhydrophobic Si nanowire arrays with water CA of ~ 150 ± 3 ° and hydrophilic Si microchannels with CA of ~ 30 ± 3 °. The resultant 3D patterned surface had a large wettability contrast and a significant structural height difference between the superhydrophobic and hydrophilic areas, both of which enhanced the dragging of the condensed droplets into the microchannels at high ΔT (Fig. 78e, f), so the departure diameters (~ 1.5 mm) of condensed droplets on the superhydrophobic areas of the 3D patterned surface were four times smaller than those on the superhydrophobic surface with Si nanowires alone (~ 6 mm). In addition, as depicted in Fig. 78g, the liquid bridges formed at high ΔT on the 3D patterned surface could be promptly absorbed by the liquid flow in the microchannels in a period of ~ 40 ms after their formation, the self-unbridging thereby prevented the condensing surface from flooding at high ΔT. Moreover, the thickness of the liquid films in the hydrophilic microchannels was confined to ~ 50 μm on the 3D patterned surface, which reduced the thermal resistance of the liquid films. As a result, the 3D patterned surface exhibited superior condensation heat transfer performance, and a high heat flux of 655 ± 10 $\mathrm{kW \cdot m^{-2}}$ and a high HTC of 37 ± 2 $\mathrm{kW \cdot m^{-2} \cdot K^{-1}}$ at $\Delta T = 18$ K were obtained when the width of the microchannels was 1300 μm.

Another strategy to prohibit flooding condensation is to replace the air “cushion” of superhydrophobic surface with a lubricant layer, namely, to use a SLIS that is repellent towards the condensates (including those ones with low surface tensions), and the high droplet mobility on SLIS is favorable to enhance the heat transfer.[33,35,573,691,707,709,712,714,716,732-734] For example, Anand *et al*. studied the condensation on SLIS, and showed that the condensed droplets pinning could be significantly reduced by using a well-designed SLIS.[573] If the surface energies of all phases present met eqn (14) (*i.e.*, cloaking), the growth of the condensed droplets would be inhibited. By introducing nanostructures on the microstructures, the droplet-solid pinning could also be drastically reduced. They showed that the condensed droplets as small as 100 μm in diameter became highly mobile and moved rapidly across the surface at speed that was several orders of magnitude higher than that on superhydrophobic surfaces with identical textures. By designing a SLIS with heterogeneous coatings, Xiao *et al*. further demonstrated the enhanced immersion condensation on a SLIS that would cloak the condensed droplets.[707] They showed that water vapor could diffuse through the cloaking layer and droplets nucleated at the high surface energy sites of lubricant-solid interface. In comparision to superhydrophobic nanostructured CuO surface, drastically increased nucleation densities were observed on the slippery heterogeneous nanostructured CuO surfaces, and the HTC increased by ~ 100% without droplets pinning or flooding over the whole range of supersaturations tested (from 1 to 1.6) in the presence of non-condensable gases. Rykaczewski *et al*. further studied the dropwise condensation of low surface tension liquids on SLISs, and found that the choice of lubricant and surface textures were crucial to stabilize the lubricant and reduce the pinning of the condensed droplets, and a four to eight-fold improvement in HTC was demonstrated on Krytox oil infused nanotextured alumina-silica surfaces as compared to filmwise condensation.[709] Preston *et al*. also verified the enhanced condensation heat transfer of hydrocarbon (*e.g.*, toluene) liquids on Krytox GPL 101 fluorinated oil infused Cu surface with CuO nanoblades, and a ~ 450% increasement in heat flux was observed in pure vapor condensation compared with that on a flat hydrophobic surface.[732] Recently, Tripathy *et al*. proposed a Cu-based SLIS with an ultrathin (~ 70 nm) vertically grown graphene nanoscaffold infused by Krytox 1525, which doubled the heat transfer performance in comparision to the control SLIS with CuO nanostructures.[714] However, owing to the inevitable lubricant depletion, the durability of SLISs during long-term condensation is still a great challenge,[732] constructing robust and durable SLISs is thereby of great importance, and slippery liquid-like smooth surfaces with physically or chemically bonded polymer molecules[735-737] could be an alternative candicate for enhanced yet durable dropwise condensation.

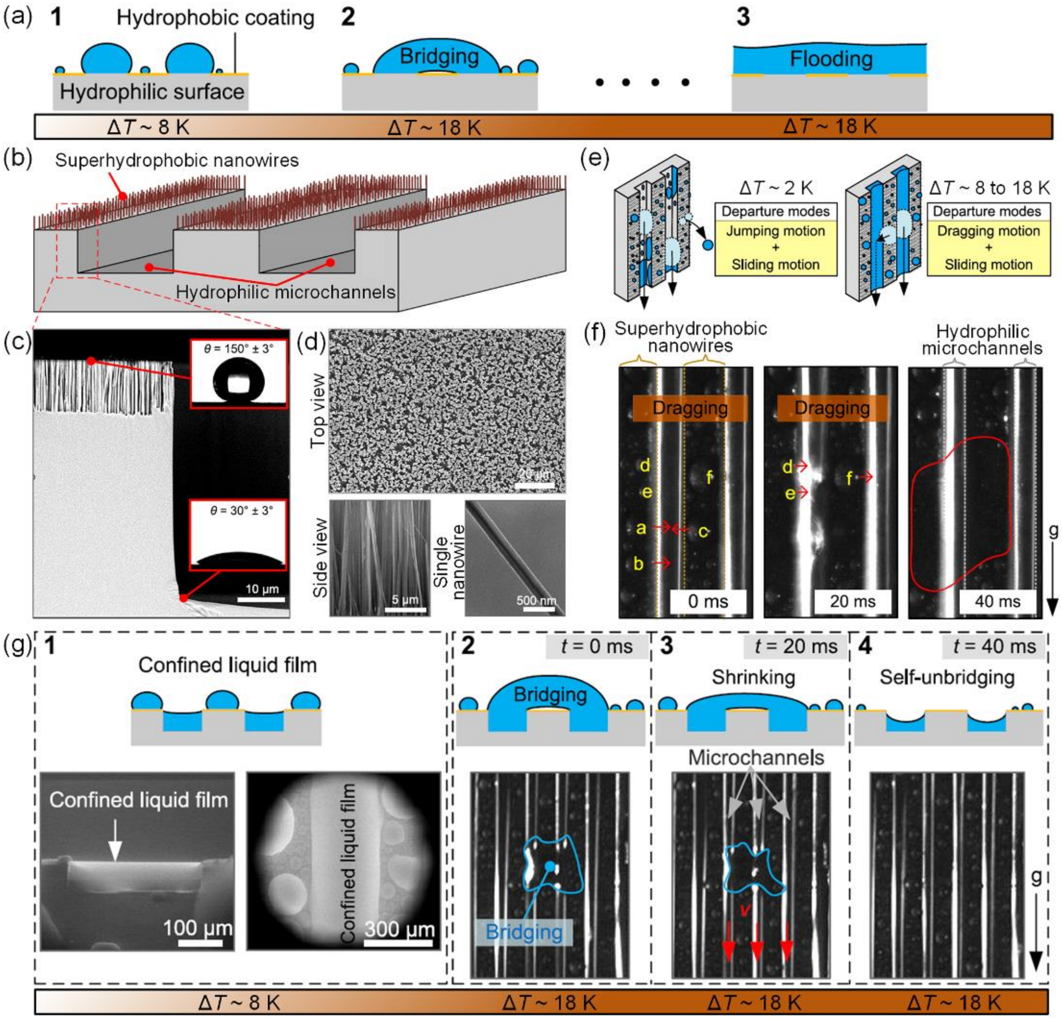

Fig. 78 (a) Liquid bridge-induced flooding on (quasi) 2D patterned superhydrophobic surface. (b) Schematic diagram and (c) SEM image of the 3D patterned superhydrophobic surface. (d) SEM images of the Si nanowires. (e) Schematic diagrams of droplet departure modes on the 3D patterned surface at

different ΔT. (f) Digital images showing the droplets formed on superhydrophobic areas were dragged into hydrophilic microchannels. (g) Confined liquid-film thickness and self-unbridging at high ΔT. Reproduced with permission from ref. 729. Copyright (2019) Elsevier Inc.

Besides the above-discussed passive methods, some active approaches (*e.g.*, applying electric field or vibration) have also been proposed to sustain stable dropwise condensation so as to enhance the heat transfer on liquid-repellent surfaces. For example, Miljkovic *et al.* found that self-propelled jumping droplets on a nanostructured superdrophobic surface obtained a net positive charge that enabled them to repel each other mid-flight, and the mechanism for the charge accumulation was associated with the formation of the electric double layer at the droplet-surface interface,[738] based on which they proposed an electric-field-enhanced condensation on superhydrophobic nanostructured surfaces to improve the overall heat transfer efficiency.[708] By considering the fact that the jumping droplets could completely reverse and return to the condensing surface under some conditions (*e.g.*, increased drag on the droplets due to vapor flow), which limits the further enhancement of heat transfer, the authors demonstrated that an externally applied electric field could prevent the reversal and return of the jumping droplets. Compared to a superhydrophobic CuO surface with no applied electric field, 50% higher overall condensation HTCs were obtained by applying electric fields of 100 and 200 V cm^{-1}. Zhang *et al.* demonstrated ultrafast sweeping removal of dropwise condensates *via* charge density gradient (CDG) induced propelling (Fig. 79a).[739] They prepared a soot-templated superhydrophobic coating on glass slide, and then the substrate was polarized by corona charging which injected CDG inside the substrate. By observing the droplet condensation process on the resultant surface, the authors showed that condensed droplet with jump-induced charges started to sweep followed by quick snowball-like sweeping and chase-like propelling (Fig. 79b). As a result, a small average diameter of the condensed droplets (~ 45 μm), low surface coverage (~ 10%), and high departure rate of the condensed droplets (~ 350 μL cm^{-2} min^{-1}) were obtained on the superhydrophobic surface with CDG inside. Indeed, the heat transfer efficiency of such surface needs to be addressed in the future. Moradi *et al.* showed that by applying a mechanical vibration on superhydrophobic aluminum alloy surface, condensed droplets shedding events were increased by 120%, resulting in a 15% increase in condensation.[740] Oh *et al.* studied vibration-assisted condensed droplet sweeping and heat transfer on a nanoporous polypropylene film-based SLIS.[741] Results showed that after applying vibration, the average radius of the departing droplet was reduced by 38.8% and the average departing velocity was increased by 8.6 times, which siginificantly reduced the overall surface coverage by condensed droplet. In addition, compared with a nonvibrating SLIS, time-averaged droplet radius distribution on a vibrating SLIS demonstrated more droplets with radii < 100 μm, and instantaneous droplet radius distribution showed a smaller average droplet radius. Heat transfer testing under an ambient environment containing noncondensable gases showed that 40.2% enhancement of heat flux was obtained, which could also be partially attributed to the vibration induced significant resonant motion of the liquid-vapor interface of the condensing droplets that created secondary flows at the interface.

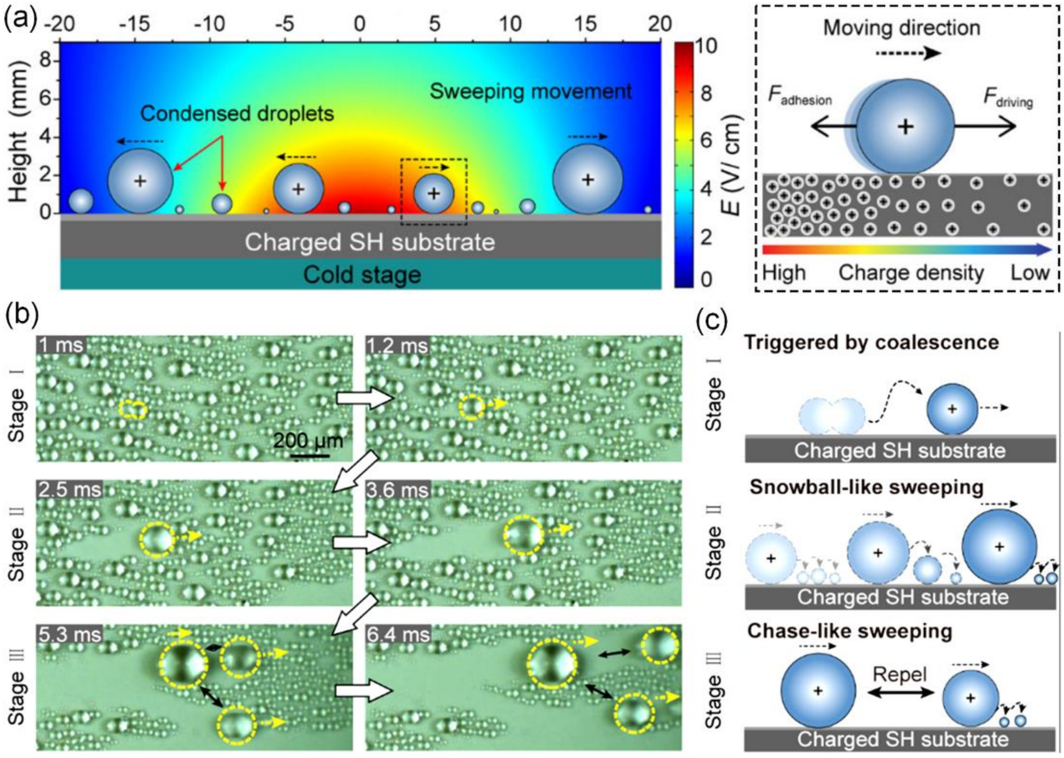

Fig. 79 (a) Electric field distribution of the superhydrophobic substrate with injected CDG inside and the schematic diagram of the condensed droplet removal behavior. (b) Time-lapsed images and (c) the corresponding schematic diagrams of the CDG-induced ultrafast sweeping removal of condensed droplets. Reproduced with permission from ref. 739. Copyright (2021) American Chemical Society.

Moreover, to further enhance condensation heat transfer performance of liquid-repellent surfaces especially for long-term operations, ultrathin coatings with low thermal resistance, low CAH, superior robustness and durability are urgently needed,[397,398,400,714,742,743] which are refered to another review.[315]

6 Conclusions and Outlook

In this review, we have systematically summarized the recent progress of liquid-repellent surfaces (including superhydrophobic surface, superoleophobic surface and SLIS) with robustness and durability. Emphasis have been put on the characterisation of wettability, the evaluation methods of the robustness and durability, as well as the design, fabrication and applications of robust and durable liquid-repellent surfaces. In spite of significant progress made over the past two decades, a number of directions still need to be further explored.

Characterisation of wettability is the foundation of research on liquid-repellent surfaces. CA measurement *via* sessile-drop goniometry is the most general method to evaluate liquid repellence, while CAH and SA have to be well considered since they reflect the mobility of droplets more accurately and directly. The precision/resolution of the goniometer setup and related software need to be further improved.[90,97] Meanwhile, the experimental factors, especially those operator-dependent details (*e.g.*, droplet volume, liquid feeding speed, tangent line/baseline determination methods, *etc*.), should be normalized and reported in the publications. Meanwhile, adhesive force mapping and solid-liquid/liquid-liquid interface imaging are recommended for the study of liquid repellence from visualized and micro perspectives, such as transition between the Wenzel and Cassie-Baxter states, wetting/de-wetting, lubricant dynamics, *etc*.

Robustness and durability should be evaluated and targeted according to the specific application scenario of the liquid-repellent surfaces. On the one hand, diverse evaluation methods have been proposed, but it may be unnecessary to test all aspects of the robustness and durability. For example, superhydrophobic self-cleaning roofs of buildings mainly suffer from raindrops, sands, sunlight, acid rain, *etc*., so the tolerance towards water droplets/falling sands impacting, UV exposure, and acid corrosion need to be addressed firstly, while other testing can be considered secondary. Meanwhile, in order to present repeatable, comparative and reliable evaluation results of robustness and durability, universal testing standards are urgently needed to be unified. On the other hand, the robustness and/or durability of liquid-repellent surfaces cannot be improved one for all. For instance, a lubricant with high surface tension generally imparts SLIS with better durability in heated water immersion, while a lubricant with high viscosity often lowers lubricant depletion but decreases the mobility of droplets on the surface.[431,744] Therefore, the strategies to enhance the robustness and durability should be prudently selected based on their practical service conditions.

Although many strategies have been proposed to prepare robust and durable liquid-repellent surfaces, it has to be noted that most of these methods can improve the robustness or durability with only a limited degree or aspects when being used alone, while their selective combination could be more effective and comprehensive.[57-59,349,354] Therefore, developing advanced composite methods to construct robust and durable liquid-repellent surfaces should be actively focused on in future research.

Most of the recent progress in preparing liquid-repellent surfaces with increasing robustness and durability remains outweighed by substantial trade-offs in large-scale feasibility, environmental unfriendliness, and expense or complexity of preparation. More significantly, fluorine-compounds that are almost indispensable for the construction of liquid-repellent surfaces may be banned in the near future due to their serious threats to human health.[417] To promote the real-world and large-area applications of liquid-repellent surfaces,[745] as well as to power the carbon dioxide emissions peak and carbon neutrality,[746] it is still urgently needed to develop simple, massively scalable, low-cost, and green methods/raw materials to construct robust and durable liquid-repellent surfaces.

Last but not least, although the emphasis on robustness and durability are continuously increasing in order to move liquid-repellent surfaces towards real-world applications, it has to be noted that the surfaces without robustness and durability are by no means useless. As one of the most typical examples, exposing liquid-repellent surfaces to plasma or UV can sometimes trigger chemical instability and thus damage the liquid repellence, but it is widely employed in creating patterned liquid-repellent surfaces,[747,748] stimuli-responsive smart surfaces,[749,750] materials with Janus wettability,[751] *etc*. Consequently, while we're focusing on robust and durable liquid-repellent surfaces, those fragile and unstable aspects (towards one or more inducements) should also be skillfully exploited to benefit the research of other functional surfaces.

Acknowledgements

F.C. acknowledges the financial support from National Postdoctoral Program for Innovative Talents (No. BX20190233) and National Natural Science Foundation of China (No. 52105477). The EPSRC are thanked for support to I.P.P. and C.J.C. (EP/L015862/1 and EP/W010798/1). Y.L. acknowledges the support from the Royal Society Research Grant (RGS\R1\201071). Y.W. thanks for the funding from China Scholarship Council (No. 202008320282).

References

1. D. Tian, Y. Song and L. Jiang, *Chem. Soc. Rev.*, 2013, **42**, 5184-5209.
2. B. Su, Y. Tian and L. Jiang, *J. Am. Chem. Soc.*, 2016, **138**, 1727-1748.
3. C. Perez-Gonzalez, R. Alert, C. Blanch-Mercader, M. Gomez-Gonzalez, T. Kolodziej, E. Bazellieres, J. Casademunt and X. Trepat, *Nat. Phys.*, 2019, **15**, 79-88.
4. C. Zhao, P. Zhang, J. Zhou, S. Qi, Y. Yamauchi, R. Shi, R. Fang, Y. Ishida, S. Wang, A. P. Tomsia, M. Liu and L. Jiang, *Nature*, 2020, **580**, 210-215.
5. P. C. Liu, Y. X. Wang, H. C. Hao, S. Basu, X. Y. Feng, Y. X. Xu, J. A. Boscoboinik, J. Nanda, J. Watt and D. Mitlin, *Adv. Mater.*, 2020, **32**, 2002908.
6. Z. Sheng, J. Zhang, J. Liu, Y. Zhang, X. Chen and X. Hou, *Chem. Soc. Rev.*, 2020, **49**, 7907-7928.
7. W. Lin, S. Gandhi, A. R. Oviedo Lara, A. K. Thomas, R. Helbig and Y. Zhang, *Adv. Mater.*, 2021, **33**, 2102349.
8. G. Liu, W. S. Y. Wong, M. Kraft, J. W. Ager, D. Vollmer and R. Xu, *Chem. Soc. Rev.*, 2021, **50**, 10674-10699.
9. T. Young, *Philos. Trans. R. Soc. London*, 1805, **95**, 65-87.
10. P. Zhang, C. Zhao, T. Zhao, M. Liu and L. Jiang, *Adv. Sci.*, 2019, **6**, 1900996.
11. J. Li, E. Ueda, D. Paulssen and P. A. Levkin, *Adv. Funct. Mater.*, 2019, **29**, 1802317.
12. H. Liu, Y. Wang, J. Huang, Z. Chen, G. Chen and Y. Lai, *Adv. Funct. Mater.*, 2018, **28**, 1707415.
13. Y. A. Mehanna, E. Sadler, R. L. Upton, A. G. Kempchinsky, Y. Lu and C. R. Crick, *Chem. Soc. Rev.*, 2021, **50**, 6569-6612.
14. S. Peppou-Chapman, J. K. Hong, A. Waterhouse and C. Neto, *Chem. Soc. Rev.*, 2020, **49**, 3688-3715.
15. W. Barthlott and C. Neinhuis, *Planta*, 1997, **202**, 1-8.
16. L. Feng, S. Li, Y. Li, H. Li, L. Zhang, J. Zhai, Y. Song, B. Liu, L. Jiang and D. Zhu, *Adv. Mater.*, 2002, **14**, 1857-1860.
17. A. Tuteja, W. Choi, M. Ma, J. M. Mabry, S. A. Mazzella, G. C. Rutledge, G. H. McKinley and R. E. Cohen, *Science*, 2007, **318**, 1618-1622.
18. R. Helbig, J. Nickerl, C. Neinhuis and C. Werner, *PLoS ONE*, 2011, **6**, e25105.
19. M. J. Liu, S. T. Wang, Z. X. Wei, Y. L. Song and L. Jiang, *Adv. Mater.*, 2009, **21**, 665-669.
20. T. S. Wong, S. H. Kang, S. K. Y. Tang, E. J. Smythe, B. D. Hatton, A. Grinthal and J. Aizenberg, *Nature*, 2011, **477**, 443-447.
21. G.-B. Fernando, *Chem. Int.*, 2021, **43**, 13-20.
22. K. Liu and L. Jiang, *Annu. Rev. Mater. Res.*, 2012, **42**, 231-263.
23. Y. Zhu, F. Yang and Z. Guo, *Nanoscale*, 2021, **13**, 3463-3482.
24. W. Zheng, J. Huang, S. Li, M. Ge, L. Teng, Z. Chen and Y. Lai, *ACS Appl. Mater. Interfaces*, 2021, **13**, 67-87.
25. J. Ge, H. Y. Zhao, H. W. Zhu, J. Huang, L. A. Shi and S. H. Yu, *Adv. Mater.*, 2016, **28**, 10459-10490.
26. R. Malinowski, I. P. Parkin and G. Volpe, *Chem. Soc. Rev.*, 2020, **49**, 7879-7892.
27. S. Zhou, L. Jiang and Z. C. Dong, *Adv. Mater. Interfaces*, 2020, **8**, 2000824.
28. Y. Wu, J. Feng, H. Gao, X. Feng and L. Jiang, *Adv. Mater.*, 2019, **31**, 1800718.

29. G. Wang and Z. Guo, *Nanoscale*, 2019, **11**, 22615-22635.
30. M. J. Kreder, J. Alvarenga, P. Kim and J. Aizenberg, *Nat. Rev. Mater.*, 2016, **1**, 1-15.
31. M. S. Selim, S. A. El-Safty, M. A. Shenashen, S. A. Higazy and A. Elmarakbi, *J Mater Chem B*, 2020, **8**, 3701-3732.
32. R. Deng, T. Shen, H. Chen, J. Lu, H.-C. Yang and W. Li, *J. Mater. Chem. A*, 2020, **8**, 7536-7547.
33. H. J. Cho, D. J. Preston, Y. Zhu and E. N. Wang, *Nat. Rev. Mater.*, 2016, **2**, 16092.
34. R. F. Wen, X. H. Ma, Y. C. Lee and R. G. Yang, *Joule*, 2018, **2**, 2307-2347.
35. L. Y. Liu, S. F. Wang, X. J. Zeng, P. H. Pi and X. F. Wen, *Adv. Mater. Interfaces*, 2021, **8**, 2101603.
36. Y. Wang, S. Gao, W. Xu and Z. Wang, *Adv. Funct. Mater.*, 2020, **30**, 1908252.
37. M. Li, C. Li, B. R. K. Blackman and E. Saiz, *Matter*, 2021, **4**, 3400-3414.
38. C. Howell, A. Grinthal, S. Sunny, M. Aizenberg and J. Aizenberg, *Adv. Mater.*, 2018, **30**, 1802724.
39. V. Jokinen, E. Kankuri, S. Hoshian, S. Franssila and R. H. A. Ras, *Adv. Mater.*, 2018, **30**, e1705104.
40. H. Cui, W. Wang, L. Shi, W. Song and S. Wang, *Small Methods*, 2020, **4**, 2000573.
41. L. Sun, J. Guo, H. Chen, D. Zhang, L. Shang, B. Zhang and Y. Zhao, *Adv. Sci.*, 2021, **8**, 2100126.
42. X. L. Tian, T. Verho and R. H. A. Ras, *Science*, 2016, **352**, 142-143.
43. A. Milionis, E. Loth and I. S. Bayer, *Adv. Colloid Interface Sci.*, 2016, **229**, 57-79.
44. L. R. J. Scarratt, U. Steiner and C. Neto, *Adv. Colloid Interface Sci.*, 2017, **246**, 133-152.
45. W. Zhang, D. Wang, Z. Sun, J. Song and X. Deng, *Chem. Soc. Rev.*, 2021, **50**, 4031-4061.
46. X. Zhang, D. Zhi, L. Sun, Y. Zhao, M. K. Tiwari, C. J. Carmalt, I. P. Parkin and Y. Lu, *J. Mater. Chem. A*, 2018, **6**, 357-362.
47. D. Wang, Q. Sun, M. J. Hokkanen, C. Zhang, F. Y. Lin, Q. Liu, S. P. Zhu, T. Zhou, Q. Chang, B. He, Q. Zhou, L. Chen, Z. Wang, R. H. A. Ras and X. Deng, *Nature*, 2020, **582**, 55-59.
48. M. Wang, D. Zhang, Z. Yang, C. Yang, Y. Tian and X. Liu, *Langmuir*, 2020, **36**, 10279-10292.
49. R. Hensel, C. Neinhuis and C. Werner, *Chem. Soc. Rev.*, 2016, **45**, 323-341.
50. S. Hu, T. Reddyhoff, J. Li, X. Cao, X. Shi, Z. Peng, A. J. deMello and D. Dini, *ACS Appl. Mater. Interfaces*, 2021, **13**, 31310-31319.
51. X. Gong, X. Gao and L. Jiang, *Adv. Mater.*, 2017, **29**, 1703002.
52. Z. Dong, M. Vuckovac, W. Cui, Q. Zhou, R. H. A. Ras and P. A. Levkin, *Adv. Mater.*, 2021, **33**, 2106068.
53. Y. Xiu, Y. Liu, D. W. Hess and C. P. Wong, *Nanotechnology*, 2010, **21**, 155705.
54. Y. Lu, S. Sathasivam, J. Song, C. R. Crick, C. J. Carmalt and I. P. Parkin, *Science*, 2015, **347**, 1132-1135.
55. E. Kobina Sam, D. Kobina Sam, X. Lv, B. Liu, X. Xiao, S. Gong, W. Yu, J. Chen and J. Liu, *Chem. Eng. J.*, 2019, **373**, 531-546.
56. C. Liu, Y. Li, C. Lu, Y. Liu, S. Feng and Y. Liu, *ACS Appl. Mater. Interfaces*, 2020, **12**, 25471-25477.
57. Y. Li, T. Hu, B. Li, J. Wei and J. Zhang, *Adv. Mater. Interfaces*, 2019, **6**, 1901255.
58. Y. Yamauchi, M. Tenjimbayashi, S. Samitsu and M. Naito, *ACS Appl. Mater. Interfaces*, 2019, **11**, 32381-32389.
59. W. X. Zhang, J. Gao, Y. J. Deng, L. F. Peng, P. Y. Yi, X. M. Lai and Z. Q. Lin, *Adv. Funct. Mater.*, 2021, **31**, 2101068.
60. R. J. Good, *J. Adhes. Sci. Technol.*, 1992, **6**, 1269-1302.
61. P. Roura, *Am. J. Phys.*, 2005, **73**, 1139-1147.
62. M. L. Zhou, X. Y. He, X. Y. Wu, L. Xiao, Z. H. Cui, X. X. Tang, L. Guo, S. Y. Liu, H. W. Liu, Y. Y. Zhu, Y. B. Zhang, G. Q. Li and J. G. Zhu, *Appl. Mater. Today*, 2020, **21**, 100851.
63. W. Li, M. Yu, J. Sun, K. Mochizuki, S. Chen, H. Zheng, J. Li, S. Yao, H. Wu, B. S. Ong, S. Kawata, Z. Wang and K. Ren, *Proc. Natl. Acad. Sci. U. S. A.*, 2019, **116**, 23909-23914.
64. J. Yong, F. Chen, Q. Yang, J. Huo and X. Hou, *Chem. Soc. Rev.*, 2017, **46**, 4168-4217.
65. H. Chen, P. Zhang, L. Zhang, H. Liu, Y. Jiang, D. Zhang, Z. Han and L. Jiang, *Nature*, 2016, **532**, 85-89.
66. J. L. Song, D. Y. Zhao, Z. J. Han, W. Xu, Y. Lu, X. Liu, B. Liu, C. J. Carmalt, X. Deng and I. P. Parkin, *J. Mater. Chem. A*, 2017, **5**, 14542-14550.
67. W. Chen, P. Zhang, R. Zang, J. Fan, S. Wang, B. Wang and J. Meng, *Adv. Mater.*, 2020, **32**, e1907413.
68. L. Zhu, J. Xue, Y. Wang, Q. Chen, J. Ding and Q. Wang, *ACS Appl. Mater. Interfaces*, 2013, **5**, 4053-4062.

69. W. L. Pei, J. H. Li, Z. Y. Guo, Y. F. Liu, C. L. Gao, L. S. Zhong, S. M. Wang, Y. P. Hou and Y. M. Zheng, *Chem. Eng. J.*, 2021, **409**, 128180.
70. D. Wu, Z. Zhang, Y. Zhang, Y. Jiao, S. Jiang, H. Wu, C. Li, C. Zhang, J. Li, Y. Hu, G. Li, J. Chu and L. Jiang, *Adv. Mater.*, 2020, **32**, 2005039.
71. X. Yang, J. Song, H. Zheng, X. Deng, X. Liu, X. Lu, J. Sun and D. Zhao, *Lab Chip*, 2017, **17**, 1041-1050.
72. F. Z. Chen, Y. Lu, X. Liu, J. L. Song, G. J. He, M. K. Tiwari, C. J. Carmalt and I. P. Parkin, *Adv. Funct. Mater.*, 2017, **27**, 1702926.
73. G. Zhu, J. Chen, T. Zhang, Q. Jing and Z. L. Wang, *Nat. Commun.*, 2014, **5**, 3426.
74. N. Miljkovic and E. N. Wang, *MRS Bull.*, 2013, **38**, 397-406.
75. D. Volpe C and S. Siboni, *Eur. J. Phys.*, 2011, **32**, 1019-1032.
76. J. W. Gibbs, *The Scientific Papers of J. Willard Gibbs*, Dover Publ, New York, 1961.
77. R. N. Wenzel, *Ind. Eng. Chem.*, 1936, **28**, 988-994.
78. G. Wolansky and A. Marmur, *Colloids Surf., A*, 1999, **156**, 381-388.
79. D. Quéré, *Annu. Rev. Mater. Res.*, 2008, **38**, 71-99.
80. T. S. Meiron, A. Marmur and I. S. Saguy, *J. Colloid Interface Sci.*, 2004, **274**, 637-644.
81. A. B. D. Cassie and S. Baxter, *Trans. Faraday Society*, 1944, **40**, 546-551.
82. A. J. B. Milne and A. Amirfazli, *Adv. Colloid Interface Sci.*, 2012, **170**, 48-55.
83. A. Marmur, *Langmuir*, 2003, **19**, 8343-8348.
84. E. Bormashenko, *J. Colloid Interface Sci.*, 2011, **360**, 317-319.
85. D. J. Preston, Y. Song, Z. Lu, D. S. Antao and E. N. Wang, *ACS Appl. Mater. Interfaces*, 2017, **9**, 42383-42392.
86. J. D. Smith, R. Dhiman, S. Anand, E. Reza-Garduno, R. E. Cohen, G. H. McKinley and K. K. Varanasi, *Soft Matter*, 2013, **9**, 1772-1780.
87. S. Sett, X. Yan, G. Barac, L. W. Bolton and N. Miljkovic, *ACS Appl. Mater. Interfaces*, 2017, **9**, 36400-36408.
88. C. Semprebon, G. McHale and H. Kusumaatmaja, *Soft Matter*, 2016, **13**, 101-110.
89. P. C. Zhang, S. S. Wang, S. T. Wang and L. Jiang, *Small*, 2015, **11**, 1939-1946.
90. T. Huhtamäki, X. L. Tian, J. T. Korhonen and R. H. A. Ras, *Nat. Protoc.*, 2018, **13**, 1521-1538.
91. A. Marmur, *Annu. Rev. Mater. Res.*, 2009, **39**, 473-489.
92. C. W. Extrand and Y. Kumagai, *J. Colloid Interface Sci.*, 1997, **191**, 378-383.
93. A. Marmur, *Colloids Surf., A*, 1998, **136**, 209-215.
94. M. A. Rodriguez-Valverde, F. J. M. Ruiz-Cabello and M. A. Cabrerizo-Vilchez, *Soft Matter*, 2011, **7**, 53-56.
95. L. Gao and T. J. McCarthy, *Langmuir*, 2006, **22**, 6234-6237.
96. M. Strobel and C. S. Lyons, *Plasma Process. Polym.*, 2011, **8**, 8-13.
97. K. Liu, M. Vuckovac, M. Latikka, T. Huhtamaki and R. H. A. Ras, *Science*, 2019, **363**, 1147-1148.
98. H. Tavana and A. W. Neumann, *Colloids Surf., A*, 2006, **282-283**, 256-262.
99. C. N. Lam, R. Wu, D. Li, M. L. Hair and A. W. Neumann, *Adv. Colloid Interface Sci.*, 2002, **96**, 169-191.
100. S. Brandon, N. Haimovich, E. Yeger and A. Marmur, *J. Colloid Interface Sci.*, 2003, **263**, 237-243.
101. N. K. Adam and G. Jessop, *J. Chem. Soc., Trans.*, 1925, **127**, 1863-1868.
102. C. H. Kung, P. K. Sow, B. Zahiri and W. Mérida, *Adv. Mater. Interfaces*, 2019, **6**, 1900839.
103. M. F. Ismail, M. A. Islam, B. Khorshidi, A. Tehrani-Bagha and M. Sadrzadeh, *Adv. Colloid Interface Sci.*, 2022, **299**, 102524.
104. J. W. Drelich, L. Boinovich, E. Chibowski, C. Della Volpe, L. Holysz, A. Marmur and S. Siboni, *Surf. Innov.*, 2020, **8**, 3-27.
105. J. Drelich, *Surf. Innov.*, 2013, **1**, 248-254.
106. F. Z. Chen, S. Liu, J. Y. Liu, S. Huang, G. Q. Xia, J. L. Song, W. J. Xu, J. Sun and X. Liu, *Appl. Surf. Sci.*, 2016, **389**, 967-976.
107. T. Wang, L. P. Shi, L. Lv and J. Q. Liu, *Plasma Process. Polym.*, 2020, **17**, e2000056.
108. M. Vuckovac, M. Latikka, K. Liu, T. Huhtamaki and R. H. A. Ras, *Soft Matter*, 2019, **15**, 7089-7096.

109. A. Shahraz, A. Borhan and K. A. Fichthorn, *Langmuir*, 2012, **28**, 14227-14237.

110. C. E. Cansoy, *RSC Adv.*, 2014, **4**, 1197-1203.

111. M. S. Bell, K. A. Fichthorn and A. Borhan, *Langmuir*, 2016, **32**, 3858-3866.

112. S. Ren, J. Chen, M. Jiang, S. Wang, Z. Wan, Y. Xie and L. Li, *Colloids Surf., A*, 2020, **601**, 125849.

113. C. W. Extrand and S. I. Moon, *Langmuir*, 2010, **26**, 17090-17099.

114. S. Srinivasan, G. H. McKinley and R. E. Cohen, *Langmuir*, 2011, **27**, 13582-13589.

115. W. S. Y. Wong and A. Tricoli, *ACS Appl. Mater. Interfaces*, 2018, **10**, 13999-14007.

116. D. Kim, M. Jeong, K. Kang and S. Ryu, *Langmuir*, 2020, **36**, 6061-6069.

117. R. Tadmor and P. S. Yadav, *J. Colloid Interface Sci.*, 2008, **317**, 241-246.

118. R. Tadmor, K. Chaurasia, P. S. Yadav, A. Leh, P. Bahadur, L. Dang and W. R. Hoffer, *Langmuir*, 2008, **24**, 9370-9374.

119. F. Villa, M. Marengo and J. De Coninck, *Sci. Rep.*, 2018, **8**, 6549.

120. T. Y. Zhao and L. Jiang, *Colloids Surf., B*, 2018, **161**, 324-330.

121. B. Krasovitski and A. Marmur, *Langmuir*, 2005, **21**, 3881-3885.

122. E. Pierce, F. J. Carmona and A. Amirfazli, *Colloids Surf., A*, 2008, **323**, 73-82.

123. F. J. Montes Ruiz-Cabello, M. A. Rodriguez-Valverde, A. Marmur and M. A. Cabrerizo-Vilchez, *Langmuir*, 2011, **27**, 9638-9643.

124. C. L. Moraila, F. J. Montes Ruiz-Cabello, M. Cabrerizo-Vilchez and M. A. Rodriguez-Valverde, *J. Colloid Interface Sci.*, 2019, **539**, 448-456.

125. S. Sarkar, T. Roy, A. Roy, S. Moitra, R. Ganguly and C. M. Megaridis, *J. Colloid Interface Sci.*, 2020, **581**, 690-697.

126. A. Schulz, M. M. Gepp, F. Stracke, H. von Briesen, J. C. Neubauer and H. Zimmermann, *J. Biomed. Mater. Res. Part A*, 2019, **107A**, 114-121.

127. R. Sekiya-Aoyama, Y. Arisaka and N. Yui, *Macromol. Biosci.*, 2020, **20**, 1900424.

128. R. Sekiya-Aoyama, Y. Arisaka, M. Hakariya, H. Masuda, T. Iwata, T. Yoda and N. Yui, *Biomater. Sci.*, 2021, **9**, 675-684.

129. J. Xue, P. Shi, L. Zhu, J. Ding, Q. Chen and Q. Wang, *Appl. Surf. Sci.*, 2014, **296**, 133-139.

130. L. Wilhelmy, *Ann. Phys.*, 1863, **195**, 177-217.

131. C. D. Volpe and S. Siboni, *Surf. Innov.*, 2018, **6**, 120-132.

132. D. Nandyala, Z. Wang, D. Hwang, T. Cubaud and C. E. Colosqui, *ACS Appl. Mater. Interfaces*, 2020, **12**, 45950-45960.

133. C. W. Karl, A. E. Krauklis, A. Lang and U. Giese, *Polymers*, 2020, **12**, 1528.

134. Z. S. Yuan, Z. W. Ke, Y. H. Qiu, L. J. Zheng, Y. Yang, Q. S. Gu and C. Y. Wang, *ACS Appl. Mater. Interfaces*, 2020, **12**, 46923-46932.

135. C. Lu, J. Wang, X. Lu, T. Zheng, Y. Liu, X. Wang, D. Zhang and D. Seveno, *ACS Appl. Mater. Interfaces*, 2019, **11**, 31520-31531.

136. J. Park, U. Pasaogullari and L. Bonville, *Appl. Surf. Sci.*, 2018, **427**, 273-280.

137. J. Vogel, H. M. Balshaw, S. H. Doerr and R. Bryant, *Geoderma*, 2020, **371**, 114384.

138. X. Wang, Q. Min, Z. M. Zhang, Y. Y. Duan, Y. N. Zhang and J. P. Zhai, *Colloids Surf., A*, 2017, **527**, 115-122.

139. A. M. Karim and H. P. Kavehpour, *Colloids Surf., A*, 2018, **548**, 54-60.

140. P. Zhang and K. Mohseni, *Phys. Rev. Fluids*, 2019, **4**, 084004.

141. X. Zhang, B. Ding, R. Cheng, S. C. Dixon and Y. Lu, *Adv. Sci.*, 2018, **5**, 1700520.

142. C. W. Extrand and A. N. Gent, *J. Colloid Interface Sci.*, 1990, **138**, 431-442.

143. L. Wang and T. J. McCarthy, *Angew. Chem. Int. Ed. Engl.*, 2016, **55**, 244-248.

144. M. Backholm, D. Molpeceres, M. Vuckovac, H. Nurmi, M. J. Hokkanen, V. Jokinen, J. V. I. Timonen and R. H. A. Ras, *Commun. Mater.*, 2020, **1**, 64.

145. D. Daniel, J. V. I. Timonen, R. Li, S. J. Velling, M. J. Kreder, A. Tetreault and J. Aizenberg, *Phys. Rev. Lett.*, 2018, **120**, 244503.

146. C. Z. Li, Y. L. Jiao, Y. Y. Zhang, S. J. Jiang, X. D. Lv, S. Z. Wu, J. W. Li, Y. L. Hu, J. X. Ye, K. Liu, D. Wu and J. R. Chu, *Adv. Funct. Mater.*, 2021, **31**, 2100543.

147. M. J. Hokkanen, M. Backholm, M. Vuckovac, Q. Zhou and R. H. A. Ras, *Adv. Mater.*, 2021, **33**, 2105130.
148. D. Daniel, A. Y. T. Chia, L. C. H. Moh, R. Liu, X. Q. Koh, X. Zhang and N. Tomczak, *Commun. Phys.*, 2019, **2**, 105.
149. D. Daniel, J. V. I. Timonen, R. P. Li, S. J. Velling and J. Aizenberg, *Nat. Phys.*, 2017, **13**, 1020-1025.
150. N. Gao, F. Geyer, D. W. Pilat, S. Wooh, D. Vollmer, H. J. Butt and R. Berger, *Nat. Phys.*, 2018, **14**, 191-196.
151. D. Daniel, C. L. Lay, A. Sng, C. J. Jun Lee, D. C. Jin Neo, X. Y. Ling and N. Tomczak, *Proc. Natl. Acad. Sci. U.S.A.*, 2019, **116**, 25008-25012.
152. X. Yao, J. Gao, Y. L. Song and L. Jiang, *Adv. Funct. Mater.*, 2011, **21**, 4270-4276.
153. Y. Li, J. Li, L. Liu, Y. Yan, Q. Zhang, N. Zhang, L. He, Y. Liu, X. Zhang, D. Tian, J. Leng and L. Jiang, *Adv. Sci.*, 2020, **7**, 2000772.
154. H. Dai, C. Gao, J. Sun, C. Li, N. Li, L. Wu, Z. Dong and L. Jiang, *Adv. Mater.*, 2019, **31**, 1905449.
155. V. Liimatainen, M. Vuckovac, V. Jokinen, V. Sariola, M. J. Hokkanen, Q. Zhou and R. H. A. Ras, *Nat. Commun.*, 2017, **8**, 1798.
156. J. Zimmermann, F. A. Reifler, G. Fortunato, L.-C. Gerhardt and S. Seeger, *Adv. Funct. Mater.*, 2008, **18**, 3662-3669.
157. Y. Lu, S. Sathasivam, J. Song, W. Xu, C. J. Carmalt and I. P. Parkin, *J. Mater. Chem. A*, 2014, **2**, 12177-12184.
158. C. R. Crick and I. P. Parkin, *Chem. Commun.*, 2011, **47**, 12059-12061.
159. X. Chen, Q. Li, K. Hou, X. Li and Z. Wang, *Langmuir*, 2019, **35**, 16275-16280.
160. X. Dai, N. Sun, S. O. Nielsen, B. B. Stogin, J. Wang, S. Yang and T. S. Wong, *Sci Adv*, 2018, **4**, eaaq0919.
161. S. Peppou-Chapman and C. Neto, *ACS Appl. Mater. Interfaces*, 2018, **10**, 33669-33677.
162. F. Schellenberger, J. Xie, N. Encinas, A. Hardy, M. Klapper, P. Papadopoulos, H. J. Butt and D. Vollmer, *Soft Matter*, 2015, **11**, 7617-7626.
163. S. Li, A. Sng, D. Daniel, H. C. Lau, O. Torsaeter and L. P. Stubbs, *ACS Appl. Mater. Interfaces*, 2021, **13**, 41182-41189.
164. X. Li, J. Yang, K. Lv, P. Papadopoulos, J. Sun, D. Wang, Y. Zhao, L. Chen, D. Wang, Z. Wang and X. Deng, *Natl. Sci. Rev.*, 2020, **8**, nwaa153.
165. Y. Xiang, S. Huang, P. Lv, Y. Xue, Q. Su and H. Duan, *Phys. Rev. Lett.*, 2017, **119**, 134501.
166. X. Gao and L. Jiang, *Nature*, 2004, **432**, 36.
167. Y. Zheng, X. Gao and L. Jiang, *Soft Matter*, 2007, **3**, 178-182.
168. X. F. Gao, X. Yan, X. Yao, L. Xu, K. Zhang, J. H. Zhang, B. Yang and L. Jiang, *Adv. Mater.*, 2007, **19**, 2213-2217.
169. Z. G. Guo and W. M. Liu, *Plant Sci.*, 2007, **172**, 1103-1112.
170. M. J. Liu, S. T. Wang and L. Jiang, *Nat. Rev. Mater.*, 2017, **2**, 17036.
171. T. Kong, G. Luo, Y. Zhao and Z. Liu, *Adv. Funct. Mater.*, 2019, **29**, 1808012.
172. M. Ghasemlou, F. Daver, E. P. Ivanova and B. Adhikari, *J. Mater. Chem. A*, 2019, **7**, 16643-16670.
173. L. Feng, Y. Zhang, J. Xi, Y. Zhu, N. Wang, F. Xia and L. Jiang, *Langmuir*, 2008, **24**, 4114-4119.
174. W. Barthlott, T. Schimmel, S. Wiersch, K. Koch, M. Brede, M. Barczewski, S. Walheim, A. Weis, A. Kaltenmaier, A. Leder and H. F. Bohn, *Adv. Mater.*, 2010, **22**, 2325-2328.
175. K. S. Liu, J. X. Du, J. T. Wu and L. Jiang, *Nanoscale*, 2012, **4**, 768-772.
176. S. Yang, J. Ju, Y. Qiu, Y. He, X. Wang, S. Dou, K. Liu and L. Jiang, *Small*, 2014, **10**, 294-299.
177. D. Wei, J. Wang, Y. Liu, D. Wang, S. Li and H. Wang, *Chem. Eng. J.*, 2021, **404**, 126444.
178. Y. Lu, Y. Shen, J. Tao, Z. Wu, H. Chen, Z. Jia, Y. Xu and X. Xie, *Langmuir*, 2020, **36**, 880-888.
179. T. Wang, L. Huang, Y. Liu, X. Li, C. Liu, S. Handschuh-Wang, Y. Xu, Y. Zhao and Y. Tang, *ACS Appl. Mater. Interfaces*, 2020, **12**, 24432-24441.
180. Y. Rahmawan, L. B. Xu and S. Yang, *J. Mater. Chem. A*, 2013, **1**, 2955-2969.
181. J. Gu, H. Fan, C. Li, J. Caro and H. Meng, *Angew. Chem. Int. Ed. Engl.*, 2019, **58**, 5297-5301.
182. T. Darmanin, E. Taffin de Givenchy, S. Amigoni and F. Guittard, *Adv. Mater.*, 2013, **25**, 1378-1394.
183. R. Wang, F. Wu, D. Xing, F. Yu and X. Gao, *ACS Appl. Mater. Interfaces*, 2020, **12**, 24512-24520.
184. L. L. Hou, N. Wang, J. Wu, Z. M. Cui, L. Jiang and Y. Zhao, *Adv. Funct. Mater.*, 2018, **28**, 1801114.
185. Y. Liao, G. T. Zheng, J. J. Huang, M. Tian and R. Wang, *J. Membr. Sci.*, 2020, **601**, 117962.

186. S. He, J. Shi, J. Huang, J. Hu, Y. Lai and Z. Chen, *Chem. Eng. J.*, 2021, **416**, 127768.
187. Y. X. Wan, M. J. Chen, W. Liu, X. X. Shen, Y. L. Min and Q. J. Xu, *Electrochim. Acta*, 2018, **270**, 310-318.
188. T. L. Liu and C. J. Kim, *Science*, 2014, **346**, 1096-1100.
189. F. Sohbatzadeh, M. Farhadi and E. Shakerinasab, *Surf. Coat. Technol.*, 2019, **374**, 944-956.
190. J. N. Wang, Y. Q. Liu, Y. L. Zhang, J. Feng, H. Wang, Y. H. Yu and H. B. Sun, *Adv. Funct. Mater.*, 2018, **28**, 1800625.
191. X. Liu, H. Gu, M. Wang, X. Du, B. Gao, A. Elbaz, L. Sun, J. Liao, P. Xiao and Z. Gu, *Adv. Mater.*, 2018, **30**, 1800103.
192. V. Liimatainen, D. M. Drotlef, D. Son and M. Sitti, *Adv. Mater.*, 2020, **32**, 2000497.
193. Y. Zhang, Y. Jiao, C. Li, C. Chen, J. Li, Y. Hu, D. Wu and J. Chu, *Int. J. Extrem. Manuf.*, 2020, **2**, 032002.
194. P. Zhu, R. Chen and L. Wang, *Adv. Sci.*, 2019, **6**, 1900798.
195. J. P. Wang, Y. L. Wu, D. G. Zhang, L. H. Li, T. Wang and S. Y. Duan, *Colloids Surf., A*, 2020, **587**, 124331.
196. L. Li, Y. Bai, L. Li, S. Wang and T. Zhang, *Adv. Mater.*, 2017, **29**, 1702517.
197. L. Kong, X. Kong, Z. Ji, X. Wang and X. Zhang, *ACS Appl. Mater. Interfaces*, 2020, **12**, 49694-49704.
198. C. Cao, B. Yi, J. Zhang, C. Hou, Z. Wang, G. Lu, X. Huang and X. Yao, *Chem. Eng. J.*, 2020, **392**, 124834.
199. P. Zhang and F. Y. Lv, *Energy*, 2015, **82**, 1068-1087.
200. D. R. Lide, *CRC Handbook of Physics and Chemistry*, CRC Press, Boca Raton, Florida, 84th edn., 2003.
201. Surface tension values of some common test liquids for surface energy analysis, http://www.surface-tension.de/.
202. K. Tsujii, T. Yamamoto, T. Onda and S. Shibuichi, *Angew. Chem. Int. Ed. Engl.*, 1997, **36**, 1011-1012.
203. A. Tuteja, W. Choi, G. H. McKinley, R. E. Cohen and M. F. Rubner, *MRS Bull.*, 2008, **33**, 752-758.
204. Z. Chu and S. Seeger, *Chem. Soc. Rev.*, 2014, **43**, 2784-2798.
205. Y. L. Pan, S. C. Huang, F. R. Li, X. Z. Zhao and W. J. Wang, *J. Mater. Chem. A*, 2018, **6**, 15057-15063.
206. F. R. Li, Z. R. Wang, S. C. Huang, Y. L. Pan and X. Z. Zhao, *Adv. Funct. Mater.*, 2018, **28**, 1706867.
207. M. Im, H. Im, J. H. Lee, J. B. Yoon and Y. K. Choi, *Soft Matter*, 2010, **6**, 1401-1404.
208. H. J. Choi, S. Choo, J. H. Shin, K. I. Kim and H. Lee, *J. Phys. Chem. C*, 2013, **117**, 24354-24359.
209. A. Tuteja, W. Choi, J. M. Mabry, G. H. McKinley and R. E. Cohen, *Proc. Natl. Acad. Sci. U. S. A.*, 2008, **105**, 18200-18205.
210. S. Dong, X. Zhang, Q. Li, C. Liu, T. Ye, J. Liu, H. Xu, X. Zhang, J. Liu, C. Jiang, L. Xue, S. Yang and X. Xiao, *Small*, 2020, **16**, 2000779.
211. H. Kim, H. Han, S. Lee, J. Woo, J. Seo and T. Lee, *ACS Appl. Mater. Interfaces*, 2019, **11**, 5484-5491.
212. H. Wang, Z. Zhang, Z. Wang, Y. Liang, Z. Cui, J. Zhao, X. Li and L. Ren, *ACS Appl. Mater. Interfaces*, 2019, **11**, 28478-28486.
213. J. Song, W. Pan, K. Wang, F. Chen and Y. Sun, *Int. J. Mach. Tool Manufact.*, 2020, **159**, 103637.
214. X. Shi, Y. Zhang, D. Wu, T. Wu, S. Jiang, Y. Jiao, S. Wu, Y. Zhang, Y. Hu, W. Ding and J. Chu, *Langmuir*, 2020, **36**, 12346-12356.
215. S. T. Hu, X. B. Cao, T. Reddyhoff, D. Puhan, S. C. Vladescu, J. Wang, X. Shi, Z. K. Peng, A. J. DeMello and D. Dini, *Sci. Adv.*, 2020, **6**, eaba9721.
216. Y. Yang, Y. Zhang, Y. Hu, G. Li, C. Zhang, Y. Song, L. Li, C. Ni, N. Dai, Y. Cai, J. Li, D. Wu and J. Chu, *Nano Lett.*, 2021, **21**, 9301-9309.
217. X. Deng, L. Mammen, H. J. Butt and D. Vollmer, *Science*, 2012, **335**, 67-70.
218. F. Z. Chen, J. L. Song, Y. Lu, S. Huang, X. Liu, J. Sun, C. J. Carmalt, I. P. Parkin and W. J. Xu, *J. Mater. Chem. A*, 2015, **3**, 20999-21008.
219. H. Teisala, F. Geyer, J. Haapanen, P. Juuti, J. M. Makela, D. Vollmer and H. J. Butt, *Adv. Mater.*, 2018, **30**, 1706529.
220. S. Pan, R. Guo, M. Bjornmalm, J. J. Richardson, L. Li, C. Peng, N. Bertleff-Zieschang, W. Xu, J. Jiang and F. Caruso, *Nat. Mater.*, 2018, **17**, 1040-1047.
221. T. Wang, C. Lv, L. Ji, X. He and S. Wang, *ACS Appl. Mater. Interfaces*, 2020, **12**, 49155-49164.
222. W. Liu, J. Liang, G. Yang, M. Huang, C. Fu, B. Zeng and H. Wu, *ACS Appl. Mater. Interfaces*, 2020, **12**, 45429-45436.
223. X. Li, D. Wang, Y. Tan, J. Yang and X. Deng, *ACS Appl. Mater. Interfaces*, 2019, **11**, 29458-29465.
224. S. Hu, X. Cao, T. Reddyhoff, D. Puhan, S. C. Vladescu, Q. Wang, X. Shi, Z. Peng, A. J. deMello and D. Dini, *ACS Appl.*

Mater. Interfaces, 2020, **12**, 4174-4182.

225. X. J. Liu, H. C. Gu, H. B. Ding, X. Du, M. X. Wei, Q. Chen and Z. Z. Gu, *Adv. Sci.*, 2020, **7**, 2000878.
226. Z. Dong, M. F. Schumann, M. J. Hokkanen, B. Chang, A. Welle, Q. Zhou, R. H. A. Ras, Z. Xu, M. Wegener and P. A. Levkin, *Adv. Mater.*, 2018, **30**, 1803890.
227. X. Liu, H. Gu, H. Ding, X. Du, Z. He, L. Sun, J. Liao, P. Xiao and Z. Gu, *Small*, 2019, **15**, 1902360.
228. D. H. Kim, S. Kim, S. R. Park, N. X. Fang and Y. T. Cho, *ACS Appl. Mater. Interfaces*, 2021, **13**, 33618-33626.
229. C. B. Dayan, S. Chun, N. Krishna-Subbaiah, D. M. Drotlef, M. B. Akolpoglu and M. Sitti, *Adv. Mater.*, 2021, **33**, 2103826.
230. A. K. Kota, G. Kwon and A. Tuteja, *NPG Asia Mater.*, 2014, **6**, e109.
231. S. Pan, A. K. Kota, J. M. Mabry and A. Tuteja, *J. Am. Chem. Soc.*, 2013, **135**, 578-581.
232. J. Yang, Z. Zhang, X. Xu, X. Zhu, X. Men and X. Zhou, *J. Mater. Chem.*, 2012, **22**, 2834.
233. J. Yang, H. J. Song, X. H. Yan, H. Tang and C. S. Li, *Cellulose*, 2014, **21**, 1851-1857.
234. P. S. Brown and B. Bhushan, *Sci. Rep.*, 2015, **5**, 14030.
235. P. S. Brown, O. D. L. A. Atkinson and J. P. S. Badyal, *ACS Appl. Mater. Interfaces*, 2014, **6**, 7504-7511.
236. Y. Sun and Z. Guo, *Chem. Eng. J.*, 2020, **381**, 122629.
237. Q. Cheng, M. Li, Y. Zheng, B. Su, S. Wang and L. Jiang, *Soft Matter*, 2011, **7**, 5948-5951.
238. X. Liu, J. Zhou, Z. Xue, J. Gao, J. Meng, S. Wang and L. Jiang, *Adv. Mater.*, 2012, **24**, 3401-3405.
239. Y. Cai, L. Lin, Z. Xue, M. Liu, S. Wang and L. Jiang, *Adv. Funct. Mater.*, 2014, **24**, 809-816.
240. Y. Cai, Q. Lu, X. Guo, S. Wang, J. Qiao and L. Jiang, *Adv. Mater.*, 2015, **27**, 4162-4168.
241. A. Shome, A. M. Rather and U. Manna, *J. Mater. Chem. A*, 2018, **6**, 22465-22471.
242. C. Wang, F. Zhang, C. Yu and S. Wang, *ACS Appl. Mater. Interfaces*, 2020, **12**, 42430-42436.
243. Z. Liao, G. Wu, D. Lee and S. Yang, *ACS Appl. Mater. Interfaces*, 2019, **11**, 13642-13651.
244. M. Liu, J. Li, Y. Hou and Z. Guo, *ACS Nano*, 2017, **11**, 1113-1119.
245. S. Kim, K. Kim, G. Jun and W. Hwang, *ACS Nano*, 2020, **14**, 17233-17240.
246. Z. Zhao, Y. Ning, X. Jin, S. Ben, J. Zha, B. Su, D. Tian, K. Liu and L. Jiang, *ACS Nano*, 2020, **14**, 14869-14877.
247. S. Zhang, G. Jiang, S. Gao, H. Jin, Y. Zhu, F. Zhang and J. Jin, *ACS Nano*, 2018, **12**, 795-803.
248. N. Liu, W. F. Zhang, X. Y. Li, R. X. Qu, Q. D. Zhang, Y. Wei, L. Feng and L. Jiang, *J. Mater. Chem. A*, 2017, **5**, 15822-15827.
249. F. Z. Chen, J. L. Song, Z. A. Liu, J. Y. Liu, H. X. Zheng, S. Huang, J. Sun, W. J. Xu and X. Liu, *ACS Sustainable Chem. Eng.*, 2016, **4**, 6828-6837.
250. G. M. Ding, W. C. Jiao, R. G. Wang, Y. Niu, L. Y. Chen and L. F. Hao, *Adv. Funct. Mater.*, 2018, **28**, 1706686.
251. Y. Cheng, Q. Yang, Y. Fang, J. L. Yong, F. Chen and X. Hou, *Adv. Mater. Interfaces*, 2019, **6**, 1900067.
252. X. Cheng, Z. Sun, X. Yang, Z. Li, Y. Zhang, P. Wang, H. Liang, J. Ma and L. Shao, *J. Mater. Chem. A*, 2020, **8**, 16933-16942.
253. S. Yang, L. Chen, S. Liu, W. Hou, J. Zhu, Q. Zhang and P. Zhao, *ACS Appl. Mater. Interfaces*, 2020, **12**, 44952-44960.
254. Z. W. Yu, F. F. Yun, Z. Y. Gong, Q. Yao, S. X. Dou, K. S. Liu, L. Jiang and X. L. Wang, *J. Mater. Chem. A*, 2017, **5**, 10821-10826.
255. W. Liu, S. Xiang, X. Liu and B. Yang, *ACS Nano*, 2020, **14**, 9166-9175.
256. J. L. Yong, F. Chen, Q. Yang, Z. D. Jiang and X. Hou, *Adv. Mater. Interfaces*, 2018, **5**, 1701370.
257. H. F. Bohn and W. Federle, *Proc. Natl. Acad. Sci. U. S. A.*, 2004, **101**, 14138-14143.
258. A. Lafuma and D. Quere, *Europhys. Lett.*, 2011, **96**, 56001.
259. M. Villegas, Y. Zhang, N. Abu Jarad, L. Soleymani and T. F. Didar, *ACS Nano*, 2019, **13**, 8517-8536.
260. S. Wooh and H. J. Butt, *Angew. Chem. Int. Ed. Engl.*, 2017, **56**, 4965-4969.
261. P. Kim, M. J. Kreder, J. Alvarenga and J. Aizenberg, *Nano Lett.*, 2013, **13**, 1793-1799.
262. X. Tan, Y. Zhang, X. Liu, S. Xi, Z. Yan, Z. Liu, T. Shi and G. Liao, *Surf. Coat. Technol.*, 2021, **405**, 126568.
263. R. Togasawa, M. Tenjimbayashi, T. Matsubayashi, T. Moriya, K. Manabe and S. Shiratori, *ACS Appl. Mater. Interfaces*, 2018, **10**, 4198-4205.

264. K. Manabe, M. Nakano, Y. Hibi and K. Miyake, *Adv. Mater. Interfaces*, 2020, **7**, 1901818.

265. P. Liu, H. Zhang, W. He, H. Li, J. Jiang, M. Liu, H. Sun, M. He, J. Cui, L. Jiang and X. Yao, *ACS Nano*, 2017, **11**, 2248-2256.

266. X. Wang, Z. B. Wang, L. P. Heng and L. Jiang, *Adv. Funct. Mater.*, 2020, **30**, 1902686.

267. B. Khatir, S. Shabanian and K. Golovin, *ACS Appl. Mater. Interfaces*, 2020, **12**, 31933-31939.

268. Y. Tian, Y. Liu, Z. Su, S. Wang, B. Zhang, H. Zhang and Q. Zhang, *ACS Appl. Mater. Interfaces*, 2020, **12**, 54041-54052.

269. J. Yang, J. Li, X. Jia, Y. Li and H. Song, *ACS Appl. Mater. Interfaces*, 2020, **12**, 28645-28654.

270. Q. Wu, C. Yang, C. Su, L. Zhong, L. Zhou, T. Hang, H. Lin, W. Chen, L. Li and X. Xie, *ACS Biomater. Sci. Eng.*, 2020, **6**, 358-366.

271. M. Yu, M. Liu, L. Zhang, M. Li, Y. Hou, D. Wang and S. Fu, *J. Colloid Interface Sci.*, 2021, **586**, 279-291.

272. A. B. Tesler, L. H. Prado, M. M. Khusniyarov, I. Thievessen, A. Mazare, L. Fischer, S. Virtanen, W. H. Goldmann and P. Schmuki, *Adv. Funct. Mater.*, 2021, **31**, 2101090.

273. J. Liu, Y. Sun, X. Zhou, X. Li, M. Kappl, W. Steffen and H. J. Butt, *Adv. Mater.*, 2021, **33**, 2100237.

274. L. Y. Fang, J. H. Zhang, Y. C. Chen, S. L. Liu, Q. Y. Chen, A. Ke, L. T. Duan, S. L. Huang, X. L. Tian and Z. Xie, *Adv. Funct. Mater.*, 2021, **31**, 2100447.

275. S. Wooh and D. Vollmer, *Angew. Chem. Int. Ed. Engl.*, 2016, **55**, 6822-6824.

276. J. Wang, L. Wang, N. Sun, R. Tierney, H. Li, M. Corsetti, L. Williams, P. K. Wong and T. S. Wong, *Nat. Sustain.*, 2019, **2**, 1097-1105.

277. L. W. Chen, S. Park, J. Yoo, H. Hwang, H. Kim, J. Lee, J. Hong and S. Wooh, *Adv. Mater. Interfaces*, 2020, **7**, 2000305.

278. N. MacCallum, C. Howell, P. Kim, D. Sun, R. Friedlander, J. Ranisau, O. Ahanotu, J. J. Lin, A. Vena, B. Hatton, T. S. Wong and J. Aizenberg, *ACS Biomater. Sci. Eng.*, 2015, **1**, 43-51.

279. S. Amini, S. Kolle, L. Petrone, O. Ahanotu, S. Sunny, C. N. Sutanto, S. Hoon, L. Cohen, J. C. Weaver, J. Aizenberg, N. Vogel and A. Miserez, *Science*, 2017, **357**, 668-673.

280. X. T. Zhu, J. W. Lu, X. M. Li, B. Wang, Y. M. Song, X. Miao, Z. J. Wang and G. N. Ren, *Ind. Eng. Chem. Res.*, 2019, **58**, 8148-8153.

281. S. Basu, B. M. Hanh, J. Q. Isaiah Chua, D. Daniel, M. H. Ismail, M. Marchioro, S. Amini, S. A. Rice and A. Miserez, *J. Colloid Interface Sci.*, 2020, **568**, 185-197.

282. T. Salbaum, Y. Galvan, M. Haumann, P. Wasserscheid, R. Zarraga and N. Vogel, *J. Mater. Chem. A*, 2021, **9**, 2357-2366.

283. Y. Xue, P. Lv, H. Lin and H. Duan, *Appl. Mech. Rev.*, 2016, **68**, 030803.

284. K. Ellinas, A. Tserepi and E. Gogolides, *Adv. Colloid Interface Sci.*, 2017, **250**, 132-157.

285. S. L. Huang, P. Y. Lv and H. L. Duan, *Extreme Mech. Lett.*, 2019, **27**, 34-51.

286. T. Verho, C. Bower, P. Andrew, S. Franssila, O. Ikkala and R. H. Ras, *Adv. Mater.*, 2011, **23**, 673-678.

287. S. Peng, X. Yang, D. Tian and W. Deng, *ACS Appl. Mater. Interfaces*, 2014, **6**, 15188-15197.

288. G. B. Darband, M. Aliofkhazraei, S. Khorsand, S. Sokhanvar and A. Kaboli, *Arab. J. Chem.*, 2020, **13**, 1763-1802.

289. X. Chen, G. Wen and Z. Guo, *Mater. Horiz.*, 2020, **7**, 1697-1726.

290. H. L. Zou, S. D. Lin, Y. Y. Tu, G. J. Liu, J. W. Hu, F. Li, L. Miao, G. W. Zhang, H. S. Luo, F. Liu, C. M. Hou and M. L. Hu, *J. Mater. Chem. A*, 2013, **1**, 11246-11260.

291. C. Peng, Z. Chen and M. K. Tiwari, *Nat. Mater.*, 2018, **17**, 355-360.

292. E. Huovinen, J. Hirvi, M. Suvanto and T. A. Pakkanen, *Langmuir*, 2012, **28**, 14747-14755.

293. I. Bayer, *Coatings*, 2017, **7**, 12.

294. S. M. Mirmohammadi, S. Hoshian, V. P. Jokinen and S. Franssila, *Sci. Rep.*, 2021, **11**, 12646.

295. D. Zhang, G. Wu, H. Li, Y. Cui and Y. Zhang, *Chem. Eng. J.*, 2021, **406**, 126753.

296. D. Li, L. Ma, B. Zhang and S. Chen, *Nanoscale*, 2021, **13**, 7810-7821.

297. H. Kitano, *Nat. Rev. Genet.*, 2004, **5**, 826-837.

298. C. D. Persis and P. Tesi, *IEEE Trans. Autom. Control*, 2020, **65**, 909-924.

299. H. Lambley, T. M. Schutzius and D. Poulikakos, *Proc. Natl. Acad. Sci. U. S. A.*, 2020, **117**, 27188-27194.

300. A. Lafuma and D. Quere, *Nat. Mater.*, 2003, **2**, 457-460.
301. Y. Li, D. Quere, C. Lv and Q. Zheng, *Proc. Natl. Acad. Sci. U. S. A.*, 2017, **114**, 3387-3392.
302. S. Shi, C. Lv and Q. Zheng, *ACS Appl. Mater. Interfaces*, 2019, **11**, 43698-43707.
303. G. Liu, L. Fu, A. V. Rode and V. S. J. Craig, *Langmuir*, 2011, **27**, 2595-2600.
304. T. Maitra, M. K. Tiwari, C. Antonini, P. Schoch, S. Jung, P. Eberle and D. Poulikakos, *Nano Lett.*, 2014, **14**, 172-182.
305. D. Liao, M. H. He and H. H. Qiu, *Int. J. Heat Mass Tran.*, 2019, **133**, 341-351.
306. W. S. Wong, G. Liu, N. Nasiri, C. Hao, Z. Wang and A. Tricoli, *ACS Nano*, 2017, **11**, 587-596.
307. M. Reyssat, J. M. Yeomans and D. Quere, *Europhys. Lett.*, 2008, **81**, 26006.
308. X. Chen, R. Ma, J. Li, C. Hao, W. Guo, B. L. Luk, S. C. Li, S. Yao and Z. Wang, *Phys. Rev. Lett.*, 2012, **109**, 116101.
309. S. M. Mehr, L. Businaro, M. Habibi and A.-R. Moradi, *AlChE J.*, 2020, **66**, e16284.
310. Y. N. Sun, X. D. Chen, Y. X. Zheng, Y. H. Song, H. R. Zhang and S. S. Zhang, *ACS Appl. Nano Mater.*, 2020, **3**, 4767-4776.
311. Y.-T. Cheng and D. E. Rodak, *Appl. Phys. Lett.*, 2005, **86**, 144101.
312. T. Mouterde, P. Lecointre, G. Lehoucq, A. Checco, C. Clanet and D. Quere, *Nat. Commun.*, 2019, **10**, 1410.
313. J. Ma, H. Cha, M.-K. Kim, D. G. Cahill and N. Miljkovic, *Adv. Funct. Mater.*, 2019, **29**, 1905222.
314. J. Ma, D. G. Cahill and N. Miljkovic, *Nano Lett.*, 2020, **20**, 3918-3924.
315. J. Y. Ho, K. F. Rabbi, S. Khodakarami, J. C. Ma, K. S. Boyina and N. Miljkovic, *J. Heat Transfer*, 2022, **144**, 050801.
316. R. Poetes, K. Holtzmann, K. Franze and U. Steiner, *Phys. Rev. Lett.*, 2010, **105**, 166104.
317. P. Lv, Y. Xue, Y. Shi, H. Lin and H. Duan, *Phys. Rev. Lett.*, 2014, **112**, 196101.
318. P. Forsberg, F. Nikolajeff and M. Karlsson, *Soft Matter*, 2011, **7**, 104-109.
319. S. M. Varughese and N. Bhandaru, *Soft Matter*, 2020, **16**, 1692-1701.
320. E. Bormashenko, R. Pogreb, G. Whyman, Y. Bormashenko and M. Erlich, *Appl. Phys. Lett.*, 2007, **90**, 201917.
321. A. Sudeepthi, L. Yeo and A. K. Sen, *Appl. Phys. Lett.*, 2020, **116**, 093704.
322. T. Deng, K. K. Varanasi, M. Hsu, N. Bhate, C. Keimel, J. Stein and M. Blohm, *Appl. Phys. Lett.*, 2009, **94**, 133109.
323. H. X. Huang and X. Wang, *Mater. Today Commun.*, 2019, **19**, 487-494.
324. A. Azimi Yancheshme, S. Hassantabar, K. Maghsoudi, S. Keshavarzi, R. Jafari and G. Momen, *Chem. Eng. J.*, 2021, **417**, 127898.
325. A. G. Papathanasiou, *Curr. Opin. Colloid Interface Sci.*, 2018, **36**, 70-77.
326. M. E. Kavousanakis, N. T. Chamakos, K. Ellinas, A. Tserepi, E. Gogolides and A. G. Papathanasiou, *Langmuir*, 2018, **34**, 4173-4179.
327. G. Manukyan, J. M. Oh, D. van den Ende, R. G. Lammertink and F. Mugele, *Phys. Rev. Lett.*, 2011, **106**, 014501.
328. X. H. Yang, D. N. Lang, Z. Y. Wang, J. J. Cao, R. L. Wu and W. Wang, *RSC Adv.*, 2018, **8**, 39657-39666.
329. K. Tsougeni, N. Vourdas, A. Tserepi, E. Gogolides and C. Cardinaud, *Langmuir*, 2009, **25**, 11748-11759.
330. F. Z. Chen, J. Y. Liu, Y. Cui, S. Huang, J. L. Song, J. Sun, W. J. Xu and X. Liu, *J. Colloid Interface Sci.*, 2016, **470**, 221-228.
331. F. Z. Chen, W. J. Xu, S. Huang, J. Y. Liu, J. L. Song and X. Liu, *Surf. Interface Anal.*, 2016, **48**, 368-372.
332. J. L. Fritz and M. J. Owen, *J. Adhes.*, 1995, **54**, 33-45.
333. J. Kim, M. K. Chaudhury, M. J. Owen and T. Orbeck, *J. Colloid Interface Sci.*, 2001, **244**, 200-207.
334. J. Bacharouche, H. Haidara, P. Kunemann, M. F. Vallat and V. Roucoules, *Sens. Actuators, A*, 2013, **197**, 25-29.
335. J. Liu, F. Chen, H. Zheng, S. Liu, J. Sun, S. Huang, J. Song, Z. Jin and X. Liu, *RSC Adv.*, 2016, **6**, 79437-79447.
336. J. Zhang, L. Wu, B. Li, L. Li, S. Seeger and A. Wang, *Langmuir*, 2014, **30**, 14292-14299.
337. M. Tress, S. Karpitschka, P. Papadopoulos, J. H. Snoeijer, D. Vollmer and H. J. Butt, *Soft Matter*, 2017, **13**, 3760-3767.
338. R. Togasawa, F. Ohnuki and S. Shiratori, *ACS Appl. Nano Mater.*, 2018, **1**, 1758-1765.
339. C. Wei, G. Zhang, Q. Zhang, X. Zhan and F. Chen, *ACS Appl. Mater. Interfaces*, 2016, **8**, 34810-34819.
340. X. Jing and Z. Guo, *ACS Appl. Mater. Interfaces*, 2019, **11**, 35949-35958.
341. M. J. Kreder, D. Daniel, A. Tetreault, Z. L. Cao, B. Lemaire, J. V. I. Timonen and J. Aizenberg, *Phys. Rev. X*, 2018, **8**, 031053.
342. S. Adera, J. Alvarenga, A. V. Shneidman, C. T. Zhang, A. Davitt and J. Aizenberg, *ACS Nano*, 2020, **14**, 8024-8035.

343. Y. Q. Wu, S. S. Jia, S. Wang, Y. Qing, N. Yan, Q. H. Wang and T. T. Meng, *Chem. Eng. J.*, 2017, **328**, 186-196.
344. Z. S. Huang, Y. Y. Quan, J. J. Mao, Y. L. Wang, Y. K. Lai, J. Zheng, Z. Chen, K. Wei and H. Q. Li, *Chem. Eng. J.*, 2019, **358**, 1610-1619.
345. Z. L. Chu and S. Seeger, *RSC Adv.*, 2015, **5**, 21999-22004.
346. W. J. Wang, R. P. Liu, H. J. Chi, T. Zhang, Z. G. Xu and Y. Zhao, *ACS Appl. Mater. Interfaces*, 2019, **11**, 35327-35332.
347. Z. Dai, G. Chen, S. Ding, J. Lin, S. Li, Y. Xu and B. Zhou, *Adv. Funct. Mater.*, 2021, **31**, 2008574.
348. X. Wang, Q. Zhang, X. Zhang, Z. Li, I. P. Parkin and Z. Zhang, *Langmuir*, 2019, **35**, 14332-14338.
349. B. R. Wu, J. J. Lyu, C. Y. Peng, D. Z. Jiang, J. Yang, J. S. Yang, S. L. Xing and L. P. Sheng, *Chem. Eng. J.*, 2020, **387**, 124066.
350. Y. Q. Qing, C. Long, K. An, C. B. Hu and C. S. Liu, *J. Colloid Interface Sci.*, 2019, **548**, 224-232.
351. Y. Li, M. Ren, P. Lv, Y. Liu, H. Shao, C. Wang, C. Tang, Y. Zhou and M. Shuai, *J. Mater. Chem. A*, 2019, **7**, 7242-7255.
352. A. B. Gurav, H. X. Shi, M. Duan, X. L. Pang and X. G. Li, *Chem. Eng. J.*, 2021, **416**, 127809.
353. M. M. Liu, Y. Y. Hou, J. Li, L. Tie and Z. G. Guo, *Colloids Surf., A*, 2018, **553**, 645-651.
354. Y. Qing, S. Shi, C. Lv and Q. Zheng, *Adv. Funct. Mater.*, 2020, **30**, 1910665.
355. G. Luo, L. Wen, K. Yang, X. Li, S. Xu, P. Pi and X. Wen, *Chem. Eng. J.*, 2020, **383**, 123125.
356. K. Golovin, M. Boban, J. M. Mabry and A. Tuteja, *ACS Appl. Mater. Interfaces*, 2017, **9**, 11212-11223.
357. N. Vogel, R. A. Belisle, B. Hatton, T. S. Wong and J. Aizenberg, *Nat. Commun.*, 2013, **4**, 2167.
358. D. Lin, X. Zhang, S. Yuan, Y. Li, F. Xu, X. Wang, C. Li and H. Wang, *ACS Appl. Mater. Interfaces*, 2020, **12**, 48216-48224.
359. X. Huang, X. Kong, Y. W. Cui, X. X. Ye, X. L. Wang and B. Shi, *Chem. Eng. J.*, 2018, **336**, 633-639.
360. Y. Zhang, D. Ge and S. Yang, *J. Colloid Interface Sci.*, 2014, **423**, 101-107.
361. C. J. Yang, J. Q. Chao, J. C. Zhang, Z. T. Zhang, X. Liu, Y. L. Tian, D. W. Zhang and F. Z. Chen, *Colloids Surf., A*, 2020, **586**, 124278.
362. S. Zhao, L. Tie, Z. Guo and J. Li, *Langmuir*, 2020, **36**, 8560-8569.
363. T. X. Zhu, Y. Cheng, J. Y. Huang, J. Q. Xiong, M. Ge, J. J. Mao, Z. Liu, X. L. Dong, Z. Chen and Y. K. Lai, *Chem. Eng. J.*, 2020, **399**, 125746.
364. C. Sansom, P. Comley, P. King, H. Almond, C. Atkinson and E. Endaya, *Energy Proc.*, 2015, **69**, 198-207.
365. C. Howell, T. L. Vu, C. P. Johnson, X. Hou, O. Ahanotu, J. Alvarenga, D. C. Leslie, O. Uzun, A. Waterhouse, P. Kim, M. Super, M. Aizenberg, D. E. Ingber and J. Aizenberg, *Chem. Mater.*, 2015, **27**, 1792-1800.
366. J. S. Wexler, I. Jacobi and H. A. Stone, *Phys. Rev. Lett.*, 2015, **114**, 168301.
367. J. F. Wei, B. C. Li, L. Y. Jing, N. Tian, X. Zhao and J. P. Zhang, *Chem. Eng. J.*, 2020, **390**, 124562.
368. J. Lyu, B. Wu, N. Wu, C. Peng, J. Yang, Y. Meng and S. Xing, *Chem. Eng. J.*, 2021, **404**, 126456.
369. L. Liu, Z. Jiao, J. Zhang, Y. Wang, C. Zhang, X. Meng, X. Jiang, S. Niu, Z. Han and L. Ren, *ACS Appl. Mater. Interfaces*, 2021, **13**, 1967-1978.
370. J. C. Luo, S. J. Gao, H. Luo, L. Wang, X. W. Huang, Z. Guo, X. J. Lai, L. W. Lin, R. K. Y. Li and J. F. Gao, *Chem. Eng. J.*, 2021, **406**, 126898.
371. P. Varshney and S. S. Mohapatra, *Tribol. Int.*, 2018, **123**, 17-25.
372. D. Nanda, A. Sahoo, A. Kumar and B. Bhushan, *J. Colloid Interface Sci.*, 2019, **535**, 50-57.
373. J. Zang, S. Ryu, N. Pugno, Q. Wang, Q. Tu, M. J. Buehler and X. Zhao, *Nat. Mater.*, 2013, **12**, 321-325.
374. L. Wang, J. Luo, Y. Chen, L. Lin, X. Huang, H. Xue and J. Gao, *ACS Appl. Mater. Interfaces*, 2019, **11**, 17774-17783.
375. J. Liu, L. J. Ye, Y. L. Sun, M. H. Hu, F. Chen, S. Wegner, V. Mailander, W. Steffen, M. Kappl and H. J. Butt, *Adv. Mater.*, 2020, **32**, 1908008.
376. J. Ahn, J. Jeon, C. S. Heu and D. R. Kim, *Adv. Mater. Interfaces*, 2018, **5**, 1800980.
377. B. Deng, R. Cai, Y. Yu, H. Jiang, C. Wang, J. Li, L. Li, M. Yu, J. Li, L. Xie, Q. Huang and C. Fan, *Adv. Mater.*, 2010, **22**, 5473-5477.
378. L. Wu, L. Wang, Z. Guo, J. Luo, H. Xue and J. Gao, *ACS Appl. Mater. Interfaces*, 2019, **11**, 34338-34347.
379. B. G. Wei, C. Yue, J. L. Liu, G. Wang, L. Dai, X. S. Song, F. P. Wu, H. Li and Q. Chang, *Sep. Purif. Technol.*, 2019, **229**,

115808.

380. Y. Cheng, T. X. Zhu, S. H. Li, J. Y. Huang, J. J. Mao, H. Yang, S. W. Gao, Z. Chen and Y. K. Lai, *Chem. Eng. J.*, 2019, **355**, 290-298.
381. C. Yang, M. Wang, Z. Yang, D. Zhang, Y. Tian, X. Jing and X. Liu, *Langmuir*, 2019, **35**, 17027-17036.
382. Z. Yang, X. P. Liu and Y. L. Tian, *Prog. Org. Coat.*, 2020, **138**, 105313.
383. K. Maji, A. Das, M. Hirtz and U. Manna, *ACS Appl. Mater. Interfaces*, 2020, **12**, 14531-14541.
384. C. Zhou, G. Q. Li, C. Z. Li, Z. Zhang, Y. C. Zhang, S. Z. Wu, Y. L. Hu, W. L. Zhu, J. W. Li, J. R. Chu, Z. J. Hu, D. Wu and L. D. Yu, *Appl. Phys. Lett.*, 2017, **111**, 141607.
385. W. Kong, F. Li, Y. Pan and X. Zhao, *ACS Appl. Mater. Interfaces*, 2021, **13**, 35142-35152.
386. R. Mardosaite, A. Jurkeviciute and S. Rackauskas, *Cryst. Growth Des.*, 2021, **21**, 4765-4779.
387. J. C. Love, L. A. Estroff, J. K. Kriebel, R. G. Nuzzo and G. M. Whitesides, *Chem. Rev.*, 2005, **105**, 1103-1170.
388. S. Kim, J.-W. Lee and W. Hwang, *ACS Appl. Mater. Interfaces*, 2020, **12**, 28869-28875.
389. Y. Sun and Z. Guo, *Adv. Mater.*, 2020, **32**, 2004875.
390. V. Multanen, G. Whyman, E. Shulzinger, V. Valtsifer and E. Bormashenko, *Colloids Surf., A*, 2018, **538**, 133-139.
391. L. O. Prieto-López, P. Herbeck-Engel, L. Yang, Q. Wu, J. Li and J. Cui, *Adv. Mater. Interfaces*, 2020, **7**, 2000876.
392. S. M. Kang, I. You, W. K. Cho, H. K. Shon, T. G. Lee, I. S. Choi, J. M. Karp and H. Lee, *Angew. Chem. Int. Ed. Engl.*, 2010, **49**, 9401-9404.
393. C. H. Xue, L. L. Zhao, X. J. Guo, Z. Y. Ji, Y. Wu, S. T. Jia and Q. F. An, *Chem. Eng. J.*, 2020, **396**, 125231.
394. Z. Xiao, L. Q. Zhang, W. W. Zhang, X. Q. Yu and Y. F. Zhang, *J. Bionic. Eng.*, 2018, **15**, 1025-1034.
395. A. Chandekar, S. K. Sengupta and J. E. Whitten, *Appl. Surf. Sci.*, 2010, **256**, 2742-2749.
396. D. Torresin, M. K. Tiwari, D. Del Col and D. Poulikakos, *Langmuir*, 2013, **29**, 840-848.
397. A. T. Paxson, J. L. Yague, K. K. Gleason and K. K. Varanasi, *Adv. Mater.*, 2014, **26**, 418-423.
398. K. L. Wilke, D. S. Antao, S. Cruz, R. Iwata, Y. Zhao, A. Leroy, D. J. Preston and E. N. Wang, *ACS Nano*, 2020, **14**, 14878-14886.
399. R. Wang, K. Jakhar, S. Ahmed and D. S. Antao, *ACS Appl. Mater. Interfaces*, 2021, **13**, 34923-34934.
400. R. Wang, J. Guo, E. A. Muckleroy and D. S. Antao, *Int. J. Heat Mass Tran.*, 2022, **194**, 123028.
401. L. Boinovich, A. M. Emelyanenko and A. S. Pashinin, *ACS Appl. Mater. Interfaces*, 2010, **2**, 1754-1758.
402. I. Malavasi, I. Bernagozzi, C. Antonini and M. Marengo, *Surf. Innov.*, 2015, **3**, 49-60.
403. H. Zhou, H. Wang, H. Niu, A. Gestos and T. Lin, *Adv. Funct. Mater.*, 2013, **23**, 1664-1670.
404. S. Foorginezhad and M. M. Zerafat, *Appl. Surf. Sci.*, 2019, **464**, 458-471.
405. C. Zhang, F. Liang, W. Zhang, H. Liu, M. Ge, Y. Zhang, J. Dai, H. Wang, G. Xing, Y. Lai and Y. Tang, *ACS Omega*, 2020, **5**, 986-994.
406. C. Ye, V. S. D. Voet, R. Folkersma and K. Loos, *Adv. Mater.*, 2021, **33**, 2008460.
407. K. Xu, S. Ren, J. Song, J. Liu, Z. Liu, J. Sun and S. Ling, *Chem. Eng. J.*, 2021, **403**, 126348.
408. J. Song, S. Li, C. Zhao, Y. Lu, D. Zhao, J. Sun, T. Roy, C. J. Carmalt, X. Deng and I. P. Parkin, *Nanoscale*, 2018, **10**, 1920-1929.
409. S. K. Yu, W. Chen, Y. X. Wang, R. Zhao, R. H. Zang, J. M. Gu, J. X. Meng and S. T. Wang, *Adv. Mater. Interfaces*, 2021, **8**, 2100852.
410. W. Chen, P. Zhang, S. Yu, R. Zang, L. Xu, S. Wang, B. Wang and J. Meng, *Nat. Protoc.*, 2022, DOI: 10.1038/s41596-022-00725-3.
411. S. Pan, J. J. Richardson, A. J. Christofferson, Q. A. Besford, T. Zheng, B. J. Wood, X. Duan, M. J. Jara Fornerod, C. F. McConville, I. Yarovsky, S. Guldin, L. Jiang and F. Caruso, *J. Am. Chem. Soc.*, 2021, **143**, 9972-9981.
412. A. Shome, A. Das, A. Borbora, M. Dhar and U. Manna, *Chem. Soc. Rev.*, 2022, **51**, 5452-5497.
413. E. F. Hare, E. G. Shafrin and W. A. Zisman, *J. Phys. Chem.*, 1954, **58**, 236-239.
414. L. Zhang, A. G. Zhou, B. R. Sun, K. S. Chen and H. Z. Yu, *Nat. Commun.*, 2021, **12**, 982.
415. A. Samanta, W. J. Huang, H. Chaudhry, Q. H. Wang, S. K. Shaw and H. T. Ding, *ACS Appl. Mater. Interfaces*, 2020, **12**,

18032-18045.

416. P. C. Sasi, A. Alinezhad, B. Yao, A. Kubatova, S. A. Golovko, M. Y. Golovko and F. Xiao, *Water Res.*, 2021, **200**, 117271.
417. European Environment Agency, Emerging chemical risks in Europe — 'PFAS', https://www.eea.europa.eu/publications/emerging-chemical-risks-in-europe.
418. H. Ye, L. Zhu, W. Li, H. Liu and H. Chen, *ACS Appl. Mater. Interfaces*, 2017, **9**, 858-867.
419. J. Ju, X. Yao, X. Hou, Q. Liu, Y. S. Zhang and A. Khademhosseini, *J. Mater. Chem. A*, 2017, **5**, 16273-16280.
420. M. Zahid, G. Mazzon, A. Athanassiou and I. S. Bayer, *Adv. Colloid Interface Sci.*, 2019, **270**, 216-250.
421. Q. Y. Wang, G. Sun, Q. D. Tong, W. Yang and W. T. Hao, *Chem. Eng. J.*, 2021, **426**, 130829.
422. W. Wu, X. Wang, X. Liu and F. Zhou, *ACS Appl. Mater. Interfaces*, 2009, **1**, 1656-1661.
423. C. Y. Cao, M. Z. Ge, J. Y. Huang, S. H. Li, S. Deng, S. N. Zhang, Z. Chen, K. Q. Zhang, S. S. Al-Deyab and Y. K. Lai, *J. Mater. Chem. A*, 2016, **4**, 12179-12187.
424. E. M. Domingues, S. Arunachalam, J. Nauruzbayeva and H. Mishra, *Nat. Commun.*, 2018, **9**, 3606.
425. Z. Cheng, H. Lai, Y. Du, K. Fu, R. Hou, N. Zhang and K. Sun, *ACS Appl. Mater. Interfaces*, 2013, **5**, 11363-11370.
426. M. Liu, Y. Hou, J. Li, L. Tie and Z. Guo, *Chem. Eng. J.*, 2018, **337**, 462-470.
427. L. Zhao, R. Li, R. Xu, D. Si, Y. Shang, H. Ye, Y. Zhang, H. Ye and Q. Xin, *J. Membr. Sci.*, 2020, **611**, 118289.
428. S. Sett, P. Sokalski, K. Boyina, L. Li, K. F. Rabbi, H. Auby, T. Foulkes, A. Mahvi, G. Barac, L. W. Bolton and N. Miljkovic, *Nano Lett.*, 2019, **19**, 5287-5296.
429. Y. Ouyang, J. Zhao, R. Qiu, S. Hu, H. Niu, M. Chen and P. Wang, *Colloids Surf., A*, 2019, **583**, 124006.
430. F. Wang, W. Ding, J. He and Z. Zhang, *Chem. Eng. J.*, 2019, **360**, 243-249.
431. R. Stoddard, K. Nithyanandam and R. Pitchumani, *J. Colloid Interface Sci.*, 2022, **608**, 662-672.
432. Y. Yu, Z. H. Zhao and Q. S. Zheng, *Langmuir*, 2007, **23**, 8212-8216.
433. W. Li and A. Amirfazli, *Soft Matter*, 2008, **4**, 462-466.
434. B. P. Dyett, A. H. Wu and R. N. Lamb, *ACS Appl. Mater. Interfaces*, 2014, **6**, 18380-18394.
435. L. Mishchenko, B. Hatton, V. Bahadur, J. A. Taylor, T. Krupenkin and J. Aizenberg, *ACS Nano*, 2010, **4**, 7699-7707.
436. S. H. Park, E. H. Cho, J. Sohn, P. Theilmann, K. Chu, S. Lee, Y. Sohn, D. Kim and B. Kim, *Nano Res.*, 2013, **6**, 389-398.
437. J. G. Kim, H. J. Choi, K. C. Park, R. E. Cohen, G. H. McKinley and G. Barbastathis, *Small*, 2014, **10**, 2487-2494.
438. R. Hensel, A. Finn, R. Helbig, H. Braun, C. Neinhuis, W. Fischer and C. Werner, *Adv. Mater.*, 2014, **26**, 2029-2033.
439. J. Sun, P. Zhu, X. Yan, C. Zhang, Y. Jin, X. Chen and Z. Wang, *Appl. Phys. Rev.*, 2021, **8**, 031403.
440. J. Shieh, F. J. Hou, Y. C. Chen, H. M. Chen, S. P. Yang, C. C. Cheng and H. L. Chen, *Adv. Mater.*, 2010, **22**, 597-601.
441. X. Jiao, M. Li, X. Yu, W. S. Y. Wong and Y. Zhang, *Chem. Eng. J.*, 2021, **420**, 127606.
442. T. Mouterde, G. Lehoucq, S. Xavier, A. Checco, C. T. Black, A. Rahman, T. Midavaine, C. Clanet and D. Quere, *Nat. Mater.*, 2017, **16**, 658-663.
443. J. B. Boreyko and C. H. Chen, *Phys. Rev. Lett.*, 2009, **103**, 184501.
444. X. M. Chen, J. Wu, R. Y. Ma, M. Hua, N. Koratkar, S. H. Yao and Z. K. Wang, *Adv. Funct. Mater.*, 2011, **21**, 4617-4623.
445. K. M. Wisdom, J. A. Watson, X. Qu, F. Liu, G. S. Watson and C. H. Chen, *Proc. Natl. Acad. Sci. U. S. A.*, 2013, **110**, 7992-7997.
446. Y. Hou, M. Yu, X. Chen, Z. Wang and S. Yao, *ACS Nano*, 2015, **9**, 71-81.
447. X. Yan, L. Zhang, S. Sett, L. Feng, C. Zhao, Z. Huang, H. Vahabi, A. K. Kota, F. Chen and N. Miljkovic, *ACS Nano*, 2019, **13**, 1309-1323.
448. S. Baba, K. Sawada, K. Tanaka and A. Okamoto, *ACS Appl. Mater. Interfaces*, 2021, **13**, 32332-32342.
449. R. Wang, J. Zhu, K. Meng, H. Wang, T. Deng, X. Gao and L. Jiang, *Adv. Funct. Mater.*, 2018, **28**, 1800634.
450. M. McCarthy, K. Gerasopoulos, R. Enright, J. N. Culver, R. Ghodssi and E. N. Wang, *Appl. Phys. Lett.*, 2012, **100**, 263701.
451. T. Verho, J. T. Korhonen, L. Sainiemi, V. Jokinen, C. Bower, K. Franze, S. Franssila, P. Andrew, O. Ikkala and R. H. Ras, *Proc. Natl. Acad. Sci. U. S. A.*, 2012, **109**, 10210-10213.
452. C. Wang, Y. Yan, D. Du, X. Xiong and Y. Ma, *ACS Appl. Mater. Interfaces*, 2020, **12**, 29767-29777.
453. S. K. Laney, M. Michalska, T. Li, F. V. Ramirez, M. Portnoi, J. Oh, I. G. Thayne, I. P. Parkin, M. K. Tiwari and I.

Papakonstantinou, *Langmuir*, 2021, **37**, 10071-10078.

454. C. Zhang, S. Adera, J. Aizenberg and Z. Chen, *ACS Appl. Mater. Interfaces*, 2021, **13**, 15901-15909.
455. A. J. Galante, S. Haghanifar, E. G. Romanowski, R. M. Q. Shanks and P. W. Leu, *ACS Appl. Mater. Interfaces*, 2020, **12**, 22120-22128.
456. M. L. Liu, Y. F. Luo and D. M. Jia, *Compos. Part A*, 2020, **133**, 105861.
457. J. Marlena, J. K. S. Tan, Z. G. Lin, D. X. Z. Y. Li, B. X. Zhao, H. L. Leo, S. Kim and C. H. Yap, *NPG Asia Mater.*, 2021, **13**, 58.
458. I. A. Larmour, G. C. Saunders and S. E. J. Bell, *ACS Appl. Mater. Interfaces*, 2010, **2**, 2703-2706.
459. A. M. Rather and U. Manna, *Chem. Mater.*, 2016, **28**, 8689-8699.
460. S. Wu, Y. Du, Y. Alsaid, D. Wu, M. Hua, Y. Yan, B. Yao, Y. Ma, X. Zhu and X. He, *Proc. Natl. Acad. Sci. U. S. A.*, 2020, **117**, 11240-11246.
461. M. I. Jamil, L. Song, J. Zhu, N. Ahmed, X. Zhan, F. Chen, D. Cheng and Q. Zhang, *RSC Adv.*, 2020, **10**, 19157-19168.
462. Q. Sun, D. Wang, Y. Li, J. Zhang, S. Ye, J. Cui, L. Chen, Z. Wang, H. J. Butt, D. Vollmer and X. Deng, *Nat. Mater.*, 2019, **18**, 936-941.
463. G. Liu, C. Zhang, M. Liu, Z. Guo, X. Wang, C. Yu and M. Cao, *Trans. Tianjin Univ.*, 2020, **26**, 441-449.
464. O. Ramirez-Soto, V. Sanjay, D. Lohse, J. T. Pham and D. Vollmer, *Sci. Adv.*, 2020, **6**, eaba4330.
465. H. Jin, X. Tian, O. Ikkala and R. H. Ras, *ACS Appl. Mater. Interfaces*, 2013, **5**, 485-488.
466. C. Chen, M. Liu, Y. Hou, L. Zhang, M. Li, D. Wang and S. Fu, *Chem. Eng. J.*, 2020, **389**, 124420.
467. M. Dhar, A. Das, A. Shome, A. Borbora and U. Manna, *Mater. Horiz.*, 2021, **8**, 2717-2725.
468. J. Groten and J. Ruhe, *Langmuir*, 2013, **29**, 3765-3772.
469. X. Lin, J. Heo, H. Jeong, M. Choi, M. Chang and J. Hong, *J. Mater. Chem. A*, 2016, **4**, 17970-17980.
470. Y. Fang, C. Liu, M. Li, X. Miao, Y. Pei, Y. Yan, W. Xiao and L. Wu, *Ind. Eng. Chem. Res.*, 2020, **59**, 6130-6140.
471. Y. Chen and Z. G. Guo, *J. Mater. Chem. A*, 2020, **8**, 24075-24085.
472. Y. Li, H. Shao, P. Lv, C. Tang, Z. He, Y. Zhou, M. Shuai, J. Mei and W.-M. Lau, *Chem. Eng. J.*, 2018, **338**, 440-449.
473. J. Chen, L. Yuan, C. Shi, C. Wu, Z. Long, H. Qiao, K. Wang and Q. H. Fan, *ACS Appl. Mater. Interfaces*, 2021, **13**, 18142-18151.
474. X. Zhao, D. S. Park, J. Choi, S. Park, S. A. Soper and M. C. Murphy, *J. Colloid Interface Sci.*, 2020, **574**, 347-354.
475. G. Ren, Y. Song, X. Li, B. Wang, Y. Zhou, Y. Wang, B. Ge and X. Zhu, *J. Colloid Interface Sci.*, 2018, **522**, 57-62.
476. J. Peng, S. Yuan, H. Geng, X. Zhang, M. Zhang, F. Xu, D. Lin, Y. Gao and H. Wang, *Chem. Eng. J.*, 2022, **428**, 131162.
477. F. Wang, J. Pi, F. Song, R. Feng, C. Xu, X.-L. Wang and Y.-Z. Wang, *Chem. Eng. J.*, 2020, **381**, 122539.
478. Q. Zhu, B. Li, S. Li, G. Luo, B. Zheng and J. Zhang, *J. Colloid Interface Sci.*, 2020, **578**, 262-272.
479. Y. Sun and Z. Guo, *Nanoscale*, 2019, **11**, 13853-13862.
480. T. Priemel, G. Palia, F. Forste, F. Jehle, S. Sviben, I. Mantouvalou, P. Zaslansky, L. Bertinetti and M. J. Harrington, *Science*, 2021, **374**, 206-211.
481. F. Guo, Q. Wen, Y. Peng and Z. Guo, *J. Mater. Chem. A*, 2017, **5**, 21866-21874.
482. W. Stöber, A. Fink and E. Bohn, *J. Colloid Interface Sci.*, 1968, **26**, 62-69.
483. K. Koch, B. Bhushan, H. J. Ensikat and W. Barthlott, *Phil. Trans. R. Soc. A.*, 2009, **367**, 1673-1688.
484. M. Wu, B. Ma, T. Pan, S. Chen and J. Sun, *Adv. Funct. Mater.*, 2016, **26**, 569-576.
485. H. Wang, H. Zhou, A. Gestos, J. Fang and T. Lin, *ACS Appl. Mater. Interfaces*, 2013, **5**, 10221-10226.
486. Y. Li, L. Li and J. Sun, *Angew. Chem. Int. Ed. Engl.*, 2010, **49**, 6129-6133.
487. Y. Liu, Y. Liu, H. Hu, Z. Liu, X. Pei, B. Yu, P. Yan and F. Zhou, *J. Phys. Chem. C*, 2015, **119**, 7109-7114.
488. C. Howell, T. L. Vu, J. J. Lin, S. Kolle, N. Juthani, E. Watson, J. C. Weaver, J. Alvarenga and J. Aizenberg, *ACS Appl. Mater. Interfaces*, 2014, **6**, 13299-13307.
489. J. Q. Li, H. B. Zhao and L. Q. Wang, *Adv. Mater. Interfaces*, 2021, **8**, 2100561.
490. S. Hoshian, V. Jokinen and S. Franssila, *Soft Matter*, 2016, **12**, 6526-6535.
491. P. B. Weisensee, J. Tian, N. Miljkovic and W. P. King, *Sci. Rep.*, 2016, **6**, 30328.

492. X. Bai, Q. Yang, Y. Fang, J. Zhang, J. Yong, X. Hou and F. Chen, *Chem. Eng. J.*, 2020, **383**, 123143.
493. U. Manna and D. M. Lynn, *Adv. Mater.*, 2013, **25**, 5104-5108.
494. J. Song, M. Gao, C. Zhao, Y. Lu, L. Huang, X. Liu, C. J. Carmalt, X. Deng and I. P. Parkin, *ACS Nano*, 2017, **11**, 9259-9267.
495. Z. Cheng, D. Zhang, X. Luo, H. Lai, Y. Liu and L. Jiang, *Adv. Mater.*, 2021, **33**, 2001718.
496. X. Bai, Q. Yang, Y. Fang, J. Yong, Y. Bai, J. Zhang, X. Hou and F. Chen, *Chem. Eng. J.*, 2020, **400**, 125930.
497. Y. Wang, Z. Qiu, Z. Lang, Y. Xie, Z. Xiao, H. Wang, D. Liang, J. Li and K. Zhang, *Adv. Mater.*, 2021, **33**, 2005263.
498. H. Ye, D. Chen, N. Li, Q. Xu, H. Li, J. He and J. Lu, *ACS Appl. Mater. Interfaces*, 2019, **11**, 38313-38320.
499. Y. Shan, Z. Zhou, H. Bai, T. Wang, L. Liu, X. Zhao and Y. Huang, *Soft Matter*, 2020, **16**, 8473-8481.
500. B. Jin, M. Liu, Q. Zhang, X. Zhan and F. Chen, *Langmuir*, 2017, **33**, 10340-10350.
501. T. Lv, Z. Cheng, E. Zhang, H. Kang, Y. Liu and L. Jiang, *Small*, 2017, **13**, 1503402.
502. D. J. Zhang, Z. J. Cheng, H. J. Kang, J. X. Yu, Y. Y. Liu and L. Jiang, *Angew. Chem. Int. Ed. Engl.*, 2018, **57**, 3701-3705.
503. S. Pan, M. Chen and L. Wu, *ACS Appl. Mater. Interfaces*, 2020, **12**, 5157-5165.
504. M. Yu, M. Liu and S. Fu, *ACS Appl. Mater. Interfaces*, 2021, **13**, 32149-32160.
505. B. H. Ren, Y. N. Chen, Y. Q. Li, W. J. Li, S. Y. Gao, H. F. Li and R. Cao, *Chem. Eng. J.*, 2020, **384**, 123389.
506. M. Ran, W. Zheng and H. Wang, *Mater. Sci. Technol.*, 2019, **35**, 313-326.
507. B. Zhang and W. Xu, *New J. Chem.*, 2021, **45**, 15170-15179.
508. Z. Wang, Q. Li, Z. She, F. Chen, L. Li, X. Zhang and P. Zhang, *Appl. Surf. Sci.*, 2013, **271**, 182-192.
509. F. Su and K. Yao, *ACS Appl. Mater. Interfaces*, 2014, **6**, 8762-8770.
510. L. Li, T. Huang, J. Lei, J. He, L. Qu, P. Huang, W. Zhou, N. Li and F. Pan, *ACS Appl. Mater. Interfaces*, 2015, **7**, 1449-1457.
511. Y. Li, X. G. Zhang, Y. X. Cui, H. Y. Wang and J. X. Wang, *Chem. Eng. J.*, 2019, **374**, 1326-1336.
512. H. Sun, F. Lei, T. Li, H. Han, B. Li, D. Li and D. Sun, *ACS Appl. Mater. Interfaces*, 2021, **13**, 6678-6687.
513. S. M. A. Mousavi and R. Pitchumani, *J. Colloid Interface Sci.*, 2022, **607**, 323-333.
514. B. Zhang, W. Xu, D. H. Xia, X. Fan, J. Duan and Y. Lu, *Langmuir*, 2021, **37**, 11061-11071.
515. J. Lee, S. Wooh and C. H. Choi, *J. Colloid Interface Sci.*, 2020, **558**, 301-309.
516. P. Zhang, L. Lin, D. Zang, X. Guo and M. Liu, *Small*, 2017, **13**, 1503334.
517. Z. Li and Z. Guo, *Nanoscale*, 2019, **11**, 22636-22663.
518. A. C. Lima and J. F. Mano, *Nanomedicine*, 2015, **10**, 103-119.
519. A. C. Lima and J. F. Mano, *Nanomedicine*, 2015, **10**, 271-297.
520. E. S. Leibner, N. Barnthip, W. Chen, C. R. Baumrucker, J. V. Badding, M. Pishko and E. A. Vogler, *Acta Biomater*, 2009, **5**, 1389-1398.
521. Q. Huang, L. Lin, Y. Yang, R. Hu, E. A. Vogler and C. Lin, *Biomaterials*, 2012, **33**, 8213-8220.
522. X. Q. Dou, D. Zhang, C. Feng and L. Jiang, *ACS Nano*, 2015, **9**, 10664-10672.
523. J. Y. Jiang, J. L. Xu, Z. H. Liu, L. Deng, B. Sun, S. D. Liu, L. Wang and H. Y. Liu, *Appl. Surf. Sci.*, 2015, **347**, 591-595.
524. J. M. Nokes, R. Liedert, M. Y. Kim, A. Siddiqui, M. Chu, E. K. Lee and M. Khine, *Adv. Healthcare Mater.*, 2016, **5**, 593-601.
525. K. Bartlet, S. Movafaghi, A. Kota and K. C. Popat, *RSC Adv.*, 2017, **7**, 35466-35476.
526. K. Han, T. Y. Park, K. Yong and H. J. Cha, *ACS Appl. Mater. Interfaces*, 2019, **11**, 9777-9785.
527. S. L. Chen, S. Y. Li, Z. P. Ye, Y. F. Zhang, S. D. Gao, H. Rong, J. H. Zhang, L. D. Deng and A. J. Dong, *Chem. Eng. J.*, 2022, **446**, 136985.
528. J. Zhang, G. Li, D. Li, X. Zhang, Q. Li, Z. Liu, Y. Fang, S. Zhang and J. Man, *ACS Appl. Mater. Interfaces*, 2021, **13**, 29021-29033.
529. G. B. Hwang, K. Page, A. Patir, S. P. Nair, E. Allan and I. P. Parkin, *ACS Nano*, 2018, **12**, 6050-6058.
530. N. Rauner, C. Mueller, S. Ring, S. Boehle, A. Strassburg, C. Schoeneweiss, M. Wasner and J. C. Tiller, *Adv. Funct. Mater.*, 2018, **28**, 1801248.
531. Y. Fu, J. Jiang, Q. Zhang, X. Zhan and F. Chen, *J. Mater. Chem. A*, 2017, **5**, 275-284.
532. L. P. Xu, J. Peng, Y. Liu, Y. Wen, X. Zhang, L. Jiang and S. Wang, *ACS Nano*, 2013, **7**, 5077-5083.

533. K. Chen, S. Zhou and L. Wu, *ACS Nano*, 2016, **10**, 1386-1394.
534. A. K. Epstein, T. S. Wong, R. A. Belisle, E. M. Boggs and J. Aizenberg, *Proc. Natl. Acad. Sci. U. S. A.*, 2012, **109**, 13182-13187.
535. K. Manabe, K. H. Kyung and S. Shiratori, *ACS Appl. Mater. Interfaces*, 2015, **7**, 4763-4771.
536. Y. Lee, Y. W. Chung, J. Park, K. Park, Y. Seo, S. N. Hong, S. H. Lee, H. Jeon and J. Seo, *Sci. Rep.*, 2020, **10**, 17454.
537. A. B. Tesler, P. Kim, S. Kolle, C. Howell, O. Ahanotu and J. Aizenberg, *Nat. Commun.*, 2015, **6**, 8649.
538. E. Kasapgil, M. Badv, C. A. Cantu, S. Rahmani, H. Y. Erbil, I. Anac Sakir, J. I. Weitz, Z. Hosseini-Doust and T. F. Didar, *ACS Biomater. Sci. Eng.*, 2021, **7**, 541-552.
539. E. Ozkan, A. Mondal, M. Douglass, S. P. Hopkins, M. Garren, R. Devine, R. Pandey, J. Manuel, P. Singha, J. Warnock and H. Handa, *J. Colloid Interface Sci.*, 2022, **608**, 1015-1024.
540. J. K. Hong, K. Mathur, A. M. Ruhoff, B. Akhavan, A. Waterhouse and C. Neto, *Adv. Mater. Interfaces*, 2022, **9**, 2102214.
541. Q. Wei, C. Schlaich, S. Prevost, A. Schulz, C. Bottcher, M. Gradzielski, Z. H. Qi, R. Haag and C. A. Schalley, *Adv. Mater.*, 2014, **26**, 7358-7364.
542. Q. Li and Z. G. Guo, *J. Mater. Chem. A*, 2018, **6**, 13549-13581.
543. K. Golovin, A. Dhyani, M. D. Thouless and A. Tuteja, *Science*, 2019, **364**, 371-375.
544. L. B. Boinovich, A. M. Emelyanenko, K. A. Emelyanenko and E. B. Modin, *ACS Nano*, 2019, **13**, 4335-4346.
545. J. Lv, Y. Song, L. Jiang and J. Wang, *ACS Nano*, 2014, **8**, 3152-3169.
546. P. Guo, Y. Zheng, M. Wen, C. Song, Y. Lin and L. Jiang, *Adv. Mater.*, 2012, **24**, 2642-2648.
547. W. S. Y. Wong, K. I. Hegner, V. Donadei, L. Hauer, A. Naga and D. Vollmer, *Nano Lett.*, 2020, **20**, 8508-8515.
548. S. S. Latthe, R. S. Sutar, A. K. Bhosale, S. Nagappan, C.-S. Ha, K. K. Sadasivuni, S. Liu and R. Xing, *Prog. Org. Coat.*, 2019, **137**, 105373.
549. T. M. Schutzius, S. Jung, T. Maitra, P. Eberle, C. Antonini, C. Stamatopoulos and D. Poulikakos, *Langmuir*, 2015, **31**, 4807-4821.
550. S. Jung, M. K. Tiwari, N. V. Doan and D. Poulikakos, *Nat. Commun.*, 2012, **3**, 615.
551. A. Alizadeh, M. Yamada, R. Li, W. Shang, S. Otta, S. Zhong, L. Ge, A. Dhinojwala, K. R. Conway, V. Bahadur, A. J. Vinciquerra, B. Stephens and M. L. Blohm, *Langmuir*, 2012, **28**, 3180-3186.
552. D. Richard, C. Clanet and D. Quéré, *Nature*, 2002, **417**, 811.
553. J. C. Bird, R. Dhiman, H. M. Kwon and K. K. Varanasi, *Nature*, 2013, **503**, 385-388.
554. Y. Liu, L. Moevius, X. Xu, T. Qian, J. M. Yeomans and Z. Wang, *Nat. Phys.*, 2014, **10**, 515-519.
555. L. Cao, A. K. Jones, V. K. Sikka, J. Wu and D. Gao, *Langmuir*, 2009, **25**, 12444-12448.
556. L. Wang, Q. Gong, S. Zhan, L. Jiang and Y. Zheng, *Adv. Mater.*, 2016, **28**, 7729-7735.
557. X. Zhou, Y. Sun and J. Liu, *Adv. Mater. Interfaces*, 2021, **8**, 2100327.
558. V. Bahadur, L. Mishchenko, B. Hatton, J. A. Taylor, J. Aizenberg and T. Krupenkin, *Langmuir*, 2011, **27**, 14143-14150.
559. T. Maitra, C. Antonini, M. K. Tiwari, A. Mularczyk, Z. Imeri, P. Schoch and D. Poulikakos, *Langmuir*, 2014, **30**, 10855-10861.
560. R. Pan, H. Zhang and M. Zhong, *ACS Appl. Mater. Interfaces*, 2021, **13**, 1743-1753.
561. P. Tourkine, M. Le Merrer and D. Quere, *Langmuir*, 2009, **25**, 7214-7216.
562. P. Eberle, M. K. Tiwari, T. Maitra and D. Poulikakos, *Nanoscale*, 2014, **6**, 4874-4881.
563. X. Chen, R. Ma, H. Zhou, X. Zhou, L. Che, S. Yao and Z. Wang, *Sci. Rep.*, 2013, **3**, 2515.
564. S. Farhadi, M. Farzaneh and S. A. Kulinich, *Appl. Surf. Sci.*, 2011, **257**, 6264-6269.
565. K. K. Varanasi, T. Deng, J. D. Smith, M. Hsu and N. Bhate, *Appl. Phys. Lett.*, 2010, **97**, 234102.
566. J. B. Boreyko and C. P. Collier, *ACS Nano*, 2013, **7**, 1618-1627.
567. Q. Zhang, M. He, J. Chen, J. Wang, Y. Song and L. Jiang, *Chem. Commun.*, 2013, **49**, 4516-4518.
568. J. B. Boreyko, B. R. Srijanto, T. D. Nguyen, C. Vega, M. Fuentes-Cabrera and C. P. Collier, *Langmuir*, 2013, **29**, 9516-9524.
569. A. Kim, C. Lee, H. Kim and J. Kim, *ACS Appl. Mater. Interfaces*, 2015, **7**, 7206-7213.

570. H. Q. Zhang, G. L. Zhao, S. W. Wu, Y. Alsaid, W. Z. Zhao, X. Yan, L. Liu, G. S. Zou, J. Y. Lv, X. M. He, Z. Y. He and J. J. Wang, *Proc. Natl. Acad. Sci. U.S.A.*, 2021, **118**, e2100978118.
571. H. R. Ren, S. Y. Zhu, Y. Xiao and C. Li, *ACS Appl. Nano Mater.*, 2022, **5**, 810-817.
572. P. Kim, T. S. Wong, J. Alvarenga, M. J. Kreder, W. E. Adorno-Martinez and J. Aizenberg, *ACS Nano*, 2012, **6**, 6569-6577.
573. S. Anand, A. T. Paxson, R. Dhiman, J. D. Smith and K. K. Varanasi, *ACS Nano*, 2012, **6**, 10122-10129.
574. S. Heydarian, R. Jafari and G. Momen, *Prog. Org. Coat.*, 2021, **151**, 106096.
575. P. W. Wilson, W. Lu, H. Xu, P. Kim, M. J. Kreder, J. Alvarenga and J. Aizenberg, *Phys. Chem. Chem. Phys.*, 2013, **15**, 581-585.
576. Q. Liu, Y. Yang, M. Huang, Y. X. Zhou, Y. Y. Liu and X. D. Liang, *Appl. Surf. Sci.*, 2015, **346**, 68-76.
577. K. Rykaczewski, S. Anand, S. B. Subramanyam and K. K. Varanasi, *Langmuir*, 2013, **29**, 5230-5238.
578. M. J. Coady, M. Wood, G. Q. Wallace, K. E. Nielsen, A. M. Kietzig, F. Lagugne-Labarthet and P. J. Ragogna, *ACS Appl. Mater. Interfaces*, 2018, **10**, 2890-2896.
579. Y. Yuan, H. Y. Xiang, G. Y. Liu, L. Wang, H. L. Liu and R. J. Liao, *Adv. Mater. Interfaces*, 2022, **9**, 2101968.
580. S. A. Kulinich and M. Farzaneh, *Appl. Surf. Sci.*, 2009, **255**, 8153-8157.
581. S. Bengaluru Subramanyam, V. Kondrashov, J. Ruhe and K. K. Varanasi, *ACS Appl. Mater. Interfaces*, 2016, **8**, 12583-12587.
582. T. B. Nguyen, S. Park and H. Lim, *Appl. Surf. Sci.*, 2018, **435**, 585-591.
583. J. W. Jiang, Y. Z. Shen, Z. Wang, J. Tao, W. L. Liu, H. F. Chen, S. Y. Liu, X. Y. Xie and C. J. Zeng, *Chem. Eng. J.*, 2022, **431**, 133276.
584. S. A. Kulinich, S. Farhadi, K. Nose and X. W. Du, *Langmuir*, 2011, **27**, 25-29.
585. Y. Wang, J. Xue, Q. Wang, Q. Chen and J. Ding, *ACS Appl. Mater. Interfaces*, 2013, **5**, 3370-3381.
586. S. Barthwal, B. Lee and S. H. Lim, *Appl. Surf. Sci.*, 2019, **496**, 143677.
587. S. B. Subramanyam, K. Rykaczewski and K. K. Varanasi, *Langmuir*, 2013, **29**, 13414-13418.
588. Y. Long, X. Yin, P. Mu, Q. Wang, J. Hu and J. Li, *Chem. Eng. J.*, 2020, **401**, 126137.
589. A. R. Parker and C. R. Lawrence, *Nature*, 2001, **414**, 33-34.
590. L. Zhai, M. C. Berg, F. C. Cebeci, Y. Kim, J. M. Milwid, M. F. Rubner and R. E. Cohen, *Nano Lett.*, 2006, **6**, 1213-1217.
591. Z. Yu, F. F. Yun, Y. Wang, L. Yao, S. Dou, K. Liu, L. Jiang and X. Wang, *Small*, 2017, **13**, 1701403.
592. C. F. Wang, W. N. Wang, S. W. Kuo, Y. W. Chiang, J. H. Hung and K. J. Lee, *Langmuir*, 2018, **34**, 11442-11448.
593. J. Son, G. Y. Bae, S. Lee, G. Lee, S. W. Kim, D. Kim, S. Chung and K. Cho, *Adv. Mater.*, 2021, **33**, 2102740.
594. B. Su, S. T. Wang, Y. L. Song and L. Jiang, *Soft Matter*, 2011, **7**, 5144-5149.
595. Y. L. Tan, B. R. Hu, Z. Y. Chu and W. J. Wu, *Adv. Funct. Mater.*, 2019, **29**, 1900266.
596. S. Ben, T. Zhou, H. Ma, J. Yao, Y. Ning, D. Tian, K. Liu and L. Jiang, *Adv. Sci.*, 2019, **6**, 1900834.
597. X. Xue, C. Yu, J. Wang and L. Jiang, *ACS Nano*, 2016, **10**, 10887-10893.
598. C. M. Yu, X. B. Zhu, K. Li, M. Y. Cao and L. Jiang, *Adv. Funct. Mater.*, 2017, **27**, 1701605.
599. J. Yong, F. Chen, Y. Fang, J. Huo, Q. Yang, J. Zhang, H. Bian and X. Hou, *ACS Appl. Mater. Interfaces*, 2017, **9**, 39863-39871.
600. K. Yin, S. Yang, X. R. Dong, D. K. Chu, X. Gong and J. A. Duan, *Appl. Surf. Sci.*, 2019, **471**, 999-1004.
601. J. L. Song, F. S. Guan, W. H. Pan, Z. A. Liu, J. Sun, S. Y. Ling, X. Deng and Y. W. Sun, *Adv. Funct. Mater.*, 2020, **30**, 1910778.
602. R. Y. Dai, G. Q. Li, L. Xiao, Y. X. Li, Z. H. Cui, L. Jia, M. L. Zhou, Y. G. Song, Y. Yang, Y. Cai, C. F. Chen and K. Yin, *Chem. Eng. J.*, 2022, **446**, 136874.
603. L. Huang, X. Y. Wang, C. L. Zhao, J. Y. Liu, Z. A. Liu, Y. K. Sun, X. Liu and J. L. Song, *Micro Nano Lett.*, 2018, **13**, 896-901.
604. T. Jiang, Z. G. Guo and W. M. Liu, *J. Mater. Chem. A*, 2015, **3**, 1811-1827.
605. J. Ju, H. Bai, Y. Zheng, T. Zhao, R. Fang and L. Jiang, *Nat. Commun.*, 2012, **3**, 1247.
606. F. Bai, J. T. Wu, G. M. Gong and L. Guo, *Adv. Sci.*, 2015, **2**, 1500047.

607. K. Yin, S. Yang, X. R. Dong, D. K. Chu, J. A. Duan and J. He, *Appl. Phys. Lett.*, 2018, **112**, 243701.
608. C. M. Yu, M. Y. Cao, Z. C. Dong, J. M. Wang, K. Li and L. Jiang, *Adv. Funct. Mater.*, 2016, **26**, 3236-3243.
609. X. Gou and Z. Guo, *Adv. Colloid Interface Sci.*, 2019, **269**, 87-121.
610. Y. Wu, M. Y. Zhao and Z. G. Guo, *Chem. Eng. J.*, 2018, **334**, 1584-1593.
611. J. Q. Chao, J. K. Feng, F. Z. Chen, B. Wang, Y. L. Tian and D. W. Zhang, *Colloids Surf., A*, 2021, **610**, 125708.
612. J. L. Yong, Q. Yang, F. Chen, H. Bian, G. Q. Du, U. Farooq and X. Hou, *Adv. Mater. Interfaces*, 2015, **2**, 1400388.
613. M. H. Sarikhani, P. Esmaeilzadeh and M. T. Sadeghi, *Mater. Chem. Phys.*, 2021, **263**, 124413.
614. J. L. Huo, Q. Yang, F. Chen, J. L. Yong, Y. Fang, J. Z. Zhang, L. Liu and X. Hou, *Langmuir*, 2017, **33**, 3659-3665.
615. S. J. Gao, Y. Z. Zhu, J. L. Wang, F. Zhang, J. Y. Li and J. Jin, *Adv. Funct. Mater.*, 2018, **28**, 1801944.
616. J. Li and Z. Guo, *Research*, 2019, **2019**, 9139535.
617. X. L. Gou and Z. G. Guo, *Chem. Eng. J.*, 2021, **411**, 128495.
618. X. Yang, K. Zhuang, Y. Lu and X. Wang, *ACS Nano*, 2021, **15**, 2589-2599.
619. Z. Cai, F. Chen, Y. Tian, D. Zhang, Z. Lian and M. Cao, *Chem. Eng. J.*, 2022, **449**, 137831.
620. X. Gou and Z. Guo, *Langmuir*, 2020, **36**, 8983-8992.
621. P. Guo, Z. B. Wang, L. P. Heng, Y. Q. Zhang, X. Wang and L. Jiang, *Adv. Funct. Mater.*, 2019, **29**, 1808717.
622. S. Zhu, Y. Bian, T. Wu, C. Chen, Y. Jiao, Z. Jiang, Z. Huang, E. Li, J. Li, J. Chu, Y. Hu, D. Wu and L. Jiang, *Nano Lett.*, 2020, **20**, 5513-5521.
623. X. Wang, H. Bai, J. Yang, Z. Li, Y. Wu, C. Yu, L. Jiang and M. Cao, *Small*, 2021, **17**, 2007803.
624. R. Feng, C. Xu, F. Song, F. Wang, X. L. Wang and Y. Z. Wang, *ACS Appl. Mater. Interfaces*, 2020, **12**, 12373-12381.
625. S. Zhang, J. Huang, Z. Chen and Y. Lai, *Small*, 2017, **13**, 1602992.
626. K. Yin, H. Du, X. Dong, C. Wang, J. A. Duan and J. He, *Nanoscale*, 2017, **9**, 14620-14626.
627. Y. Dong, Y. Liu, C. Hu, I. R. MacDonald and Y. Lu, *Science*, 2022, **376**, 300-1304.
628. The International Tanker Owners Pollution Federation, Oil Tanker Spill Statistics 2019, http://www.itopf.com/knowledge-resources/data-statistics/statistics/.
629. M. Duan, Z. He, X. Wang, B. Jing, Z. Xu, Y. Xiong and S. Fang, *J. Mol. Liq.*, 2019, **286**, 110868.
630. A. Xie, J. Cui, J. Yang, Y. Chen, J. Dai, J. Lang, C. Li and Y. Yan, *J. Mater. Chem. A*, 2019, **7**, 8491-8502.
631. D. D. Ejeta, C.-F. Wang, S.-W. Kuo, J.-K. Chen, H.-C. Tsai, W.-S. Hung, C.-C. Hu and J.-Y. Lai, *Chem. Eng. J.*, 2020, **402**, 126289.
632. X. Lin and J. Hong, *Adv. Mater. Interfaces*, 2019, **6**, 1900126.
633. L. Qiu, Y. Sun and Z. Guo, *J. Mater. Chem. A*, 2020, **8**, 16831-16853.
634. A. Pavia-Sanders, S. Zhang, J. A. Flores, J. E. Sanders, J. E. Raymond and K. L. Wooley, *ACS Nano*, 2013, **7**, 7552-7561.
635. T. Arbatan, X. Y. Fang and W. Shen, *Chem. Eng. J.*, 2011, **166**, 787-791.
636. S. M. Davoodi, M. Taheran, S. K. Brar, R. Galvez-Cloutier and R. Martel, *Fuel*, 2019, **251**, 57-72.
637. M. Sarcletti, D. Vivod, T. Luchs, T. Rejek, L. Portilla, L. Muller, H. Dietrich, A. Hirsch, D. Zahn and M. Halik, *Adv. Funct. Mater.*, 2019, **29**, 1805742.
638. Q. Zhu, F. Tao and Q. Pan, *ACS Appl. Mater. Interfaces*, 2010, **2**, 3141-3146.
639. L. H. Yu, G. Z. Hao, Q. Q. Liang, S. Zhou, N. Zhang and W. Jiang, *Appl. Surf. Sci.*, 2015, **357**, 2297-2305.
640. M. Patowary, R. Ananthakrishnan and K. Pathak, *Environ. Sci. Pollut. Res.*, 2017, **24**, 18063-18072.
641. F. Zhang, W. B. Zhang, Z. Shi, D. Wang, J. Jin and L. Jiang, *Adv. Mater.*, 2013, **25**, 4192-4198.
642. X. K. Zhang, H. Li, W. Z. Miao, Q. Shen, J. Wang, D. L. Peng, J. D. Liu and Y. T. Zhang, *AlChE J.*, 2019, **65**, e16596.
643. J. Li, R. M. Kang, X. H. Tang, H. D. She, Y. X. Yang and F. Zha, *Nanoscale*, 2016, **8**, 7638-7645.
644. X. Wang, P. Yu, K. Zhang, M. Wu, Q. Wu, J. Liu, J. Yang and J. Zhang, *ACS Appl. Polym. Mater.*, 2019, **1**, 2875-2882.
645. C. Zhou, Z. Chen, H. Yang, K. Hou, X. Zeng, Y. Zheng and J. Cheng, *ACS Appl. Mater. Interfaces*, 2017, **9**, 9184-9194.
646. X. Zhou, Z. Zhang, X. Xu, F. Guo, X. Zhu, X. Men and B. Ge, *ACS Appl. Mater. Interfaces*, 2013, **5**, 7208-7214.
647. M. Zhang, W. Ma, J. Cui, S. Wu, J. Han, Y. Zou and C. Huang, *J. Hazard. Mater.*, 2020, **383**, 121152.
648. B. Wang, W. Liang, Z. Guo and W. Liu, *Chem. Soc. Rev.*, 2015, **44**, 336-361.

649. J. Ge, L. A. Shi, Y. C. Wang, H. Y. Zhao, H. B. Yao, Y. B. Zhu, Y. Zhang, H. W. Zhu, H. A. Wu and S. H. Yu, *Nat Nanotechnol*, 2017, **12**, 434-440.
650. D. Chen, H. Zhu, S. Yang, N. Li, Q. Xu, H. Li, J. He and J. Lu, *Adv. Mater.*, 2016, **28**, 10443-10458.
651. Y. Ding, W. Xu, Y. Yu, H. Hou and Z. Zhu, *ACS Appl. Mater. Interfaces*, 2018, **10**, 6652-6660.
652. V. H. Pham and J. H. Dickerson, *ACS Appl. Mater. Interfaces*, 2014, **6**, 14181-14188.
653. H. Zhu, Q. Zhang, B. G. Li and S. P. Zhu, *Adv. Mater. Interfaces*, 2017, **4**, 1700560.
654. H. Zhu, D. Chen, W. An, N. Li, Q. Xu, H. Li, J. He and J. Lu, *Small*, 2015, **11**, 5222-5229.
655. Q. Zhu, Y. Chu, Z. K. Wang, N. Chen, L. Lin, F. T. Liu and Q. M. Pan, *J. Mater. Chem. A*, 2013, **1**, 5386-5393.
656. L. Xia, F. Chen, Z. Cai, J. Chao, Y. Tian and D. Zhang, *Sep. Purif. Technol.*, 2022, **282**, 120119.
657. X. Gui, J. Wei, K. Wang, A. Cao, H. Zhu, Y. Jia, Q. Shu and D. Wu, *Adv. Mater.*, 2010, **22**, 617-621.
658. H. C. Bi, Z. Y. Yin, X. H. Cao, X. Xie, C. L. Tan, X. Huang, B. Chen, F. T. Chen, Q. L. Yang, X. Y. Bu, X. H. Lu, L. T. Sun and H. Zhang, *Adv. Mater.*, 2013, **25**, 5916-5921.
659. Z. Y. Wu, C. Li, H. W. Liang, J. F. Chen and S. H. Yu, *Angew. Chem. Int. Ed. Engl.*, 2013, **52**, 2925-2929.
660. H. Z. Liu, B. Y. Geng, Y. F. Chen and H. Y. Wang, *ACS Sustainable Chem. Eng.*, 2017, **5**, 49-66.
661. Y. Chen, L. Zhang, Y. Yang, B. Pang, W. Xu, G. Duan, S. Jiang and K. Zhang, *Adv. Mater.*, 2021, **33**, e2005569.
662. P. Phanthong, P. Reubroycharoen, S. Kongparakul, C. Samart, Z. Wang, X. Hao, A. Abudula and G. Guan, *Carbohydr. Polym.*, 2018, **190**, 184-189.
663. Q. Shang, J. Chen, Y. Hu, X. Yang, L. Hu, C. Liu, X. Ren and Y. Zhou, *Polymers*, 2021, **13**, 625.
664. F. Fan, Z. Tian and Z. Wang, *Nano Energy*, 2012, **1**, 328-334.
665. N. Zhang, H. J. Gu, K. Y. Lu, S. M. Ye, W. H. Xu, H. X. Zheng, Y. X. Song, C. R. Liu, J. W. Jiao, Z. K. Wang and X. F. Zhou, *Nano Energy*, 2021, **82**, 105735.
666. Z. H. Lin, G. Cheng, S. Lee, K. C. Pradel and Z. L. Wang, *Adv. Mater.*, 2014, **26**, 4690-4696.
667. X. Li, L. Zhang, Y. Feng, Y. Zheng, Z. Wu, X. Zhang, N. Wang, D. Wang and F. Zhou, *Adv. Funct. Mater.*, 2021, **31**, 2010220.
668. W. H. Xu, Y. X. Song, R. X. Xu and Z. K. Wang, *Adv. Mater. Interfaces*, 2021, **8**, 2000670.
669. L. Wang, Y. Song, W. Xu, W. Li, Y. Jin, S. Gao, S. Yang, C. Wu, S. Wang and Z. Wang, *EcoMat*, 2021, **3**, e12116.
670. H. Cho, J. Chung, G. Shin, J. Y. Sim, D. S. Kim, S. Lee and W. Hwang, *Nano Energy*, 2019, **56**, 56-64.
671. J. Zhao, D. Wang, F. Zhang, J. Pan, P. Claesson, R. Larsson and Y. Shi, *Nano-Micro Lett.*, 2022, **14**, 160.
672. L. L. Zhao, L. Q. Liu, X. Y. Yang, H. X. Hong, Q. M. Yang, J. W. Wang and Q. W. Tang, *J. Mater. Chem. A*, 2020, **8**, 7880-7888.
673. S. M. Hu, Z. J. Shi, R. Z. Zheng, W. L. Ye, X. Gao, W. W. Zhao and G. Yang, *ACS Appl. Mater. Interfaces*, 2020, **12**, 40021-40030.
674. Q. Zhang, C. Jiang, X. Li, S. Dai, Y. Ying and J. Ping, *ACS Nano*, 2021, **15**, 12314-12323.
675. Y. Chen, B. Xie, J. Long, Y. Kuang, X. Chen, M. Hou, J. Gao, S. Zhou, B. Fan, Y. He, Y. T. Zhang, C. P. Wong, Z. Wang and N. Zhao, *Adv. Mater.*, 2021, **33**, 2104290.
676. W. Xu, X. Zhou, C. Hao, H. Zheng, Y. Liu, X. Yan, Z. Yang, M. Leung, X. C. Zeng, R. X. Xu and Z. Wang, *Natl. Sci. Rev.*, 2019, **6**, 540-550.
677. W. H. Xu and Z. K. Wang, *Joule*, 2020, **4**, 2527-2531.
678. Z. Ma, J. Ai, Y. Shi, K. Wang and B. Su, *Adv. Mater.*, 2020, **32**, 2006839.
679. Z. Ma, Q. Wang, J. Ai and B. Su, *ACS Nano*, 2021, **15**, 12151-12160.
680. J. Y. Huang, Q. Wang, Z. H. Wu, Z. Ma, C. Z. Yan, Y. S. Shi and B. Su, *Adv. Funct. Mater.*, 2021, **31**, 2103776.
681. S. Liu and M. Sakr, *Renew. Sustain. Energy Rev.*, 2013, **19**, 64-81.
682. S. M. S. Murshed and C. A. N. de Castro, *Renew. Sustain. Energy Rev.*, 2017, **78**, 821-833.
683. H. E. Ahmed, B. H. Salman, A. S. Kherbeet and M. I. Ahmed, *Int. J. Heat Mass Tran.*, 2018, **118**, 129-153.
684. D. H. Nguyen and H. S. Ahn, *Int. J. Heat Mass Tran.*, 2021, **178**, 121601.
685. K. H. Chu, R. Enright and E. N. Wang, *Appl. Phys. Lett.*, 2012, **100**, 241603.

686. A. R. Betz, J. Jenkins, C. J. Kim and D. Attinger, *Int. J. Heat Mass Tran.*, 2013, **57**, 733-741.
687. N. Miljkovic, R. Enright, Y. Nam, K. Lopez, N. Dou, J. Sack and E. N. Wang, *Nano Lett.*, 2013, **13**, 179-187.
688. L. N. Dong, X. J. Quan and P. Cheng, *Int. J. Heat Mass Tran.*, 2014, **71**, 189-196.
689. D. Attinger, C. Frankiewicz, A. R. Betz, T. M. Schutzius, R. Ganguly, A. Das, C.-J. Kim and C. M. Megaridis, *MRS Energy Sustain.*, 2014, **1**, 4.
690. D. E. Kim, D. I. Yu, D. W. Jerng, M. H. Kim and H. S. Ahn, *Exp. Therm Fluid Sci.*, 2015, **66**, 173-196.
691. K. C. Park, P. Kim, A. Grinthal, N. He, D. Fox, J. C. Weaver and J. Aizenberg, *Nature*, 2016, **531**, 78-82.
692. L. Zhou, W. He, M. Wang and X. Hou, *ChemSusChem*, 2022, **15**, e202102531.
693. C. H. Wang and V. K. Dhir, *J. Heat Transfer.*, 1993, **115**, 659-669.
694. D. S. Wen and B. X. Wang, *Int. J. Heat Mass Tran.*, 2002, **45**, 1739-1747.
695. H. O'Hanley, C. Coyle, J. Buongiorno, T. McKrell, L. W. Hu, M. Rubner and R. Cohen, *Appl. Phys. Lett.*, 2013, **103**, 24102.
696. A. Goswami, S. C. Pillai and G. McGranaghan, *Surfaces and Interfaces*, 2021, **25**, 101143.
697. H. Jo, H. S. Ahn, S. Kane and M. H. Kim, *Int. J. Heat Mass Tran.*, 2011, **54**, 5643-5652.
698. I. U. Vakarelski, N. A. Patankar, J. O. Marston, D. Y. Chan and S. T. Thoroddsen, *Nature*, 2012, **489**, 274-277.
699. M. Searle, P. Emerson, J. Crockett and D. Maynes, *Int. J. Heat Mass Tran.*, 2018, **127**, 772-783.
700. G. T. Liang and I. Mudawar, *Int. J. Heat Mass Tran.*, 2019, **128**, 892-933.
701. A. R. Betz, J. Xu, H. H. Qiu and D. Attinger, *Appl. Phys. Lett.*, 2010, **97**, 141909.
702. P. Pontes, R. Cautela, E. Teodori, A. Moita, Y. Liu, A. L. N. Moreira, A. Nikulin and E. P. del Barrio, *Exp. Therm Fluid Sci.*, 2020, **115**, 110088.
703. M. Može, M. Zupančič and I. Golobič, *Int. J. Heat Mass Tran.*, 2020, **161**, 120265.
704. T. P. Allred, J. A. Weibel and S. V. Garimella, *Phys. Rev. Lett.*, 2018, **120**, 174501.
705. M. Moze, M. Senegacnik, P. Gregorcic, M. Hocevar, M. Zupancic and I. Golobic, *ACS Appl. Mater. Interfaces*, 2020, **12**, 24419-24431.
706. N. Miljkovic, R. Enright and E. N. Wang, *ACS Nano*, 2012, **6**, 1776-1785.
707. R. Xiao, N. Miljkovic, R. Enright and E. N. Wang, *Sci. Rep.*, 2013, **3**, 1988.
708. N. Miljkovic, D. J. Preston, R. Enright and E. N. Wang, *ACS Nano*, 2013, **7**, 11043-11054.
709. K. Rykaczewski, A. T. Paxson, M. Staymates, M. L. Walker, X. Sun, S. Anand, S. Srinivasan, G. H. McKinley, J. Chinn, J. H. Scott and K. K. Varanasi, *Sci. Rep.*, 2014, **4**, 4158.
710. R. F. Wen, Q. Li, J. F. Wu, G. S. Wu, W. Wang, Y. F. Chen, X. H. Ma, D. L. Zhao and R. G. Yang, *Nano Energy*, 2017, **33**, 177-183.
711. R. F. Wen, S. S. Xu, X. H. Ma, Y. C. Lee and R. G. Yang, *Joule*, 2018, **2**, 269-279.
712. Y. Maeda, F. Lv, P. Zhang, Y. Takata and D. Orejon, *Appl. Therm. Eng.*, 2020, **176**, 115386.
713. B. El Fil, G. Kini and S. Garimella, *Int. J. Heat Mass Tran.*, 2020, **160**, 120172.
714. A. Tripathy, C. W. E. Lam, D. Davila, M. Donati, A. Milionis, C. S. Sharma and D. Poulikakos, *ACS Nano*, 2021, **15**, 14305-14315.
715. S. F. Zheng, U. Gross and X. D. Wang, *Adv. Colloid Interface Sci.*, 2021, **295**, 102503.
716. R. Gulfam, T. E. Huang, C. X. Lv, D. Orejon and P. Zhang, *Int. J. Heat Mass Tran.*, 2022, **185**, 122384.
717. C. W. Lo, C. C. Wang and M. C. Lu, *ACS Appl. Mater. Interfaces*, 2014, **6**, 14353-14359.
718. Y. Tang, X. Yang, Y. Li, Y. Lu and D. Zhu, *Nano Lett.*, 2021, DOI: 10.1021/acs.nanolett.1c01584.
719. R. Enright, N. Miljkovic, A. Al-Obeidi, C. V. Thompson and E. N. Wang, *Langmuir*, 2012, **28**, 14424-14432.
720. N. Miljkovic, R. Enright and E. N. Wang, *J. Heat Transfer.*, 2013, **135**, 111004.
721. R. Wen, Z. Lan, B. Peng, W. Xu, R. Yang and X. Ma, *ACS Appl. Mater. Interfaces*, 2017, **9**, 13770-13777.
722. J. Cheng, A. Vandadi and C.-L. Chen, *Appl. Phys. Lett.*, 2012, **101**, 131909.
723. E. Ölçeroğlu and M. McCarthy, *ACS Appl. Mater. Interfaces*, 2016, **8**, 5729-5736.
724. D. Seo, J. Shim, B. Moon, K. Lee, J. Lee, C. Lee and Y. Nam, *ACS Appl. Mater. Interfaces*, 2020, **12**, 4068-4080.
725. R. Wen, S. Xu, D. Zhao, Y. C. Lee, X. Ma and R. Yang, *ACS Appl. Mater. Interfaces*, 2017, **9**, 44911-44921.

726. D. J. Preston and E. N. Wang, *Joule*, 2018, **2**, 205-207.
727. B. Mondal, M. M. G. Eain, Q. F. Xu, V. M. Egan, J. Punch and A. M. Lyons, *ACS Appl. Mater. Interfaces*, 2015, **7**, 23575-23588.
728. Y. Cho, T. S. Shim and S. Yang, *Adv. Mater.*, 2016, **28**, 1433-1439.
729. C. W. Lo, Y. C. Chu, M. H. Yen and M. C. Lu, *Joule*, 2019, **3**, 2806-2823.
730. M. J. Hoque, S. Chavan, R. Lundy, L. N. Li, J. C. Ma, X. Yan, S. H. Lei, N. Miljkovic and R. Enright, *Cell Reports Physical Science*, 2022, **3**, 100823.
731. M. Alwazzan, K. Egab, B. L. Peng, J. Khan and C. Li, *Int. J. Heat Mass Tran.*, 2017, **112**, 991-1004.
732. D. J. Preston, Z. Lu, Y. Song, Y. Zhao, K. L. Wilke, D. S. Antao, M. Louis and E. N. Wang, *Sci. Rep.*, 2018, **8**, 540.
733. D. Seo, J. Shim, C. Lee and Y. Nam, *Sci. Rep.*, 2020, **10**, 2959.
734. J. Y. Ho, K. F. Rabbi, S. Sett, T. N. Wong and N. Miljkovic, *Int. J. Heat Mass Tran.*, 2021, **172**, 121149.
735. H. Tsuchiya, M. Tenjimbayashi, T. Moriya, R. Yoshikawa, K. Sasaki, R. Togasawa, T. Yamazaki, K. Manabe and S. Shiratori, *Langmuir*, 2017, **33**, 8950-8960.
736. K. F. Rabbi, J. Y. Ho, X. Yan, J. C. Ma, M. J. Hoque, S. Sett and N. Miljkovic, *Adv. Funct. Mater.*, 2022, **32**, 2112837.
737. D. Monga, Z. Guo, L. Shan, S. A. Taba, J. Sarma and X. Dai, *ACS Appl. Mater. Interfaces*, 2022, **14**, 13932-13941.
738. N. Miljkovic, D. J. Preston, R. Enright and E. N. Wang, *Nat. Commun.*, 2013, **4**, 2517.
739. C. Zhang, D. Wang, J. Yang, W. Zhang, Q. Sun, F. Yu, Y. Fan, Y. Li, L. Chen and X. Deng, *J. Phys. Chem. B*, 2021, **125**, 1936-1943.
740. M. Moradi, S. F. Chini and M. H. Rahimian, *AIP Adv.*, 2020, **10**, 095123.
741. I. Oh, H. Cha, J. Chen, S. Chavan, H. Kong, N. Miljkovic and Y. Hu, *ACS Nano*, 2020, **14**, 13367-13379.
742. J. Ma, L. E. Porath, M. F. Haque, S. Sett, K. F. Rabbi, S. Nam, N. Miljkovic and C. M. Evans, *Nat. Commun.*, 2021, **12**, 5210.
743. W. Chang, B. Peng, K. Egab, Y. Zhang, Y. Cheng, X. Li, X. Ma and C. Li, *Science Bulletin*, 2021, **66**, 1877-1884.
744. A. Keiser, L. Keiser, C. Clanet and D. Quere, *Soft Matter*, 2017, **13**, 6981-6987.
745. X. Tian, S. Shaw, K. R. Lind and L. Cademartiri, *Adv. Mater.*, 2016, **28**, 3677-3682.
746. United Nations, Paris Agreement, https://unfccc.int/process/the-paris-agreement/status-of-ratification.
747. H. Li, W. Fang, Z. Zhao, A. Li, Z. Li, M. Li, Q. Li, X. Feng and Y. Song, *Angew. Chem. Int. Ed.*, 2020, **59**, 10535-10539.
748. W.-P. Huang, X. Chen, M. Hu, D.-F. Hu, J. Wang, H.-Y. Li, K.-F. Ren and J. Ji, *Chem. Mater.*, 2019, **31**, 834-841.
749. Y. Wang, K. Ma and J. H. Xin, *Adv. Funct. Mater.*, 2018, **28**, 1705128.
750. X. Lou, Y. Huang, X. Yang, H. Zhu, L. Heng and F. Xia, *Adv. Funct. Mater.*, 2020, **30**, 1901130.
751. L. Yan, X. Yang, Y. Zhang, Y. Wu, Z. Cheng, S. B. Darling and L. Shao, *Mater. Today*, 2021, **51**, 626-647.